Search for Quantum Black Holes with the Horizon Quantum Mechanics Model in Dijet Angular Distributions using ATLAS Detector

by

Haojie Ni

A thesis submitted in partial fulfillment of the requirements for the degree of

Master of Science

Department of Physics

University of Alberta

Abstract

Quantum black holes can be described by theories with extra dimensions. Its production at the Large Hadron Collider is studied by both the ATLAS and CMS collaborations but no evidence is found for such states. The lack of evidence may arise from the inaccurate description of models. The horizon quantum mechanics model treats the horizon of a black hole as a quantum object instead of a classic object. This model modification reduces our sensitivity in resonance searches but favours angular searches. This is the first analysis searching for evidence of the horizon quantum mechanics model in dijet angular distributions using data taken with the ATLAS detector. Using data corresponding to an integrated luminosity of 36.2 fb^{-1} at $\sqrt{s} = 13$ TeV, no significant evidence for a quantum black hole is found. We are able to exclude the parameter space of the horizon quantum mechanics model for $M_D < 8.0$, 7.4 and 6.7 TeV for n =2, 4 and 6, respectively at 95% confidence level, where M_D is the higher dimensional Planck scale and n is the number of extra dimensions. If black holes are not discovered in the ATLAS full Run2 data corresponding to 139 fb^{-1}, we expect to further exclude the parameter space where $M_D < 8.6$, 7.9 and 7.0 TeV for $n = 2$, 4 and 6, respectively.

Preface

Some of the research content of this thesis is part of a research project in the ATLAS collaboration. The derivations of data samples and quantum chromodynamics simulations are prepared by Simone Francescato at National Institute for Nuclear Physics (INFN) in Italy. The theoretical quantum chromodynamics correction in Chapter 5 and theoretical uncertainties in Chapter 6 are provided by Trine Poulsen at Lund University in Sweden. The modification and application of these uncertainties are my original work. The study of jet selections and kinematics in Chapter 4, updated binning strategy in Chapter 5, systematic uncertainties in Chapter 6 and data analysis in Chapter 8 are my original work as well.

Acknowledgements

First of all, I would like to sincerely say "thank you" to my supervisor, Doug Gingrich, for providing me with the opportunity to study at the University of Alberta and supporting me throughout the program. I appreciate your patience and encouragement, especially during the pandemic time, which makes me feel worry-free. I also want to thank the post-docs in our research group, especially Jyoti Prakash Biswal and Miguel Villaplana. Thank you for discussing the materials and sharing your experiences on doing ATLAS analyses.

My study experience at the University of Alberta is fantastic. I want to thank Brittany Lu, Md Sarmiur Rahman Mir, Fairhurst Lyons and Yuqi Deng for having helpful discussions on course materials. It was because of you that I did not feel helpless when I started my study here. I also want to thank the professors and teaching assistants for delivering excellent courses. These courses are the best I have ever taken. And, thank you, every staff in the physics department, for creating a supportive environment for graduate students. I really feel assured about everything because I know I can get help from you if I have any questions or troubles.

Contents

List of Tables

List of Figures

Chapter 1

Introduction

The hierarchy problem in physics refers to the large gap in strength between the gravitational force and the weak force. The weak force is 10^{34} times stronger than the gravitational force in terms of their interaction strengths. Theories with extra dimensions are developed which can solve this problem. Some theories, such as the models developed by Nima Arkani-Hamed, Savas Dimopoulos and Gia Dvali (ADD) [1, 2] and by Lisa Randall and Raman Sundrum (RS) [3], allow the existence of quantum black holes (QBH). The production of QBH[1] in the Large Hadron Collider (LHC) is studied [4], and searches for QBH are performed in several channels [5, 6, 7, 8, 9, 10] by both the ATLAS and CMS collaborations while no evidence of QBH is found.

Most of the analyses look for a bump-like signal in the invariant-mass spectrum on the top of a smooth background. However, such a bump-like shape is based on an assumption that QBH can only exist above the Planck mass M_D where D is the total number of space-time dimensions. This assumption may not be valid because it is based on the classic concept of the event horizon. The horizon quantum mechanics model (HQM) [11, 12] modifies the horizon of QBH as an independent quantum object with its own wave function. This modification broadens the invariant mass spectrum of QBH, which makes the sensitivity of resonance searches highly suppressed [13].

Despite the low sensitivity of resonance searches, angular searches are less impacted by the HQM modification. In the Standard Model (SM), jet-jet (di-

[1] QBH is refereed to the ADD model in the following contents of this thesis if not explicitly explained.

jet) event production is dominated by t-channel scattering in quantum chromodynamics (QCD). QCD dijet events tend to have a flat χ distribution where χ is an angular variable and will be further explained in Chapter 2. In contrast, dijet events originating from HQM decays tend to peak in the low χ region of the χ distribution, which is a distinguishable feature in angular analyses. The last angular search in ATLAS was performed at a centre-of-mass $\sqrt{s} = 13$ TeV with an integrated luminosity of 37 fb^{-1} [14]. This thesis updates that analysis with new procedure choices designed for using full Run 2 data corresponding to 139 fb^{-1}. We aim to report the discovery significance of HQM events. If they are not observed, limits at 95% confidence level on the parameters of the HQM model are given.

This thesis is organized as follows: Chapter 2 introduces theories of QCD and HQM as well as their simulations. Chapter 3 describes the ATLAS detector. Chapter 4 introduces the jet reconstruction, calibrations and selections. Chapter 5 introduces estimation strategies for QCD and HQM yields. Chapter 6 focuses on the systematic uncertainties of the analysis. Chapter 7 describes the likelihood model and the statistical techniques to set limits at 95% confidence level on the production cross-section of the HQM model. Chapter 8 shows the results of fitting data and simulations to the likelihood model. Discovery significance and parameter limits are given. Chapter 9 summarizes the analysis.

Chapter 2

Theories and models

In this chapter, we introduce the Standard Model of particle physics which plays a critical role in describing fundamental blocks of our universe. Theories with large extra dimensions which interest us the most are discussed as well. They predict the existence of quantum black holes created in ATLAS and have the potential to solve some of the problems left by the Standard Model.

2.1 The Standard Model

In particle physics, there are four fundamental forces: electromagnetic force, weak force, strong force and gravitational force. The Standard Model [15, 16] is the most successful theory describing elementary particles and the first three forces mentioned above. Elementary particles have several intrinsic properties, such as charge, colour and spin. Table 2.1 lists the particles in the model. They are categorized into bosons and fermions by their spins. Bosons are the ones having spins of 0 or 1 that obey Bose-Einstein statistics. Bosons include the gluon (g), photon (γ), W bosons ($W^{\pm}$), Z boson (Z) and Higgs boson (H). Fermions are the particles having spin 1/2 and obey Fermi–Dirac statistics. They are further classified into quarks and leptons. Quarks come in three generations and two flavours for each generation: the first generation of up (u) and down (d) quarks, the second generation of charm (c) and strange (s) quarks, and the third generation of top (t) and bottom (b) quarks. Similar to quarks, leptons also include three generations: the first generation of electron (e) and electron neutrino (ν_e), the second generation of muon (μ) and muon

Table 2.1: Particles described by the Standard Model.

Quarks of spin $\frac{1}{2}$	up (u)	charm (c)	top (t)
	down (d)	strange (s)	bottom (b)
Fermions of spin $\frac{1}{2}$	electron (e)	muon (μ)	tau (τ)
	e-neutrino (ν_e)	μ-neutrino (ν_μ)	τ-neutrino (ν_τ)

Bosons of spin 1	W-boson ($W^\pm$)	Z-boson (Z)	gluon (g)	photon (γ)
Boson of spin 0	Higgs (H)			

neutrino (ν_μ), and the third generation of tau particle (τ) and tau neutrino (ν_τ). In addition to quarks and leptons, there are also anti-quarks and anti-leptons. A anti-particle has the same mass as the corresponding particle but opposite electrical charges and quantum numbers.

Fundamental forces refer to the interactions between particles. They interact with each other by exchanging the force carriers, namely, bosons. The electromagnetic interaction exists among particles carrying electrical charges. Up, charm and top quarks carry $\frac{2}{3}$ charge while down, strange and bottom quarks carry $-\frac{1}{3}$ charge. Electron, muon and tau carry -1 charge while the neutrinos are charge-neutral particles. $W^\pm$ bosons are the only charged bosons. Quantum electrodynamics (QED) describes the interaction between charged particles by exchanging photons.

Another interaction, the strong interaction, exists between the particles carrying colours. Colour is an intrinsic property of a particle just like its electrical charge. Both quarks and gluon carry colours while other particles are colour-neutral. QCD describes the strong interaction by exchanging gluons. It is the dominant experimental phenomenon in ATLAS. Thus, it will be further discussed in the next subsection.

The weak interaction is another interaction described in the Standard Model. The weak interaction exists between fermions and allows them to change their types. The mediators are $W^\pm$ and Z bosons. Figure 2.1 is a Feynman diagram showing the beta decay where a down quark decays into an up quark by emitting a W^- boson. The W^- boson further decays to an electron and an anti-electron-neutrino. This process turns a neutron into a

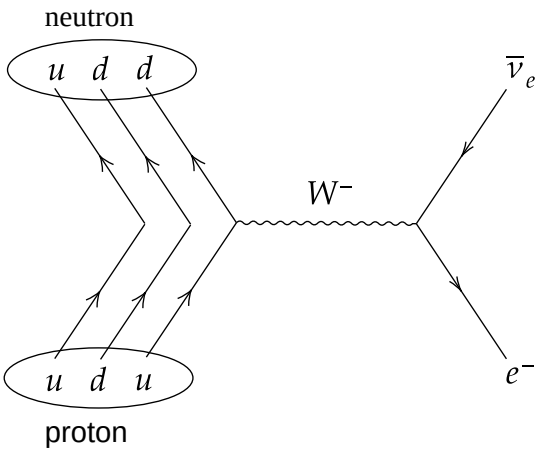

Figure 2.1: A Feynman diagram of the beta decay which turns a neutron into a proton.

proton.

The Standard Model has shown great success in particle physics. The most famous study could be the discovery of the Higgs boson [17]. The Brout-Englert-Higgs mechanism [18, 19, 20, 21, 22, 23] was proposed to explain the origin of particle mass in 1964. This mechanism predicts the existence of a spin 0 particle, namely, the Higgs boson. One year after the discovery, the physics Nobel Prize was awarded to François Englert and Peter W. Higgs for their contribution in developing the Brout-Englert-Higgs mechanism.

Although the Standard Model is successful in predicting the existence of particles and explaining the interactions among them, it is still not perfect. There are some questions that it can not answer. The hierarchy problem mentioned in Chapter 1 is one of them. Another problem of the Standard Model is its incapability of describing the gravitational force. Thus, we have to explore models beyond the Standard Model (BSM) which provide different perspectives and have the potential to solve these problems. The high centre-of-mass energy achieved by LHC enables us to not only verify SM predictions but also examine BSM models which may lead to discoveries of new phenomena.

2.2 Quantum chromodynamics and the parton model

QCD is crucial to collider physics because the strong interaction dominates proton-proton (pp) collisions. In QCD, there are three colours defined as red, blue and green and three corresponding anti-colours. The definition of colour has nothing to do with the visible colours but serves as a convenient way of presenting the concept. A quark carries one colour while an anti-quark carries one anti-colour. In comparison, a gluon carries one colour and one anti-colour. One of the important properties of QCD is "colour confinement". It requires quarks to be confined in hadrons to form colour-neutral particles. For example, a neutron is made of three quarks: one up quark and two down quarks. These quarks carry one colour each: red, blue or green. Thus the neutron is in a colour-neutral state. The assignment of colours to the quarks are arbitrary. As for mesons, such as π^+, it is made of an up quark and an anti-down quark. The up quark carries a colour while the anti-down quarks carry the corresponding anti-colour to make π^+ colour-neutral.

The parton model [24] is proposed to describe the internal structure of hadrons. In this model, a hadron is composed of point-like particles called "partons". Now we know that partons are gluons and quarks in the Standard Model. Inside a hadron, there are gluons and two types of quarks: valance quarks and sea quarks. Gluons bind the quarks together by the strong force. Valance quarks are the ones determining the quantum numbers of hadrons, such as charge and spin. Sea quarks have infinite numbers of quarks but no impact on hadron characteristics. In pp collisions, partons from the protons interact with each other and some of them are kicked out from the proton. The parton type and the momentum carried by the parton follow probability functions named as parton distribution functions (PDFs). PDFs not only depend on the parton type, but also the momentum transferred from another parton to the kicked-out parton. The momentum transfer is denoted as Q. Figure 2.2 shows the nominal leading-order PDFs of NNPDF2.3 [25]. The kicked-out parton can go through a series of interactions and result in a shower

of hadrons. A hadron shower has momentum approximately aligned to the momentum of the originating parton. Thus, most of the hadrons in the shower are distributed in a small cone. The hadron shower is called a jet which is an important proxy to study the partons in pp collisions.

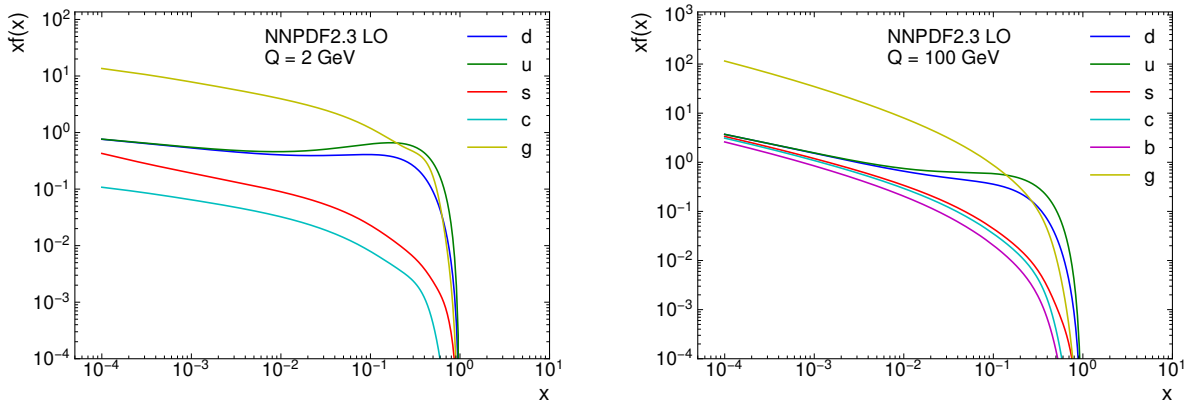

Figure 2.2: Parton distribution functions at (left) $Q = 2$ and (right) $Q = 100$ GeVof leading-order NNPDF2.3 where Q is the momentum transfer. The x-axis is the momentum fraction x carried by the parton and the y-axis is the fraction times the parton distribution functions $xf(x)$.

2.2.1 QCD dijet physics

Dijet events originate from

$$\text{parton}_i(p_1) + \text{parton}_j(p_2) \to \text{parton}_k(p_3) + \text{parton}_l(p_4)$$

scattering events where $\text{parton}_{i,j}$ ($\text{parton}_{k,l}$) are the two incoming (outcoming) partons. Variables $p_{1,2,3,4}$ denotes the four-momenta of the partons. We use the ATLAS coordinate system to discuss the kinematics of the parton-parton system. The coordinate system is illustrated in Figure 2.3. The z-axis is defined in the direction of the proton beam pipe. The direction pointing to the centre of the LHC ring is referred to as the x-axis and the upward direction is referred to as the y-axis. The azimuthal angle on the x-y plane is denoted as ϕ and measured from the x-axis. The polar angle is denoted as θ and measured from the z-axis. Pseudorapidity is defined as $\eta = -\ln\tan(\theta/2)$ which approaches the rapidity $y = \frac{1}{2}\ln\left(\frac{E+p_z}{E-p_z}\right)$ in the massless-particle limit

where p_z is the z-direction momentum. Gluon is massless in nature. The production rates of light quarks (u, d and s) are much larger than heavy quarks (c, b and t). Considering the small masses of light quarks relative to the proton energies and the small production rates of heavy quarks, we assume that partons in QCD interactions are massless. However, this assumption may not be valid in theories other than QCD. For example, quantum black holes described in Ref. [4] have equal probability for producing quark flavours which makes the top quark mass non-negligible. The four-momentum of a massless parton is given as

$$\begin{aligned} p &= (E, p_x, p_y, p_z) \\ &= (p_{\mathrm{T}} \cosh(y), p_{\mathrm{T}} \cos(\phi), p_{\mathrm{T}} \sin(\phi), p_{\mathrm{T}} \sinh(y)) \end{aligned} \tag{2.1}$$

where p_{T} is the transverse momentum

$$p_{\mathrm{T}} = \sqrt{p_x^2 + p_y^2}. \tag{2.2}$$

It is simplest to discuss the kinematics in a centre-of-mass frame of the parton-parton system instead of a lab frame. The boost speed of the centre-of-mass frame is in the direction of the proton beam pipe that is the z-direction. Therefore, only variables having z-direction dependence are transformed and labelled with a star superscript, such as $\theta \to \theta^*$. The transformation of rapidity is additive under a boost in the z-direction. According to this feature, the boost rapidity y_b of the centre-of-mass frame and the rapidity $\pm y^*$ of partons relative the centre of mass are

$$\begin{aligned} y_b &= (y_3 + y_4)/2, \\ y^* &= (y_3 - y_4)/2. \end{aligned} \tag{2.3}$$

Other variables defined in the x-y plane, such as p_{T} and ϕ, are not transformed. The four-momenta of the outcoming partons in the centre-of-mass frame are given as:

$$\begin{aligned} q_3 &= (p_{\mathrm{T}} \cosh(y^*), p_{\mathrm{T}} \cos(\phi), p_{\mathrm{T}} \sin(\phi), p_{\mathrm{T}} \sinh(y^*)), \\ q_4 &= (p_{\mathrm{T}} \cosh(-y^*), p_{\mathrm{T}} \cos(\phi + \pi), p_{\mathrm{T}} \sin(\phi + \pi), p_{\mathrm{T}} \sinh(-y^*)). \end{aligned} \tag{2.4}$$

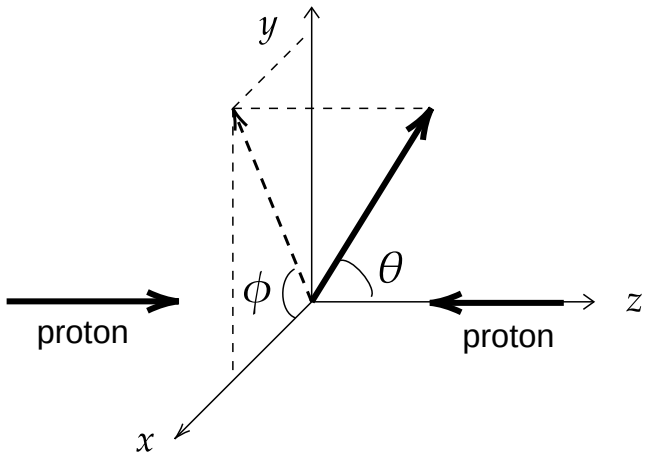

Figure 2.3: The coordinate system used by the ATLAS experiment.

To calculate the cross-section of $2 \to 2$ scattering, Mandelstam variables ($\hat{s}$, $\hat{t}$, $\hat{u}$) are introduced for convenience:

$$\begin{aligned} \hat{s} &= (p_1 + p_2)^2, \\ \hat{t} &= (p_1 - p_3)^2 \xrightarrow[\text{approximation}]{\text{massless-parton}} -\frac{1}{2}\hat{s}(1 - \cos\theta^*), \\ \hat{u} &= (p_1 - p_4)^2 \xrightarrow[\text{approximation}]{\text{massless-parton}} -\frac{1}{2}\hat{s}(1 + \cos\theta^*). \end{aligned} \tag{2.5}$$

The variable $\hat{s}$ is the squared centre-of-mass energy in the parton-parton system while the variable s is the one in the proton-proton system. $\hat{s}$ is only a fraction of s since a parton only carries a part of the momentum of a proton. Mandelstam variables are invariant under Lorentz transformations. They correspond to three channels of $2 \to 2$ scattering, as shown in Figure 2.4. In terms of physics meaning, $\hat{s}$ is the square of the parton-parton invariant mass M:

$$M^2 = \hat{s} = (p_1 + p_2)^2 = (p_3 + p_4)^2 = 4p_{\mathrm{T}}^2 \cosh^2(y^*). \tag{2.6}$$

Variable $\hat{t}$ corresponds to the transferred momentum from one parton to the other in the $\hat{t}$-channel scattering. Variable $\hat{u}$ is an analog of $\hat{t}$ in the $\hat{u}$-channel scattering.

The basic $2 \to 2$ interactions in QCD, referred to as the leading order (LO) interactions, are partly shown in Figure 2.5. The rest of the LO interactions can be obtained by reversing the incoming and outcoming particles as well as reversing quark and anti-quarks of the interactions shown in Figure 2.5. The

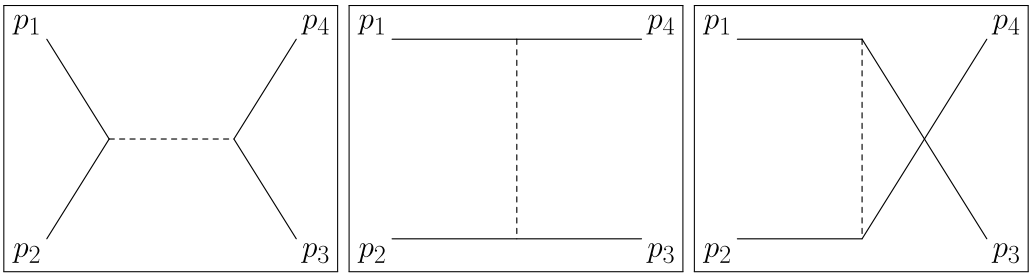

Figure 2.4: Illustration of (left) $\hat{s}$-, (middle) $\hat{t}$- and (right) $\hat{u}$-channels of the $2 \to 2$ scattering processes. Solid lines are partons and dashed lines are bosons.

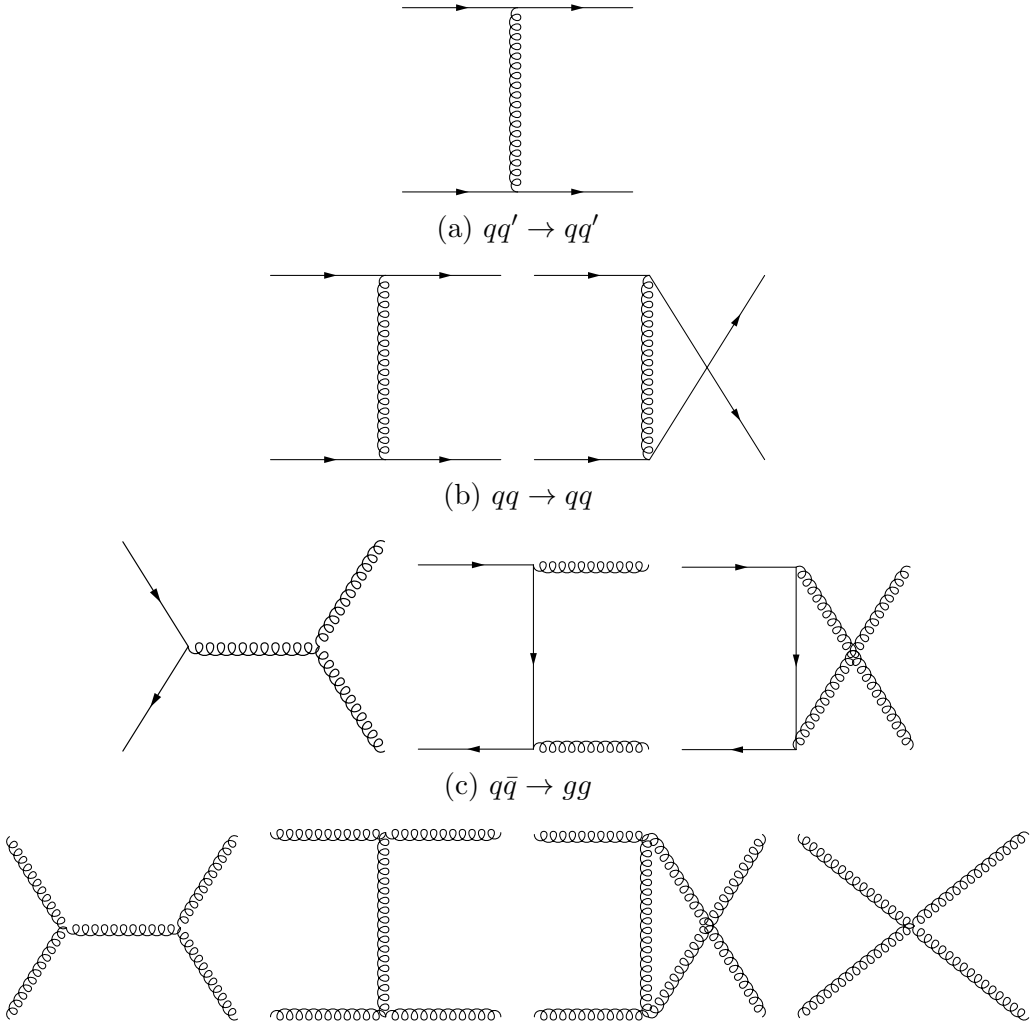

(a) $qq' \to qq'$

(b) $qq \to qq$

(c) $q\bar{q} \to gg$

(d) $gg \to gg$

Figure 2.5: Feynman diagrams of LO QCD jet-jet production, taken from Ref. [26]. Quark q' denotes a different flavour from quark q. Other leading-order interactions can be obtained by reversing the incoming and outcoming partons as well as reversing quarks and anti-quarks.

differential cross-section of each type of interaction can be calculated as

$$\frac{\mathrm{d}\sigma^{ij}}{\mathrm{d}\cos\theta^*} = \sum_{k,l} \frac{1}{32\pi M} \overline{\sum} |\mathcal{M}(ij \to kl)|^2 \frac{1}{1+\delta_{kl}} \sim \sum_{k,l} \overline{\sum} |\mathcal{M}(ij \to kl)|^2 \quad (2.7)$$

where $\mathcal{M}(ij \to kl)$ is a matrix element [26]. $\overline{\sum}$ denotes the average over initial-state and sum over final-state spins and colours respectively. The LO calculation of $\overline{\sum}|\mathcal{M}(ij \to jk)|^2$ is given in Table 2.2. In a small θ^* approxi-

Table 2.2: The matrix elements for $2 \to 2$ parton scattering sub-processes assuming partons are massless. The first three columns are taken from Refs. [26, 27]. Quark q' denotes a different flavour from quark q. The $\theta^* = \pi/2$ column shows the numerical results of the matrix elements while the $\theta^* \to 0$ shows the asymptotic results.

Process	$\overline{\sum}\lvert\mathcal{M}\rvert^2/g^4$	$\theta^* = \pi/2$	$\theta^* \to 0$
$qq' \to qq'$	$\frac{4}{9}\frac{\hat{s}^2+\hat{u}^2}{\hat{t}^2}$	2.22	$\frac{8}{9}\frac{\hat{s}^2}{\hat{t}^2}$
$q\overline{q'} \to q\overline{q'}$	$\frac{4}{9}\frac{\hat{s}^2+\hat{u}^2}{\hat{t}^2}$	2.22	$\frac{8}{9}\frac{\hat{s}^2}{\hat{t}^2}$
$qq \to qq$	$\frac{4}{9}\left(\frac{\hat{s}^2+\hat{u}^2}{\hat{t}^2}+\frac{\hat{s}^2+\hat{t}^2}{\hat{u}^2}\right)-\frac{8}{27}\frac{\hat{s}^2}{\hat{u}\hat{t}}$	3.26	$\frac{8}{9}\frac{\hat{s}^2}{\hat{t}^2}$
$q\overline{q} \to q'\overline{q'}$	$\frac{4}{9}\frac{\hat{t}^2+\hat{u}^2}{\hat{s}^2}$	0.22	0
$q\overline{q} \to q\overline{q}$	$\frac{4}{9}\left(\frac{\hat{s}^2+\hat{u}^2}{\hat{t}^2}+\frac{\hat{u}^2+\hat{t}^2}{\hat{s}^2}\right)-\frac{8}{27}\frac{\hat{u}^2}{\hat{s}\hat{t}}$	2.59	$\frac{8}{9}\frac{\hat{s}^2}{\hat{t}^2}$
$q\overline{q} \to gg$	$\frac{32}{27}\frac{\hat{t}^2+\hat{u}^2}{\hat{t}\hat{u}}-\frac{8}{3}\frac{\hat{t}^2+\hat{u}^2}{\hat{s}^2}$	1.04	$\frac{32}{27}\frac{\hat{s}}{\hat{t}}$
$gg \to q\overline{q}$	$\frac{1}{6}\frac{\hat{t}^2+\hat{u}^2}{\hat{t}\hat{u}}-\frac{3}{8}\frac{\hat{t}^2+\hat{u}^2}{\hat{s}^2}$	0.15	$\frac{1}{6}\frac{\hat{s}}{\hat{t}}$
$gq \to gq$	$-\frac{4}{9}\frac{\hat{s}^2+\hat{u}^2}{\hat{s}\hat{u}}+\frac{\hat{s}^2+\hat{u}^2}{\hat{t}^2}$	6.11	$2\frac{\hat{s}^2}{\hat{t}^2}$
$gg \to gg$	$\frac{9}{2}\left(3-\frac{\hat{t}\hat{u}}{\hat{s}^2}-\frac{\hat{s}\hat{u}}{\hat{t}^2}-\frac{\hat{s}\hat{t}}{\hat{u}^2}\right)$	30.4	$\frac{9}{2}\frac{\hat{s}^2}{\hat{t}^2}$

mation, we can rewrite $\hat{t}$ and $\hat{u}$ to the following forms:

$$\begin{aligned} \hat{t} &\sim -\sin^2\left(\frac{\theta^*}{2}\right)\cdot\hat{s}, \\ \hat{u} &\sim -\hat{s}. \end{aligned} \tag{2.8}$$

Substituting the row of $\theta^* \to \pi/2$ in Table 2.2 to Equation 2.7 can give us an estimation of cross-sections of these processes. To get the small angle approximation of the cross-section, we can substitute Equation 2.8 into the cross-section formula of each main process given by Equation 2.7 and Table 2.2. It turns out the differential cross-sections share a similar form of

$$\frac{\mathrm{d}\sigma^{i,j}}{\mathrm{d}\cos\theta^*} \sim \frac{1}{\sin^4(\frac{\theta^*}{2})} \tag{2.9}$$

which features the $\hat{t}$-channel scattering process similar to the Rutherford scattering in a small angle. An angular variable χ is defined as

$$\chi = \frac{1+\cos\theta^*}{1-\cos\theta^*} \approx \exp(2|y^*|) \tag{2.10}$$

where the latter is a massless-parton approximation. The differential cross-section of χ of each process turns out to be a approximately constant:

$$\frac{\mathrm{d}\sigma^{i,j}}{\mathrm{d}\chi} \sim \text{constant}. \tag{2.11}$$

Experimentally, the QCD dijet events will have an approximately flat χ distribution.

2.2.2 Monte Carlo simulations of QCD dijet production

The Monte Carlo (MC) simulations of QCD dijet events are generated using the Pythia 8 generator [28] with leading-order NNPDF2.3 PDFs [29]. Detector simulation follows the standard ATLAS workflow [30] using Geant 4 [31]. The specific ATLAS samples used can be found in Appendix A. They are prepared by ATLAS colleagues and divided into thirteen slices covering exclusive leading-jet p_{T} regions [32]. The advantage of splitting the simulation work is that all slices can have close statistical uncertainties. Otherwise, generating one sample covering the whole p_{T} spectrum will lead to extreme small statistical uncertainty in the low p_{T} region but undesired large uncertainty in the

high p_{T} region, because an event has a much larger possibility of being a low p_{T} event than a high p_{T} event.

To combine the thirteen slices into an integrated simulation sample, an event weight $\mathcal{W}_i^s$ is developed as

$$\mathcal{W}_i^s = \frac{\sigma^s \varepsilon^s}{\sum_i w_i^s} \cdot \mathcal{L} \tag{2.12}$$

where the superscript s indicates a slice-level number and the subscript i indicates an event-level number. σ^s is the cross-section of a slice. ε^s, referred to as the filter efficiency, is the fraction of sample that passes from generator simulation to full GEANT 4 simulation. The denominator $\sum_i w_i^s$ sums over the generator weight w_i^s of all events in a slice. $\mathcal{L}$ is the luminosity of the analysis. The weight $\mathcal{W}_i^s$ is applied at the event level to normalize each slice to the luminosity. To simulate the different stages of the Run2 data-taking period, three independent campaigns are generated as MC16a, MC16d and MC16e which correspond to 2015+2016, 2017 and 2018 data taking conditions respectively [33]. They are weighted according to the luminosity measurement as listed in Table 2.3.

Table 2.3: The ATLAS luminosity measurement of the Run2 period, taken from Ref. [33].

	2015+2016	2017	2018	Comb.
Integrated luminosity (fb^{-1})	36.2	44.3	58.5	139.0
Total uncertainty (fb^{-1})	0.8	1.0	1.2	2.4

2.3 Quantum black holes

The ADD model introduces large extra dimensions at small distance scales. It assumes that extra space dimensions are compact within a distance R. The gravitational potential energy of two massive objects (m_1, m_2) separated by distance r is

$$V(r) \sim \begin{cases} \frac{m_1 m_2}{M_D^{n+2}} \frac{1}{r^{n+1}} (r < R) \\ \\ \frac{m_1 m_2}{M_D^{n+2}} \frac{1}{r R^n} (r > R) \end{cases}, \tag{2.13}$$

where n is the number of extra dimensions and M_D is the Planck scale in the D-dimensional space. The relation between D and n is simply $D = n+4$. The potential energy at the boundary R should be consistent with the one in the four-dimensional space given by Newtonian gravity, which gives

$$M_P^2 = M_D^{2+n} R^n \;\Rightarrow\; R = \left(\frac{M_P^2}{M_D^{2+n}} \right)^{1/n} \tag{2.14}$$

where M_P is the four-dimensional Planck scale. It is possible that the Planck scale in the D-dimensional space is close to the electroweak scale $m_{EW} \sim 10^3$ GeV. If this is the case, the hierarchy problem is solved naturally. By substituting M_P with 10^{19} GeV and M_D with 10^3 GeV in Equation 2.14, the parameter R can be parameterized by n:

$$R = 10^{\left(\frac{32}{n} - 3\right)} \text{ GeV}^{-1} \xrightarrow[\text{transform to SI units}]{\times\, \hbar c \sim 10^{-16} \text{GeV·m}} 10^{\left(\frac{32}{n} - 19\right)} \text{ m}. \tag{2.15}$$

The case of $n = 1$ is excluded because $R \sim 10^{13}$ m contradicts the established Newtonian gravity. For $n \geq 2$, $R \leq 10^{-3}$ m can be tested in LHC.

2.3.1 Black hole production

A black hole is formed if its mass is compressed within the corresponding horizon. In ATLAS, a black hole can be produced if two colliding partons are within the horizon of their centre of mass. In this scenario, the black hole inherits the attributes of the two partons, such as colour, charge and spin. The simplest form of a black hole is a Schwarzschild black hole which is non-rotating and charge-neutral. Adding rotation to a Schwarzschild black hole will transform it to a Kerr black hole which is described by the Kerr solution to Einstein field equations. However, general solutions describing rotating black holes with charge are not developed yet. Thus, we will neglect the charge impact on black hole production. The event horizon radius r_h of the Kerr solution is

$$r_h^{n-1} \left[r_h^2 + \frac{(n+2)^2 J^2}{4M^2} \right] = \frac{16\pi G_D M}{(n+2)\Omega_{n+2}} \tag{2.16}$$

where J is the angular momentum in the four-dimensional space and M is the black hole mass. Ω_{n+2} is the area of a unit $n+2$ sphere, given by

$$\Omega_{n+2} = \frac{2\pi^{(n+3)/2}}{\Gamma\left(\frac{n+3}{2}\right)}. \tag{2.17}$$

The D-dimensional Newton constant is denoted as G_D. It can be expressed in terms of the Planck mass

$$G_D = \frac{(2\pi)^n}{8\pi M_P^{n+2}} \tag{2.18}$$

using the PDG convention [34]. Taking the simplest case, a Schwarzschild black hole of $J = 0$ has a horizon radius of

$$r_h = \frac{1}{\sqrt{\pi} M_P} \left[\frac{M}{M_P} \cdot \frac{8\Gamma\left(\frac{n+3}{2}\right)}{n+2} \right]^{\frac{1}{n+1}}. \tag{2.19}$$

The cross-section of a quantum black hole is extrapolated from the geometry cross-section of a semi-classic black hole:

$$\hat{\sigma}_{BH}(M) = F(n) \cdot \pi r_h^2(M) \tag{2.20}$$

where $F(n)$ is a form factor close to unity [35]. By definition, r_h is Lorentz invariant as well as $\hat{\sigma}_{BH}$. Assuming there is no energy loss in the formation of a black hole, its invariant mass is equal to the centre-of-mass energy of the parton pair. Since a parton only carries a fractional energy of a colliding proton, we can define

$$M^2 = \hat{s} = s x_a x_b \equiv s\tau \tag{2.21}$$

where x_a and x_b are the energy fractions carried by the partons relative to the protons. The variable τ has a a minimum boundary $\tau_{\min} = M_{\min}^2/s$ where $M_{\min}$ is the minimum black hole mass. The cross-section in forms of x_a and x_b integrals can be expressed:

$$\sigma_{BH}(s) = \sum_{a,b} \int_{\tau_{\min}}^{1} \mathrm{d}x_a \int_{\tau_{\min}/x_a}^{1} \mathrm{d}x_b f_a(x_a) f_b(x_b) \hat{\sigma}_{BH}(M = \sqrt{s x_a x_b}) \tag{2.22}$$

where a and b sums over parton types. $f_a(x_a)$ and $f_b(x_b)$ are the PDFs of the parton types, a and b.

2.3.2 Horizon quantum mechanics

Searches for ADD black holes has been performed in both ATLAS [14, 36, 37, 38, 39, 40, 41, 42] and CMS [43, 44, 45, 46]. However, black hole events are not found in those studies. The lack of experimental evidence can be caused by

insufficient data or an invalid theoretical description of black holes. To better understand the potential of discovering black holes in ATLAS, we adapt a modification, the horizon quantum mechanics [12], to the typical ADD model and exam it with Run2 data collected by ATLAS.

Horizon quantum mechanics studies the non-locality of the horizon of quantum black holes. Typical ADD models searched for in ATLAS set $M_{\min}$ of black holes at M_D [47]. This setting can be emphasized by adding a Heaviside function $\Theta(\frac{M}{M_D} - 1)$ to the cross-section of QBH production:

$$\sigma_{BH}(s) = \sum_{a,b} \int_{\tau_{\min}}^{1} \mathrm{d}x_a \int_{\tau_{\min}/x_a}^{1} \mathrm{d}x_b f_a(x_a) f_b(x_b) \cdot \Theta\left(\frac{M}{M_D} - 1\right) \hat{\sigma}_{BH}(M). \tag{2.23}$$

The limit on M comes from an argument that the Compton length of a massive particle $\lambda \sim 1/M$ should be the minimal possible radius of its Schwarzschild radius $r_h \sim M$ in the four-dimensional space, which gives $M \sim M_P$.

However, the argument stated above does not really answer the question: what is the event horizon of an object if it is smaller than the Compton length? Ref. [12] proposes the idea of horizon quantum mechanics where the horizon is described by its own wave function $\Phi_H(r_h)$ that is similar to its position wave function $\Phi_S(r)$. The probability of an object being a black hole can be expressed as

$$P_{BH} = \int_0^\infty P_S(r < R_H) \mathcal{P}_H(R_H) \mathrm{d}r \tag{2.24}$$

where $\mathcal{P}_H(R_H)$ is the probability density that the event horizon is located at radius $r = R_H$:

$$\mathcal{P}_H(R_H) = 4\pi R_H^2 |\Phi_H(R_H)|^2; \tag{2.25}$$

and $P_S(r < R_H)$ is the probability that the particle is located within the radius $r < R_H$:

$$P_S(r < R_H) = \int_0^{R_H} |\Phi_S(r)|^2 \mathrm{d}r. \tag{2.26}$$

In this way, the concept of the classic Schwarzschild radius is replaced by a wave function and the probability of an object being a black hole is established. It allows objects lighter than the Planck mass M_D to be found as black holes.

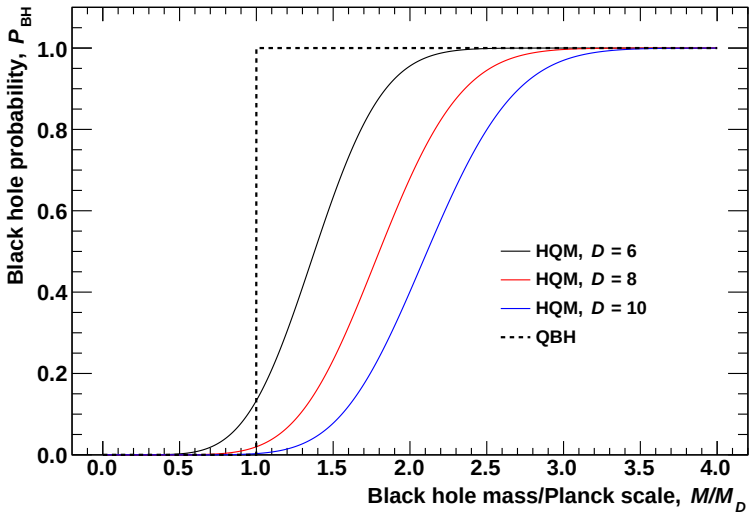

Figure 2.6: Comparison of the black hole probability function P_{BH} of HQM in $D = 6, 8, 10$ dimensional spaces with the Heaviside function of QBH, taken from Ref. [13].

Comparing QBH and HQM

To take HQM into account, the Heaviside function in Equation 2.23 is replaced with P_{BH}, which gives

$$\sigma_{BH}(s) = \sum_{a,b} \int_{\tau_{\min}}^{1} \mathrm{d}x_a \int_{\tau_{\min}/x_a}^{1} \mathrm{d}x_b f_a(x_a) f_b(x_b) \cdot P_{BH}(M) \hat{\sigma}_{BH}(M). \quad (2.27)$$

Figure 2.6 compares the Heaviside function in QBH production and the probability function in HQM production. P_{BH} prefers black holes that are heavier than M_D but leaves a small fraction of probability for those lighter than M_D. The comparison of cross-sections between QBH and HQM is shown in Figure 2.7. Generally speaking, HQM has smaller cross-sections than QBH in the low mass region about $M_D < 8$ TeV and vice versa.

2.3.3 HQM sample generation

HQM dijet events are generated using the QBH 3.0 generator [48] with HQM modifications.[1] The dataset containers of the HQM simulations are listed in Appendix A.

[1]Due the same name of the generator as the abbreviation to quantum black holes, we use a different font to denote the generator QBH while using QBH for the abbreviation.

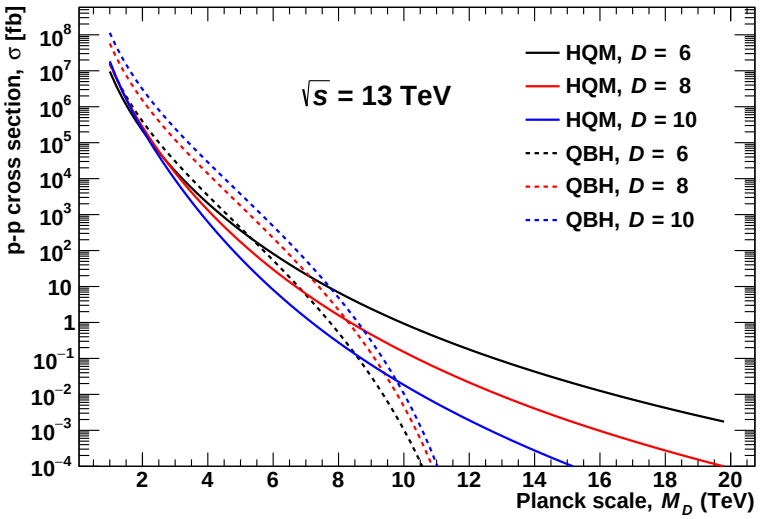

Figure 2.7: Comparison of the black hole cross-sections of HQM and QBH in $D = 6, 8, 10$ dimensional spaces, taken from Ref. [13].

The QBH generator

As for the production process, QBH 3.0 interfaces with PYTHIA 8 and takes all the possible combinations of incoming particles into account. CTEQ6L1 PDFs [25] are used in the generator. Quantum black holes are assumed to inherit charge, colour and spin from the parent parton pair. The cross-section is calculated by Equation 2.27 assuming the form factor $F(n)$ in Equation 2.20 is 1. Figure 2.8 shows the cross-sections of individual states grouped in colour and charge. The state created by an up-type quark and a gluon has the largest cross-section among all the 14 states for $D = 6$ and $M_D = 1$ TeV.

A quantum black hole is assumed to decay into SM particles and massless gravitons. To determine the types of the decay products, we assume that angular momentum, charge and colour are conserved during the decay process. Ref. [4] shows that two-particle decay is the dominant process. The branching ratios of two-particle decay are listed in Table 2.4. In this analysis, we do not assume global symmetry conservation. Quarks and gluons are the dominant decay products no matter if we assume global symmetry conservation or not. Quarks and gluons directly from a black hole can create jets in the ATLAS detector. The decay products of W/Z bosons and top quarks can also create

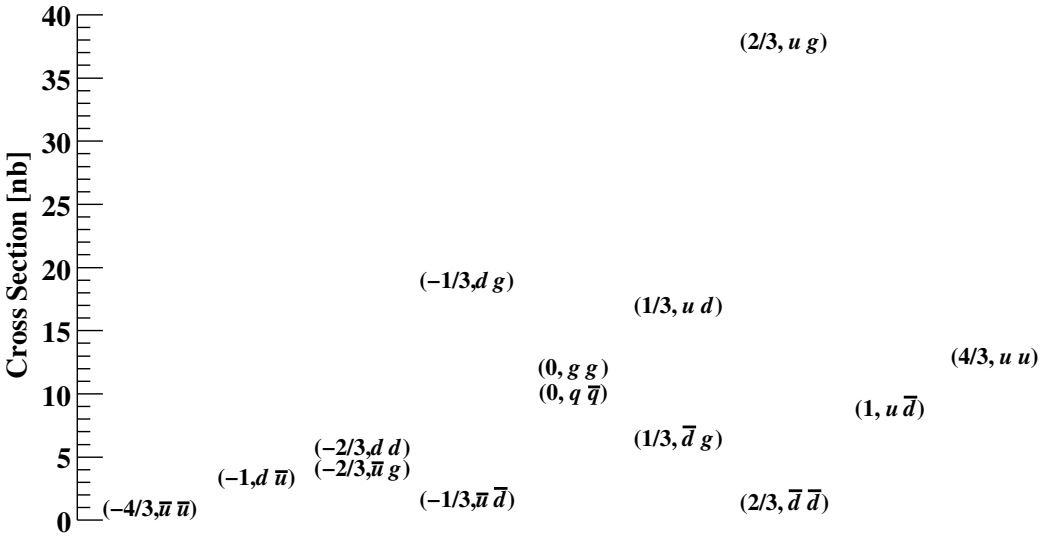

Figure 2.8: Cross-sections of different quantum black hole states assuming $D = 6$ and $M_D = 1$ TeV at a centre-of-mass of 14 TeV, taken from Ref [4]. The states are aligned by charge on the horizontal direction. u presents all the up-type quarks (u, c and t) and d presents all the down-type quarks (d, s and b).

jets in the detector. Ref. [4] shows that at least 87% of the decay events contain at least two jets. Considering the influence of jet reconstruction algorithms, we find the rate of HQM to dijet events is nearly 100%. Thus, studies of dijet events can provide important insights into black hole production in ATLAS.

Angular distribution

A quantum black hole can be considered as an intermediate state of the two incoming partons, then it decays dominantly through the $\hat{s}$-channel. For the two-particle decay process, the two decay products do not have a preference on any direction in the rest frame of the black hole, which gives

$$\frac{\mathrm{d}\hat{\sigma}_{BH}}{\mathrm{d}\cos\theta^*} \sim \text{costant}. \tag{2.28}$$

Table 2.4: Branching fractions of the $QBH \to 2$ process taken from Ref. [4]. The superscript denotes the charge while the subscript denotes the incoming parton pair. Column C is obtained when assuming global symmetry conservation while Column V is obtained assuming global violation.

State		Decay	BR (%)		State		Decay	BR (%)	
			C	V				C	V
$QBH^{4/3}_{uu}$	$\to$	uu	100	67	$QBH^{0}_{q\bar{q}}$	$\to$	$u\bar{u}$	41.5	36.5
		$\bar{d}\ell^+$		33			$d\bar{d}$	41.5	36.5
$QBH^{1}_{u\bar{d}}$	$\to$	ud	86	79.8			gZ	4.1	3.6
		$\nu\ell^+$	3	8.9			gg	4.1	3.6
		W^+g	9	7.9			$g\gamma$	4.1	3.6
		W^+Z	1	1.0			$\ell^+\ell^-$	1.5	4.1
		$W^+\gamma$	1	1.0			$\nu\nu$	1.2	2.7
		W^+H		0.7			W^+W^-	0.5	0.5
		W^+G		0.7			$\gamma\gamma$	0.5	0.5
$QBH^{2/3}_{ug}$	$\to$	ug	73	66.7			ZZ	0.5	0.5
		dW^+	9	8.3			γZ	0.5	0.5
		$u\gamma$	9	8.3			gH		2.7
		uZ	9	8.3			γH		0.3
		uH		2.8			ZH		0.5
		uG		5.6			HH		0.1
$QBH^{2/3}_{\bar{d}\bar{d}}$	$\to$	$\bar{d}\bar{d}$	100	50			gG		2.7
		$u\nu$		25			γG		0.3
		$d\ell^+$		25			ZG		0.3
$QBH^{1/3}_{\bar{d}g}$	$\to$	$\bar{d}g$	73	66.7			GG		0.5
		$\bar{u}W^+$	9	8.3	QBH^{0}_{gg}	$\to$	$u\bar{u}$	27.8	27.1
		$\bar{d}\gamma$	9	8.3			$d\bar{d}$	27.8	27.1
		$\bar{d}Z$	9	8.3			gg	27.9	27.1
		$\bar{d}H$		2.8			gZ	7.0	6.8
		$\bar{d}G$		5.6			$g\gamma$	7.0	6.8
$QBH^{1/3}_{ud}$	$\to$	ud	100	60			$\ell^+\ell^-$	0.5	1.6
		$\bar{d}\nu$		20			$\nu\nu$	0.3	1.1
		$\bar{u}\ell^+$		20			W^+W^-	0.4	0.4
							$\gamma\gamma$	0.4	0.4
							ZZ	0.4	0.4
							γZ	0.4	0.4
							ZH		0.1
							HH		0.1
							HG		0.2
							GG		0.4

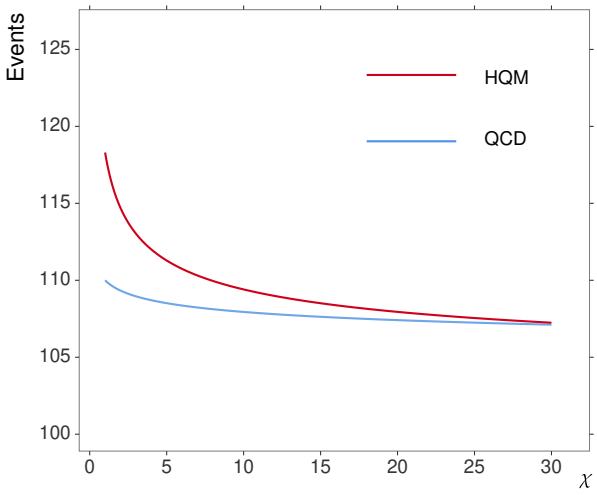

Figure 2.9: Illustration of HQM events on top of QCD events in the χ distribution.

According to the definition of χ in Equation 2.10, we have

$$\begin{aligned} \cos\theta^* &= \frac{\chi - 1}{\chi + 1} \\ \Rightarrow \mathrm{d}\cos\theta^* &= \frac{(\chi+1)-(\chi-1)}{(\chi+1)^2}\mathrm{d}\chi \\ &= \frac{2}{(1+\chi)^2}\mathrm{d}\chi \end{aligned} \tag{2.29}$$

The differential cross-section against χ can be obtained by substituting $\mathrm{d}\cos\theta^*$ in Equation 2.28 with Equation 2.29:

$$\frac{\mathrm{d}\hat{\sigma}_{BH}}{\mathrm{d}\chi} \sim \frac{1}{(1+\chi)^2} \tag{2.30}$$

which peaks in the low χ region. As Figure 2.9 illustrates, the χ distribution will largely deviates from the flat shape of QCD dijet events if a significant amount of quantum black holes are produced in ATLAS.

HQM sample generation

To cover a reasonable parameter space of the HQM model, a preliminary study is performed to estimate its discovery potential. As a result, the samples are generated covering three different dimension settings $n = 2, 4, 6$ and six M_D settings for each dimension setting. Table. 2.5 lists the cross-sections of these configurations. Fast ATLAS detector simulation is performed by Atlfast-II

(AFII) [49] in official ATLAS production. Similar to the QCD simulation, three campaigns are generated for each configuration. Each campaign sample contains 20,000 generated events.

Table 2.5: Simulated HQM samples of extra dimensions n and Planck scale M_D and their cross-sections.

n	M_D [TeV]	Cross-section [fb]
2	7.0	$(1.99 \pm 0.05) \times 10^{1}$
	7.5	$(1.08 \pm 0.03) \times 10^{1}$
	8.0	$(6.08 \pm 0.16) \times 10^{0}$
	8.5	$(3.55 \pm 0.09) \times 10^{0}$
	9.0	$(2.13 \pm 0.06) \times 10^{0}$
	9.5	$(1.31 \pm 0.03) \times 10^{0}$
4	6.5	$(1.35 \pm 0.06) \times 10^{1}$
	7.0	$(6.34 \pm 0.28) \times 10^{0}$
	7.5	$(3.12 \pm 0.14) \times 10^{0}$
	8.0	$(1.68 \pm 0.07) \times 10^{0}$
	8.5	$(8.46 \pm 0.38) \times 10^{-1}$
	9.0	$(4.64 \pm 0.21) \times 10^{-1}$
6	5.5	$(2.21 \pm 0.13) \times 10^{1}$
	6.0	$(8.32 \pm 0.51) \times 10^{0}$
	6.5	$(3.32 \pm 0.21) \times 10^{0}$
	7.0	$(1.40 \pm 0.09) \times 10^{0}$
	7.5	$(6.21 \pm 0.39) \times 10^{-1}$
	8.0	$(2.87 \pm 0.18) \times 10^{-1}$

Chapter 3

The ATLAS detector

3.1 Overview of the detector

The ATLAS experiment is one of the major detectors located in LHC. The coordinate system was already introduced in Section 2.2.1 in the context of dijet kinematics. The detector is designed in a multi-layered style, as shown in Figure 3.1. The inner part is a tracking detector that measures the momentum, direction and charge of a particle. It includes a pixel detector, a semiconductor tracker and a transition radiation tracker and covers the range $|\eta| < 2.5$. Charged particles are curved by a superconducting solenoid which provides a 2 Tesla magnetic field surrounding the inner detector.

Figure 3.2 shows the layout of the calorimeter system. It includes the liquid-argon (LAr) electromagnetic calorimeter, the LAr end-cap and forwarding hadronic calorimeters, and the tile hadronic calorimeter. The calorimeter system provides energy measurement of hadron showers which are fed to jet reconstruction algorithms. We briefly introduce the calorimeter system here while details can be found in the following section. The LAr electromagnetic calorimeter, covering $|\eta| < 3.2$, is designed in high granularity which provides outstanding energy resolution. The LAr end-cap calorimeters provide hadronic energy measurement of a range covering $1.5 < |\eta| < 3.2$. The LAr forward calorimeter provides both electromagnetic and hadronic energy measurements and extends the measurement range to $|\eta| = 4.9$. The tile hadronic calorimeter, covering $|\eta| < 1.7$, is installed outside the LAr calorimeters.

The muon system, surrounding the calorimeter system, includes three su-

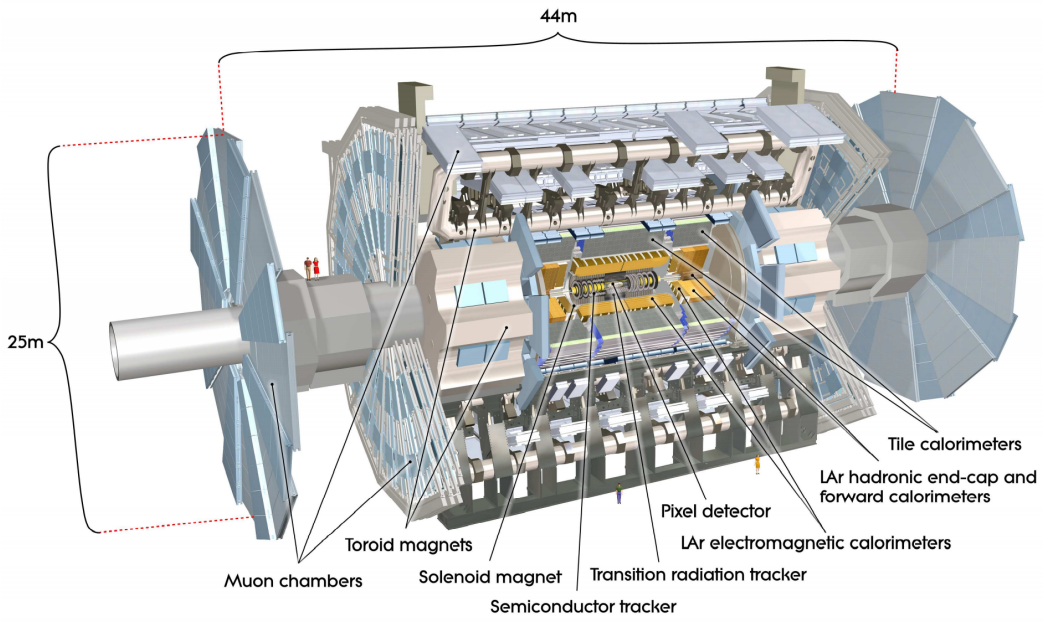

Figure 3.1: Layout of the ATLAS detector, taken from Ref. [50].

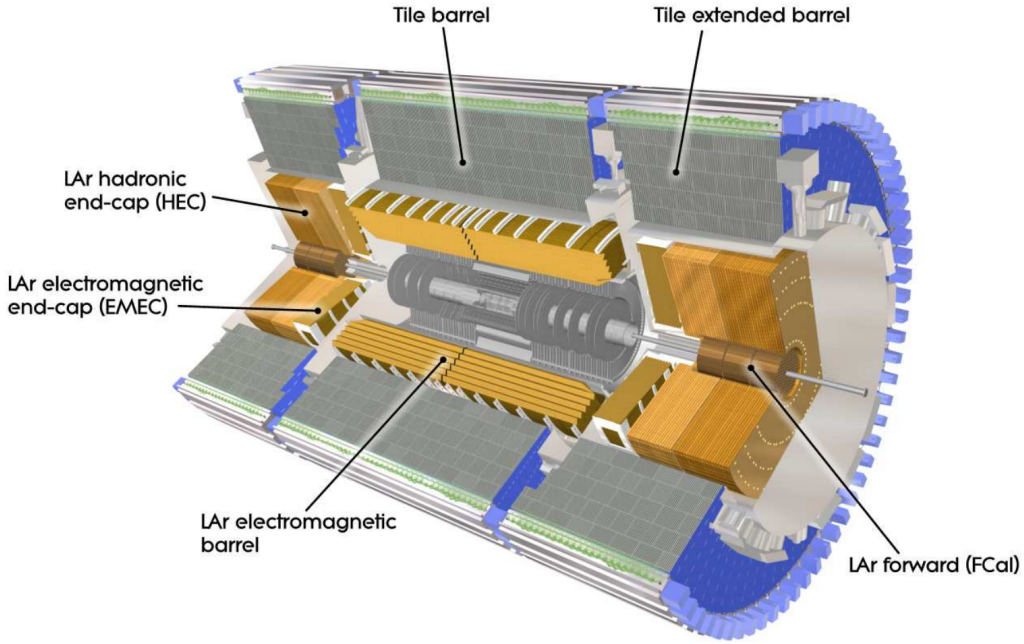

Figure 3.2: Layout of the calorimeter system, taken from Ref. [50].

perconducting magnets and the muon spectrometer which consists of cathode strip chambers, resistive plate chambers, thin gap chambers and monitored drift tubes. The momenta of muons are measured by the spectrometer.

Three detectors are installed in the forward region. A Cherenkov detector, LUCID (LUminosity measurement using Cherenkov Integrating Detector), is installed at $\pm 17\,\mathrm{m}$ from the interaction point (IP). Another detector, ALFA (Absolute Luminosity For ATLAS), is made of scintillating-fibre trackers and installed around $\pm 240\,\mathrm{m}$ from IP. Both LUCID and ALFA provide luminosity measurements. Zero-Degree Calorimeter (ZDC) is installed between LUCID and ALFA to detect neutrons produced in heavy-ion collisions.

The trigger system is implemented in two levels. The first level, a high-level trigger (HLT), is a hardware trigger that accepts about 10^6 collisions out of 1.7×10^9 per second. The second level is a software trigger which further reduces the rate to 10^6 Hz. Filtered data after the second level is written to a storage system.

3.2 Calorimeter system

Calorimeters are built to measure the energy deposits of passing particles, as well as their positions and directions. Figure 3.3 shows the basic structure of a calorimeter which consists of absorbers and activate layers. Absorbers are designed to absorb the energy of incoming particles as much as possible. Thus, they are usually made from dense materials. In ATLAS, depending on the need and cost of the calorimeter part, steel/copper/tungsten/lead plates are used as absorbers. Activate layers are designed to produce electrical signals whose strength is proportional to the energy of an incoming particle. Liquid argon is widely used as activate layers in ATLAS because of its response linearity over a large energy range. Scintillators are used in the tile calorimeter as activate layers.

The ATLAS calorimeter system consists of two sub-systems: the electromagnetic calorimeter system and the hadronic calorimeter system. The electromagnetic calorimeter system measures the energy of incoming electrons

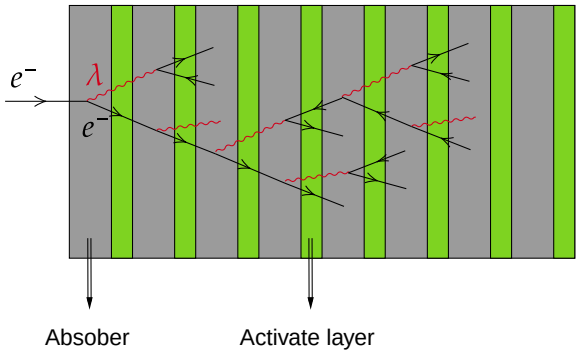

Figure 3.3: Illustration of a calorimeter and a electromagnetic cascade.

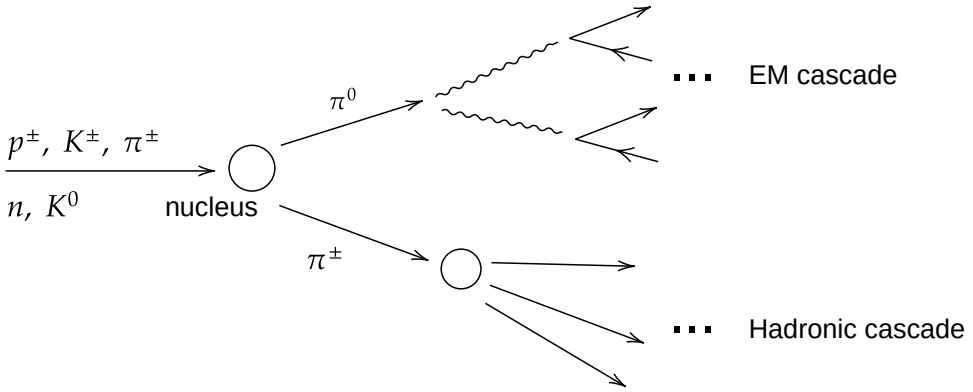

Figure 3.4: Illustration of interactions involved in hadronic calorimeters.

and positrons. Electro-magnetic cascade are created in the calorimeter by Bremsstrahlung ($e^{\pm} \rightarrow e^{\pm} + \gamma$) and photon pair production ($\gamma \rightarrow e^{+} + e^{-}$), as Figure 3.3 illustrates. Low energy electrons/positrons are created at the end of the cascade, and they further lose energy mainly through ionization.

Hadronic calorimeters are designed to measure the energy of hadrons, including charged particles such as $p^{\pm}$, $K^{\pm}$ and $\pi^{\pm}$ and neutral particles such as n and K^0. The involved interactions are illustrated in Figure 3.4. Incoming high energy hadrons interact with nuclei in absorbers and produce secondary particles which are mostly $\pi^{\pm}$ and π^0. Charged $\pi^{\pm}$ can further interact with nuclei and create hadronic cascades. Neutral π^0 decays into photons and creates electromagnetic cascades.

Table 3.1 summarizes the η resolution and coverage of the ATLAS calorimeter system. The η resolution determines how fine jets are measured in the η

direction which is the most relevant specification to the angular analysis. The η coverage is most relevant to jet calibrations which will be discussed in Section 4.2. Technical details of the calorimeter systems can be found in Ref. [50].

Table 3.1: List of the η resolution and coverage of the calorimeter system, summarized from Ref. [50]. The resolution and coverage of a calorimeter varies in different parts and only the minimum and maximum η segmentation are listed with its total coverage.

Calorimeter	Resolution (min – max)	Coverage
EM calorimeter	0.025/8 – 0.1	$\lvert\eta\rvert < 3.2$
LAr hadronic calorimeter	0.1 – 0.2	$1.5 < \lvert\eta\rvert < 3.2$
LAr forward calorimeter	3.0/4 – 3.0	$3.1 < \lvert\eta\rvert < 4.9$
Tile calorimeter	0.1 – 0.2	$\lvert\eta\rvert < 1.7$

Chapter 4

Jets

Figure 4.1 illustrates the jet production and detection in ATLAS. A jet consists of a cluster of particles as a result of the hadronization process of a parton. Most of the hadrons are $\pi^{\pm}$ and π^{0}. The inner detector of ATLAS collects the track information of charged hadrons and provides momentum measurements. The calorimeter system collects energy information of both charged and neutral hadrons and provides energy measurement of clustered energy deposits. A jet algorithm, anti-k_t [51], is used to reconstruct jets from these measurements. Jet calibration techniques are developed to restore jet measurement to the truth level. Finally, selections are applied for the needs of the analysis. The dataset is listed in Appendix A. Details of jet reconstruction can be found in the following subsections.

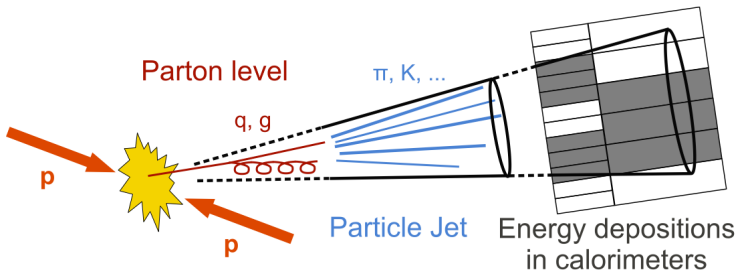

Figure 4.1: Illustration of jet production and detection in ATLAS, taken from Ref. [52].

4.1 Jet reconstruction

In ATLAS, jets are reconstructed from more fundamental objects, including track-reconstructed particles and cluster-reconstructed pseudo-particles. The particle flow algorithm takes these reconstructed particles as inputs and removes the double-counting effects. The outputs of the particle flow algorithm, namely the modified particles, are grouped as jets by the anti-k_t algorithm. This section introduces the steps of jet reconstruction one by one in the following subsections.

4.1.1 Track reconstruction

Charged particles hit the pixels of the inner detector when they pass through. The hits are reconstructed to tracks. A track is characterized by its location, charge and momentum. The geometry information of a track, including its location and radius, can be obtained from the inner detectors. The momentum of the track can be calculated from its radius and the strength of the magnetic field. The four-momentum of the particle can be determined along with energy measurement given by calorimeters and particle identification techniques which provides information of charge and invariant mass of the passing particle.

4.1.2 Topo-cluster reconstruction

Hadrons deposits their energy in the calorimeter system in the forms of electromagnetic showers and hadronic showers. One hadron can create one or multiple showers because of sub-processes. Energy deposits from showers are reconstructed as topo-clusters [53] in ATLAS. The smallest readout unit in a calorimeter is referred to as a cell. The significance of an energy signal measured by a cell in a calorimeter is defined as

$$\varsigma_{\text{cell}} = \frac{E_{\text{cell}}}{\sigma_{\text{cell}}} \tag{4.1}$$

where E_{cell} is the energy signal and σ_{cell} is the average noise level of the cell. Figure 4.2 illustrates the process of growing a topo-cluster according to the significance. Cells with $\varsigma_{\text{cell}} > 4$ are selected as seeds and each seed forms

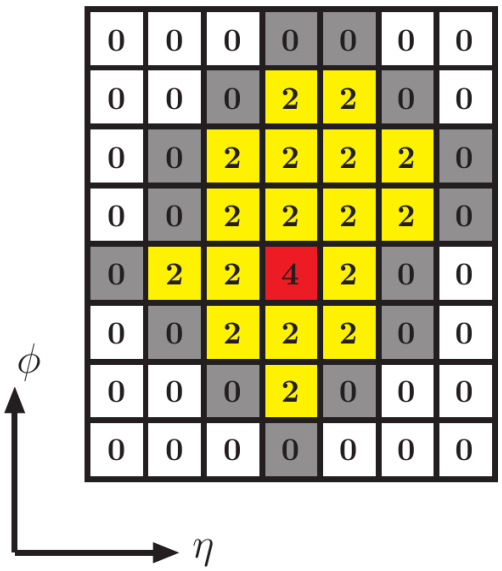

Figure 4.2: Illustration of growing a topo-cluster where the numbers are the signal significance of the cells, taken from Ref. [54].

a proto-cluster. Neighbouring cells of a seed grow to the proto-cluster. If a growing cell has $\varsigma_{\text{cell}} > 2$, its neighbouring cells can further grow into the proto-cluster. Such process continues until all cells at the edge of a proto-cluster have $0 < \varsigma_{\text{cell}} < 2$. Meanwhile, a growing cell can have a neighbouring cell with $\varsigma_{\text{cell}} > 4$, namely, a seed from another proto-cluster. In this case, two proto-clusters are merged.

A proto-cluster formed from the above description can have multiple local maxima, which can be a result of two or more hard particles depositing their energy to an overlapping area. A local maximum is defined as a cell having a signal $E_{\text{cell}} > 500$ GeV and at least four neighbouring cells with smaller signals. If multiple local maxima are found, a proto-cluster splits into smaller clusters spatially among the local maxima. The proto-clusters after splitting are called topo-clusters.

A topo-cluster spreads in the calorimeter spatially, which is not convenient for application since it does not have well defined positions and kinematics. To solve this problem, topo-clusters are interpreted as massless pseudo-particles. The position of a topo-cluster, $(\eta_{\text{clus}}, \phi_{\text{clus}})$, is defined as a weighted sum of its

cells' positions

$$\eta_{\text{clus}} = \frac{\sum_{i=1}^{N}(E_{\text{cell}} \cdot \eta_{\text{cell}})}{\sum_{i=1}^{N} E_{\text{cell}}}, \qquad \phi_{\text{clus}} = \frac{\sum_{i=1}^{N}(E_{\text{cell}} \cdot \phi_{\text{cell}})}{\sum_{i=1}^{N} E_{\text{cell}}}, \tag{4.2}$$

where (η_{clus}, ϕ_{clus}) is th position of a cell and N is the number of cells in the topo-cluster. The energy of a topo-cluster is defined as the sum of the energy from its cells:

$$E_{\text{clus}} = \sum_{i=1}^{N} E_{\text{cell}}. \tag{4.3}$$

The four-momentum of a cluster is

$$P_{\text{clus}} = E_{\text{clus}} \cdot (1, \sin\theta_{\text{clus}} \cos\phi_{\text{clus}}, \sin\theta_{\text{clus}} \sin\phi_{\text{clus}}, \cos\theta_{\text{clus}}), \tag{4.4}$$

where θ_{clus} can be calculated from η_{clus} and ϕ_{clus}. Extra weights can be assigned to the cells if cell sharing is considered, which is discussed in Ref. [53].

4.1.3 The particle flow algorithm

Both particles reconstructed from tracks and pseudo-particles from topo-clusters can be used to reconstruct jets. They have both pros and cons in different aspects. Jets reconstructed solely from topo-clusters were widely used in ATLAS because pseudo-particles have better energy resolution than track-reconstructed particles in the high energy region. However, track-reconstructed particles offer better momentum resolution when considering the low energy region. Besides, the angular resolution of charged particles is also better measured from track-reconstructed particles than pseudo-particles. Both jet energy and angular resolutions can be improved if jets are reconstructed from both tracks and topo-clusters. The problem of combining the two is energy double counting since a particle reconstructed from a track can also create topo-clusters in the calorimeter system. The particle flow algorithm [55] is proposed to solve this problem.

Figure 4.3 shows the workflow of the algorithm. It takes tracks and topo-clusters as inputs. Only well-reconstructed tracks are selected to proceed forward. It requires that a track has at least nine hits and satisfy $|\eta| < 2.5$ and

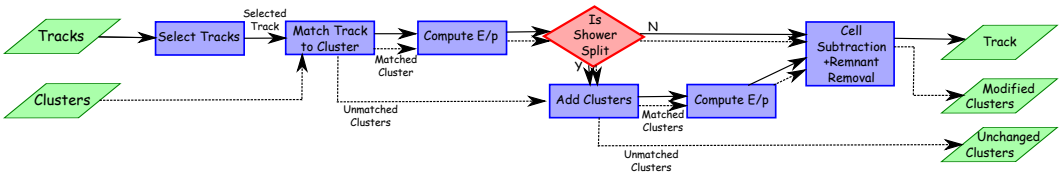

Figure 4.3: Workflow of the particle flow algorithm, taken from Ref. [55].

$p_{\mathrm{T}} > 0.5$ GeV. Then, a distance metric between a track and a topo-cluster is defined as

$$\Delta R' = \sqrt{\left(\frac{\Delta\phi}{\sigma_\phi}\right)^2 + \left(\frac{\Delta\eta}{\sigma_\eta}\right)^2} \tag{4.5}$$

where σ_ϕ and σ_η are the angular widths of the topo-cluster. It is used to match topo-clusters to tracks. A preliminary selection on topo-clusters requires $E^{\mathrm{cluster}}/p^{\mathrm{track}} > 0.1$ where E^{cluster} is the energy of the topo-cluster and p^{track} is the momentum of the track. The closest topo-cluster in $\Delta R'$ among the pre-selected ones is matched to the track and the energy of the matched topo-cluster is subtracted. Additional topo-clusters are matched to the track if the energy of the first matched topo-cluster can not fully match the momentum of the track. The energy subtraction is performed at the cell level. It means a topo-cluster may only be partially removed. If the remnant of a topo-cluster is within its standard energy fluctuation, the topo-cluster will be fully removed. Otherwise, the remnant will be treated as a modified topo-cluster which may contain energy deposits from other tracks.

4.1.4 The anti-k_t algorithm

The anti-k_t algorithm [51] takes the output of the particle flow algorithm as input, namely reconstructed track particles and reconstructed topo-cluster pseudo-particles . The algorithm determines the number of reconstructed jets and the components of each jet from inputs. In the algorithm, distance metrics from particle$_i$ to particle$_j$ and to the beam are respectively defined as

$$\begin{aligned} d_{ij} &= \min(k_{ti}^{2p}, k_{tj}^{2p})\frac{\Delta_{ij}^2}{R^2}, \\ d_{iB} &= k_{ti}^{2p}, \end{aligned} \tag{4.6}$$

where $\Delta_{ij}^2 = (y_i - y_j)^2 + (\phi_i - \phi_j)$. Variables k_{ti} and y_i are the transverse momentum and rapidity of particle$_i$ respectively. The anti-k_t algorithm fixes parameter $p = -1$, which is indicated by "anti" in its name. Parameter R controls the spatial size of a jet. In ATLAS, jets reconstructed with setting $R = 0.4$ are referred to as small-R jets. They contain most of quark-initiated and gluon-initiated jets. In comparison, jets reconstructed with setting $R = 1.0$ are referred to as large-R jets and they include decay products from massive particles such as W/Z bosons and top quarks. The algorithm decides whether to group two particles by comparing d_{ij} and d_{iB}. For particle$_i$, it will be grouped with particle$_j$ if $d_{ij} < d_{iB}$. Otherwise the combination procedure ends. More specifically, the anti-k_t algorithm selects hard particles as seeds of jets and sorts them by transverse momenta in decreasing order k_{t1}, k_{t2}, ..., k_{tn}. The rest of the particles are considered soft particles. Starting with the hard particle of k_{t1}, the distance between soft particles of k_{ti} and the hard particle will be $d_{1i} = k_{t1}^{-2} \frac{\Delta_{1i}^2}{R^2}$ while the beam distance is $d_{1B} = k_{t1}^{-2}$. Both d_{1i} and d_{1B} are exclusively determined by the hard particle. If there are no other hard particles in the range of $2R$ around the particle of k_{t1}, a perfect conical jet with radius R will be reconstructed from the hard particle and all the soft particles within R. If another hard particle, taking the one of k_{t2} for example, is located within R around the particle of k_{t1}, then the jets reconstructed from the two particles will be merged. Things become more complex if a particle of k_{t2} is located between R and $2R$ around the particle of k_{t1}. In this case, some soft particles are located at the overlapping area of the two cones influenced by the hard particles. The distances of a soft particle to the hard particles will be $d_{1i} = \frac{\Delta_{1i}^2}{k_{t1}^2} \frac{1}{R^2}$ and $d_{2i} = \frac{\Delta_{2i}^2}{k_{t2}^2} \frac{1}{R^2}$. The soft particle will be grouped to the particle of k_{t1} if $d_{1i} < d_{2i}$ and vice versa.

4.2 Jet calibration

Many factors can cause bias on the reconstructed jet energy scale (JES), such as detector noise and energy loss in dead materials. Thus, reconstructed jets have to be calibrated to restore their energy and momenta to the particle level

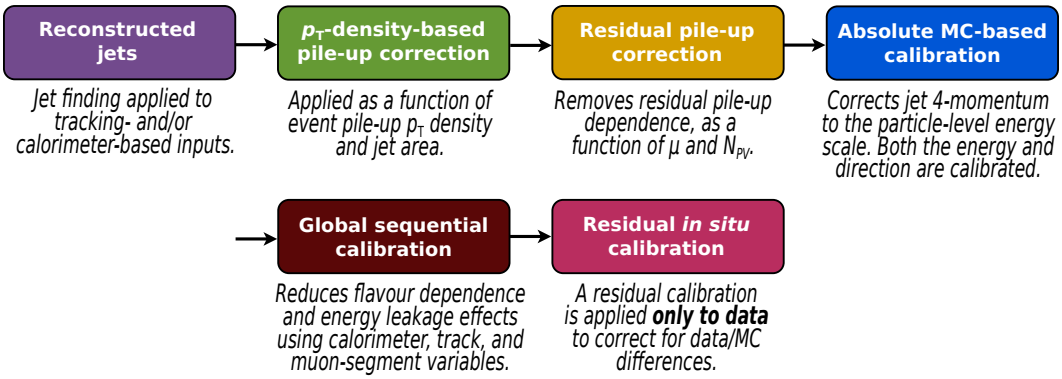

Figure 4.4: Workflow of jet energy scale calibration. The four-momentum of jet is calibrated at each stage. The figure is taken from Ref. [56].

which refers to the stage before track and topo-cluster reconstructions. The particle level is also called the truth level. The calibration process is shown in Figure 4.4. It is summarized here while details can be found in Ref [56].

4.2.1 Pile-up correction

The first stage is to remove the pile-up effect which refers to contamination from additional proton-proton collisions. The protons in the LHC beam pipe comes in bunches with a short interval time. It means that additional collisions can come from the same bunch as the interesting collision. Additional collisions can also originate from neighbouring crossing bunches since the response time of most calorimeter components is longer than the bunch interval. Extra energy deposited in the reconstructed jet from additional collisions is removed at the first stage of jet calibration. To calculate the pipe-up correction, jet p_{T} is used as the reference variable instead of jet energy. This is because soft interactions, such as the interaction between proton remnants, are more likely to contaminate jet energy because they can carry part of the energy from the proton beam pipe along the z-direction. However, due to the small momentum transfer in soft interactions, their products usually have small p_{T} which makes their impact on the transverse plane small. Thus, jet p_{T} is preferred over jet energy in developing calibrations. The jet p_{T} after pile-up correction is given

by

$$p_{\mathrm{T}}^{\mathrm{corr}} = p_{\mathrm{T}}^{\mathrm{reco}} - \mathcal{O}(\rho, N_{\mathrm{PV}}, \mu, \eta_{\mathrm{dec}}) \tag{4.7}$$

where $p_{\mathrm{T}}^{\mathrm{corr}}$ is the corrected transverse momentum and $p_{\mathrm{T}}^{\mathrm{reco}}$ is the reconstructed transverse momentum before applying pile-up correction. $\mathcal{O}(\rho, N_{\mathrm{PV}}, \mu, \eta_{\mathrm{dec}})$ is an offset term which depends on the pile-up p_{T} density (ρ), number of reconstructed primary vertices (N_{PV}), number of interactions per bunch crossing (μ) and the jet pointing to the geometric centre of the detector (η_{dec}). The ratio of $p_{\mathrm{T}}^{\mathrm{corr}}$ to $p_{\mathrm{T}}^{\mathrm{reco}}$ is applied to the four-momentum of a jet. Thus, the direction of the jet is not changed by the pile-up correction.

4.2.2 Jet energy scale and η calibration

After the pile-up correction, the *absolute* JES calibration corrects the energy and direction η for jets, derived from matching reconstructed jets to particle-level jets in dijet MC simulations. More specifically, the jet response factor $\mathcal{R}$ is defined as the Gaussian mean of the $E^{\mathrm{true}}/E^{\mathrm{reco}}$ distribution where E^{true} is the jet truth energy and E^{reco} the reconstructed energy. The factor is studied in bins of E^{true} and parameterized as a function of $\mathcal{R}$. The reconstructed jet energy is restored to the truth level by a numerical inversion technique [57].

Difference between the reconstructed jet η and truth jet η is observed and corrected. The difference is studied as a function of E^{truth} and η_{dec}. It is most significant for high energy jets and in detector transition areas. The numerical inversion technique used for calibrating jet energy scale is used to correct the jet η. This correction changes the direction of a jet as it only calibrates the jet p_{T} and η.

4.2.3 Global sequential calibration

Although the jet response $\mathcal{R}$ is constructed as a function of E^{truth} and η_{dec} in the *absolute* jet energy scale and η calibration, it also has other dependence that needs to be removed. The *global sequential* calibration removes the dependence on jet composition. It comes from the difference of detector responses between quark-initiated and gluon-initiated jets, as well as the difference in

flavours among the quark-initiated jets. The calibration utilizes several global jet observables described in Ref. [56]. Corrections for each observable is applied sequentially to the four-momenta of jets.

4.2.4 In situ calibration

With the above calibration procedures, jets are considered being corrected to the particle level. However, differences still exist between MC and data, which are most likely from imperfect detector simulation and physics process. The *in situ* calibration takes the remaining difference into account by studying the jet response ratio

$$c = \frac{\mathcal{R}_{\text{situ}}^{\text{data}}}{\mathcal{R}_{\text{situ}}^{\text{MC}}} \tag{4.8}$$

where $\mathcal{R}_{\text{situ}}^{data} = p_{\text{T}}^{\text{data}}/p_{\text{T}}^{\text{ref}}$, $\mathcal{R}_{\text{situ}}^{\text{MC}} = p_{\text{T}}^{\text{MC}}/p_{\text{T}}^{\text{truth}}$ and $p_{\text{T}}^{\text{ref}}$ is the transverse momentum of a well-studied reference object. The inverse of the ratio is considered as the correction factor for data. The calibration consists of three sequential corrections. The first correction is developed from dijet analyses using a jet in the central region $|\eta| < 0.8$ as the reference object. The second correction is obtained from Z/γ+jet analyses using Z/γ as the reference object. The third correction is established using the multi-jet transverse momentum balance technique.

4.2.5 Jet energy resolution measurement

Measurement of the jet energy resolution (JER) is critical to ensure good agreement between simulation and data. JER is formulated as

$$\frac{\sigma(p_{\text{T}})}{p_{\text{T}}} = \frac{N}{p_{\text{T}}} \oplus \frac{S}{\sqrt{p_{\text{T}}}} \oplus C \tag{4.9}$$

where N is the noise parameter describing pile-up and electronic noise, S the stochastic parameter originated from sampler calorimeters and C the constant parameter. The resolution $\frac{\sigma(p_{\text{T}})}{p_{\text{T}}}$ distribution is obtained from dijet events containing at least one reference jet located in $0.2 < |\eta_{\text{det}}| < 0.7$. The noise term is obtained from MC simulations using a *random cones* method [56]. The $\frac{\sigma(p_{\text{T}})}{p_{\text{T}}}$ distribution obtained from dijet events fits to Equation 4.9 with noise

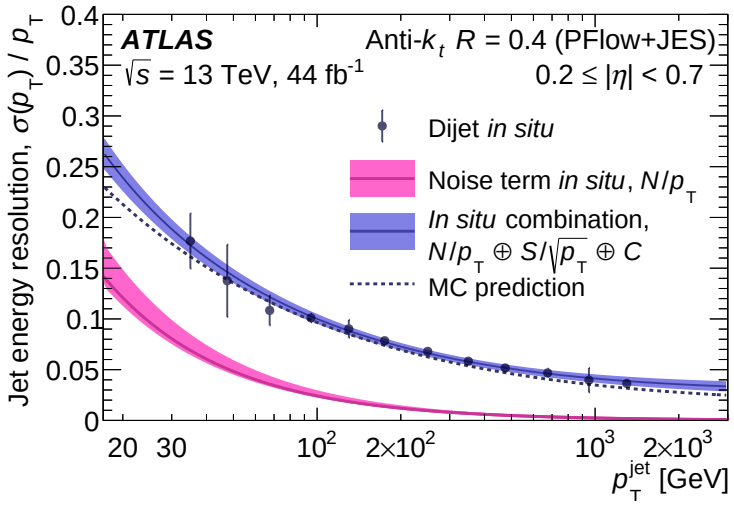

Figure 4.5: Jet energy resolution as a function of p_{T} for JES calibrated particle-flow jets, taken from Ref. [56].

term fixed to the measured value by the *random cones* method. Figure 4.5 shows the jet energy resolutions measured in MC simulations and collected data. In regions where the jet energy resolution in simulation is smaller than in data, both jet p_{T} and energy in the simulation are smeared until their resolutions match data. Otherwise, no smearing is performed.

4.3 Jet selection

A series of selections are applied to improve the quality of jets in both data and MC simulations, as well as to reduce their file sizes. They are listed in Table 4.1 and described as follows. The selections are designed to be simple and loose to just exclude poor reconstructed events and low p_{T} events which fall out of our interested region. Events are removed if the two jets with the largest p_{T} do not meet the requirement of the following selections. Jet cleaning rejects jets with fake, out-of-time or mis-measured energy deposits. The `LooseBad` set of selections described in Ref [58] are applied for the jet cleaning purpose. We require an event having at least one primary vertex that is the pp collision point reconstructed with two associated tracks. It is intuitive to have this selection because of the topology of a $2 \to 2$ scattering process. A high-level trigger [59], namely `HLT_j420`, as well as a loose jet selection of

$p_{\mathrm{T}} > 50$ and $\eta < 5$, are applied to remove low energy jets which are not the interest of the analysis. Data quality-control requirements are applied to data to remove low-quality data samples. The cuts at $|y^*| < 1.7$ and $|y_b| < 1.1$ further reduce QCD events and increase signal significance because most of the HQM events centre around $|y^*| \sim 0$ and $|y_b| \sim 0$. To reduce the dataset size for easier data handling, data skimming selections are applied: leading-jet $p_{\mathrm{T}} > 400$ (200) GeV for QCD simulation (data and HQM simulation) and subleading-jet $p_{\mathrm{T}} > 50$ GeV. It is proved that these selections do not enter our interested invariant mass region which is $m_{jj} > 3.4$ TeV.

The efficiencies of the selections on data, QCD simulation and a HQM sample ($n = 2$, M_D=7 TeV) are shown in Table 4.2, 4.3 and 4.4 respectively. The efficiencies of the selections on other HQM samples are listed in Appendix B.

Table 4.1: List of applied selections. Pre-selections filters the events in object containers and reduces the dataset size. Post-selections are applied based on the interest the analysis to increase signal significance.

Term	Requirement
	Pre-selections
Jet cleaning	The `LooseBad` criteria for rejecting jets with bad energy deposits.
NPV	At least one primary vertex is reconstructed with at least two associated tracks.
High level trigger	`HLT_j420` for data and QCD simulations and `(HLT_j420 or HLT_j380)` for HQM simulations.
Jet select	At least two jets pass $p_{\mathrm{T}} > 50$ GeV and $\|\eta\| < 5$.
Skimming	Leading-jet $p_{\mathrm{T}} > 400$ (200) GeV for QCD simulations (data and HQM simulations) and subleading-jet $p_{\mathrm{T}} > 50$ GeV.
	Data quality control only for collected data
GRL	In the `GoodRunList` where data are considered to have good quality.
LAr	Data quality control of the liquid argon calorimeter system.
Tile	Data quality control of the tile calorimeter system.
SCT	Data quality control of the semiconductor tracker inner detector system.
Core	Reject incomplete events by the timing, trigger and control system.
	Post-selections
abs(y^*)	$\|y^*\| < 1.7$
abs(y_b)	$\|y_b\| < 1.1$

Table 4.2: Selections of Run2 data.

	Selection	Num. of Events	Rela. Decrease [%]	Cumulative Eff. [%]
Pre-selections	Initial	4898228506	73.66	26.34
	GRL	4457685143	8.99	23.97
	LAr	4453526575	0.09	23.95
	Tile	4453421991	2.35e-03	23.95
	SCT	4453154294	6.01e-03	23.95
	Core	4453154294	0.00	23.95
	Jet cleaning	4393878512	1.33	23.63
	NPV	4393869210	2.12e-04	23.63
	Trigger	267158846	93.92	1.44
	Jet select	266490677	0.25	1.43
	Skimming	263708827	1.04	1.42
Post-selections	abs(y^*)< 1.7	258546311	1.96	1.39
	abs(y_b)< 1.1	205702408	20.44	1.11

Table 4.3: Selections of the QCD simulation weighted with event weight described by Equation 2.12.

	Selection	Num. of Events	Rela. Decrease [%]	Cumulative Eff. [%]
Pre-selections	all	311959.01	0.00	100.00
	Jet cleaning	310584.42	0.44	99.56
	NPV	310584.42	1.22e-08	99.56
	Trigger	2381.32	99.23	0.76
	Jet Select	2327.17	2.27	0.75
	Skimming	2327.17	0.00	0.75
Post-selections	abs(y^*)< 1.7	2268.84	2.48	0.73
	abs(y_b)< 1.1	1784.27	21.36	0.57

Table 4.4: Selections of a HQM sample ($n = 2$, $M_D = 7.0$ TeV). The trigger in pre-selections is (`HLT_j380 or HLT_j420`). Thus, trigger `HLT_j420` is added in the post-selections.

	Selection	Num. of Events	Rela. Decrease [%]	Cumulative Eff. [%]
Pre-selections	all	20000.00	0.00	100.00
	Jet cleaning	19831.54	0.84	99.16
	NPV	19831.54	0.00	99.16
	Trigger	19270.35	2.83	96.35
	Jet select	17510.94	9.13	87.55
	Skimming	17510.94	0.00	87.55
Post-selections	`HLT_j420`	17418.38	0.53	87.09
	abs(y^*)< 1.7	16752.17	3.82	83.76
	abs(y_b)< 1.1	16259.51	2.94	81.30

4.4 Kinematic checks

Kinematic distributions of the samples related to the selections are checked. Additional cuts at leading-jet $p_{\mathrm{T}} > 400$ GeV and $m_{jj} > 2.5$ TeV are applied to remove the skimming difference on samples. The kinematic distributions of the samples are shown in Figure 4.6 for m_{jj}, Figure 4.7 for leading-jet p_{T}, Figure 4.8 for subleading-jet p_{T}, Figure 4.9 for η, Figure 4.10 for ϕ, Figure 4.11 for y^* and Figure 4.12 for y_b. The small bumps around 1.5 TeV on both the leading-jet and subleading-jet p_{T} distributions of QCD simulation and data, as well as the dip in the η distribution, are caused by the $m_{jj} > 2.5$ TeV skimming cut. Data and QCD distributions are plotted together to check potential problems in the data preparing stage. The large discrepancy in y^* distributions is expected because data includes higher-order QCD effects and electroweak effects while the QCD simulation is simulated with LO PDFs. Corrections are applied at a later stage of the analysis to achieve a better agreement, as discussed in Chapter 5.2. The kinematic distributions of all simulated HQM samples can be found in Appendix C.

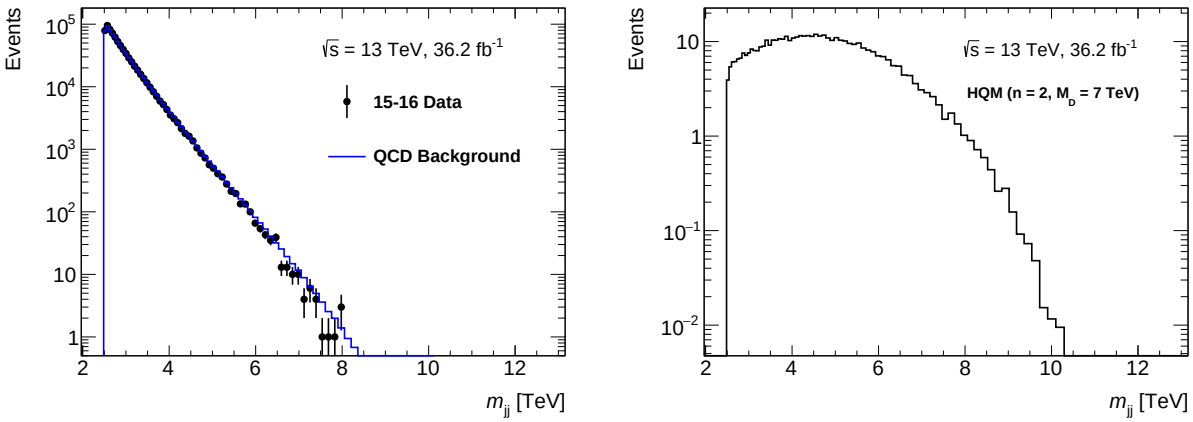

Figure 4.6: m_{jj} distributions of (left) data, QCD simulation and (right) HQM ($n = 2$, $M_D = 7$ TeV).

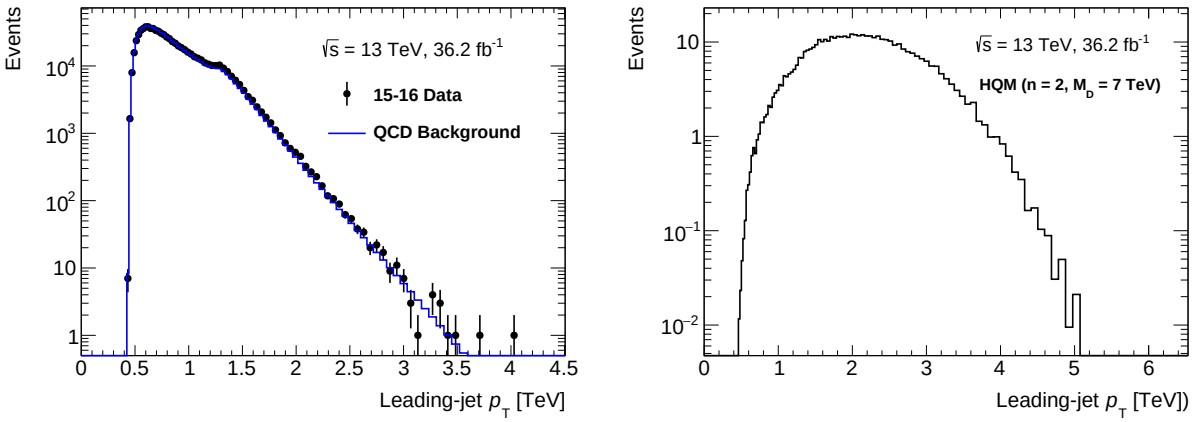

Figure 4.7: Leading-jet p_{T} distributions of (left) data, QCD simulation and (right) HQM ($n = 2$, $M_D = 7$ TeV).

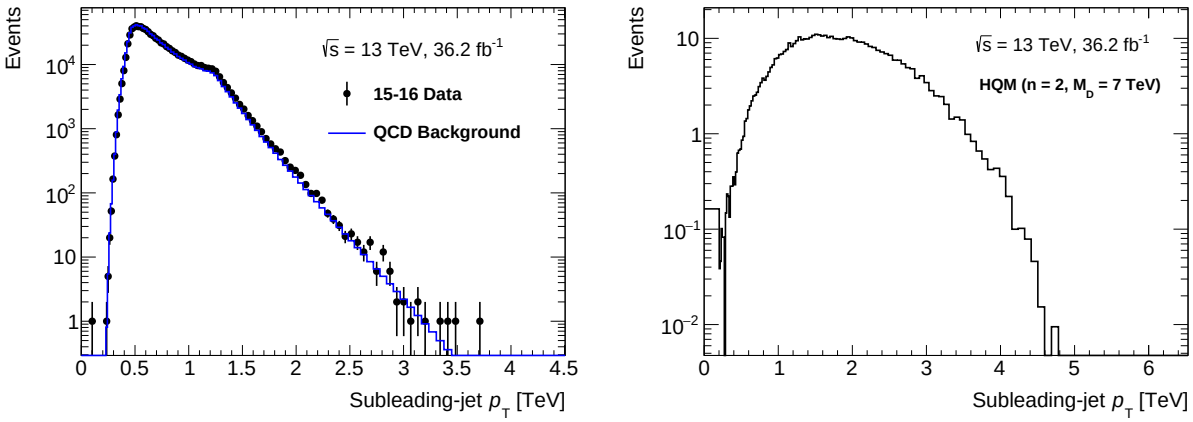

Figure 4.8: Subleading-jet distributions of (left) data, QCD simulation and (right) HQM ($n = 2$, $M_D = 7$ TeV).

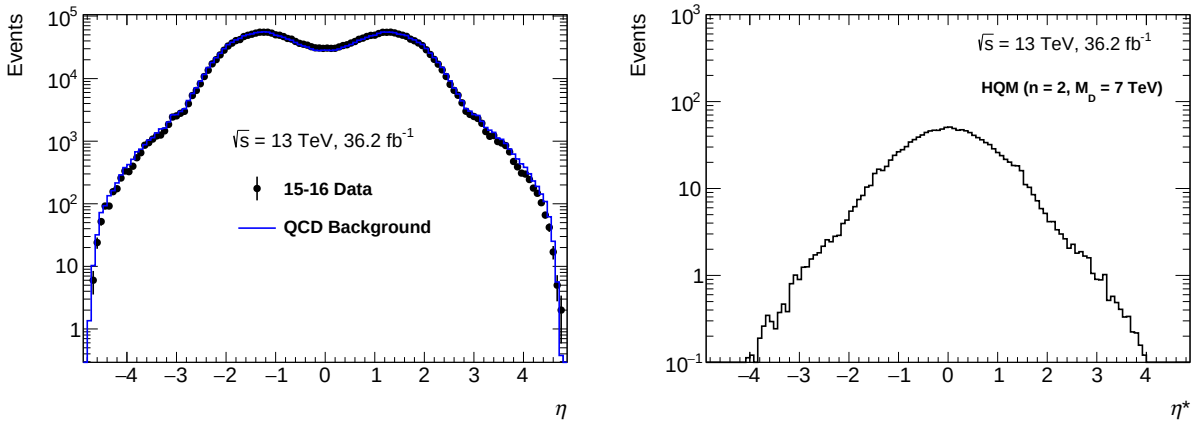

Figure 4.9: η distributions of (left) data, QCD simulation and (right) HQM ($n = 2$, $M_D = 7$ TeV).

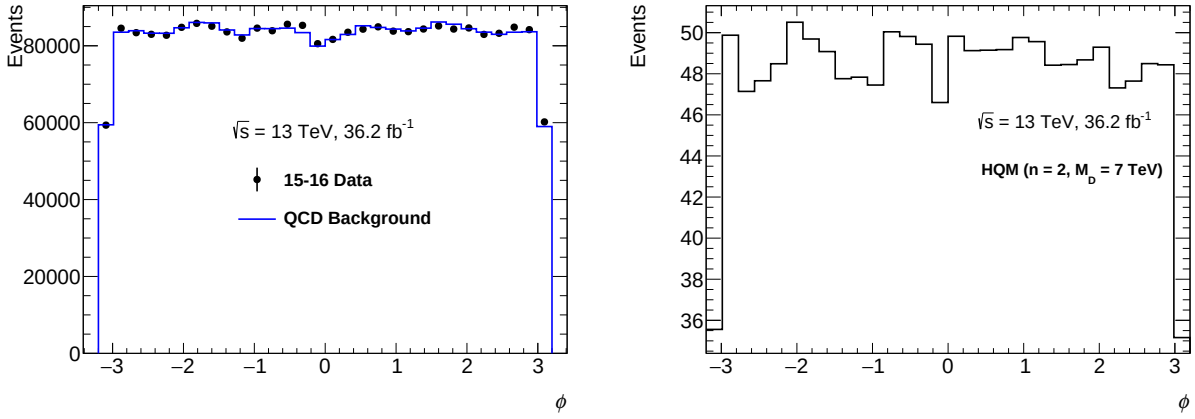

Figure 4.10: ϕ distributions of (left) data, QCD simulation and (right) HQM ($n = 2$, $M_D = 7$ TeV).

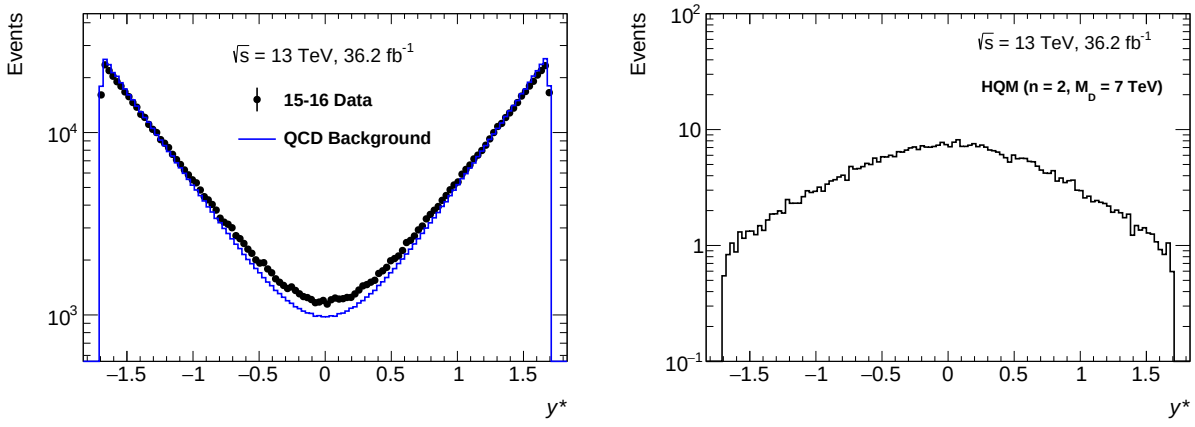

Figure 4.11: y^* distributions of (left) data, QCD simulation and (right) HQM ($n = 2$, $M_D = 7$ TeV). The difference between data and QCD simulation is partially caused higher order QCD effects and electroweak effects.

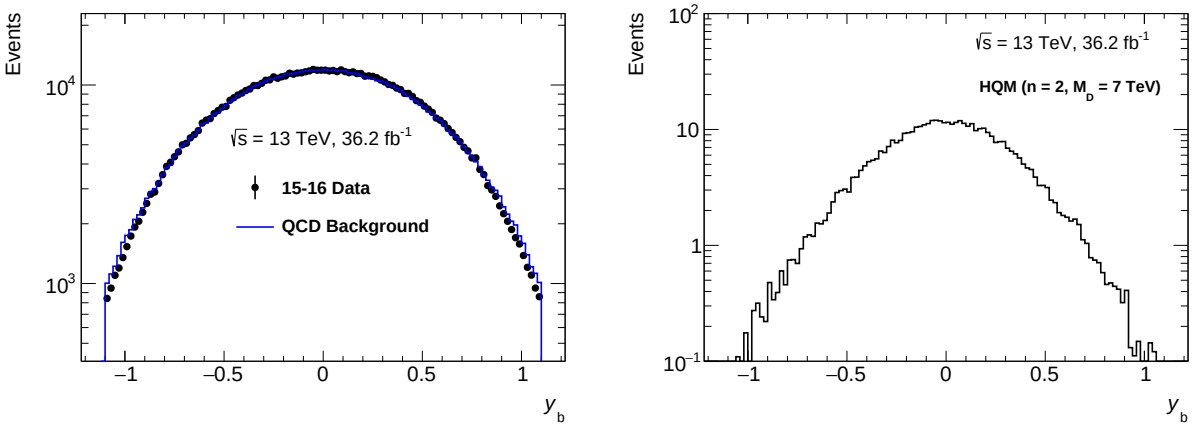

Figure 4.12: y_b distributions of (left) data, QCD simulation and (right) HQM ($n = 2$, $M_D = 7$ TeV).

Chapter 5

Observable and estimation strategy

As mentioned in Section 2.2, the χ distribution is expected to have a different shape for QCD dijet events and HQM dijet events. In the analysis, the QCD dijet simulation will be corrected and treated as the Standard Model background prediction. The HQM dijet simulation is regarded as the signal prediction. In this chapter, we introduce more details of the χ distribution and the estimation strategy for background and signal yields.

5.1 Observable

Theoretically, the χ distribution is only flat for at a fixed $\sqrt{\hat{s}}$ value in t-channel scattering. However, the value of $\sqrt{\hat{s}}$ varies from event to event in pp collisions in the lab frame. To translate this theoretical observable into experimental observable, both data and simulation samples are divided into eight m_{jj} slices, which reduces the $\sqrt{\hat{s}}$ range. The widths of the m_{jj} slices are determined in a way that they are small enough to make the background distribution approximately flat but large enough to have reasonably small statistical fluctuations. The slicing for this analysis is determined to be $m_{jj} \in$ [3.4, 3.7, 4.0, 4.3, 4.6, 4.9, 5.4, 5.7, 13.0] TeV. It is partially inherited from the last angular analysis [14]. An additional bin is added at 5.7 TeV between 5.4 and 13.0 TeV to profit from the increased dataset size. The event yields of data, QCD and HQM simulations in m_{jj} slices are listed in Table 5.1. With the 5.7 TeV bin,

the two highest m_{jj} slices have similar numbers of events. We do notice the HQM yield in the slice of 5.4–5.7 TeV is smaller than both its neighbouring slices, which is not desirable. However, it is hard to keep both the QCD and HQM yields balanced in high m_{jj} slices because of their different invariant mass distributions. We prefer to balance the QCD yield instead of the HQM yield, which makes the slicing also suitable for searching other BSM signals.

Table 5.1: Number of events and corresponding percentage in each m_{jj} slice. The numbers of QCD and HQM simulations are scaled to 36.2 fb^{-1}and rounded to integers.

Sample	m_{jj} slices [TeV]							
	3.4–3.7	3.7–4.0	4.0–4.3	4.3–4.6	4.6–4.9	4.9–5.4	5.4-5.7	5.7–13.0
Data	41183	20297	10289	5421	2706	2025	500	538
(collected in 2015–16)	49.64%	24.47%	12.40%	6.53%	3.26%	2.44%	0.60%	0.65%
LO QCD simulation	40801	20378	10391	5388	2816	2084	521	580
	49.18%	24.56%	12.53%	6.49%	3.39%	2.51%	0.63%	0.70%
HQM simulation	41	40	40	39	36	51	25	80
($n = 2$, $M_D = 7$ TeV)	11.64%	11.36%	11.36%	11.07%	10.22%	14.48%	7.10%	22.71%

The binning of χ is determined to be $\chi \in$ [1.00, 1.35, 1.82, 2.46, 3.32, 4.48, 6.05, 8.17, 11.02, 14.88, 20.06, 30.00] [54]. The bin edges follow the exponential expression $e^{0.3\times i}$, where i is the bin number while the last bin is extended to 30. The exponential form of the edges comes from the definition of χ in Equation 2.10, considering the typical cell granularity of tile calorimeters is 0.1. Such binning can reduces the jet migration between χ bins while keeping a reasonable resolution for studying the χ distribution [54].

5.2 Background yield estimation

In this section, corrections are applied to improve the accuracy of the background yield prediction. As the QCD simulation is produced with leading-order PDFs, the next-leading-order QCD correction needs to be calculated and applied. The ratio of NLO jet production to LO is referred to as the correction factor. It is obtained by comparing the NLO prediction from NLOJET++ [60] to that of PYTHIA 8. Moreover, although QCD processes dominate the jet

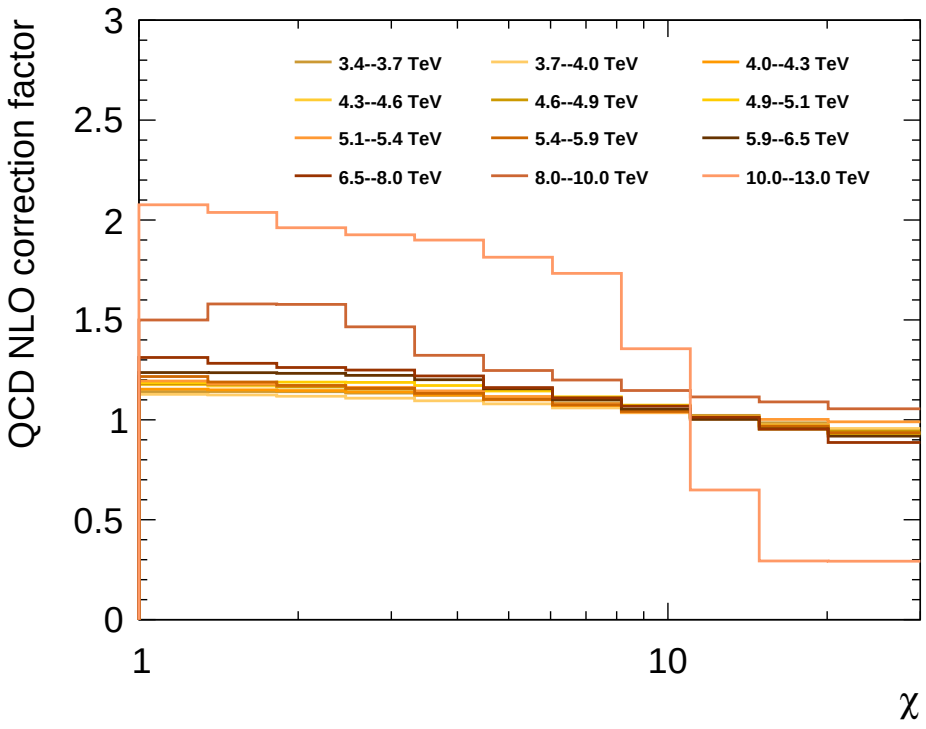

Figure 5.1: Next-leading-order QCD corrections to the QCD simulation.

production in ATLAS, contributions from electroweak (EW) processes are not negligible. EW corrections from Ref [61] are applied to take the EW contribution into account. Figures 5.1 and Figure 5.2 respectively shows the NLO QCD and LO EW corrections. Since they are calculated before the determination of the m_{jj} slicing, one of the correction bin edges at 5.9 TeV is not consistent with the 5.7 TeV edge. To solve this problem, χ distributions are generated in finer m_{jj} slices of 0.1 TeV and corrected first. Then, the 0.1-TeV distributions are added to the desired slicing. Figure 5.2 indicates that the corrections only vary in a small degree in the range of $5.7 - 5.9$ TeV. Thus, the loss of correction accuracy in $5.7 - 5.9$ TeV is expected to be negligible.

The background prediction will be scaled to the number of data events in every m_{jj} slice. We mention it here for the integrity of this section but details are discussed in Section 7.2 in the context of the likelihood model.

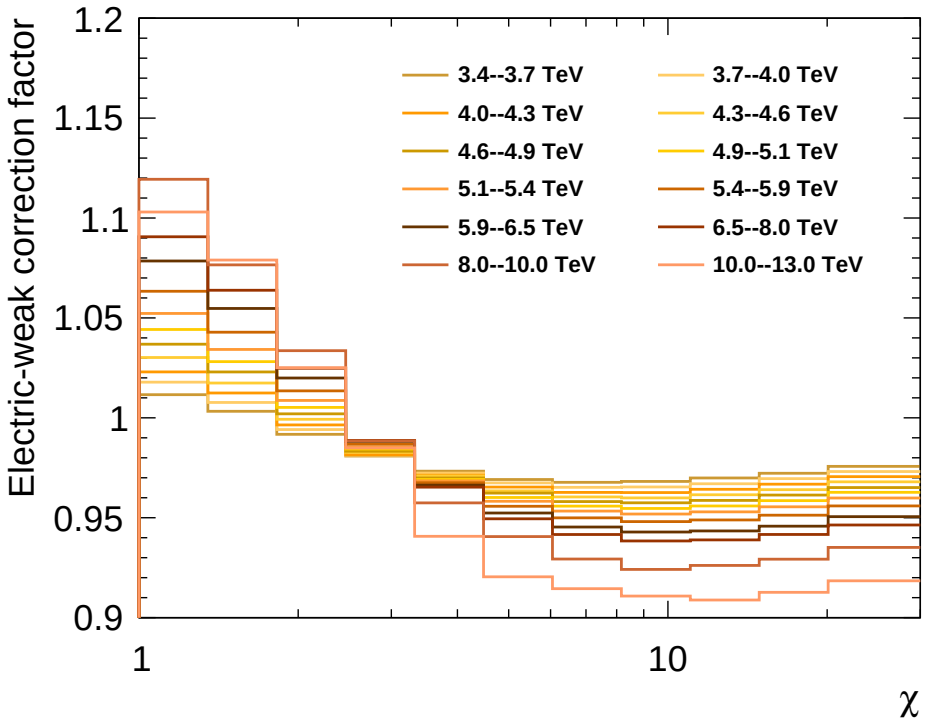

Figure 5.2: Leading order electroweak corrections to the QCD simulation, calculated by the author of Ref. [61].

5.3 Signal yield estimation

The production of HQM dijet events is the interest in this analysis. However, relevant theories are still under development and lack inputs from experiments, which makes it difficult to have accurate predictions on the signal yield. Thus, they are simply scaled to 139 fb^{-1} according to their theoretical cross-sections as a starting point for signal estimation. More specifically, the signal yield after selection is

$$N_s = \sigma_{HQM} \times \mathcal{L} \times \epsilon_{\text{tot}} \tag{5.1}$$

where σ_{HQM} is the cross-section listed in Table 2.5. $\mathcal{L}$ is the integrated luminosity. ϵ_{tot} is the total efficiency that can be obtained from Table 4.4. It is the ratio of selected events to generated events.

Figure 5.3 and Figure 5.4 shows the χ distributions, where the HQM events are stacked on top of simulated QCD events, in χ and $\mathrm{d}N/\mathrm{d}\chi$ histograms respectively. The number of events in a $\mathrm{d}N/\mathrm{d}\chi$ histogram is simply the one in

a χ histogram divided by the bin width of χ. The bin width can be a constant for a uniform χ histogram or a series of constants for a non-uniform histogram. Because we are using a non-uniform χ binning, the QCD events only peak in the high χ region in a χ histogram but not in a $\mathrm{d}N/\mathrm{d}\chi$ histogram. In terms of physics observations, the two types of histograms are equivalent in presenting the χ distribution.

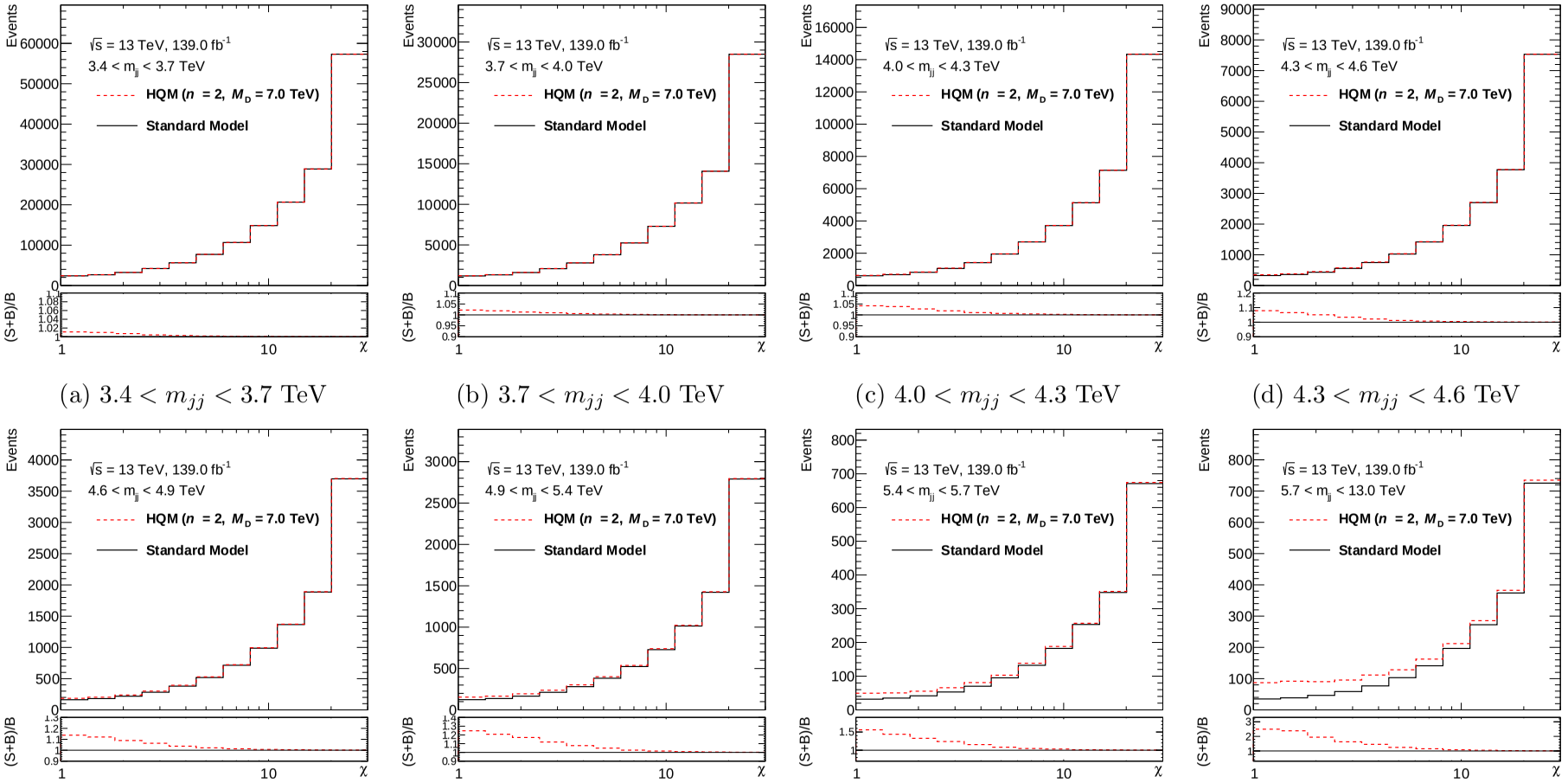

(a) $3.4 < m_{jj} < 3.7$ TeV (b) $3.7 < m_{jj} < 4.0$ TeV (c) $4.0 < m_{jj} < 4.3$ TeV (d) $4.3 < m_{jj} < 4.6$ TeV

(e) $4.6 < m_{jj} < 4.9$ TeV (f) $4.9 < m_{jj} < 5.4$ TeV (g) $5.4 < m_{jj} < 5.7$ TeV (h) $5.7 < m_{jj} < 13.0$ TeV

Figure 5.3: The χ distributions of HQM events stacked on top of simulated QCD events, shown in χ histograms.

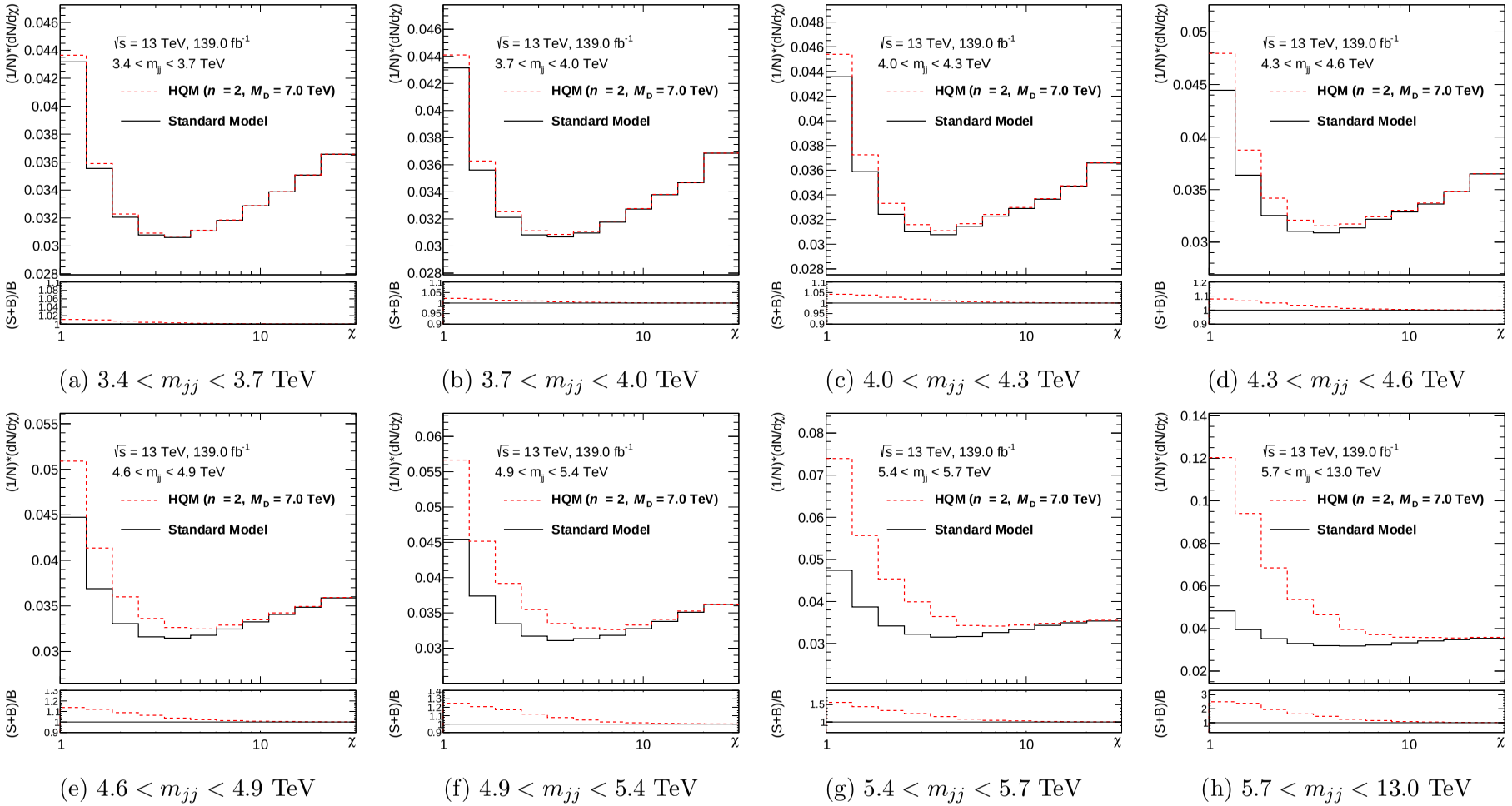

(a) $3.4 < m_{jj} < 3.7$ TeV (b) $3.7 < m_{jj} < 4.0$ TeV (c) $4.0 < m_{jj} < 4.3$ TeV (d) $4.3 < m_{jj} < 4.6$ TeV

(e) $4.6 < m_{jj} < 4.9$ TeV (f) $4.9 < m_{jj} < 5.4$ TeV (g) $5.4 < m_{jj} < 5.7$ TeV (h) $5.7 < m_{jj} < 13.0$ TeV

Figure 5.4: The χ distributions of HQM events stacked on top of simulated QCD events, shown in $\mathrm{d}N/\mathrm{d}\chi$ histograms.

Chapter 6

Systematic uncertainties

This chapter discusses the systematic uncertainties on background and signal predictions.

6.1 Uncertainties on background

Both experimental and theoretical uncertainties of the background prediction are considered and described blow.

6.1.1 Experimental uncertainties

Table 6.1 lists the abbreviations and descriptions of experimental uncertainties. The relative variations of these uncertainties in the highest m_{jj} slice are shown in Figure 6.1 and Figure 6.2. Uncertainties are most significant in the highest m_{jj} slice. Uncertainties in other m_{jj} slices can be found in Appendix D.

The pile-up correction introduced in Section 4.2.1 has uncertainties on modelling its variables: N_{PV}, μ and ρ in the offset term in Equation 4.7. Another uncertainty is introduced by the residual pile-up correction and it is derived from a parameter fitting process of the correction. The η inter-calibration introduced in Section 4.2.2 has six uncertainties. One covers the systematic uncertainty of the calibration, such as the choice of the generator. One covers the statistical uncertainty of the calibration. Three of them are on describing the non-closure, that is the residual difference between MC and data, on the detector transition regions $\eta \sim \pm 2.4$ and the high energy jets. Additional uncertainty is introduced due to the tile calibration in 2018 data.

The *global sequential* calibration described in Section 4.2.3 introduces uncertainties on modelling the jet responses on b-initiated and gluon-initiated jets, as well as the proportion of quark-initiated and gluon-initiated jets. Additional uncertainty is introduced for the correction for punch-through jets that are partially contained in the detector. The *in situ* calibration introduces 98 uncertainties because it consists of three analyses for sequential calibrations. These uncertainties are grouped and simplified so that they can be used more conveniently for a variety of ATLAS analyses without comprising their applicability [56]. This analysis uses the *global reduction* version of the reduced uncertainties described in Ref [56], which results in eight JES uncertainties.

The jet energy resolution measurement described in Section 4.2.5 introduces 34 uncertainty terms. In a similar method of reducing the *in situ* JES uncertainties, the JER uncertainties are reduced to eight terms. They are presented as one-side uncertainties but are symmetrized in the analysis.

The uncertainty from the single-particle response measurement is the largest one in high m_{jj} slices according to Figure 6.1. The uncertainty is developed by comparing calorimeter responses of isolated high energy particles in data to that in MC simulations [62]. The difference is taken as the uncertainty and propagated from single particles to jets.

6.1.2 Theoretical uncertainties on QCD

Theoretical uncertainties on QCD include QCD scale uncertainties, tune uncertainty and PDF uncertainty. The variations of theoretical uncertainties are shown in Figure 6.3.

Scale uncertainties come from the QCD renormalization (μ_R) and factorization (μ_F) scales which are introduced to solve the divergence problems in QCD. They are usually set to the momentum transfer Q which is not experimentally measured. As an approximation, they are set to the average of the two leading jet p_{T}: $\mu_R = \mu_F = \frac{p_{\mathrm{T}}^{\text{leading}} + p_{\mathrm{T}}^{\text{sub-leading}}}{2}$. The values two times as large/small as the average p_{T} are regarded as the uncertainty on the approximation choice. The uncertainty propagated to the χ distribution is calculated as the cross-section ratio of the varied scales to the un-varied, obtained from

Table 6.1: List of experimental uncertainties. The abbreviations are used in the plots in this thesis, and the corresponding descriptions are taken from Ref. [56].

Abbreviation	Decription
	Pileup
PileupOffsetMu	Uncertainty in the μ modelling in MC simulation
PileupOffsetNPV	Uncertainty in the N_{PV} modelling in MC simulation
PileupPtTerm	Uncertainty in the residual p_{T} dependence
PileupRhoTopology	Uncertainty in the per-event p_{T} density modelling in MC simulation
	η intercalibration
EtaIntercalData2018	Single component describing non-closure at $\eta \sim \pm 1.5$ due to tile calibration
EtaIntercalTotalStat	Statistical uncertainty in the η intercalibration
EtaIntercalModelling	Envelope of the generator, pileup, and event topology variations
EtaIntercalNegEta	Uncertainty on describing non-closure at $\eta \sim +2.4$
EtaIntercalPosEta	Uncertainty on describing non-closure at $\eta \sim -2.4$
EtaIntercalHighE	Uncertainty on describing non-closure at high energy
	Jet flavour
BJESResp	Uncertainty in the response of b-quark-initiated jets
FlavComposition	Uncertainty in the proportional sample composition of quarks and gluons
FlavResp	Uncertainty in the response of gluon-initiated jets
JES[1–8]	Reduced JES uncertainties on the *in situ* calibration
JER[1–7]	Reduced JER uncertainties
JERMC16/AFII	Uncertainty accounting the difference between data and full/AFII simulation
PunchThroughMC16/AFII	Uncertainty in *global sequential calibration* punch-through correction
RelativeNonClosureAFII	Difference in the absolute JES calibration for simulations in AFII
SingleParticleHighPt	High-p_{T} jet uncertainty from single-particle and test-beam measurements

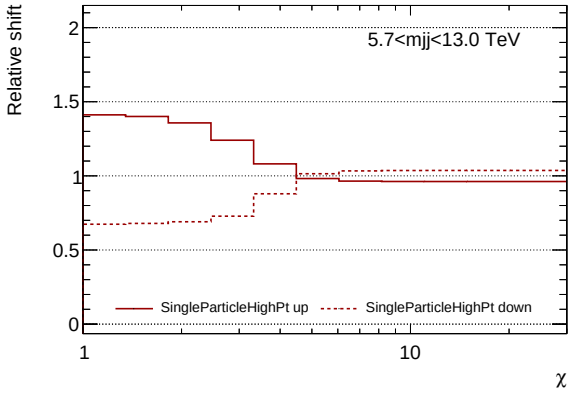

(a) Uncertainty in the single-particle response measurement.

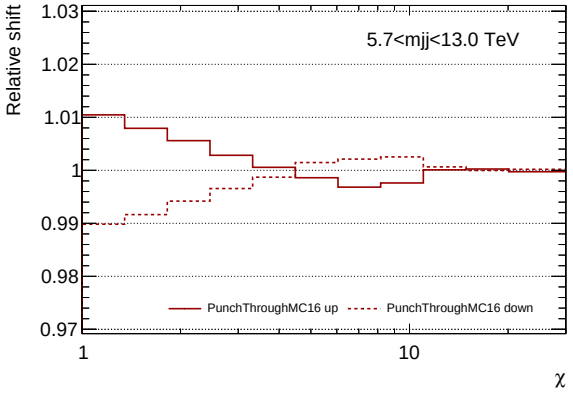

(b) Uncertainty in the remaining difference between data and MC simulation.

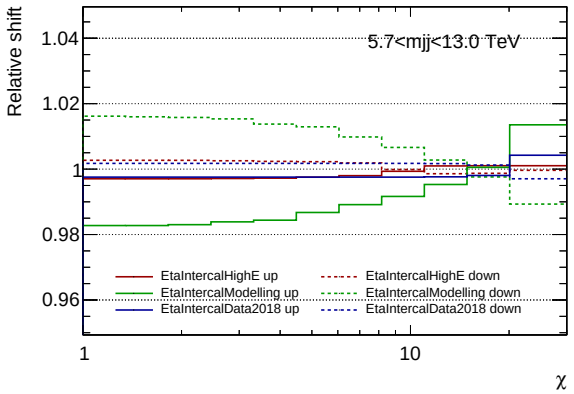

(c) Uncertainties on modelling and describing non-closure in high energy, and tile calibration.

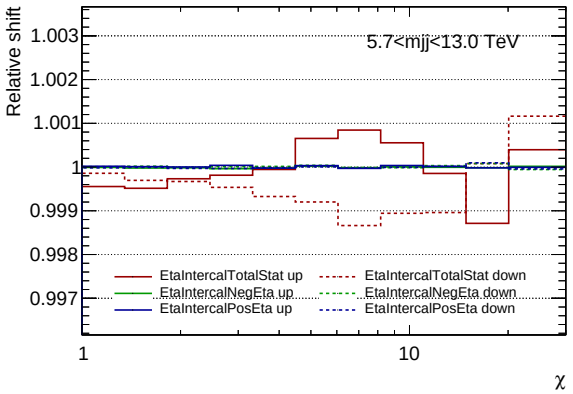

(d) Statistical uncertainty in η intercalibration and systematic uncertainty on describing non-closure at $\eta \sim \pm 2.4$.

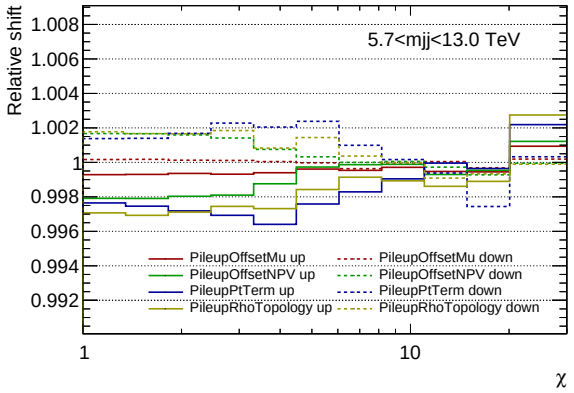

(e) Uncertainties on modelling the pile-up offset term and residual correction.

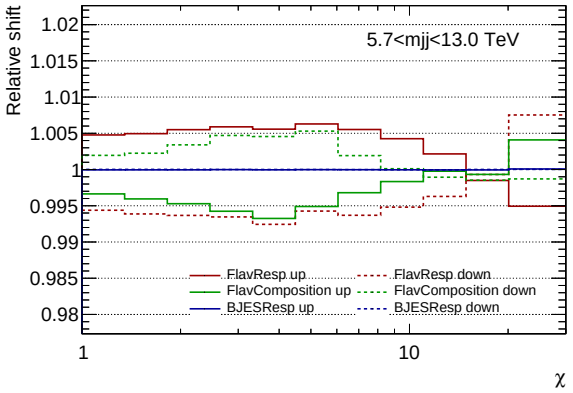

(f) Uncertainty in the response of gluon-initiated and b-quark initiated jets and the composition of quarks and gluons.

Figure 6.1: Experimental uncertainties of the background prediction in $5.7 < m_{jj} < 13.0$ TeV.

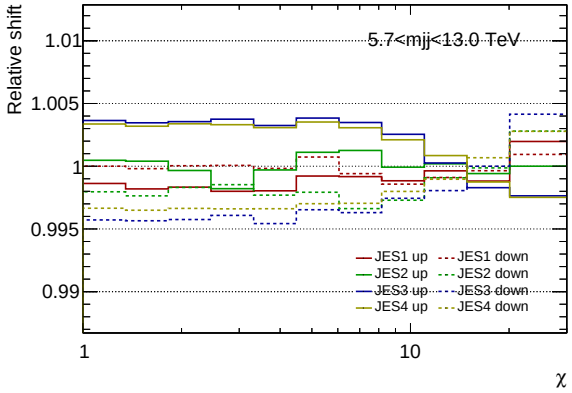

(a) Reduced *in situ* JES uncertainties 1–4.

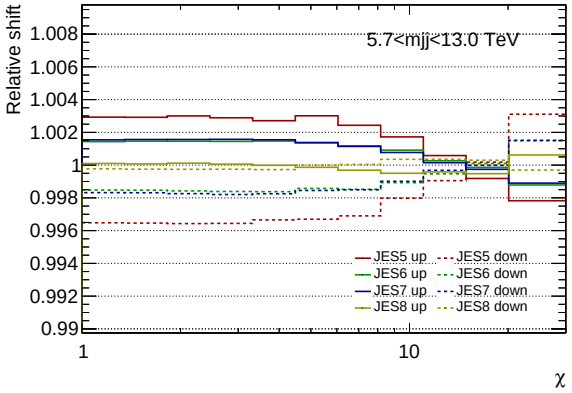

(b) Reduced *in situ* JES uncertainties 5–8.

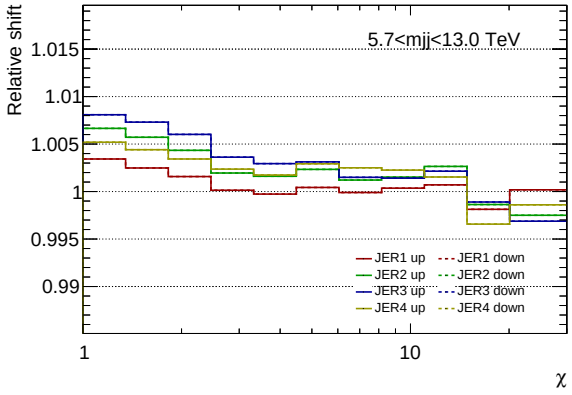

(c) Reduced JER uncertainties 1–4.

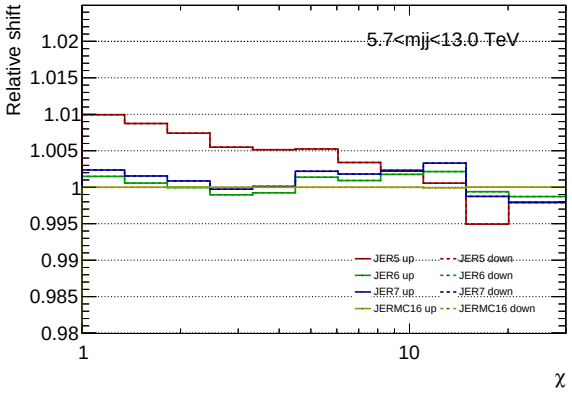

(d) Reduced JER uncertainties 5–7 and uncertainty in difference between simulation and data.

Figure 6.2: Reduced experimental uncertainties of the background prediction in $5.7 < m_{jj} < 13.0$ TeV.

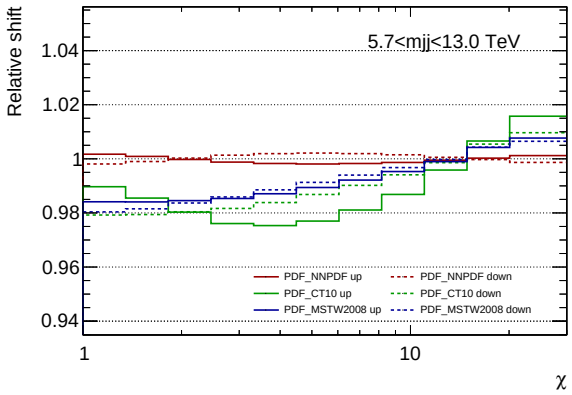

(a) PDF uncertainties in NNPDF2.3, CT10 and MSTW2008.

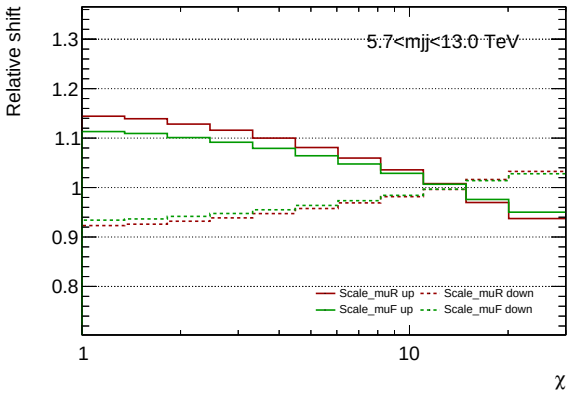

(b) Scale uncertainties in μ_R and μ_F.

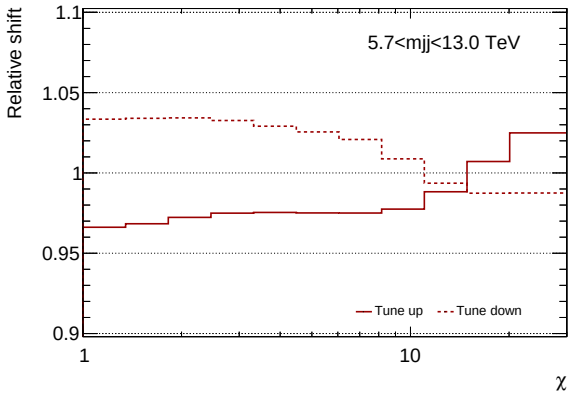

(c) Tune uncertainty.

Figure 6.3: Theoretical uncertainties of the background prediction in $5.7 < m_{jj} < 13.0$ TeV.

NLOJet++.

The tune uncertainty comes from the parameter optimization of the generator. Pythia 8, the generator used to simulate physics processes of the QCD dijet production, has built-in parameters. Parton shower and multi-parton interaction parameters are tuned to data to improve the data-MC agreement. This analysis uses the A14 tune version described in Ref. [63] and an uncertainty is introduced from the tuning process.

Parton distribution functions can not be calculated by the non-perturbative QCD but can only be obtained by fitting experimental data. Thus, they have uncertainties on their internal parameters and these uncertainties are propagated to our observable distribution. There are several working groups working on PDFs with various methods. The uncertainty on PDFs is constructed in a way that considers three widely used PDF sets: NNPDF2.3 [29], CT10 [64] and MSTW2008 [65]. Each PDF set has a collection of nominal and varied PDFs. Different methods are considered and tested to construct the uncertainty. One of the methods is to take the envelope of these PDF sets and extract the high and low bounds, which is the recommended method given by the PDF4LHC group in 2010 [66]. However, this recommendation does not work for a shape analysis very well. On the one hand, the shape difference between PDF sets is lost when constructing the combined envelope. The envelope only gives the uncertainty on the production rate which is not the interest of a shape analysis. On the other hand, the up and down bounds are calculated as the ratio to the median value of the two bounds, which makes the uncertainty symmetric. The symmetry feature is not a natural feature of the PDF uncertainty. The ideal way of dealing with PDF uncertainty is to include every varied PDF set as an independent uncertainty source. However, this is not practical because it will add too much complexity to the analysis.

To extract the shape difference as much as possible while not adding too much complexity for presumably little gain, a modified method has been used. First, to decorrelate the uncertainties from different PDF sets, three PDF uncertainties are constructed from the envelopes of the corresponding PDF sets. Second, all envelopes are calculated as the ratio to the nominal PDF of

NNPDF2.3 instead of to the median value. Such modifications make the PDF uncertainties have clear physical meanings: the uncertainty from NNPDF2.3 can be understood as the one from the built-in parameters of NNPDF2.3, and the uncertainties from MSTW2008 and CT10 can be translated as the difference between them and NNPDF2.3. Details of this method can be found in Appendix E. Despite this method gives larger PDF uncertainties compared to the version recommended by PDF4LHC, the impact on the analysis is small as discussed in Section 8.3.3. In this analysis, we use the separated PDF uncertainties on NNPDF2.3, CT10 and MSTW2008 as the default choice instead of the PDF4LHC recommendation.

6.2 Uncertainties on signal

The same experimental uncertainties considered for the QCD simulation, are considered for the signal samples. Due to the small number of simulated signal events, the uncertainties on angular distributions have unexpected irregular statistical fluctuations. To remove these fluctuations, the y^* distribution is fit to a Gaussian function centring at 0. Then, uncertainties on the y^* distribution are transferred to the angular distribution which results in smoothed uncertainties. Figure 6.4 and Figure 6.5 shows the non-smoothed uncertainties while Figure 6.6 and Figure 6.7 show the smoothed ones. Uncertainties in other m_{jj} slices can be found in Appendix F. By comparing the two sets of uncertainties, it is clear that the smoothing process only works for some of the uncertainties, such as the uncertainty in the punch-through correction. As for other uncertainties whose variations are too small to stand out from the statistical fluctuations, the fitting procedure does not work and introduces extra systematic errors on small uncertainties. Several common smoothing algorithms are also tried as alternative choices but the results are still far from ideal. We decide to proceed with the smoothed uncertainties obtained by fitting y^* distributions. By doing this, we are able to smooth large signal uncertainties and reduce computational problems despite introducing errors on small uncertainties. As later tested in Section 8.3.3, small signal uncertainties,

even all signal uncertainties, have negligible impact on the analysis results. It is because the QCD background dominates the event yield and the uncertainties on the background model dominate the statistic likelihood model of the analysis which will be introduced in Section 7. Thus, it is safe to proceed with the smoothed signal uncertainties without worrying about the side effects.

Theoretical uncertainties, such as the PDF uncertainty and scale uncertainties from the perturbative QCD theory, are not considered. We assume that gravity is the dominating interaction in producing black holes and those uncertainties are negligible.

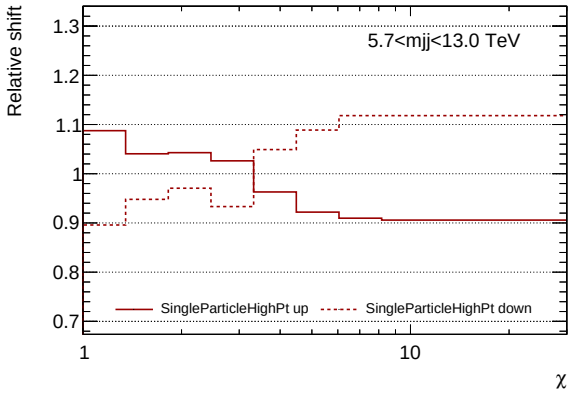

(a) Uncertainty in the single-particle response measurement.

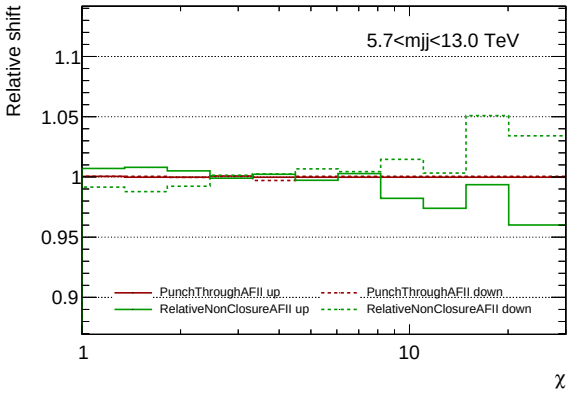

(b) Uncertainties in the correction of partially contained jets and remaining difference between data and MC simulation.

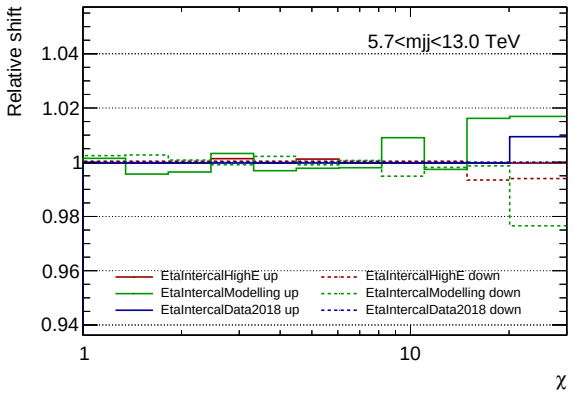

(c) Uncertainties on modelling and describing non-closure in high energy.

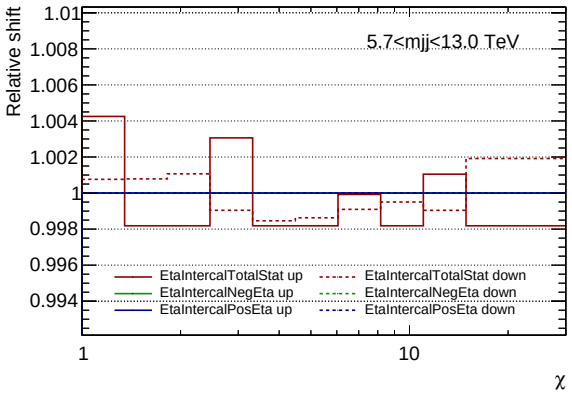

(d) Statistical uncertainty in η intercalibration and systematic uncertainty on describing non-closure at $\eta \approx \pm 2.4$.

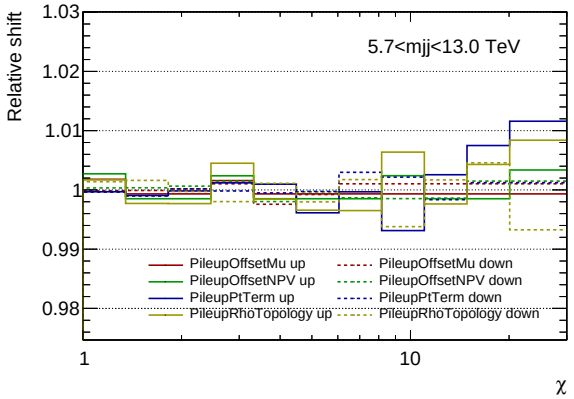

(e) Uncertainties on modelling the pile-up offset term and residual correction.

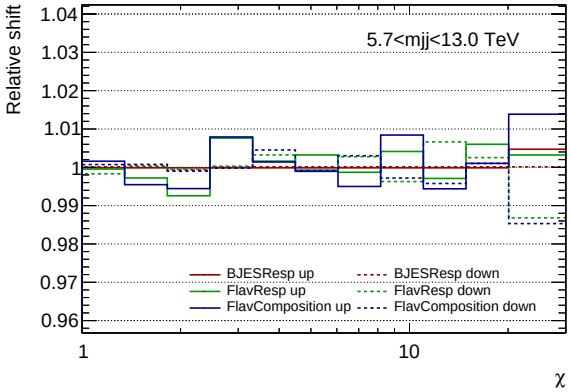

(f) Uncertainty in the response of gluon-initiated and b-quark initiated jets and the composition of quarks and gluons.

Figure 6.4: Non-smoothed experimental uncertainties of the signal prediction in $5.7 < m_{jj} < 13.0$ TeV.

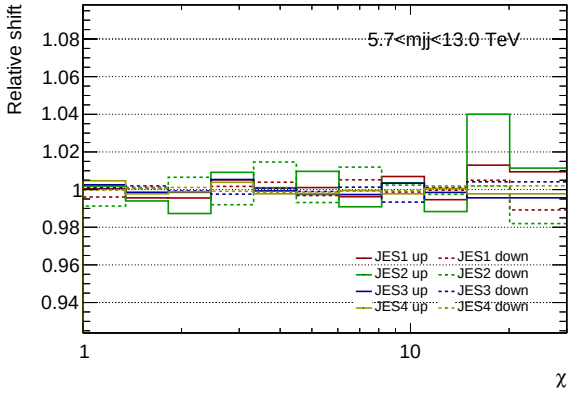

(a) Reduced *in situ* JES uncertainties 1–4.

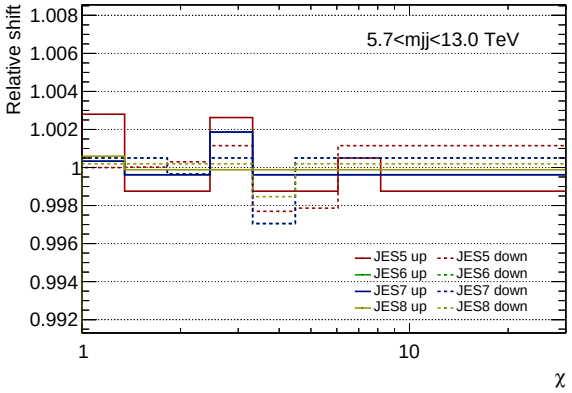

(b) Reduced *in situ* JES uncertainties 5–8.

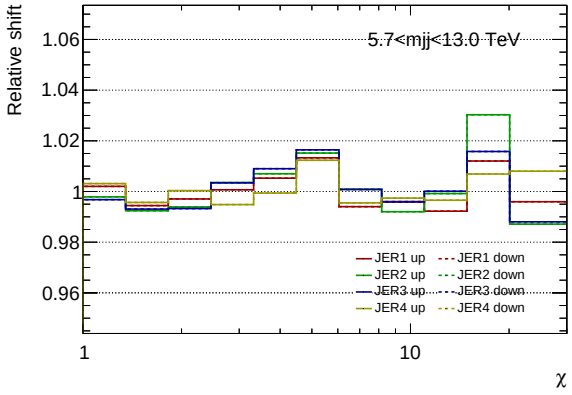

(c) Reduced JER uncertainties 1–4.

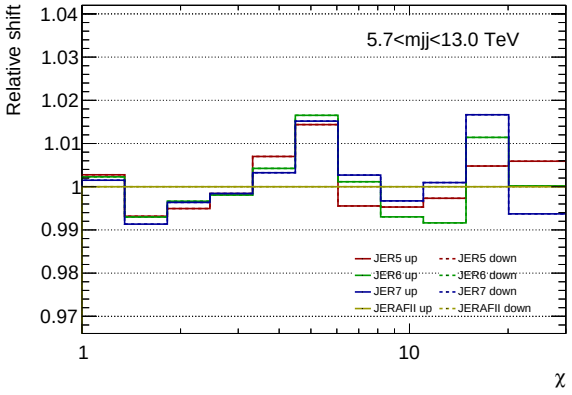

(d) Reduced JER uncertainties 5–7 and uncertainty in difference between simulation and data.

Figure 6.5: Non-smoothed reduced experimental uncertainties of the signal prediction in $5.7 < m_{jj} < 13.0$ TeV.

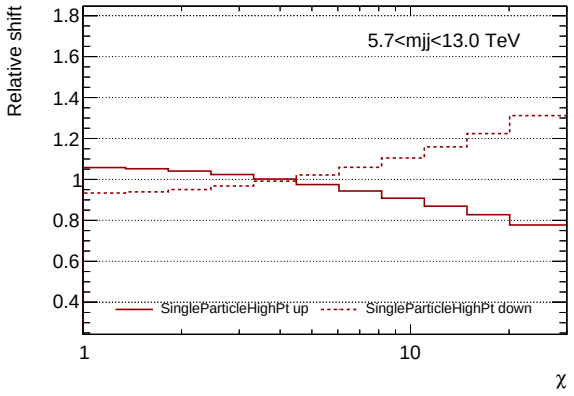

(a) Uncertainty in the single particle response measurement.

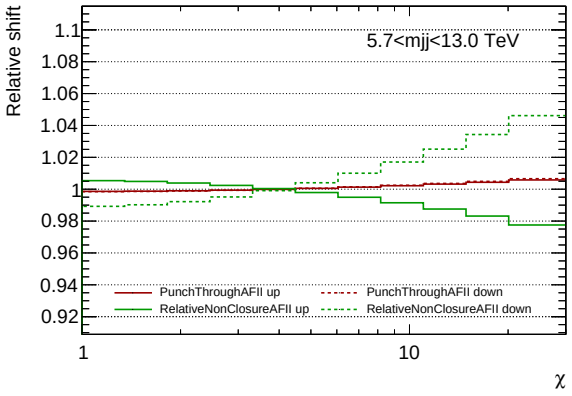

(b) Uncertainties in the correction of partially contained jets and remaining difference between data and MC simulation.

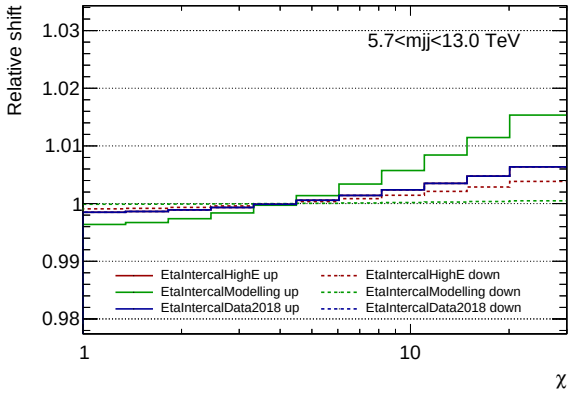

(c) Uncertainties on modelling and describing non-closure in high energy.

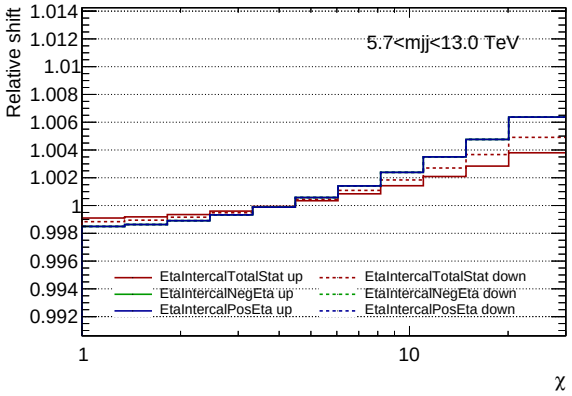

(d) Statistical uncertainty in η intercalibration and systematic uncertainty on describing non-closure at $\eta \approx \pm 2.4$.

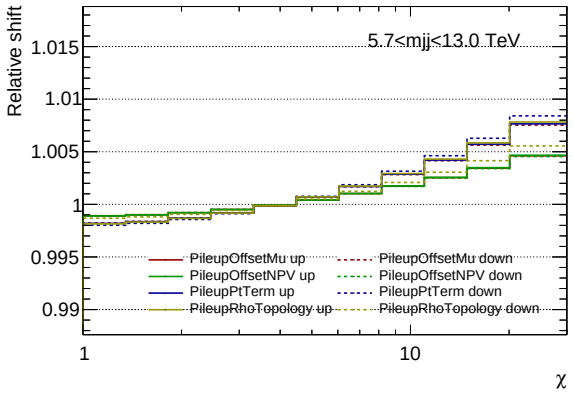

(e) Uncertainties on modelling the pile-up offset term and residual correction.

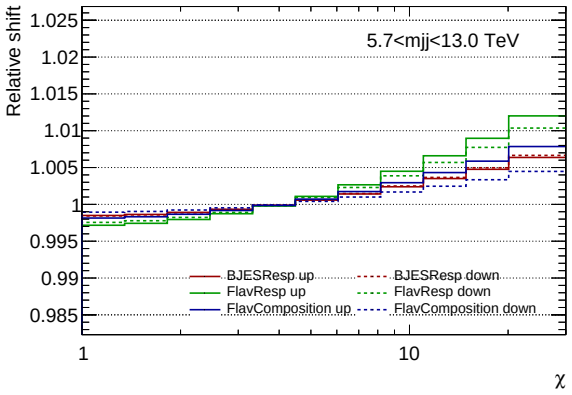

(f) Uncertainty in the response of gluon-initiated and b-quark initiated jets and the composition of quarks and gluons.

Figure 6.6: Smoothed experimental uncertainties of the signal prediction in $5.7 < m_{jj} < 13.0$ TeV.

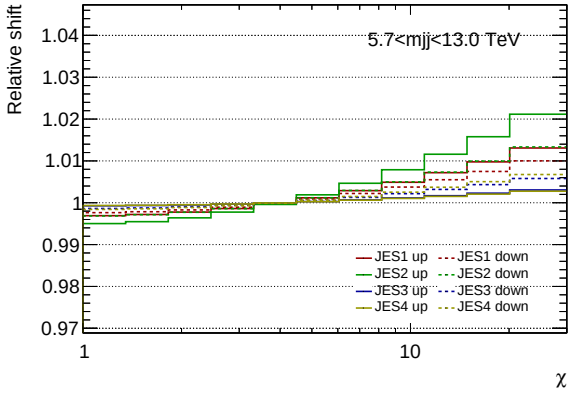

(a) Reduced *in situ* JES uncertainties 1–4.

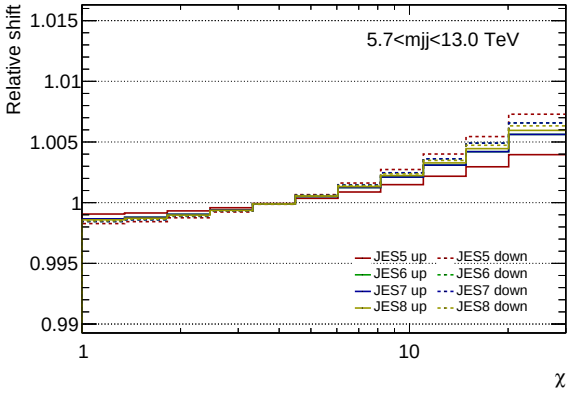

(b) Reduced *in situ* JES uncertainties 5–8.

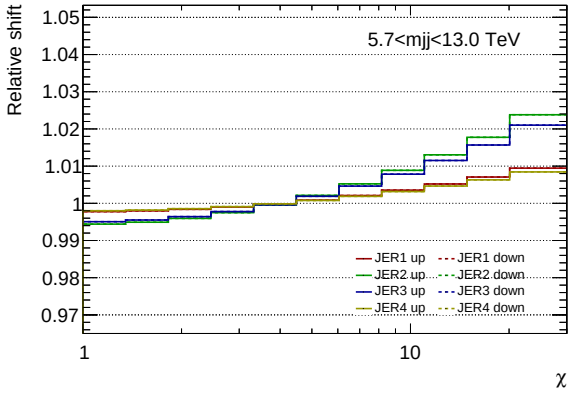

(c) Reduced JER uncertainties 1–4.

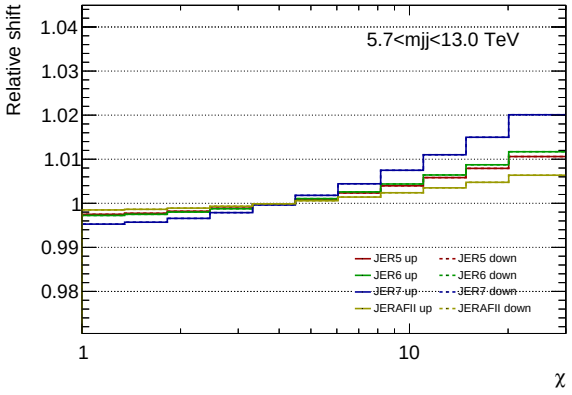

(d) Reduced JER uncertainties 5–7 and uncertainty in difference between simulation and data.

Figure 6.7: Smoothed reduced experimental uncertainties of the signal prediction in $5.7 < m_{jj} < 13.0$ TeV.

Chapter 7

Statistic tools

This chapter introduces the frequentist method to build the likelihood model of the analysis and calculate signal significance and parameter upper limits at 95% confidence level. Figure 7.1 shows the workflow of this method. The sections are organized following the workflow. Section 7.1 builds the likelihood model of the signal-plus-background ($s+b$) prediction. Section 7.2 introduces the strategy for the shape-only fit. Section 7.3 defines the test statistics and introduces the methods to calculate the signal significance and upper limit.

7.1 The likelihood model

To be consistent with the terminologies in literature, we refer a m_{jj} slice to as a *channel*. The χ variable is the observable and the *bin* refers to a bin of the χ distribution in one of the m_{jj} channels. More specifically, there are 8 channels and 8×11 bins in our analysis. The likelihood of obtaining an observed dataset under a $s+b$ prediction with a signal production rate of μ is denoted as $L(\mu)$. It is a product of Poisson probabilities

$$L(\mu) = \prod_{c=1}^{c=8} \prod_{i=1}^{i=11} \text{Poisson}(N_{c,i}|\mu S_{c,i} + B_{c,i}), \tag{7.1}$$

where the subscript c indicates a channel and the subscript i indicates a bin. $N_{c,i}$ is the number of observed events in bin (c,i) while $S_{c,i}$ and $B_{c,i}$ are the numbers of expected signal and background events. The signal production rate μ is also referred to as the signal strength parameter. It is the parameter

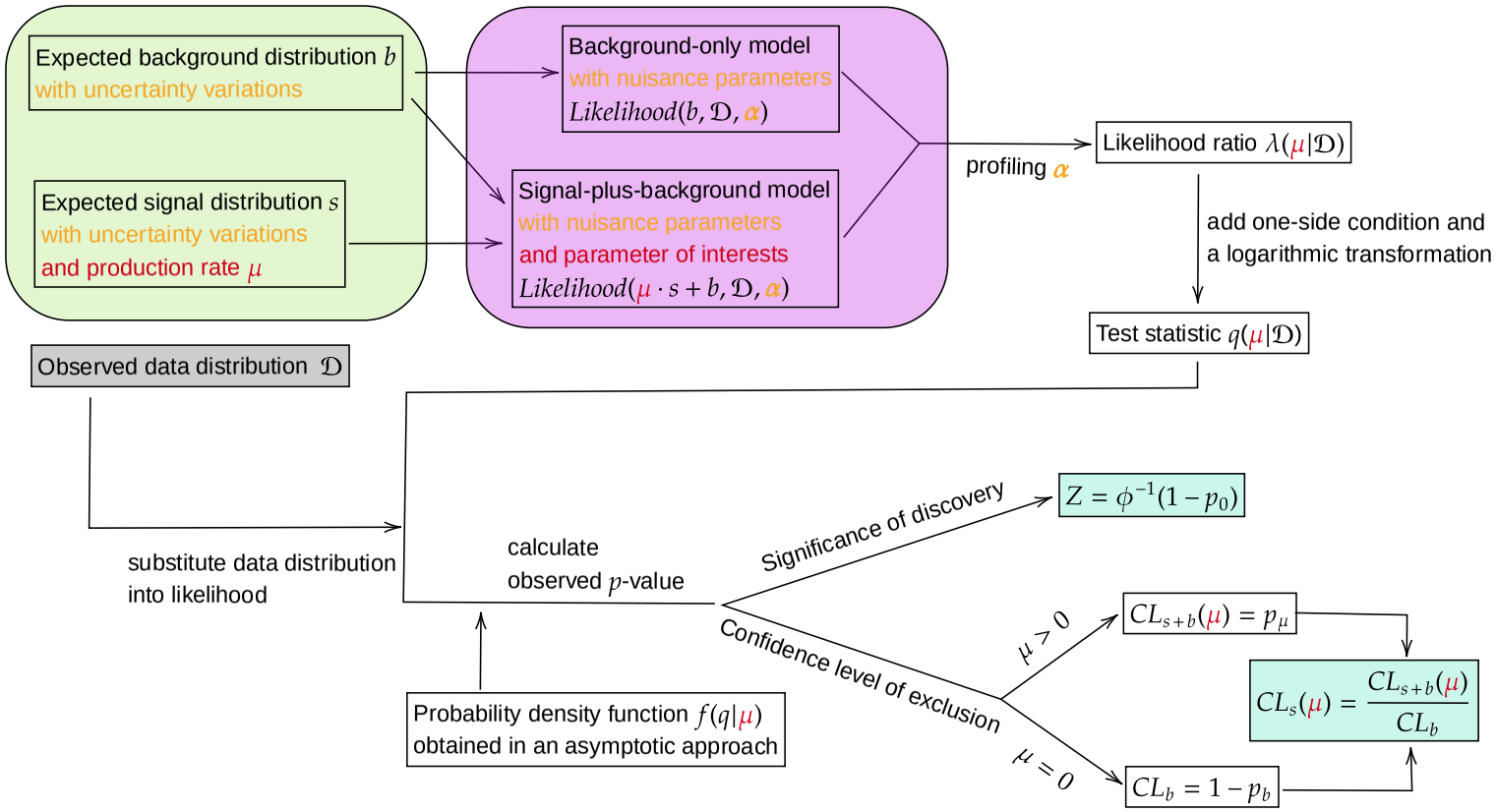

Figure 7.1: Workflow of the frequentist method to calculate signal significance and upper limits. The likelihood models (shown in the purple box) are built according to simulated signal and background samples (shown in the green box). A test statistic q is defined to reflect the compatibility between data and prediction as a single number. Finally, for a given observed dataset, the significance is calculated for a discovery hypothesis test, and confidence levels of excluding the signal models are calculated as a function of μ.

of interest (POI) in the analysis. We limit $\mu \geq 0$ because negative signal production lacks a physics explanation. Equation 7.1 is only the barebone of the likelihood model which does not include any uncertainties. The incorporation of uncertainties on the $s + b$ prediction in the likelihood model is introduced in the following subsection.

7.1.1 Systematic uncertainties

Systematic uncertainties of simulations come from multiple sources, as discussed in Section 6. Taking JER for example, the p_{T} spectrum in simulation has to be smeared to make simulation agree with data in Figure 4.5. The difference between data and simulation has dependence on the parameter S in Equation 4.9 which is obtained from data. The fit of data to Equation 4.9 gives us an estimation of $S \pm \sigma_S$ where σ_S is the uncertainty on S. The uncertainty on S first propagates to the data-simulation difference, then to the p_{T} spectrum of simulations, and finally to the χ distribution. As Figure 7.2 illustrates, the nominal χ distribution is obtained with nominal S value. The $\pm 1\sigma$ varied χ distributions are obtained with $S \pm 1\sigma_S$ values. The varied χ distribution responds to parameter variations in two aspects: shape and yield. In Figure 7.2, the variation on shape is straightforward as the blue lines are more or less curved than the red line. It reflects the uncertainty on the probability density function (pdf) of the observable. The yield variation is the difference between the areas under the blue lines and the red line. It reflects the uncertainty on the cross-section of the simulated sample. In conclusion, S is a measured JER parameter and its uncertainty propagates to our observable distribution. This narrative can be generalized to other uncertainties. Accordingly, we can incorporate uncertainty into the likelihood model in two steps: mapping it to a parameter first and then building a response function to interpret the χ variations caused by the uncertainty propagation.

To start with the parameter mapping, parameters of uncertainties are referred to as nuisance parameters (NPs) because they are not the primary interest of this analysis. Their original measurements are referred to as auxiliary measurements. To simplify the math in the likelihood model, we map a

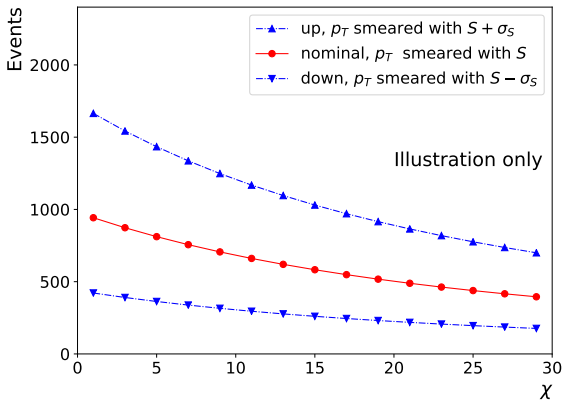

Figure 7.2: An illustration of uncertainty propagated from a jet energy resolution (JER) parameter S to the χ distribution. The (red) nominal distribution is obtained when p_{T} is smeared according to the nominal S value while the (blue) varied distributions are obtained according to varied S values.

NP's nominal value α_s^0 and its standard deviation σ_{α_s} to the following values

$$\begin{aligned} \alpha_s^0 &\to 0, \\ \sigma_{\alpha_s} &\to 1, \end{aligned} \tag{7.2}$$

no matter what the auxiliary measurement is. In this mapping scenario, the value of α_s only reflects how many standard deviations it deviates in this analysis from its auxiliary measurement. The actual parameter value is hidden behind this mapping because it is not our interest. However, we do expect the estimation of α_s^0 close to 0 in our analysis. Otherwise, it conflicts with the auxiliary measurement.

After parameter mapping, we are able to build response functions for NPs to interpret their impacts on the χ distribution. As mentioned, the systematic variation propagates to the observable distribution in terms of shape and yield. Both are taken account of by considering the yield variation at a bin-by-bin level. The yield in a single bin varies up and down from the nominal yield and the variations in all bins compose the shape variation. At a bin-by-bin level, we write the varied bin yield $B_{c,i,s}$ as a function of the parameter α_s

$$B_{c,i,s}(\alpha_s) = B_{c,i} \cdot \eta_{c,i}(\alpha_s) \tag{7.3}$$

where $\eta_{c,i}(\alpha_s)$ is a response function. Given the varied simulations, we can

determine three points on the response function:

$$\begin{aligned} \eta_{c,i}(\alpha_s^0) &= 1, \\ \eta_{c,i}(\alpha_s|_{\alpha_s^0 \pm \sigma_{\alpha_s}}) &= B_{c,i}^{\pm}/B_{c,i}, \end{aligned} \tag{7.4}$$

where $B_{c,i}^{\pm}$ are the varied yields. The rest of the response function is obtained by a 6th-order polynomial interpolation and exponential extrapolation [67], as illustrated in Figure 7.3. The exponential extrapolation uses two points at each side, $\eta(0)$ and $\eta(+1)$ ($\eta(-1)$) in region $\alpha_s > 1$ ($\alpha_s < -1$). The polynomial interpolation is determined with points $\eta(0)$, $\eta(\pm 1)$ and a boundary smooth requirement. More specifically, the first and second derivatives of the polynomial function at $\eta(\pm 1)$ are required to be consistent with the exponential extrapolation. At this point, the likelihood model considering the response functions of systematic uncertainties is

$$\begin{aligned} L(\mu, \boldsymbol{\alpha}) &= \prod_{c=1}^{c=8} \prod_{i=1}^{i=11} \text{Poisson}(N_{c,i}|\mu S_{c,i} \cdot \prod_s \eta_{c,i,s}^{sig}(\alpha_s) + B_{c,i} \cdot \prod_s \eta_{c,i,s}^{bkg}(\alpha_s)) \\ &= \prod_{c=1}^{c=8} \prod_{i=1}^{i=11} \text{Poisson}(N_{c,i}|\lambda_{c,i}(\mu, \boldsymbol{\alpha})) \end{aligned} \tag{7.5}$$

where $\lambda_{c,i}(\mu, \boldsymbol{\alpha})$ is the number of expected events and $\boldsymbol{\alpha} = (\alpha_1, \alpha_2, ..., \alpha_s, ...)$. Using $\lambda_{c,i}(\mu, \boldsymbol{\alpha})$ hides the details of constructing uncertainty responses and treats the $s + b$ prediction as a function of parameters μ and $\boldsymbol{\alpha}$. Response functions are multiplied on both the signal and background predictions bin-by-bin. The likelihood $L(\mu, \boldsymbol{\alpha})$ is a function explicitly depending on the POI (μ) and NPs ($\boldsymbol{\alpha}$). We take μ as a free parameter in maximum-likelihood fit, but $\boldsymbol{\alpha}$ should be limited because it is originally measured by auxiliary measurements. This is achieved by adding constraint terms for $\boldsymbol{\alpha}$ in our likelihood model. A constraint term for an individual NP should peak at $\alpha_s = 0$ that corresponds to zero deviation from its auxiliary measurement, and approach to 0 when $|\alpha_s| \gg 0$ that corresponds to a large deviation. In other words, the constraint term is a penalty term to prevent α_s deviating away from 0. The specific form of the constraint term depends on the auxiliary measurement. However, it is complex, even impossible, to derive the constraint term mathematically. Conventionally, we assume that α_s follows a Gaussian distribution. Based on

the parameter mapping of $\alpha_s = 0 \pm 1$, the constraint term is constructed as a Gaussian probability density function: Gaussian(α_s) that centres at 0 with a standard deviation of 1. With the constraint terms described above, we have the finalized likelihood

$$\begin{aligned} L(\mu, \boldsymbol{\alpha}) &= \prod_{c=1}^{c=8} \prod_{i=1}^{i=11} \text{Poisson}(N_{c,i} | \lambda_{c,i}(\mu, \boldsymbol{\alpha})) \cdot \prod_{s} \text{Gaussian}(\alpha_s) \\ &= \textbf{Poisson}(\mathcal{D} | \lambda(\mu, \boldsymbol{\alpha})) \cdot \textbf{Gaussian}(\boldsymbol{\alpha}). \end{aligned} \tag{7.6}$$

where $\textbf{Poisson}(\mathcal{D}|\lambda(\mu, \boldsymbol{\alpha}))$ is the product of Poisson probabilities and $\textbf{Gaussian}(\boldsymbol{\alpha})$ is the product of Gaussian probabilities. NP $\boldsymbol{\alpha}$ has impact on both the Poisson and Gaussian functions. The combination of the observed yields $N_{c,i}$ is denoted as the observed dataset $\mathcal{D}$.

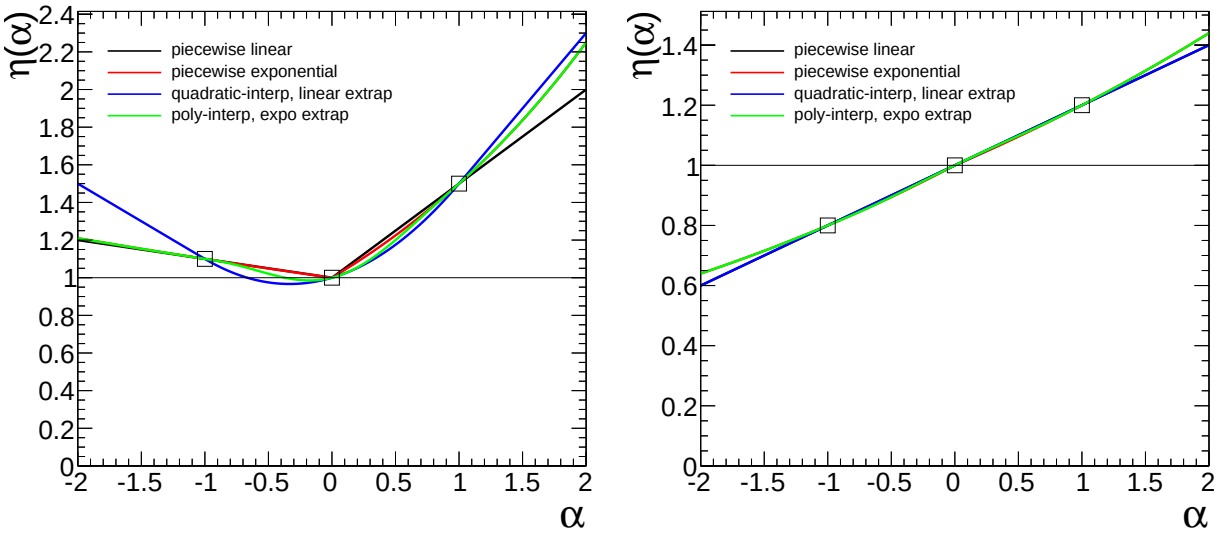

Figure 7.3: Illustration of two examples of interpolating response functions $\eta(\alpha)$, taken from Ref. [68]. Lines of different colours represents different interpolation methods as discussed in Ref. [68]. The value of $\eta(0)$ is fixed to 1 since it is defined as the nominal response without variation. Values of $\eta(\pm 1)$ depend on the responses of a specific uncertainty. The left plot shows a case of increased yields at both $\eta(1)$ and $\eta(-1)$ while the right plot shows a case of an increased yield at $\eta(1)$ but decreased at $\eta(-1)$.

7.1.2 Statistical uncertainty

Statistical uncertainties on the background and signal samples come from the size of available MC simulations. These samples in our analysis are large

enough to keep the uncertainty smaller than 5% in every bin. One could similarly incorporate MC statistical uncertainties as systematic uncertainties. However, it will introduce a large number of extra NPs equal to the number of bins in all channels for every sample because the statistical fluctuations are independent in bins. The number of NPs introduced by the statistical uncertainty will be 88 for this analysis. Such a large number of NPs will make the maximum-likelihood fit hard to converge. We have compared results between considering statistical uncertainty and not. The difference is negligible. Thus, we drop all the statistical uncertainties on the MC in our analysis to avoid computational problems.

Although some other systematic uncertainties are also smaller than 5%, we do not drop them because they do not add much complexity to the analysis.

7.1.3 Parameter constraint and correlation

Parameter constraint

We refer to the initially mapped values of the parameters in Equation 7.6 as pre-fit values. The pre-fit value of μ is set to 1 which corresponds to the full production of a signal model. The pre-fit value of $\boldsymbol{\alpha}$ is set to $\mathbf{0}$ which corresponds to zero deviation from the auxiliary measurements. The values of parameters estimated by a maximum-likelihood fit are referred as post-fit values. They are denoted as $\hat{\mu}$ and $\hat{\boldsymbol{\alpha}}$.

The pre-fit value and post-fit value of a parameter α_s can be translated as two results from two measurements. The pre-fit value is the one from its auxiliary measurement while the post-fit value is from this analysis. Usually, the auxiliary measurements are performed with well-established methods and widely used in ATLAS. Thus, comparing the pre-fit and post-fit values can help validate the analysis. If the nominal value of post-fit α_s deviates from 0, it indicates a conflict between the two analyses. If the standard deviation of post-fit α_s, denoted as σ_{α_s}, is much larger (smaller) than 1, it indicates a worse (better) measurement of α_s than the auxiliary measurement. Usually, we do not expect $\sigma_{\alpha_s} \ll 1$ because the auxiliary measurement is designed and

optimized specifically for measuring the parameter. However, it can happen to have a small σ_{α_s} in our maximum-likelihood fit, and we call this parameter over-constrained. Sometimes it is caused by using a larger dataset in this analysis than the one in the auxiliary measurement. The increased statistic power can improve the parameter measurement. In this case, we do not worry about the constraint. However, it may also be caused by imperfect modelling of the likelihood. Thus, the appearance of over-constrained parameters requires careful investigations to exclude the latter situation.

Parameter correlation among channels

Equation 7.6 assumes every parameter varies simultaneously in all channels. We call the parameters correlated under this assumption. In our analysis, the channels in the low m_{jj} range have the strongest statistical power and dominate the maximum-likelihood fit. As a result, the maximum-likelihood fit prioritizes improving the agreement between the $s + b$ prediction and data observation in the low m_{jj} channels instead of the high m_{jj} channels. Thus, the statistical power in the low m_{jj} channels serves as a constraint to prevent overfitting in high m_{jj} channels. The opposite assumption is that uncertainties are uncorrelated among channels. It introduces one NP per uncertainty per channel instead of one NP for all channels, which makes the number of NPs eight times as large as the fully correlated assumption. Sometimes de-correlating the uncertainties may ease the over-constrained parameters but always reduces the sensitivity of the analysis due to the extra degrees of freedom. In this analysis, assuming uncorrelated uncertainties does not ease the constraint of parameters and it is not physically motivated. Thus, we prefer the fully-correlated assumption over the de-correlated one.

7.2 Shape-only analysis

Typical search analyses in ATLAS usually predict the background production in a signal region by extrapolating control regions where signal contamination is negligible into the signal region. The yield difference between the back-

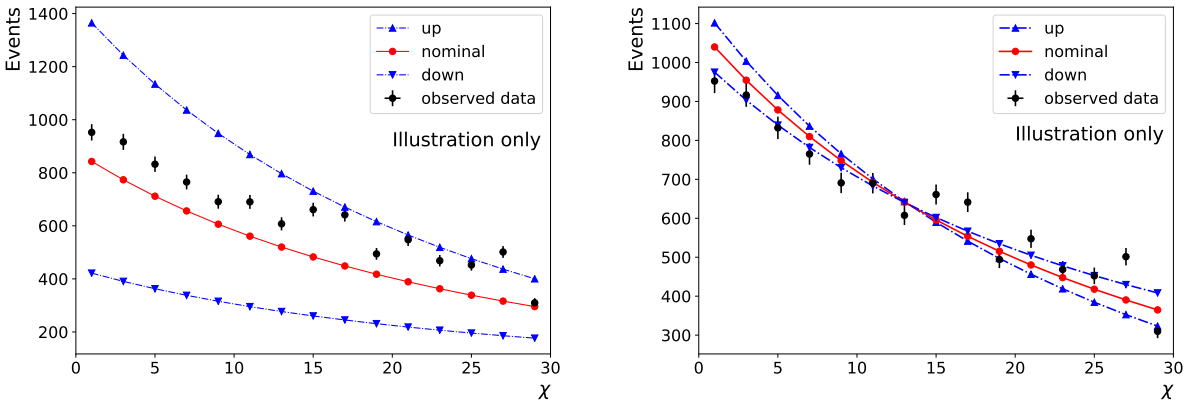

Figure 7.4: Illustration of background normalization. The left plot illustrates the distributions of observed data and predicted nominal/up/down background predictions. The left plot illustrates the distributions of background predictions after normalization. The data distribution is not modified while the areas under the lines are normalized to the data.

ground prediction and observation is the key to claim discoveries in those analyses. However, such control regions are not available in our analysis because the production of HQM dijet events covers the entire m_{jj} spectrum. Thus, the angular analysis is designed as a shape-only analysis that emphasizes the shape difference in all channels between the background prediction and observation instead of the yield difference. It is implemented via background normalization and illustrated in Figure 7.4. In each channel, the yield of the nominal background prediction is normalized to the observed data by a factor of B_c^{MC}/N_c^{data}. B_c^{MC} and N_c^{data} are respectively the yields of the background prediction and observation in a given channel. The background from the uncertainties are also normalized in the same way as the nominal prediction. Therefore, the channel-level yield difference is zero by definition. The shape difference, which is a composition of the bin-level yield difference, still has an impact on the POI when performing a maximum-likelihood fit.

7.3 Test statistic and hypothesis test

With the likelihood model defined, we can further define a test statistic to perform hypothesis tests. The likelihood ratio is defined as

$$\lambda(\mu) = \frac{L(\mu, \hat{\hat{\boldsymbol{\alpha}}}(\mu))}{L(\hat{\mu}, \hat{\boldsymbol{\alpha}})} \tag{7.7}$$

where $\hat{\hat{\boldsymbol{\alpha}}}(\mu)$ is the profiled value of $\boldsymbol{\alpha}$ maximizing the likelihood for a given μ. $\hat{\mu}$ and $\hat{\boldsymbol{\alpha}}$ are the maximum-likelihood estimations. The likelihood ratio explicitly depends only on μ. A large value of $\lambda(\mu)$ indicates a good agreement between the observed dataset and model prediction given μ, and vice versa. Since we are only interested in cases of positive signal production, a modified likelihood ratio is defined as

$$\tilde{\lambda}(\mu) = \begin{cases} \dfrac{L(\mu, \hat{\hat{\boldsymbol{\alpha}}}(\mu))}{L(\hat{\mu}, \hat{\boldsymbol{\alpha}})} & (\hat{\mu} \geq 0), \\ \\ \dfrac{L(\mu, \hat{\hat{\boldsymbol{\alpha}}}(\mu))}{L(0, \hat{\hat{\boldsymbol{\alpha}}}(0))} & (\hat{\mu} < 0). \end{cases} \tag{7.8}$$

It serves as a basic building block of test statistics in the following subsections.

7.3.1 Discovery significance

Hypothesis test involves two hypothesis: a null hypothesis and an alternative hypothesis. To claim a discovery, we define the background-only prediction that corresponds $\mu = 0$ as the null hypothesis, and the $s + b$ prediction that is $\mu > 0$ as our alternative hypothesis. The test statistic for discovery is defined as

$$\tilde{q}_0 = \begin{cases} -2\ln(\tilde{\lambda}(0)) & \hat{\mu} \geq 0, \\ 0 & \hat{\mu} < 0. \end{cases} \tag{7.9}$$

By definition $\tilde{q}_0$ is non-negative and it only evaluates the discrepancy between the background prediction and observation caused by positive signal production. A small value of $\tilde{q}_0$ indicates a good agreement between the observed dataset and background prediction, and vice versa. Although the case of $\hat{\mu} < 0$ also indicates discrepancy, it is more likely to be caused by some systematic errors instead of unknown negative signal production. In this case, the discrepancy does not contribute to the discovery significance.

Another property of $\tilde{q}_0$ is that it is not a constant but implicitly depends on the observed dataset. We will have different values of $\tilde{q}_0$ if we repeat our experiment multiple times because of statistical fluctuations. Thus, $\tilde{q}_0$ follows a distribution. The pdf of $\tilde{q}_0$, denoted as $f(\tilde{q}_0)$, can be obtained by performing MC toy experiments which are computationally expensive. According to Ref [69], $f(\tilde{q}_0)$ can also be obtained in an asymptotic approach with a large sample. It shows that the asymptotic approach agrees well with MC toy experiments even when the total expected yield is only about 20 events. The asymptotic approach is used in the analysis because the expected yields in the m_{jj} channels are way more than 20 events. The value of $\tilde{q}_0$ obtained with the observed dataset is denoted as $\tilde{q}_{0,obs}$. The p-value for making a discovery is

$$p_0 = \int_{\tilde{q}_{0,obs}}^{\infty} f(\tilde{q}_0|\mu = 0)\mathrm{d}\tilde{q}_0. \tag{7.10}$$

It can be translated as the probability of having another observed dataset that disagrees with the background-only prediction more than the current dataset. If we obtain a small value of p_0, it means that the current observed dataset is very unlikely to be obtained if the background-only hypothesis is true. Alternatively, the chance of the background-only hypothesis being true is very small. In this case, we will reject the background-only hypothesis and favour the $s + b$ hypothesis.

In practice, we define the significance of signal discovery as

$$Z = \Phi^{-1}(1 - p_0) \tag{7.11}$$

where Φ^{-1} is the inverse cumulative function of a Gaussian density function. It is convention to have $Z \geq 5$ to reject the background-only hypothesis and making a claim of discovery. In case of $Z < 5$, we report an upper limit of μ on the signal model.

7.3.2 Upper limits on the signal strength

The null and alternative hypotheses for setting limits are different from the ones for making a discovery because of the different interests. For setting limits, we want to maximize our ability to make a statement about the largest

possible signal strength μ. Thus, the alternative hypothesis for that purpose is a signal strength smaller than μ and the null hypothesis is a signal strength at μ.

According to the hypotheses, we define the test statistic as

$$\tilde{q}_\mu = \begin{cases} -2\ln(\tilde{\lambda}(\mu)) & \mu \geq \hat{\mu}, \\ 0 & \mu < \hat{\mu}. \end{cases} \tag{7.12}$$

It reflects the compatibility between the μ hypothesis and the observed dataset. Only discrepancy caused by insufficient signal production contributes to the power of rejecting the μ hypothesis.

Denoting the observed test statistic as $\tilde{q}_{\mu,obs}$, we obtain the p-value of the null hypothesis

$$p_\mu = \int_{\tilde{q}_{\mu,obs}}^{\infty} f(\tilde{q}_\mu|\mu)\mathrm{d}\tilde{q}_\mu, \tag{7.13}$$

where $f(\tilde{q}_\mu|\mu)$ is the pdf of $\tilde{q}_\mu$. It can also be obtained by the asymptotic method [69]. In practice, we scan a range of μ and calculate the corresponding p-values of scanned μ values. As a result, we obtain a general form of p_μ as a function of μ. By convention, we reject null hypotheses of $p_\mu < 0.05$ for setting an upper limit on μ at 95% confidence level. By doing this we are performing a series of hypothesis tests. The null hypotheses in tests where $p_\mu < 0.05$ are rejected. The rejected ones hypothesize the signal strength at μ but fail to describe the observed dataset because the hypothesized μ is too large to explain the small discrepancy between the background prediction and observation. The upper limit of μ of not being rejected is obtained by solving $p_\mu = 0.05$ and denoted as μ_{95}. In terms of the statistic meaning of the limit, if the μ_{95} hypothesis is true, we only have a 5% chance of obtaining a dataset being less compatible than the current one. Thus, we say that we have a 95% confidence level to reject the μ_{95} hypothesis, and we are more confident to reject hypotheses whose hypothesized μ is larger than μ_{95}.

The above procedure is known as the Feldman-Cousins method [70]. However, it can be problematic in experiments with low sensitivity to signals, as described in Ref [71]. Thus, a modified method is proposed to solve the prob-

lem, namely the CL_s method [72]. It defines a p-value ratio

$$p'_\mu = \frac{p_\mu}{1 - p_b} \tag{7.14}$$

where p_b is the p-value under the background-only hypothesis

$$p_b = 1 - \int_{\tilde{q}_{\mu,obs}}^{\infty} f(\tilde{q}_\mu|\mu = 0) d\tilde{q}_\mu. \tag{7.15}$$

Figure 7.5 illustrates the concept of CL_s. In the figure, Equation 7.14 can be presented as

$$CL_s = \frac{CL_{s+b}}{CL_b} \tag{7.16}$$

using the notation $p'_\mu \to CL_s$, $p_\mu \to CL_{s+b}$ and $p_b \to CL_b$. The μ upper limit of the CL_s method is obtained by solving $p'_\mu = 0.05$ instead of $p_\mu = 0.05$. p'_μ approaches to p_μ if a notable amount of discrepancy is found between the observed dataset and background-only prediction. Otherwise, $p'_\mu > p_\mu$ and setting a threshold at 0.05 for p'_μ leads to a larger μ_{95} value than the one from p_μ. In other words, using p'_μ is being more conservative about excluding signals.

The uncertainty on p'_μ is introduced by $\tilde{q}_{\mu,obs}$ in Equation 7.13. If p'_μ is calculated using the $s + b$ prediction as the observed dataset, the obtained p'_μ is regarded as the expected median p-value. This is because simulations have negligible statistical uncertainties and the simulation χ distributions can be assumed as sitting at the median of statistical fluctuations. However, data collected from the detector usually contains notable fluctuations and $\tilde{q}_{\mu,obs}$ is not the median value. We call the $\tilde{q}_{\mu,obs}$ obtained with observed data as the observed p-value. The discrepancy between the expected and observed p-value can be caused by either statistical fluctuations or signal production. To determine how compatible the observed and expected p-values are, "uncertainty" in p'_μ caused by statistical fluctuations needs to be calculated as well. It does not reflect how uncertain we are about the expected p-value under the null hypothesis but reflects how sensitive the null hypothesis is to statistical fluctuations in data observations. It is found that the uncertainty in p'_μ is directly related to the hypothesized μ value. A standard deviation of μ is defined as

$\sigma_\mu \propto \mu$ and the varied p'_μ for a given hypothesized μ is the nominal value of $p'_{\mu\pm\sigma_\mu}$. Detailed derivations can be found in Ref [69].

At this point, we have discussed the details of the frequentist method to build the likelihood model of the analysis. Figure 7.6 shows a simplified statistical workflow. With inputs from observed dataset and MC simulated background and signal models, we will be able to calculate the discovery significance and an upper limit on μ at a 95% confidence level.

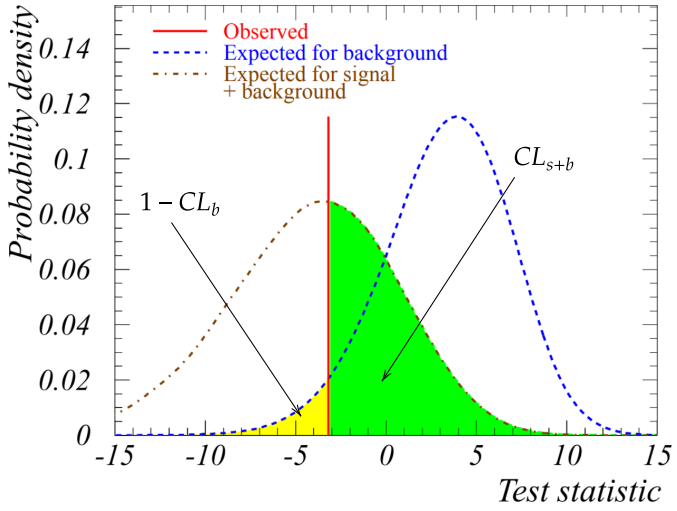

Figure 7.5: Illustration of different p-values, taken from Ref. [72] and annotated. The red line indicates the test statistic obtained from the observed data given μ. The blue dashed line is the probability function of the test statistic under a signal-plus-background model given μ. The brown dashed line is the probability function of the test statistic under a background-only model. The yellow area at the left side of the observed test statistic is $1 - CL_b$ and the green area at the right side is CL_{s+b}.

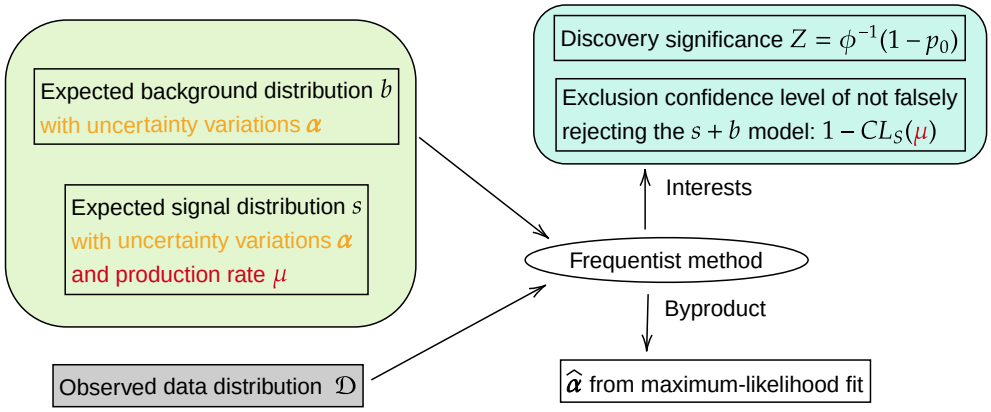

Figure 7.6: Simplified illustration of the statistic workflow.

Chapter 8

Maximum-likelihood fit and hypothesis tests

In this chapter, we discuss the implementation of the frequentist method introduced in the previous chapter. HistFitter [73] is used to handle data inputs and perform the maximum-likelihood fit. To validate this method and our datasets, the implementation is broken down into three steps. At first, we perform the maximum-likelihood fit with the background-only hypothesis to study the constraints of the nuisance parameters. Second, we perform the discovery hypothesis test with the signal-injected background to study the discovery sensitivity of the analysis. Finally, we calculate the discovery significance and exclusion limits at 95% confidence level using partial Run2 data collected in 2015–16. We are not allowed to explore the rest of the Run2 data, that is collected in 2017 and 2018, according to the ATLAS analysis policy. We refer to it as blinded. Because the analysis is targeted to use full Run2 data, the 2015–16 data and simulations are scaled up to 139 fb^{-1}. The scaled-up 2015–16 data is regarded as a place holder for full Run2 data. Details of the implementation are described in the following sections.

8.1 Background-only fit

As an analysis searching for new physics, we want to be careful and do not make a false statement of discovery. It is not only about using the correct statistical tools but also making a valid and effective background prediction. To valid the

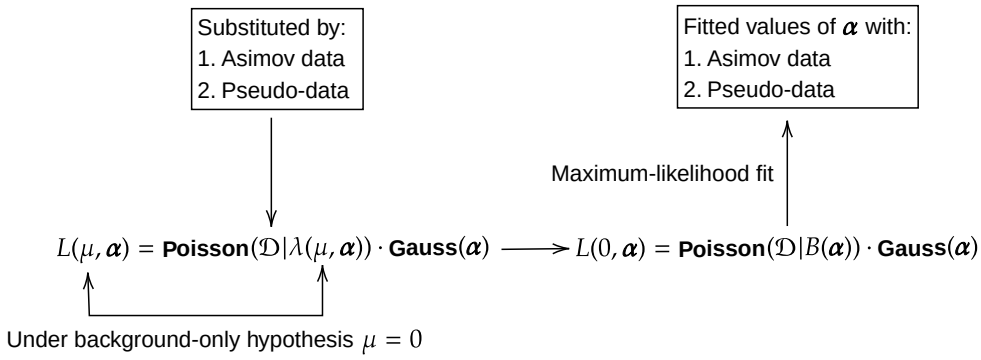

Figure 8.1: Worflow of the background-only fit.

background prediction and the likelihood model, we perform the maximum-likelihood fit with the background-only hypothesis to exam the estimation of nuisance parameters.

Figure 8.1 shows the workflow of the background-only fit. Under the background-only hypothesis, the likelihood in Equation 7.6 only explicitly depends on $\boldsymbol{\alpha}$ as we fix $\mu = 0$ and implicitly depends on the observed dataset $\mathcal{D}$. We will perform the background-only fit with two background-based datasets substituting for $\mathcal{D}$ in the likelihood model: an Asimov dataset and a pseudo-data set. Figure 8.2 compare the χ distributions of the background-based datasets with scaled-up 2015–16 data. The Asimov dataset is the smooth background model.[1] It can provide a straightforward view about how NPs are constrained in the maximum-likelihood fit. A pseudo-data set is one Poisson fluctuated instance of the background model. The fit with pseudo-data is performed 10^3 times with a random pseudo-data each time. With pseudo-data, we will be able to see how sensitive NPs are to statistical fluctuations. With these background-based datasets, we can have a good understanding of the behaviour of $\boldsymbol{\alpha}$ in the fit.

[1]In Ref [69], Asimov data refers to as a dataset that perfectly agrees with the null hypothesis which does not have to be a background-only hypothesis. However, in this thesis, it is referred to the one that is the background-only hypothesis for consistency.

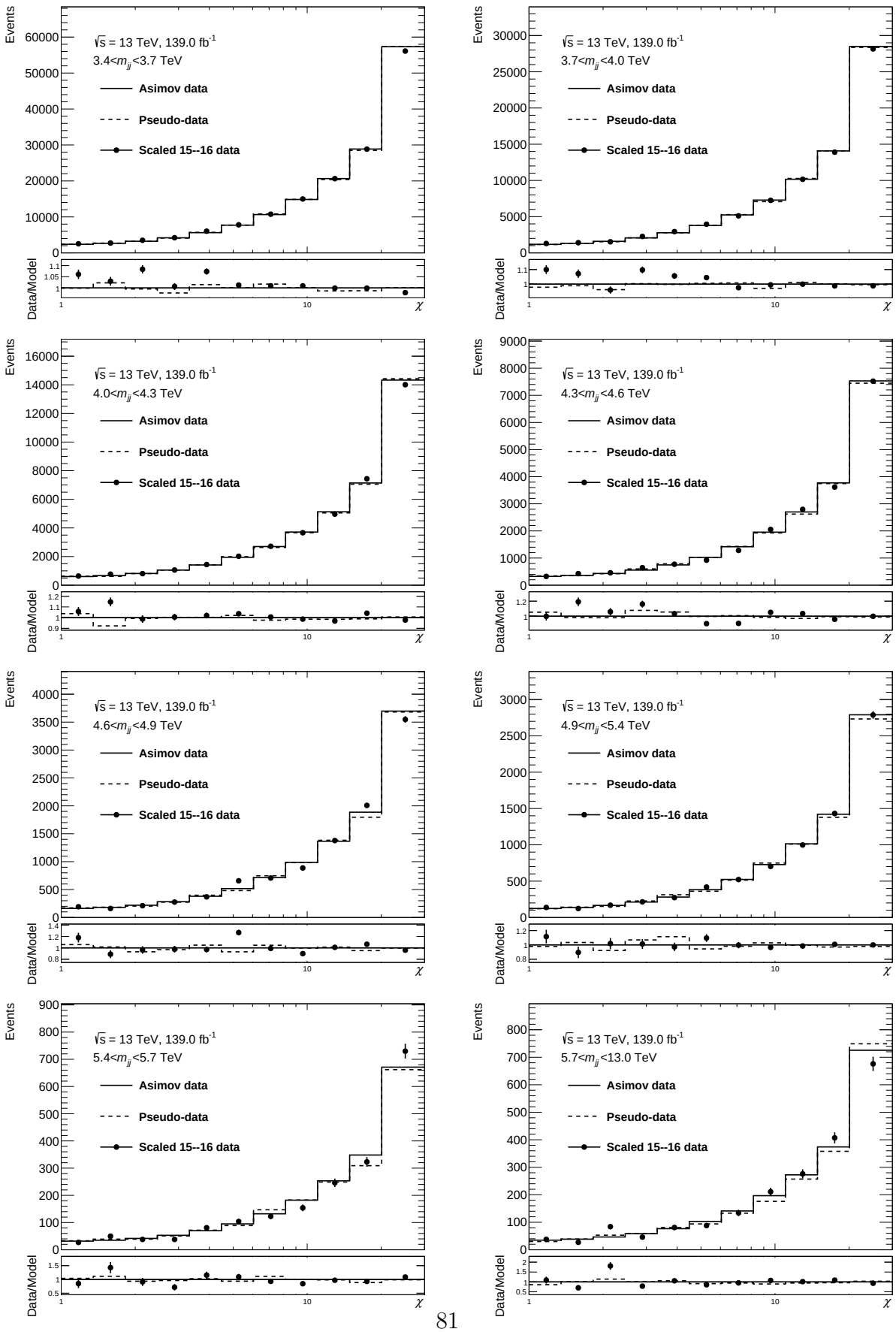

Figure 8.2: The χ distributions of (solid line) Asimov data, (dashed line) a pseudo-data set and (points) scaled partial Run2 data collected in 2015–16.

8.1.1 Asimov dataset

In this subsection, we present the result of the background-only fit with the Asimov dataset. No signal simulation is involved since it is under the background-only hypothesis. The observed dataset is substituted by the Asimov dataset. Because the Asimov dataset is equivalent to the nominal background prediction, we expect to see post-fit NPs being estimated at their pre-fit nominal values.

As a result of the maximum likelihood fit, Figure 8.3 shows the correlation coefficients between NPs. A correlation coefficient of -0.84 between μ_R (`Scale_muR` in the figure) and μ_F (`Scale_muF`) stands out as the largest correlation. Figure 8.4 shows the post-fit values of NPs. As expected, they are estimated at their pre-fit nominal values. The NP of luminosity uncertainty (`Lumi`) is an exception whose pre-fit value is mapped to 1 ± 0.017 instead of 0 ± 1. It is also estimated at its pre-fit value despite having a different location from other NPs. Thus, the background distribution does not change after the maximum-likelihood fit. Figure 8.5 and Figure 8.6 show the pre-fit and post-fit χ distributions respectively with the uncertainty bands. The post-fit uncertainty bands are calculated according to the equation [73]

$$\sigma_{tot.}^2 = \sum_s^n \left(\frac{\partial b}{\partial \alpha_s}\right)^2 \sigma_{\alpha_s}^2 + \sum_i^n \sum_{j \neq i}^n \rho_{ij} \left(\frac{\partial b}{\partial \alpha_i}\right) \left(\frac{\partial b}{\partial \alpha_j}\right) \sigma_{\alpha_i} \sigma_{\alpha_j} \qquad (8.1)$$

where $\dfrac{\partial b}{\partial \alpha_s}$ is the variation of the background prediction b caused by varying α_s, σ_{α_s} is the standard deviation of α_s and ρ_{ij} is the correlation matrix shown in Figure 8.4. Figure 8.7 and Figure 8.8 show the corresponding pre-fit and post-fit $\mathrm{d}N/\mathrm{d}\chi$ histograms for better visualization than the χ histograms. The post-fit uncertainty bands in Figure 8.8 are much narrower than the pre-fit ones in Figure 8.7. Such a difference is caused by the constrained NPs. As shown in Figure 8.4, the post-fit standard deviations of SPHP (`SingleParticle_HighPt` in the figure), tune, μ_R and μ_F are smaller than their pre-fit standard deviations. SPHP is the largest uncertainty in the high m_{jj} region and it is the most constrained parameter. Thus, it contribute most to the shrinking of the uncertainty bands.

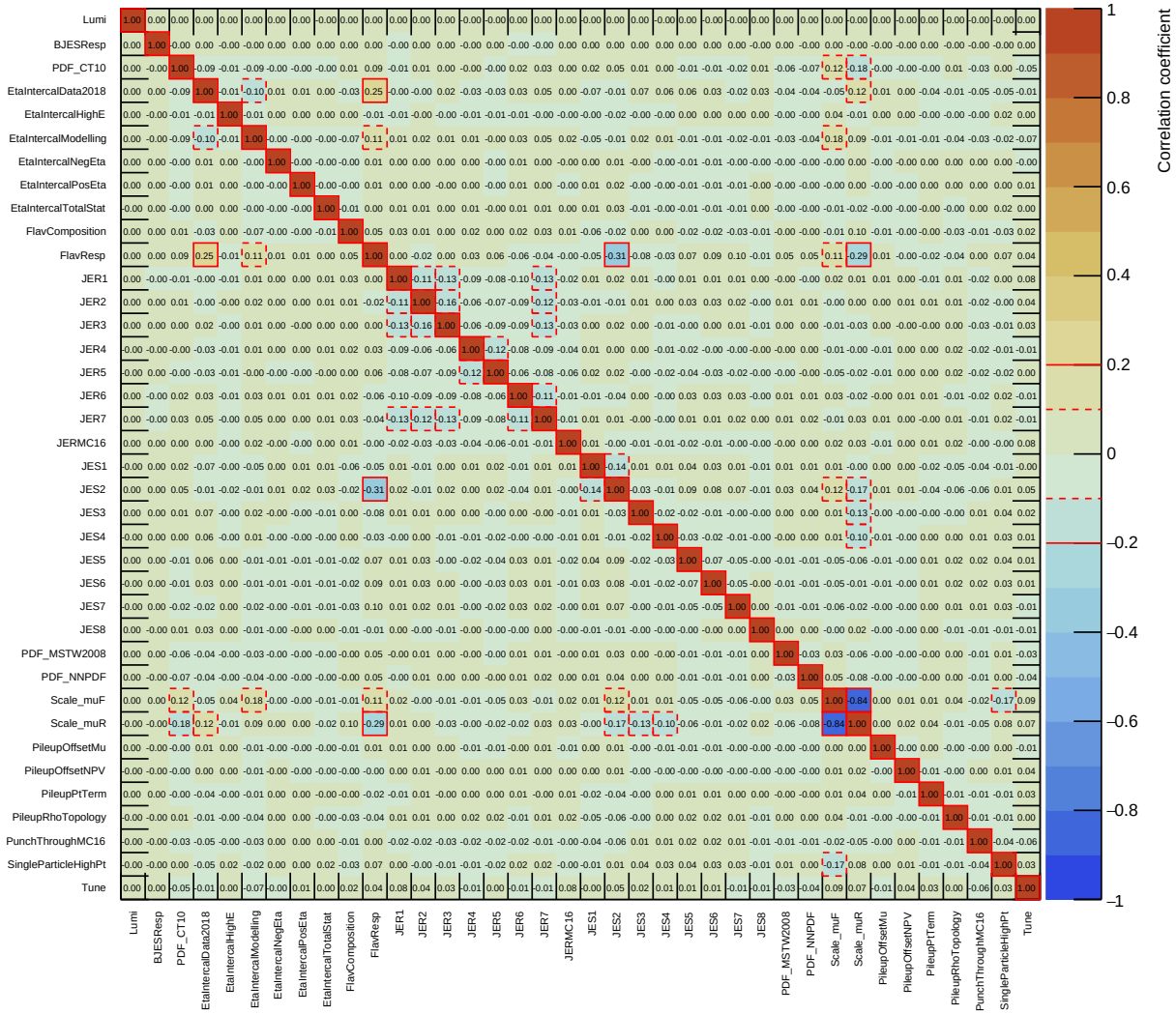

Figure 8.3: The correlation coefficient matrix of nuisance parameters obtained with Asimov data as the observed dataset.

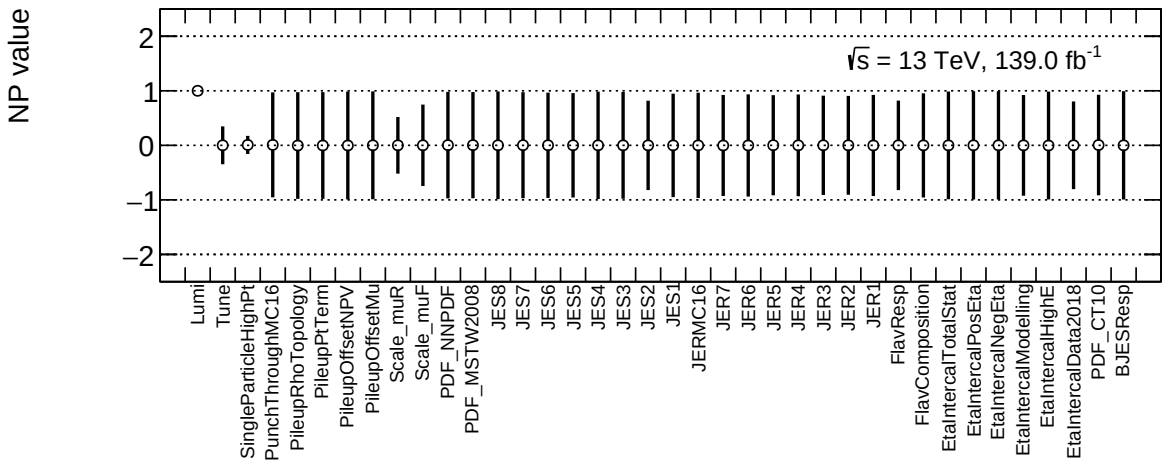

Figure 8.4: The post-fit nuisance parameters obtained with Asimov data as the observed dataset.

The constraint on SPHP is expected due to the increase in the number of events. We are introducing a dataset corresponding to 139 fb^{-1} compared to the previous one of 37 fb^{-1}. We have tried to de-correlate the uncertainty parameter by assigning independent parameters to the eight m_{jj} slices but it does not help in reducing the constraint power. We also have presented and discussed our results with the JetEtMiss[2] group and have been approved to proceed with this constrained parameter.

As for the constraints on the tune, μ_R and μ_F, we do not consider this a problem. On the one hand, they are not as constrained as SPHP. Moreover, they are theoretical uncertainties and their pre-fit standard deviations are not obtained from auxiliary measurements but instead from comparisons of different assumptions. As mentioned in Section 6.1.2, the uncertainty on μ_R is obtained by varying its approximation by a factor of 2. This factor of 2 does not correspond to any statistic deviations such as the standard deviation of a Gaussian likelihood function. Thus, the pre-fit standard deviation may not be valid in the first place despite they are constructed in the same form as experimental uncertainties when building the likelihood model.

[2]JetEtMiss is an ATLAS group studying the jet energy scale.

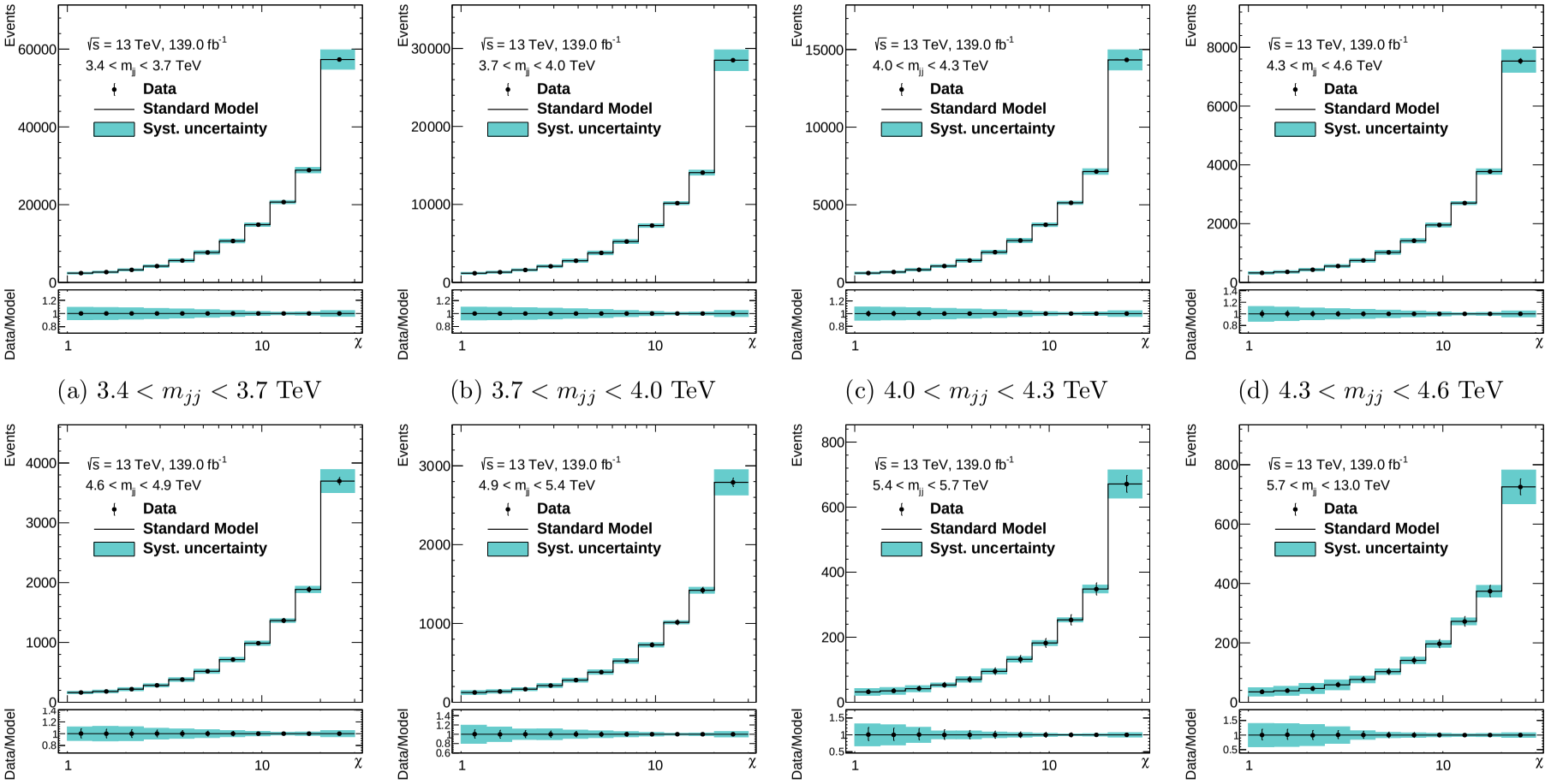

(a) $3.4 < m_{jj} < 3.7$ TeV (b) $3.7 < m_{jj} < 4.0$ TeV (c) $4.0 < m_{jj} < 4.3$ TeV (d) $4.3 < m_{jj} < 4.6$ TeV

(e) $4.6 < m_{jj} < 4.9$ TeV (f) $4.9 < m_{jj} < 5.4$ TeV (g) $5.4 < m_{jj} < 5.7$ TeV (h) $5.7 < m_{jj} < 13.0$ TeV

Figure 8.5: Pre-fit χ distributions obtained with the Asimov dataset as the observed dataset and plotted in χ histograms.

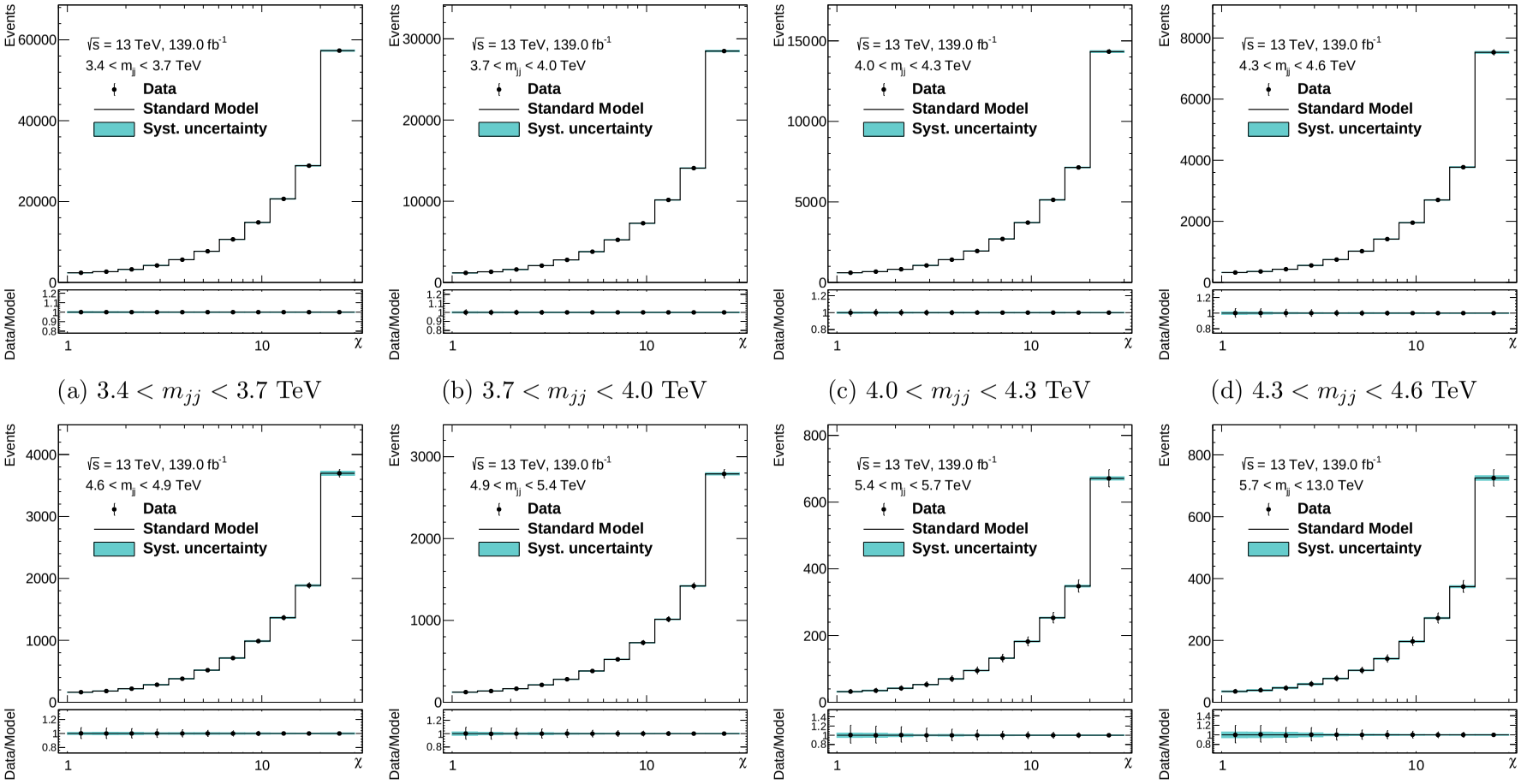

(a) $3.4 < m_{jj} < 3.7$ TeV (b) $3.7 < m_{jj} < 4.0$ TeV (c) $4.0 < m_{jj} < 4.3$ TeV (d) $4.3 < m_{jj} < 4.6$ TeV

(e) $4.6 < m_{jj} < 4.9$ TeV (f) $4.9 < m_{jj} < 5.4$ TeV (g) $5.4 < m_{jj} < 5.7$ TeV (h) $5.7 < m_{jj} < 13.0$ TeV

Figure 8.6: Post-fit χ distributions obtained with the Asimov dataset as the observed dataset and plotted in χ histograms.

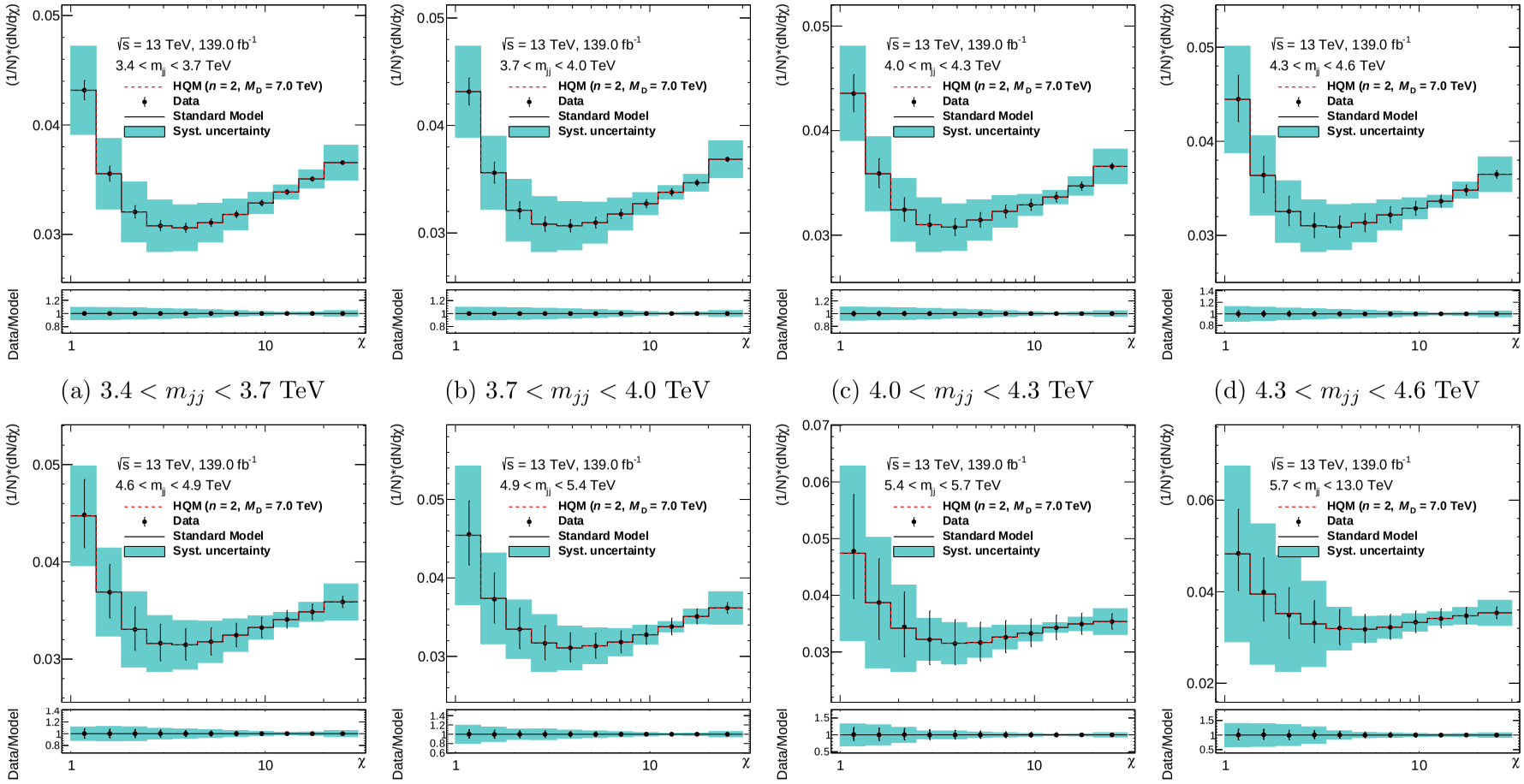

(a) $3.4 < m_{jj} < 3.7$ TeV (b) $3.7 < m_{jj} < 4.0$ TeV (c) $4.0 < m_{jj} < 4.3$ TeV (d) $4.3 < m_{jj} < 4.6$ TeV

(e) $4.6 < m_{jj} < 4.9$ TeV (f) $4.9 < m_{jj} < 5.4$ TeV (g) $5.4 < m_{jj} < 5.7$ TeV (h) $5.7 < m_{jj} < 13.0$ TeV

Figure 8.7: Pre-fit χ distribution obtained with the Asimov dataset as the observed dataset and plotted in $\mathrm{d}N/\mathrm{d}\chi$ histograms.

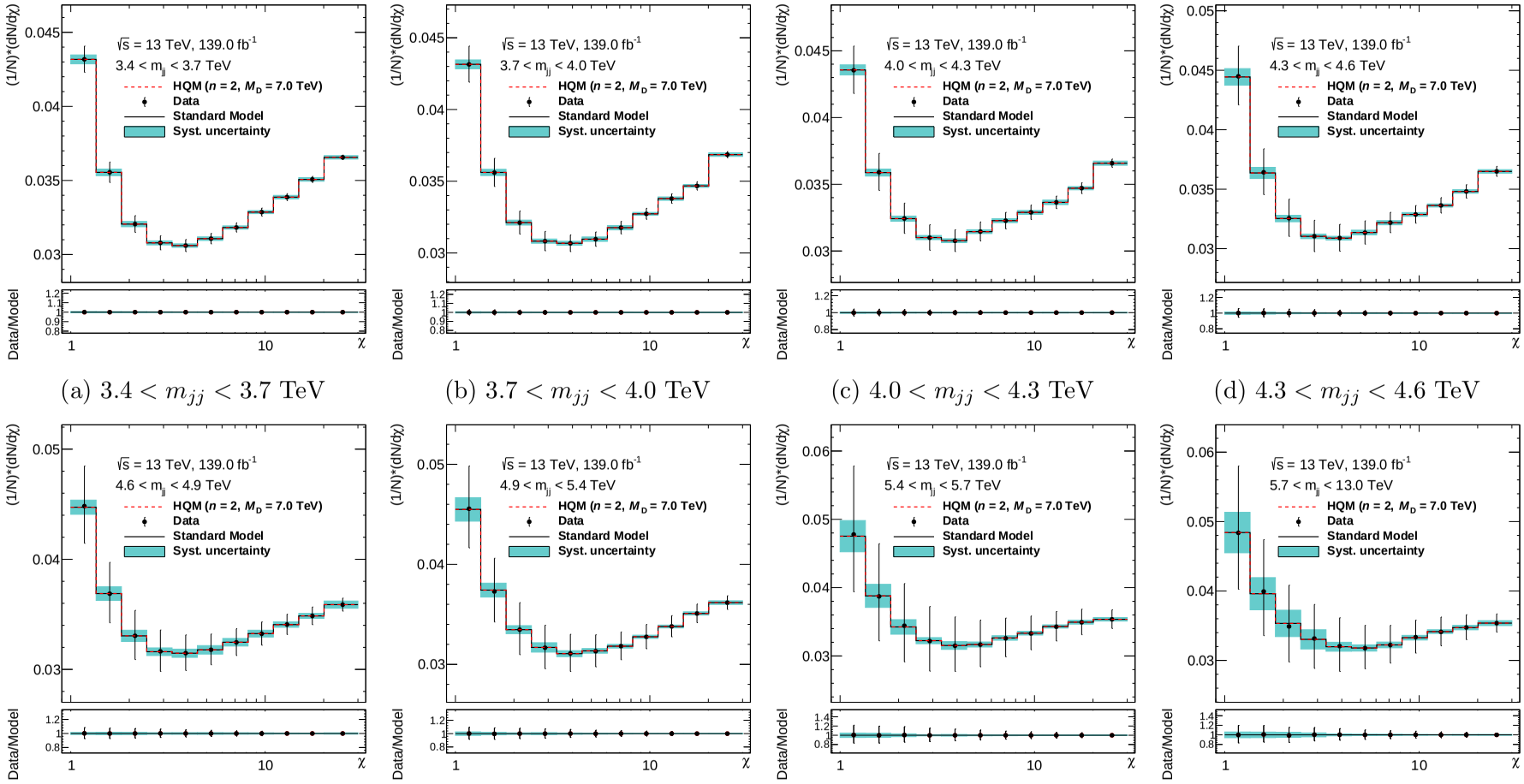

(a) $3.4 < m_{jj} < 3.7$ TeV (b) $3.7 < m_{jj} < 4.0$ TeV (c) $4.0 < m_{jj} < 4.3$ TeV (d) $4.3 < m_{jj} < 4.6$ TeV

(e) $4.6 < m_{jj} < 4.9$ TeV (f) $4.9 < m_{jj} < 5.4$ TeV (g) $5.4 < m_{jj} < 5.7$ TeV (h) $5.7 < m_{jj} < 13.0$ TeV

Figure 8.8: Post-fit χ distributions obtained with the Asimov dataset as the observed dataset and plotted in $\mathrm{d}N/\mathrm{d}\chi$ histograms.

In conclusion, the results from the background-only fit with Asimov data are reasonable.

8.1.2 Pseudo-data set

A pseudo-data set is generated from the background prediction but with some random effect. At first, the total number of events in a m_{jj} slice, denoted as N_c^{pseudo}, is randomly generated by a Poisson pdf whose mean value is set to the expected number of background events B_c. Then, we normalize the χ distribution of the background prediction to unity and interpret it as a pdf $f_c(\chi)$. After that, N_c^{pseudo} events are randomly generated following $f_c(\chi)$. The procedure is repeated in every m_{jj} slice and the generated χ distributions make up the pseudo-data set. The difference between the pseudo-data set and the background prediction mimics a single statistical fluctuation of the background production.

Figure 8.9 shows the post-fit NPs of using one instance of pseudo-data. Compared to the results of the Asimov dataset, the centre values are more or less shifted due to the difference between the pseudo-data and background prediction. The fit is also performed 10^3 times with random pseudo-data to study the distributions of the parameter estimations. We call each fit a pseudo-experiment. The mean post-fit estimations of the pseudo-experiments are shown in Figure 8.10. Both the estimation values and uncertainty bars in the figure are the means of the corresponding values in the 10^3 pseudo-experiments. They are located within 1σ of pre-fit estimations. It indicates that the statistical fluctuations are not likely to cause significant deviations of NP estimations. We expect to see similar results if the observed dataset only contains background events.

8.2 Sensitivity test

It is important to know how our analysis procedure will affect the discovery potential if there were signals produced in the data. Thus, we replace the observed dataset with the $s+b$ prediction. We refer to the replacement as the

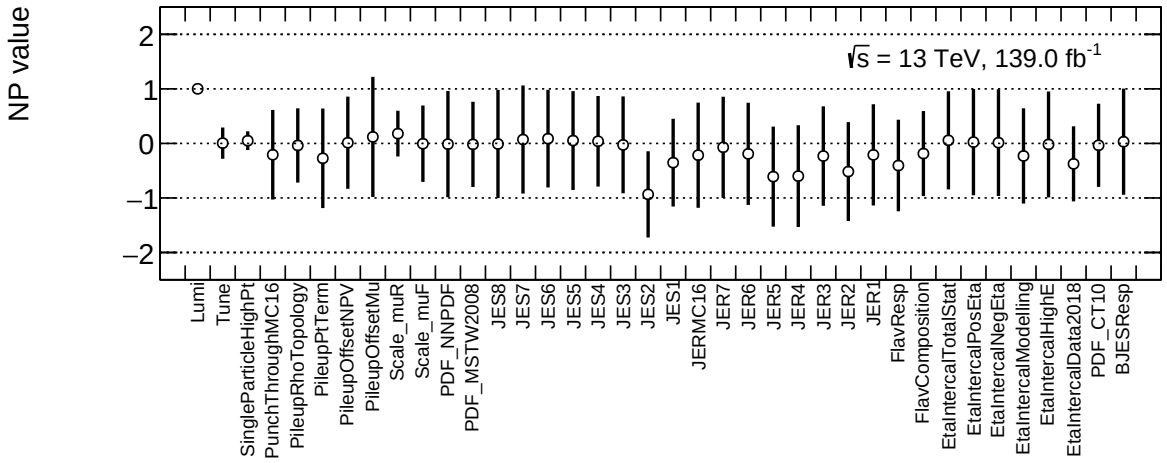

Figure 8.9: The post-fit nuisance parameters obtained with a pseudo-data set as the observed dataset.

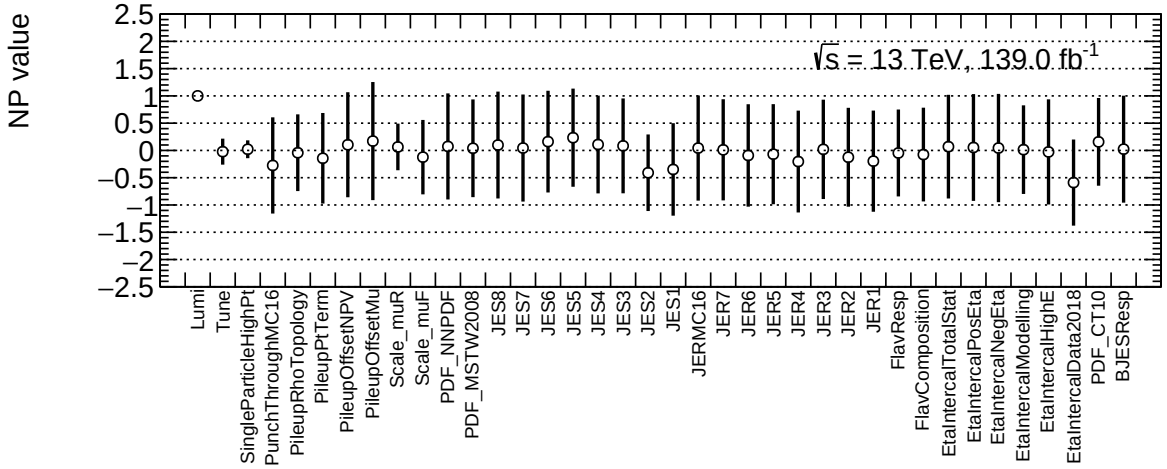

Figure 8.10: The mean estimation of NPs from 10^3 pseudo-experiments. Both the centre values and errors are the corresponding mean values and errors in the pseudo-experiments.

signal-injected dataset. With the signal-injected dataset, we can learn how sensitive our analysis is to signal events.

8.2.1 Signal injection test

To learn about how the maximum-likelihood fit will change the post-fit χ distributions if there were signals, we replace the observed dataset with a signal-injected dataset and perform the maximum-likelihood fit. The signal-injected dataset is built with the HQM sample of $n = 2$ and $M_D = 7$ TeV, hypothesizing $\mu = 1$.

Figure 8.11 shows the estimation of parameters. Figure 8.12 and Figure 8.13 respectively shows the pre-fit and post-fit χ distributions. Most of the NPs of systematic uncertainties are estimated within $\pm 1\sigma$ of their pre-fit estimation. SPHP is estimated at 0.81 ± 0.24 which contribute to most of the background shape change. The signal strength is estimated at 0.43 ± 0.11 despite the signal-injected dataset is built with $\mu = 1$. The discovery significance is found to be 3.92, according to Equation 7.11. The underestimated μ is a result of the background normalization strategy and systematic uncertainties. On the one hand, the background normalization strategy scales the background yield to the data yield. If there were signal events, the correct background yield should be smaller than the data yield. Thus, the room for accommodating signals to data is suppressed by this normalization strategy. On the other hand, some systematic uncertainties have similar shapes as the signals have. They can be varied in the maximum-likelihood fit to accommodate the discrepancy between data and background which is created by signal production. Therefore, systematic uncertainties can also suppress the signal strength estimation. To evaluate the impact of the background normalization strategy, we remove all the systematic uncertainties and perform the maximum-likelihood fit. Thus, the impact of the normalization strategy is isolated from systematic uncertainties. The fit estimates $\mu = 0.80 \pm 0.07$ which is a noticeable underestimation from $\mu = 1$.

The impact of systematic uncertainties needs to be defined and evaluated. Figure 8.14 shows the workflow of post-fit impact calculation. First, the best

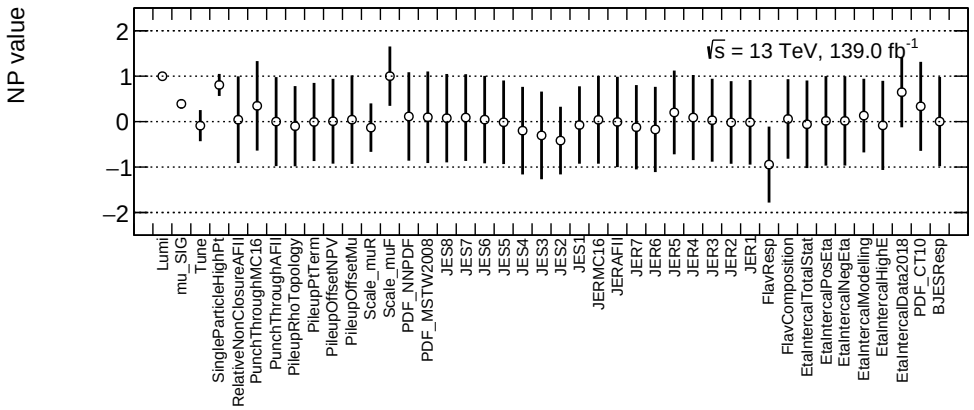

Figure 8.11: Post-fit parameter estimation obtained with a signal-injected dataset as the observed dataset, using the HQM sample $n = 2$ and $M_D = 7$ TeV.

estimation of μ denoted as $\hat{\mu}$ is taken as the reference. It is obtained by performing maximum-likelihood fit where all parameters are free. From that fit, we can also obtain the best estimation of an individual NP, denoted as $\hat{\alpha}_s$, with a post-fit standard deviation of σ_{α_s}. To calculate the impact of α_s, we fix $\alpha_s = \hat{\alpha}_s \pm \sigma_{\alpha_s}$ and perform the maximum-likelihood fit again. From that fit, we will obtain another best estimation of μ, denoted as $\hat{\mu}|_{\alpha_s=\hat{\alpha}_s\pm\sigma_{\alpha_s}}$. The difference between $\hat{\mu}$ and $\hat{\mu}|_{\alpha_s=\hat{\alpha}_s\pm\sigma_{\alpha_s}}$, denoted as Δ_μ and calculated as

$$\Delta\mu = \hat{\mu} - \hat{\mu}|_{\alpha_s=\hat{\alpha}_s\pm\sigma_{\alpha_s}}, \tag{8.2}$$

is regarded as the post-fit impact of α_s. Fixing α_s to its pre-fit deviation and following the same procedure gives the pre-fit impact. Figure 8.15 shows top 10 NPs which have the largest post-fit impact on μ. SPHP has the largest impact while the uncertainties on flavour response and μ_F follow. The ranking agrees with Figure 8.11 where these three NPs deviate most from their pre-fit values. Based on the ranking, several tests are performed with fewer systematic uncertainties. Table 8.1 summarizes the estimated μ in these tests. The maximum-likelihood fit only including SPHP is performed and it estimates $\mu = 0.65 \pm 0.09$. The fit including uncertainties on SPHP, flavour response and μ_F estimates $\mu = 0.43 \pm 0.10$. The contribution from other uncertainties

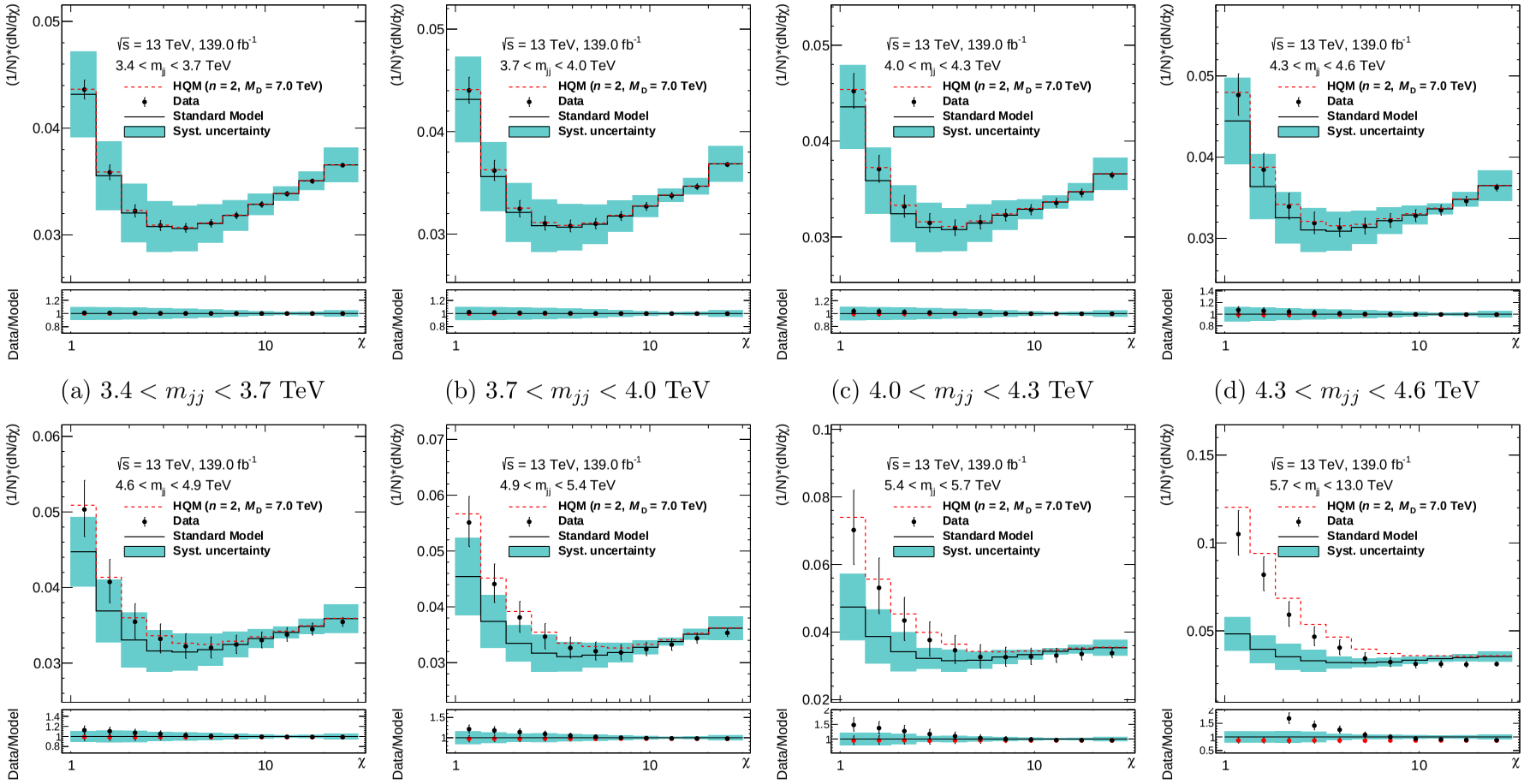

(a) $3.4 < m_{jj} < 3.7$ TeV (b) $3.7 < m_{jj} < 4.0$ TeV (c) $4.0 < m_{jj} < 4.3$ TeV (d) $4.3 < m_{jj} < 4.6$ TeV

(e) $4.6 < m_{jj} < 4.9$ TeV (f) $4.9 < m_{jj} < 5.4$ TeV (g) $5.4 < m_{jj} < 5.7$ TeV (h) $5.7 < m_{jj} < 13.0$ TeV

Figure 8.12: Pre-fit χ distributions obtained with a signal-injected dataset as the observed dataset.

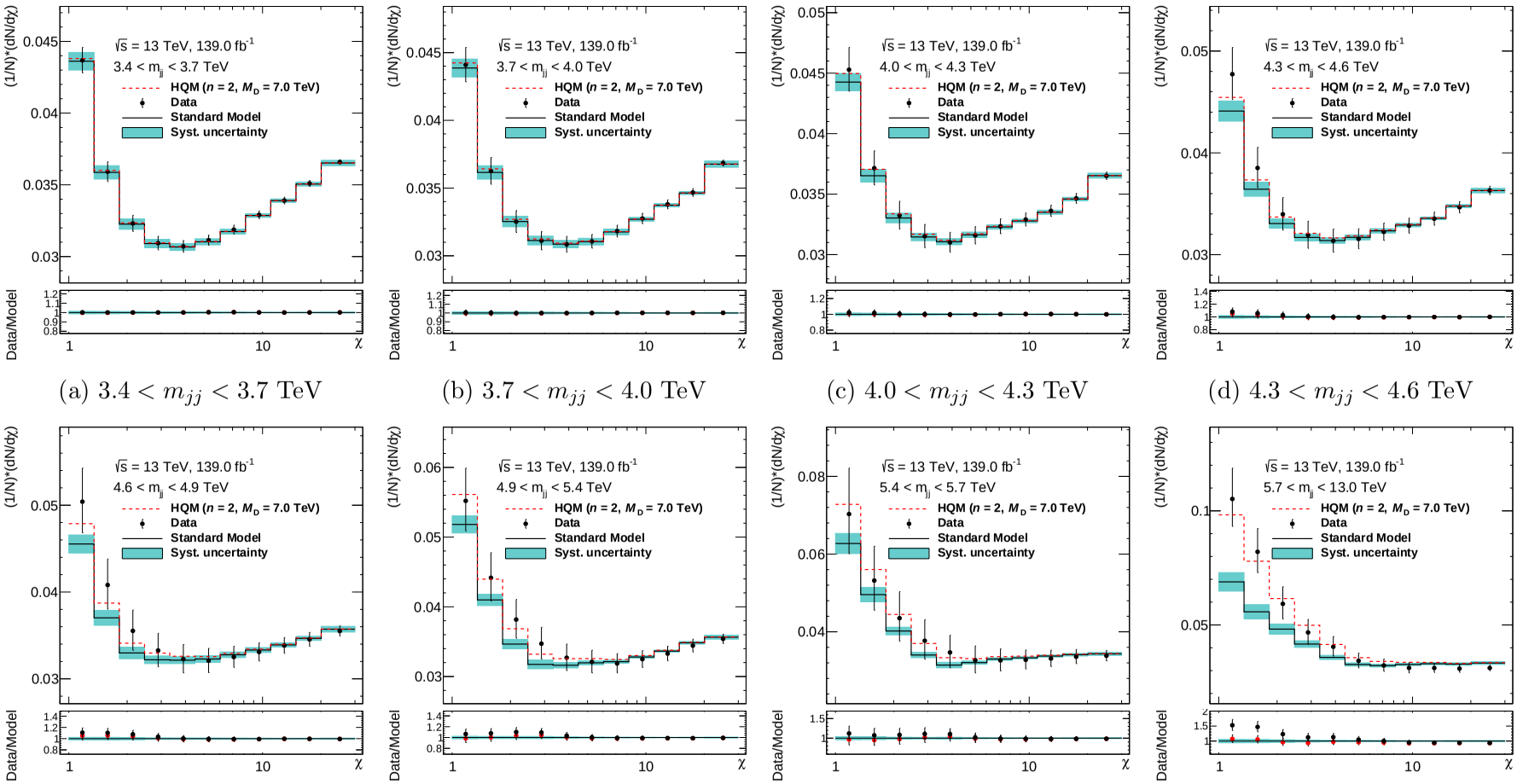

(a) $3.4 < m_{jj} < 3.7$ TeV (b) $3.7 < m_{jj} < 4.0$ TeV (c) $4.0 < m_{jj} < 4.3$ TeV (d) $4.3 < m_{jj} < 4.6$ TeV

(e) $4.6 < m_{jj} < 4.9$ TeV (f) $4.9 < m_{jj} < 5.4$ TeV (g) $5.4 < m_{jj} < 5.7$ TeV (h) $5.7 < m_{jj} < 13.0$ TeV

Figure 8.13: Post-fit χ distributions obtained with a signal-injected dataset as the observed dataset..

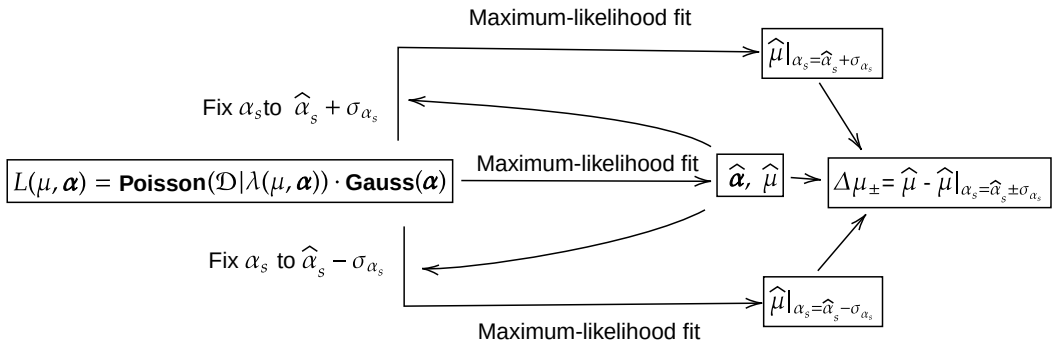

Figure 8.14: Workflow of calculating the post-fit impact of nuisance parameters on μ.

is only a small fraction of the underestimation.

We also have performed a series of maximum-likelihood fit with varied hypothesized μ. We refer to the hypothesized μ as the injected signal strength and its maximum-likelihood estimation as the extracted signal strength. Figure 8.16 shows the relationship between injected and extracted μ. It indicates that only about half of the injected μ can be extracted under our analysis strategy.

8.2.2 Discovery significance test

We perform discovery hypothesis tests with all simulated HQM samples, assuming a full signal production rate $\mu = 1$ to see the discovery potential of the simulated HQM samples. The discovery significance is calculated and the results are shown in Figure 8.17. We find only one HQM sample ($n = 6$, $M_D = 5.5$ TeV) has the potential to exceed 5σ for making a discovery claim in

Table 8.1: Estimated μ and discovery significance in scenarios with fewer systematic uncertainties. A signal-injected dataset is used, built from the HQM sample of $n = 2$, $M_D = 7$ TeV and $\mu = 1$.

Uncertainties	Estimated μ	Significance
No uncertainty	0.80 ± 0.07	12.4
Single-particle response	0.65 ± 0.09	7.4
Single-particle response, flavor response and μ_F	0.47 ± 0.11	4.5
All	0.43 ± 0.11	3.9

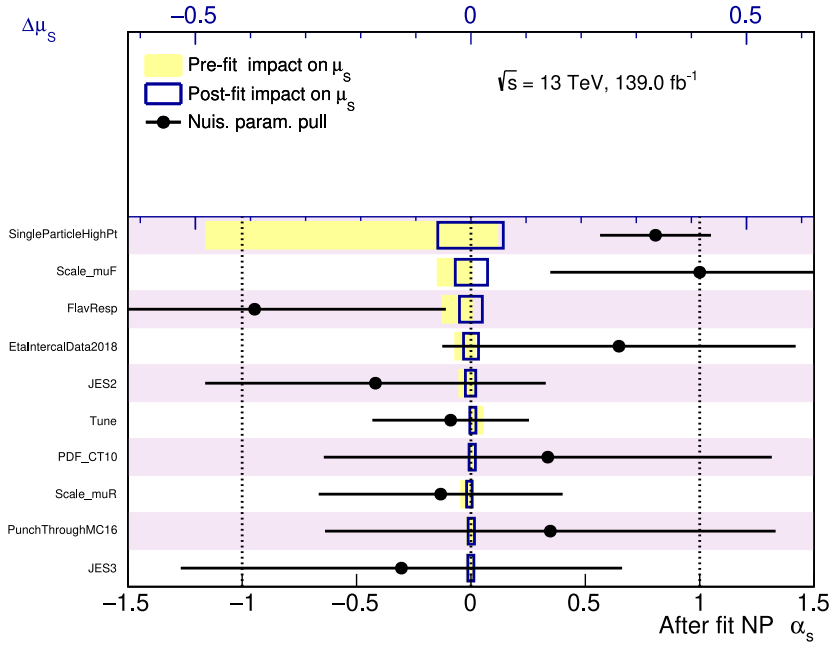

Figure 8.15: Top 10 uncertainties ranked by their post-fit impacts on μ, obtained with a signal-injected dataset. The points with error bars are the post-fit NP values corresponding to the bottom x-axis. The yellow bars (blue boxes) are the pre-fit (post-fit) impact of NPs on μ, corresponding to the top x-axis.

this search analysis. This was not expected when doing preliminary studies at the sample generation stage, because the impact of the normalization strategy and the large SPHP uncertainty were not considered.

8.2.3 Discussion on signal underestimation

Intuitively we can overcome the underestimation problem by normalizing the $s + b$ prediction to data instead of solely normalizing the background prediction. However, it brings more serious problems than it solves. Normalizing the $s+b$ prediction to data makes the normalization procedure become signal-dependent. It is not desired because we do not know what signal model is waiting for us in the data and the dependence can introduce biases in the analysis. From the statistic view, we want to start with the null hypothesis and reject it in case of discovery. The background-only normalization procedure is based on the null hypothesis. However, the $s + b$ normalization procedure assumes the existence of signals that is the alternative hypothesis, which contradicts the

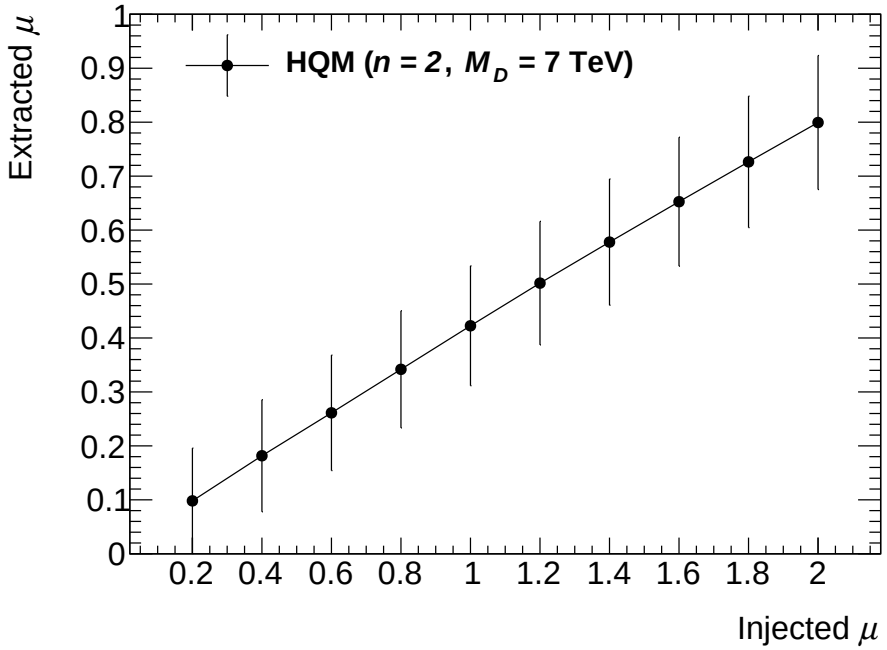

Figure 8.16: Injected μ versus extracted μ. The line connecting points is a polyline for better visualization.

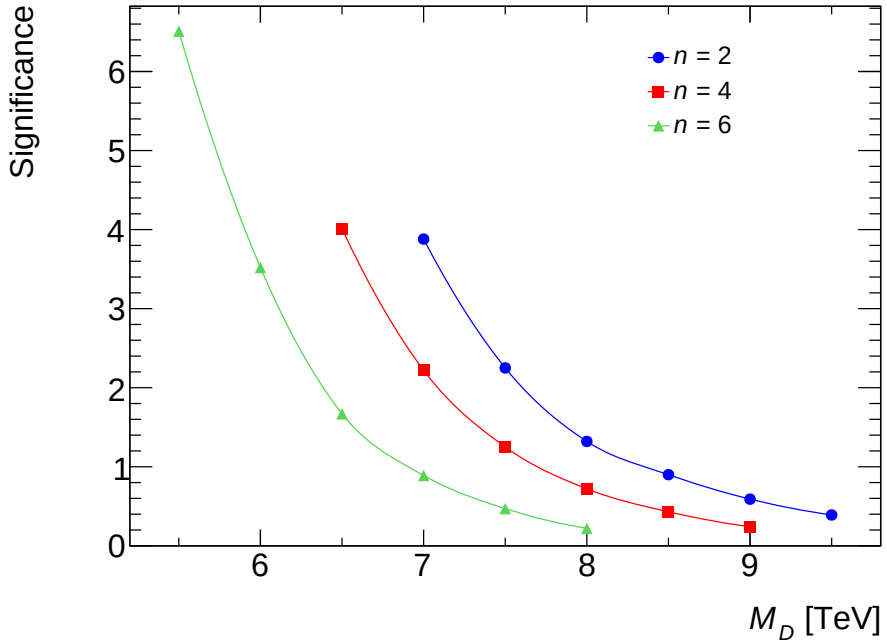

Figure 8.17: Discovery significance of HQM samples when they are fully injected into the background model.

procedure of hypothesis test. The key to solving the signal-underestimation problem is to have an accurate prediction of SM dijet production which is not available for this analysis. Usually, background prediction can be derived from control regions, and the premise of determining control regions is to have a good understanding of signal contamination. For example, ATLAS and CMS were able to exclude the Higgs mass outside the region of (116, 127) GeV at 95% before its discovery [17, 74, 75]. Thus, the background estimation for the Higgs search can be obtained by interpolating the sidebands of that region. However, for the angular analysis, various BSM models are studied in ATLAS and the corresponding signal contamination varies model by model. Signal-free control regions are not well defined in the analysis. On the conservative side, assuming no BSM signal production in data is the most adaptable solution to perform an angular analysis. Developing an improved normalization strategy is not in high priority for searching new phenomena in dijet events but it will be if significant BSM signals are discovered under the current strategy.

As for the large uncertainty from the single-particle response measurement, we can expect improvement in the near future. As mentioned, this uncertainty is transferred from the single-particle response measurement to jets, because JES measurement lacks statistical strength in the high p_{T} region. The uncertainty in our analysis is a combination from individual components of the uncertainty in the single-particle response measurement. In the short term, we can expect these individual components to be released within the ATLAS collaboration. With these components, we can pin down the one which has the largest impact and possibly improve that term in the single-particle response measurement. In the long run, with the upgrade of LHC, more data in the high p_{T} region will be collected in the coming years and the uncertainty may be reduced with more data.

8.3 Exclusion limits

In cases where signals are not significant enough for us to claim a discovery, the upper limit at 95% confidence level on the signal strength is presented.

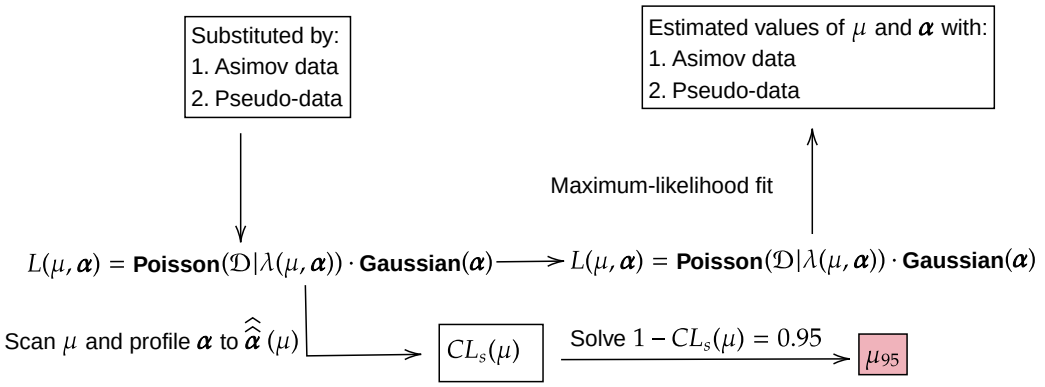

Figure 8.18: Workflow of calculating the upper limit on the signal strength at 95% confidence level.

The workflow of calculating the upper limit is shown in Figure 8.18. At first, we take both μ and $\boldsymbol{\alpha}$ as free parameters and perform the maximum-likelihood fit to estimate the parameters. In the meantime, we also perform maximum-likelihood fits to obtained the best estimation of $\hat{\hat{\boldsymbol{\alpha}}}$ for given μ to calculate CL_b, CL_{s+b} and CL_s. A range of μ is scanned and confidence levels are also obtained from the scan. We are most interested in the value of μ corresponding to $1 - CL_s(\mu) = 0.95$. The solved value is the upper limit for the signal strength parameter at 95% confidence level. The same procedure is repeated over simulated HQM samples of n and M_D. The upper limits on μ are then transported to n and M_D. We test this procedure with the Asimov data and pseudo-data first to gain a sense of results under a background-only hypothesis. Then, to exam the robustness of our analysis choice, alternative choices for the analysis are tested and compared to the default one. Finally, results using 2015–16 data are reported.

8.3.1 Asimov data

Following a similar procedure of the background-only fit, we perform the maximum likelihood fit with Asimov data first. More specifically, we are fitting Asimov data to the $s+b$ prediction. Figure 8.19 shows the post-fit parameters. The estimation of μ is at 0 which is expected since Asimov data is exactly the

background-only prediction. Figure 8.20 shows the ranking of systematic uncertainties. As the figure shows, all the NPs have negative impacts. This is because we have $\hat{\mu} = 0$ in this case and μ can only be fitted to a larger value as we limit μ to positive values. The impact $\Delta\mu$ given by Equation 8.2 can only be negative. The ranking generally agrees with the one in the signal-injection test except μ_F and flavour response are swapped.

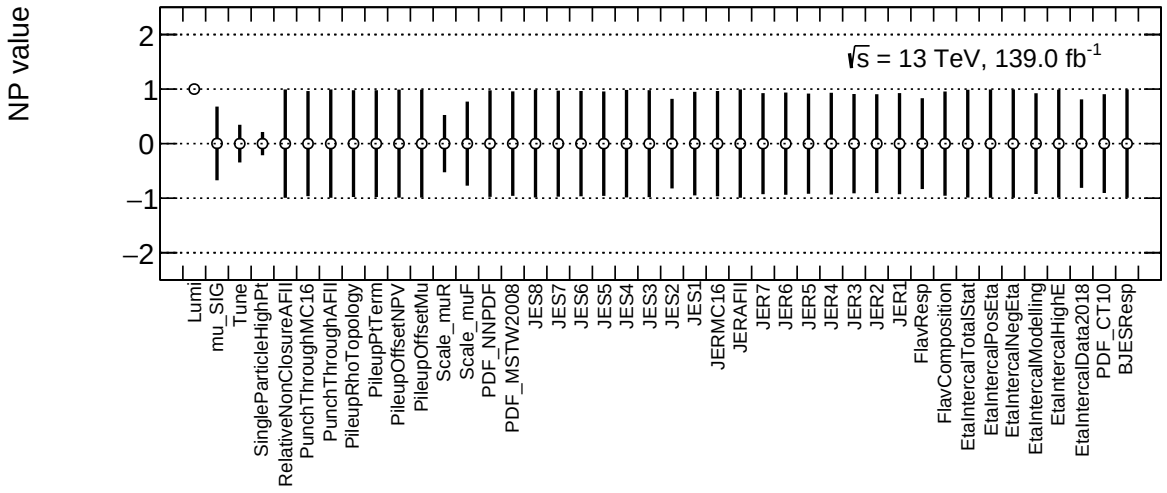

Figure 8.19: The post-fit parameter estimation obtained with the Asimov dataset as the observed dataset.

As expected, all hypothesis tests of simulated HQM samples estimate μ at 0 and report a discovery significance of 0. Thus, the upper limit on μ needs to be calculated. As mention in Section 7.3.2, CL_s is a function of μ for a given dataset. Figure 8.21 shows the CL_s curve against μ of simulated HQM models ($n = 2$). Taking the subplot (a) of Figure 8.21 for example, it has four curves and two colour bands. The observed CL_s curve is calculated according to Equation 7.14, CL_{s+b} according to Equation 7.13 and CL_b according to Equation 7.15. Replacing the observed dataset with the expected background prediction will give us the expected CL_s curve. Because we have already replaced the observed dataset with Asimov data in this subsection, the expected and observed curves overlap each other in the plot. The green and yellow bands are the $\pm 1\sigma$ and $\pm 2\sigma$ uncertainty bands of the expected CL_s, as dis-

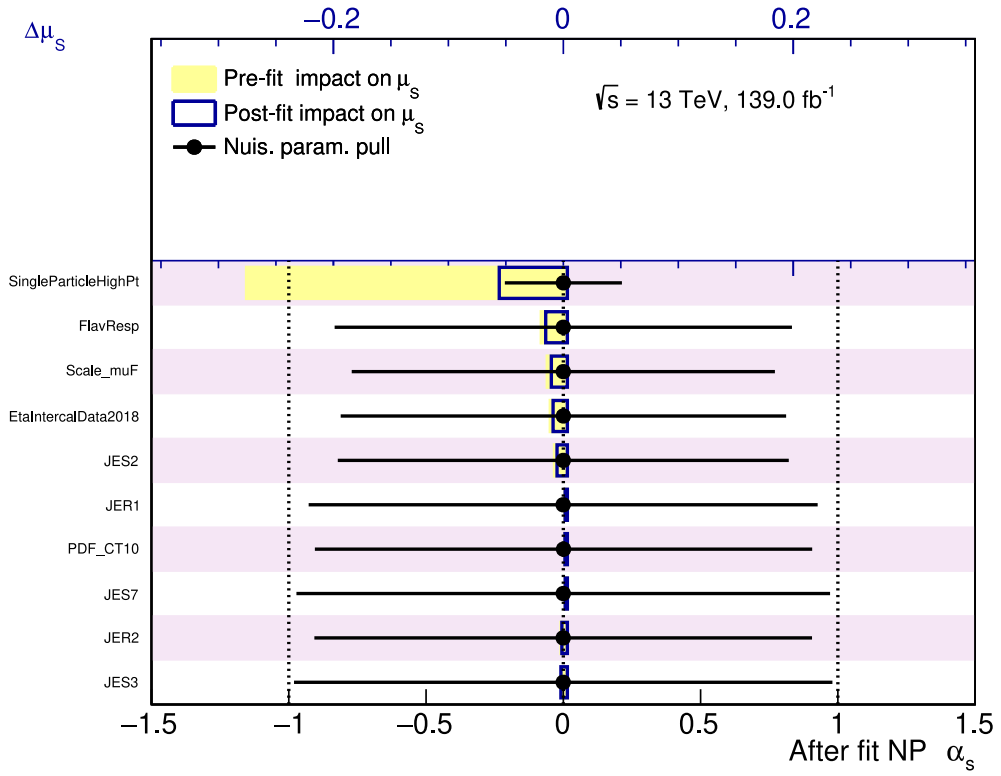

Figure 8.20: Top 10 uncertainties ranked by post-fit impacts on μ, obtained with Asimov data. The points with error bars are the post-fit NP values corresponding to the bottom x-axis. The yellow bars (blue boxes) are the pre-fit (post-fit) impact of NPs on μ, corresponding to the top x-axis.

cussed in Section 7.3.2. Considering the statistical fluctuations, each observed CL_s point has a chance of 68% to be contained in the $\pm 1\sigma$ band and 95% in the $\pm 2\sigma$ band if the hypothesized μ is true.

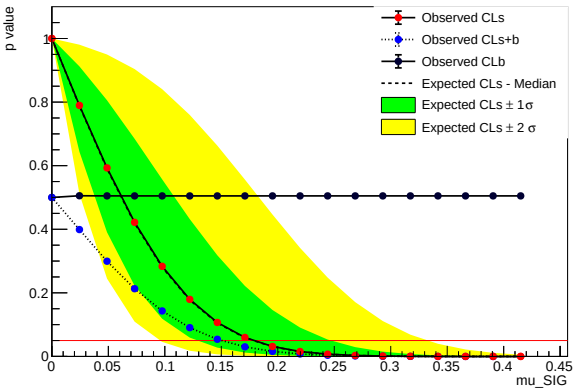

(a) $n = 2$ and $M_D = 7.0$ TeV

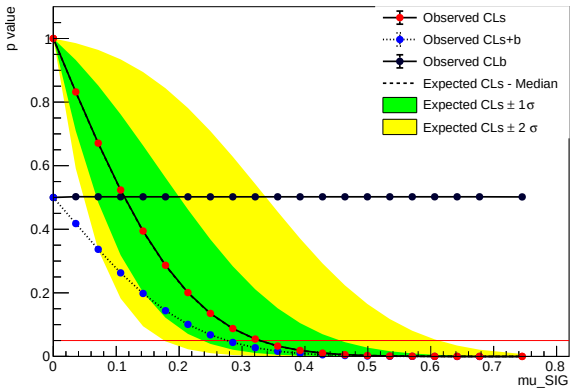

(b) $n = 2$ and $M_D = 7.5$ TeV

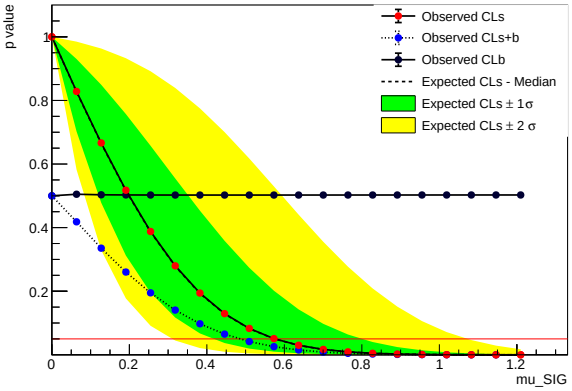

(c) $n = 2$ and $M_D = 8.0$ TeV

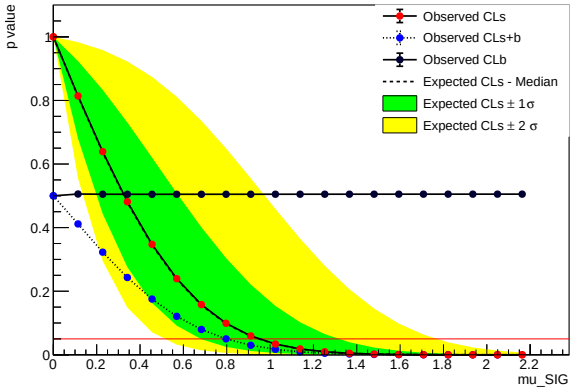

(d) $n = 2$ and $M_D = 8.5$ TeV

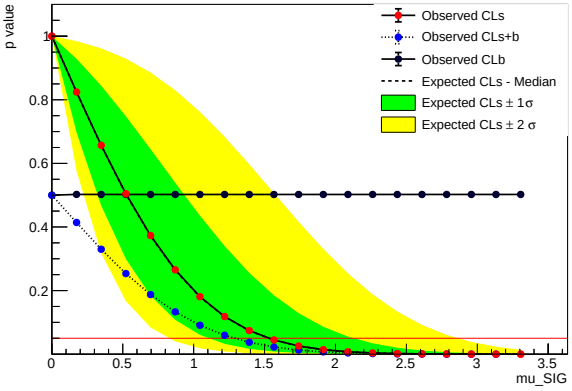

(e) $n = 2$ and $M_D = 9.0$ TeV

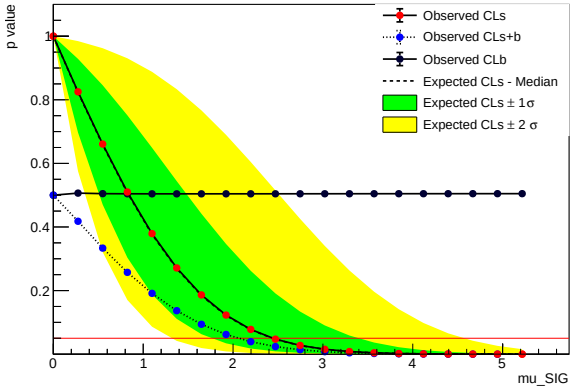

(f) $n = 2$ and $M_D = 9.5$ TeV

Figure 8.21: Signal strength scans of HQM samples ($n = 2$).

With the solved μ value at $CL_s = 0.05$, we can give the limit at 95% confidence level on HQM cross-section times branching ratio. The total cross-section and branching ratio can vary depending on specific theories and assumptions. Thus, we can only put limits on the production of the two instead of solely on the total cross-section. The limit is obtained by solving

$$(\sigma \times B)_{95} \times A \times \epsilon_{\text{rec}} \times \epsilon_{\text{sel}} = \frac{\mu_{95} \times N_s}{\mathcal{L}} \tag{8.3}$$

where B is the branching ratio of HQM decaying into particles that can be identified as dijet events. A is the acceptance of the detector. ϵ_{rec} and ϵ_{sel} are the reconstruction and selection efficiencies. N_s is the expected signal yield and $\mathcal{L}$ is the luminosity. In this analysis, N_s is calculated in Equation 5.1 where the ϵ_{tot} includes $A \times \epsilon_{\text{rec}} \times \epsilon_{\text{sel}}$ considering the branching ratio of our HQM model is close to 1. The experiment-related terms are cancelled out in Equation 8.3 and we are left with

$$(\sigma \times B)_{95} = \mu_{95} \times \sigma_{\text{HQM}}. \tag{8.4}$$

The limits on $\sigma \times B$ are plotted in Figure 8.22. Again, the observed and expected limits overlap each other. The cross-section of the HQM model is also plotted. By calculating the intersection point between the HQM cross-section curve and the observed limit curve, we can exclude the models with M_D smaller than the intersection point at a 95% confidence level. According to the intersection calculation, we expect to exclude model where $M_D < 8.0$, 7.4 and 6.7 TeV for $n = 2$, 4 and 6, respectively at 95% confidence level. The corresponding limits on $\sigma \times B$ are 3.4, 2.0 and 1.4 fb. A 2D plot is also given in the figure. The parameter space under the expected curve is excluded at a 95% confidence level.

8.3.2 Pseudo-data

This subsection presents the exclusion limits obtained with pseudo-data. Figure 8.23 shows the estimation of parameters in one pseudo-experiment. The estimation of NPs is similar to the one in the background-only fit. Pseudo-experiments are performed 10^4 times and the distributions of estimated μ and

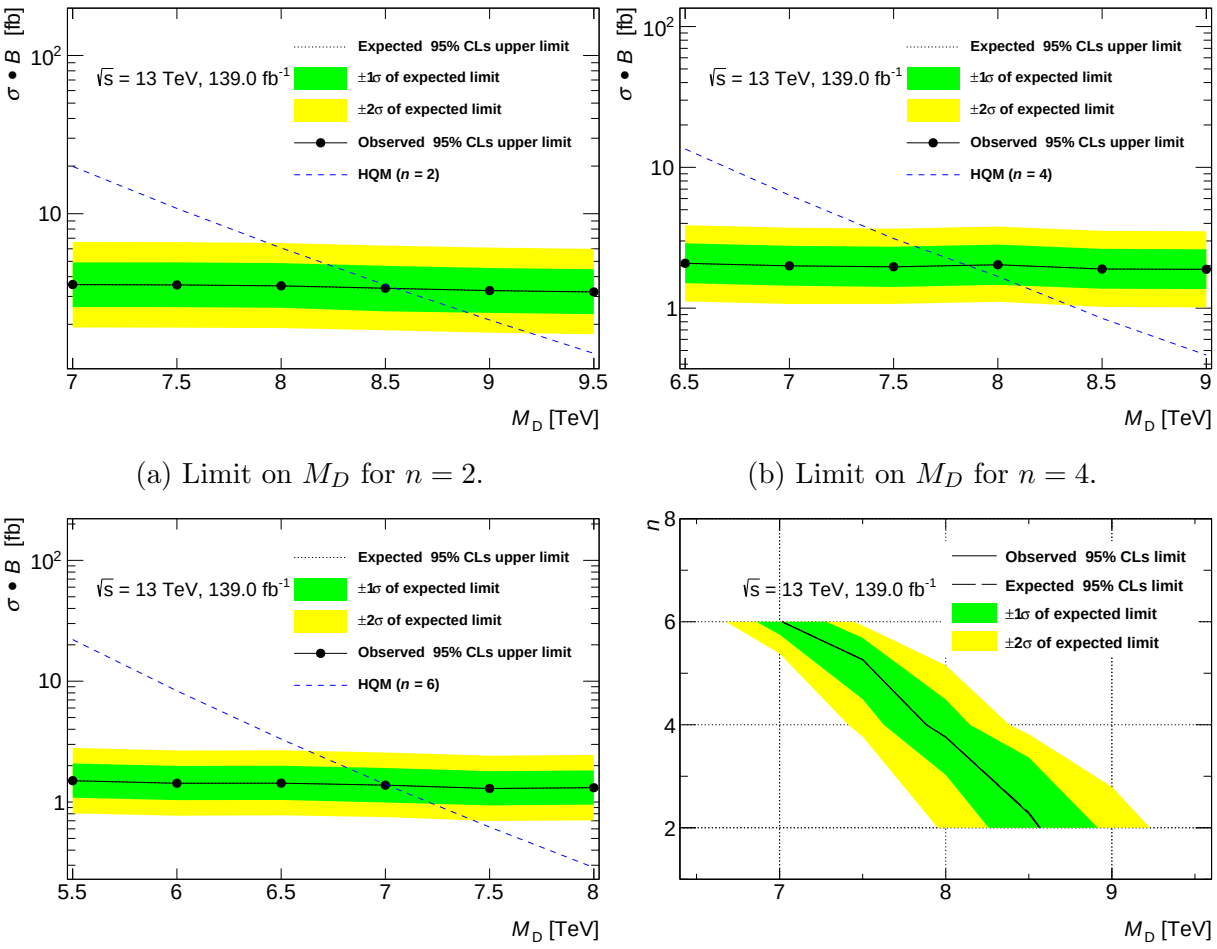

(a) Limit on M_D for $n = 2$.

(b) Limit on M_D for $n = 4$.

(c) Limit on M_D for $n = 6$.

(d) Limit on the 2D space of M_D and n.

Figure 8.22: Limits on parameters M_D and n obtained with Asimov data. The lines between the points are linear interpolations. In plots (a, b, c), M_D values smaller than the cross point of the dashed HQM line and solid observed line are excluded at 95% confidence level in the cross-section band plots. In plot (d), The parameter space under the curve in the 2D plane is excluded at 95% confidence level.

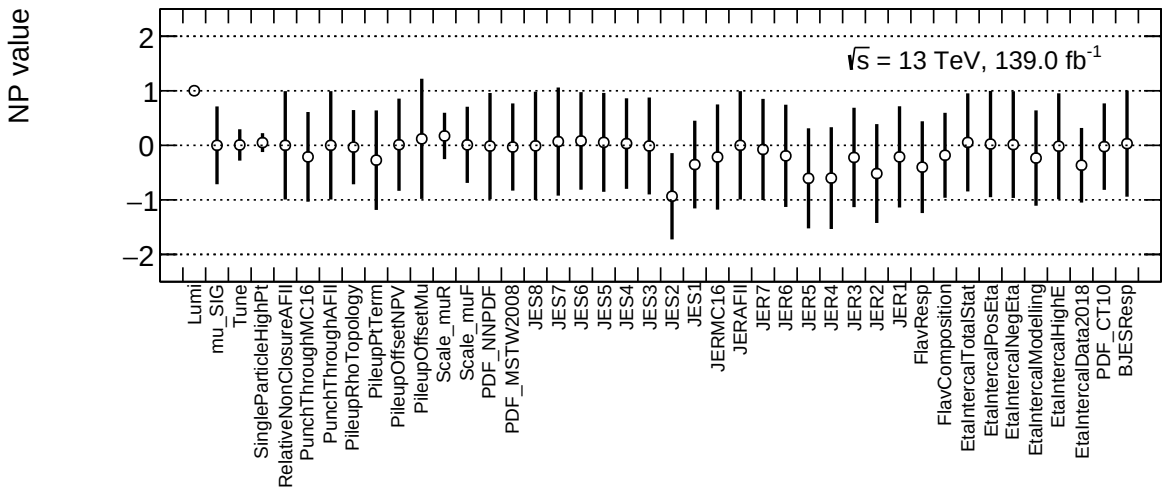

Figure 8.23: The post-fit parameter estimation obtained with a pseudo-data set as the observed dataset.

significance are shown in Figure 8.24. The estimated μ distribution clusters around 0 and does not exceed 0.2 in the fit. The significance distribution clusters around 0 and does not exceed 2.5. It indicates that the statistical fluctuations of the background production are not likely to create fake signal events significant enough to lead a discovery. Figure 8.25 shows the impact of NPs which is similar to the rank in the signal-injection study.

Figure 8.26 shows the limits on n and M_D using a pseudo-data set. Due to the difference between pseudo-data and background prediction, the observed limit is not overlapped by the expected limit anymore but within 1σ of the expected limit.

8.3.3 Tests with alternative procedure choices

The exclusion hypothesis test is tested with alternative procedure choices which are described below.

- One of the choices is to construct the PDF uncertainty according to the PDF4LHC recommendation and construct scale uncertainties in a similar method. This method was used in the previous angular analy-

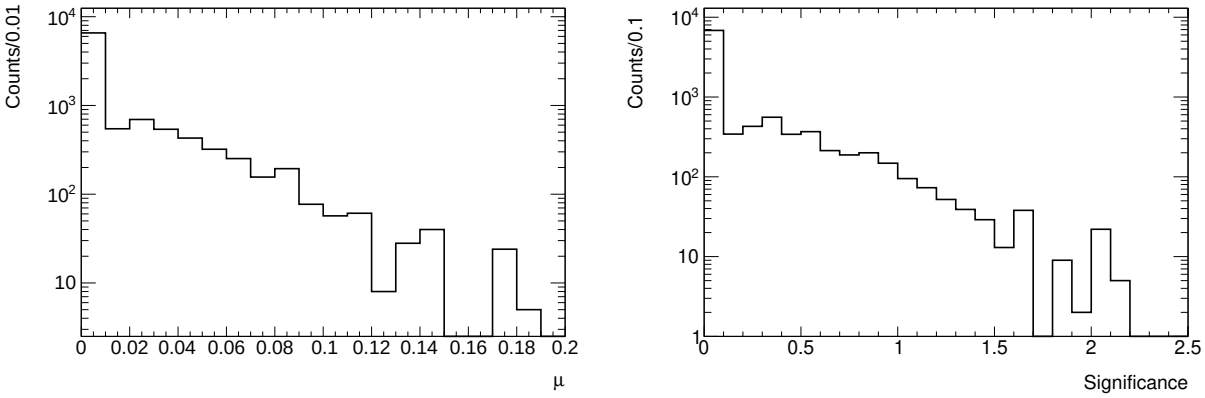

Figure 8.24: Distributions of (left) estimated μ and (right) significance in 10^4 pseudo-experiments.

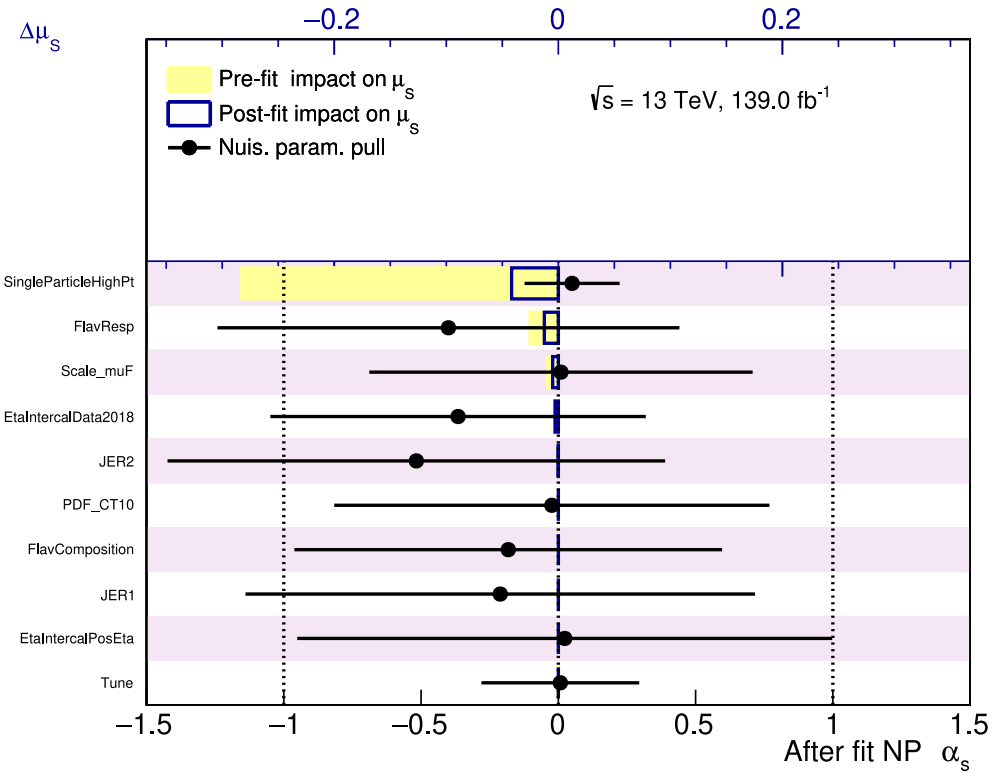

Figure 8.25: Top 10 uncertainties ranked by post-fit impacts on μ, obtained with a pseudo-data set. The points with error bars are the post-fit NP values corresponding to the bottom x-axis. The yellow bars (blue boxes) are the pre-fit (post-fit) impact of NPs on μ, corresponding to the top x-axis..

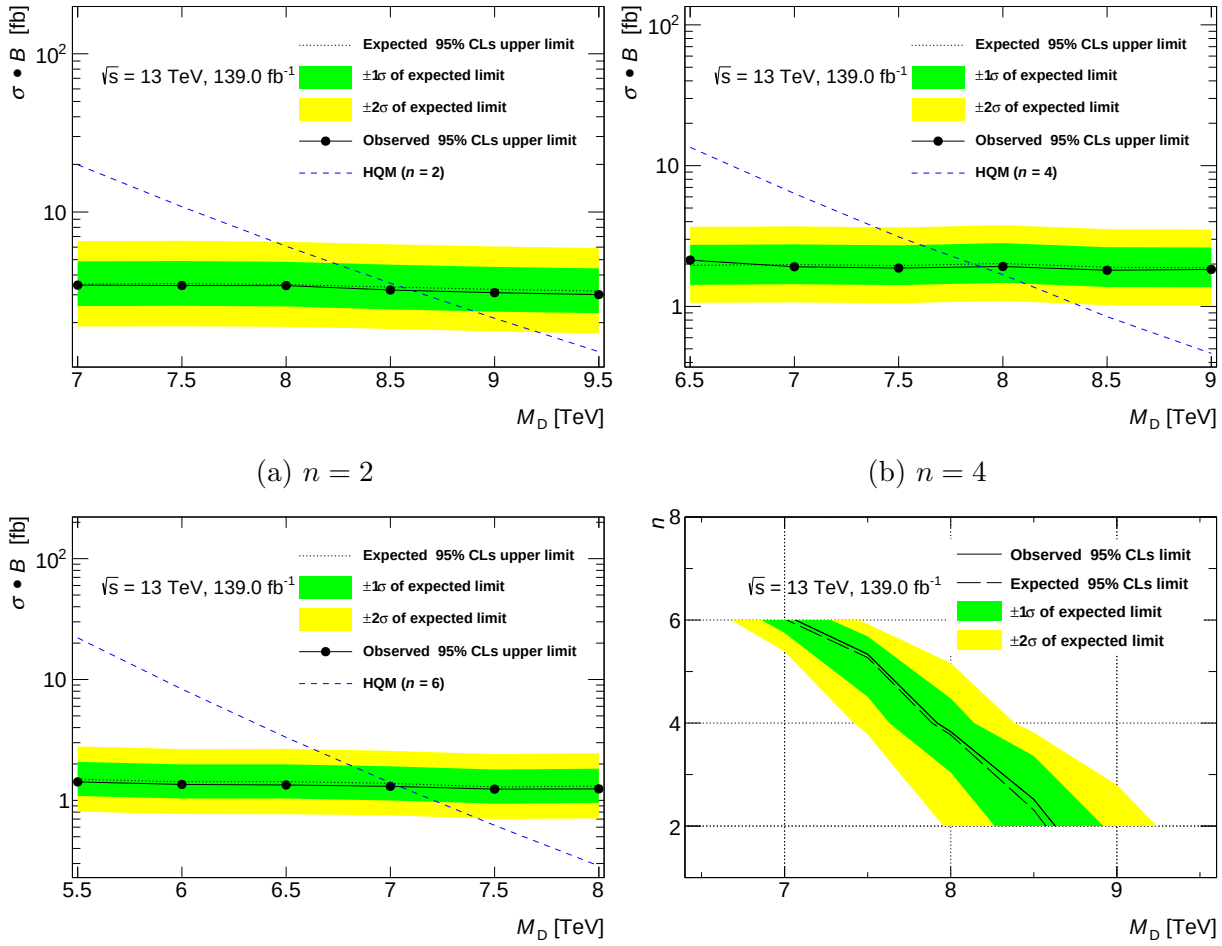

(a) $n = 2$

(b) $n = 4$

(c) $n = 6$

(d) Limit on the 2D plane of M_D and n.

Figure 8.26: Limits on parameters M_D and n obtained with a pseudo-data set.

Table 8.2: The expected limits on M_D with alternative procedure choices.

	Expected M_D (TeV) limit at 95% CL_s		
Choice	$n = 2$	$n = 4$	$n = 6$
Nominal	$8.57^{+0.31}_{-0.35}$	$7.88^{+0.26}_{-0.26}$	$7.02^{+0.15}_{-0.27}$
Construct PDF and scale uncertainties in envelopes	8.58	7.90	7.02
Add a background normalization parameter	8.58	7.90	7.03
Drop systematic uncertainties on signal models	8.56	7.87	7.00
Drop systematic uncertainties smaller than 5%	8.63	7.90	7.02

sis [14]. Although we think this way of constructing theory uncertainties is neither appropriate to a shape-only analysis nor consistent with the experimental uncertainties, it is tested here.

- Another choice is to introduce a free background normalization factor which may reduce the impact of the normalization strategy in estimating μ.

- Considering the fluctuations on signal uncertainty variations, we could drop the uncertainties on signals because they share the NPs with the background, which may cause undesired constraints on NPs.

- To be consistent with the pruning threshold of 5% on statistical uncertainties, we could also drop the systematic uncertainties under 5%, which can accelerate the fit procedure.

Table 8.2 lists the choices and their corresponding results in terms of expected limits on M_D. The impact of these choices is around $\mathcal{O}(0.01)$ TeV which is smaller than the impact from statistical fluctuations. Therefore, we consider the analysis to be robust against procedure choices.

8.4 Results from 2015–16 data

This subsection presents the results using partial Run2 data collected in 2015 and 2016. To explore the possible results using full Run2 data, the partial dataset is scaled up from 36.2 fb^{-1} to 139 fb^{-1}. We regard the scaled-up

dataset as a placeholder for full Run2 data. We want to learn what we may get if we are allowed to unblind the 2017–18 data.

Figure 8.27 shows the estimation of the parameters. The estimated μ is close to 0. We find that all simulated HQM samples are estimated to have μ around $10^{-4} \sim 10^{-9}$, which means the signature of the existence of HQM events in the collect 2015–16 data is very small. The discovery significance for all simulated HQM samples is 0. Figure 8.28 shows the impacts of NPs. Comparing this ranking to the ones using Asimov data and pseudo-data, all post-fit impacts are decreased and SPHP is the only uncertainty that still has a noticeable impact. It is most likely to be caused by irregular fluctuations in the dataset. Figure 8.29 and Figure 8.30 respectively shows the pre-fit and post-fit χ distributions. The 2015–16 dataset agrees with the background model in most bins. Although in some bins the data observation deviates from the background model about 3σ, the deviation has no clear tendency to be over/under background prediction in certain areas. Thus, the deviation is more likely to be caused by statistical fluctuations instead of the production of HQM events. Because of the small discovery significance, we go through the upper limit calculation and gives the 95% CL_s limits on n and MD. Figure 8.31, Figure 8.32 and Figure 8.33 respectively shows the CL_s scans of HQM samples $n = 2$, $n = 4$ and $n = 6$. Figure 8.27 shows the excluded parameter space for the HQM model.

Table 8.3 summarize the expected and observed limits on n ad M_D. We expect to exclude $M_D < 8.6$ TeV for $n = 2$ at 95% confidence level, $M_D < 7.9$ TeV for $n = 4$ and $M_D < 7.0$ TeV for $n = 6$ if no evidence of HQM events is found in the full Run2 data.

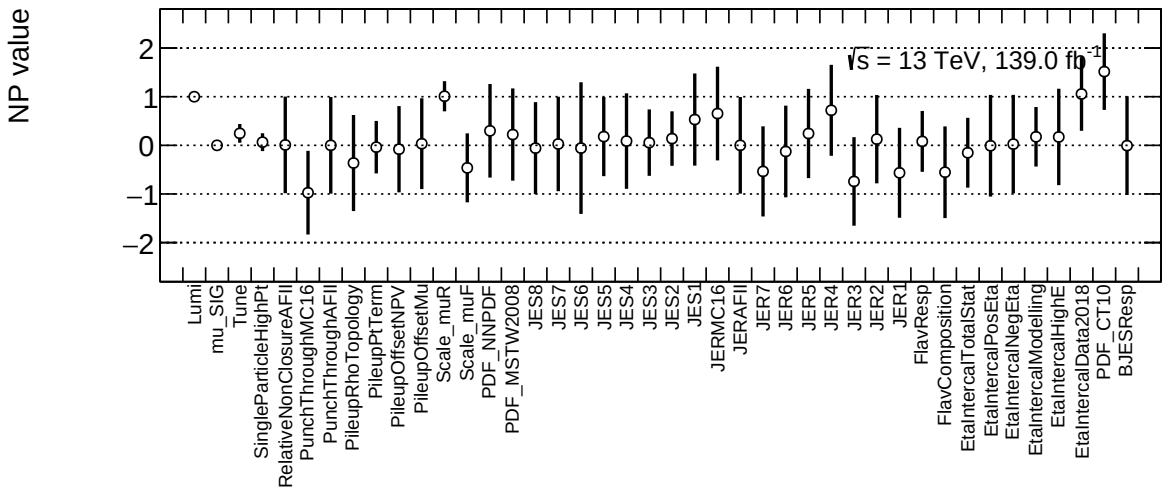

Figure 8.27: The post-fit parameter estimation obtained with the 2015–16 dataset as the observed dataset.

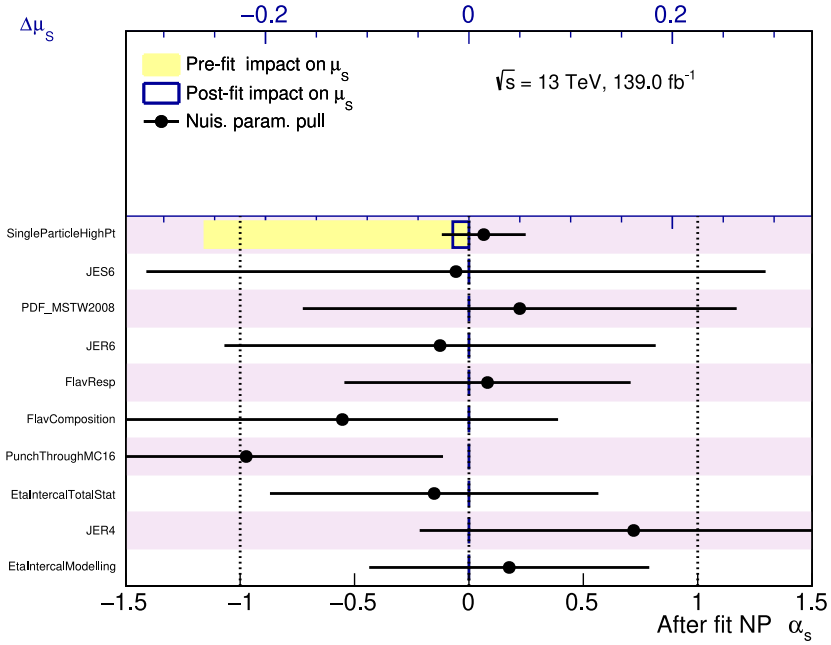

Figure 8.28: Top 10 uncertainties ranked by post-fit impacts on μ, obtained with 215–16 data. The error bars are the post-fit NP values corresponding to the bottom x-axis. The bars are the impact of the NPs on μ corresponding to the top x-axis.

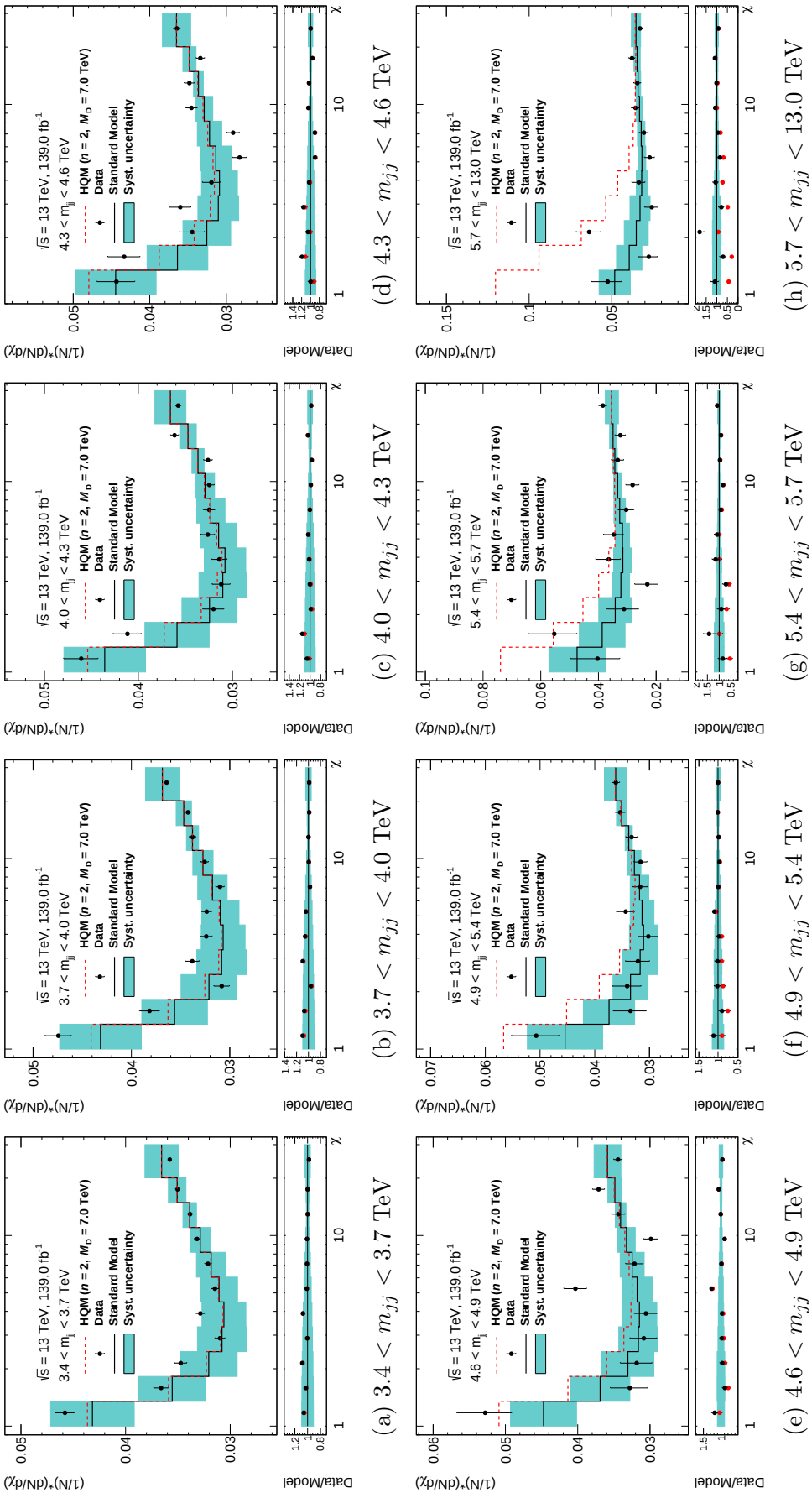

(a) $3.4 < m_{jj} < 3.7$ TeV (b) $3.7 < m_{jj} < 4.0$ TeV (c) $4.0 < m_{jj} < 4.3$ TeV (d) $4.3 < m_{jj} < 4.6$ TeV

(e) $4.6 < m_{jj} < 4.9$ TeV (f) $4.9 < m_{jj} < 5.4$ TeV (g) $5.4 < m_{jj} < 5.7$ TeV (h) $5.7 < m_{jj} < 13.0$ TeV

Figure 8.29: Pre-fit χ distributions obtained with 2015–16 data.

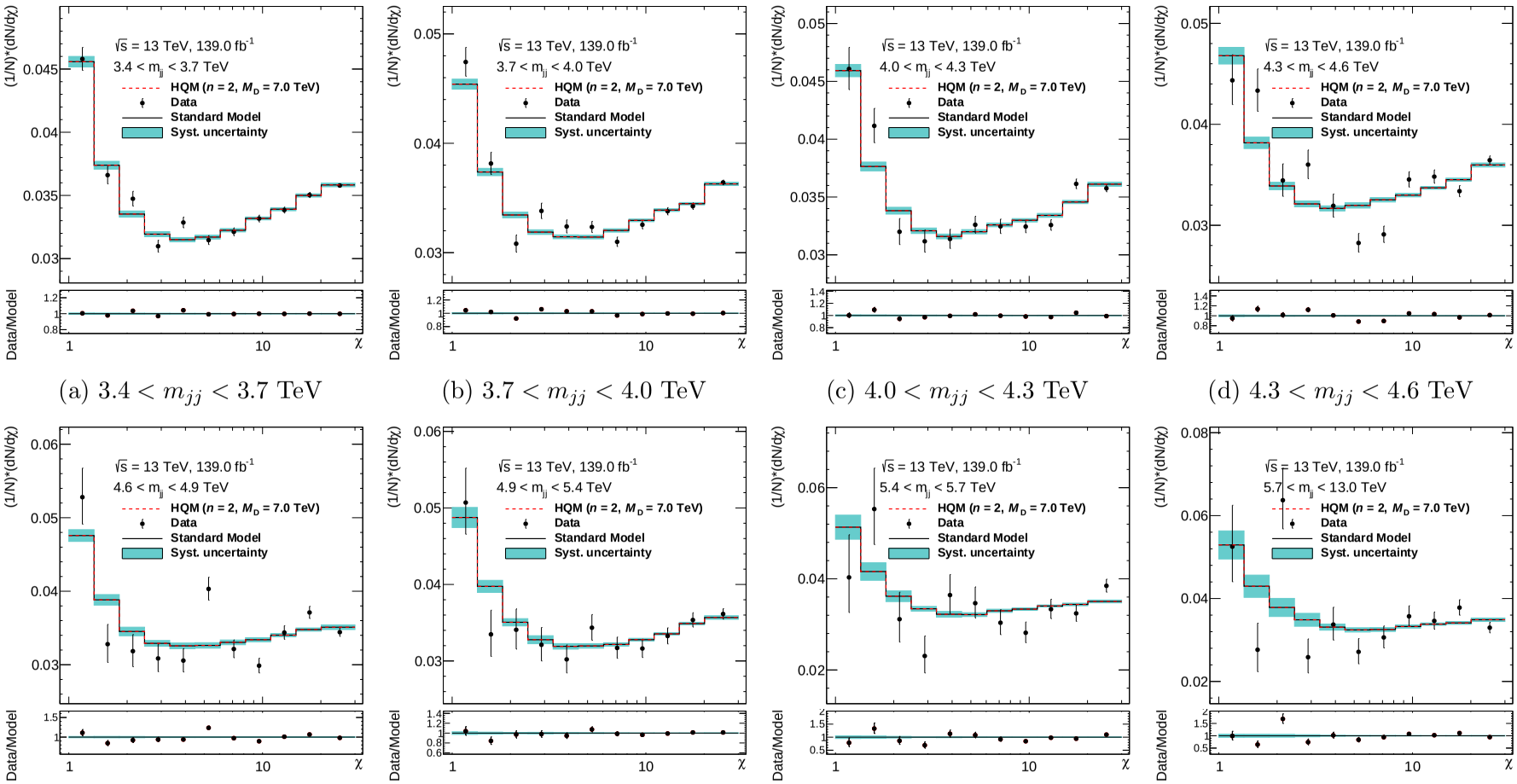

(a) $3.4 < m_{jj} < 3.7$ TeV (b) $3.7 < m_{jj} < 4.0$ TeV (c) $4.0 < m_{jj} < 4.3$ TeV (d) $4.3 < m_{jj} < 4.6$ TeV

(e) $4.6 < m_{jj} < 4.9$ TeV (f) $4.9 < m_{jj} < 5.4$ TeV (g) $5.4 < m_{jj} < 5.7$ TeV (h) $5.7 < m_{jj} < 13.0$ TeV

Figure 8.30: Post-fit χ distributions obtained with 2015–16 data.

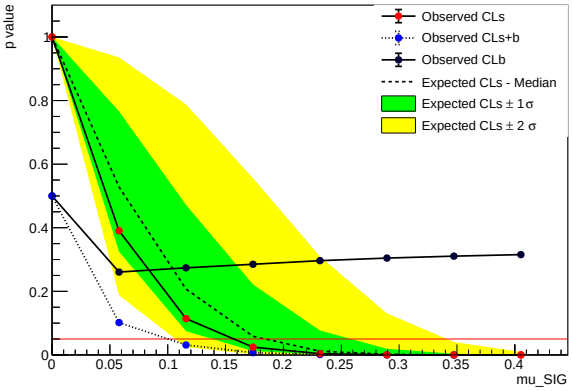

(a) $n = 2$ and $M_D = 7.0$ TeV

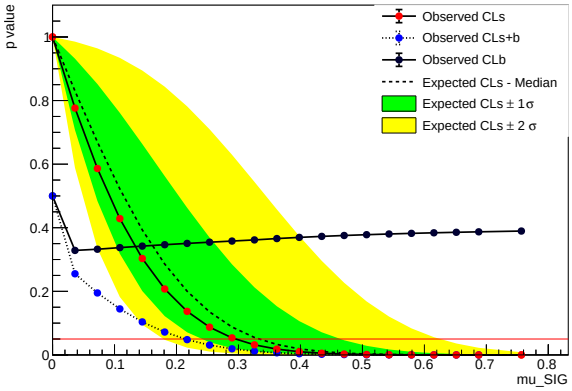

(b) $n = 2$ and $M_D = 7.5$ TeV

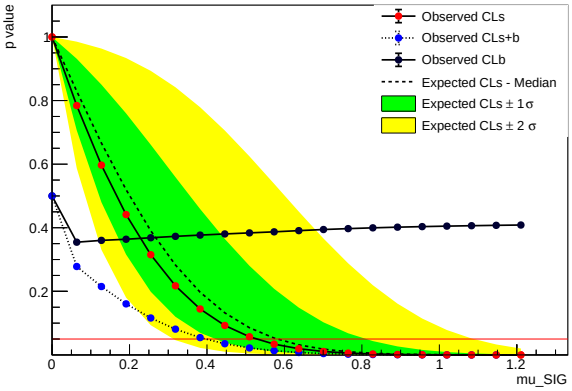

(c) $n = 2$ and $M_D = 8.0$ TeV

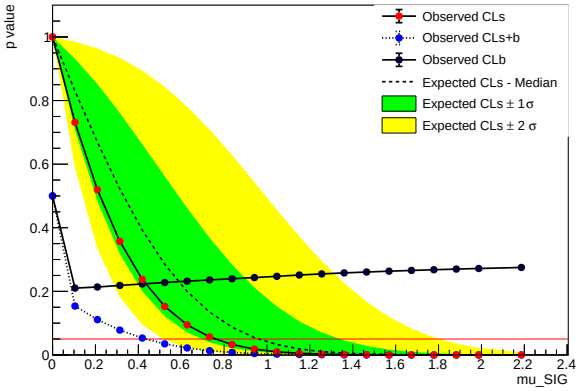

(d) $n = 2$ and $M_D = 8.5$ TeV

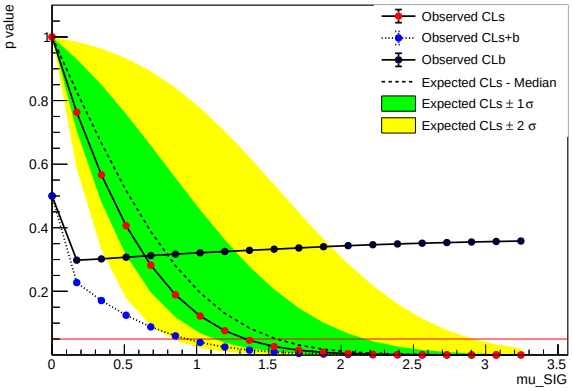

(e) $n = 2$ and $M_D = 9.0$ TeV

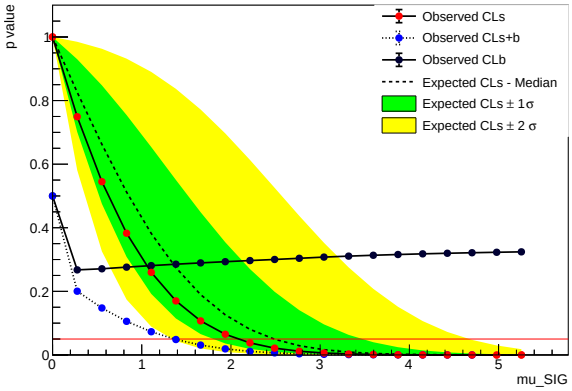

(f) $n = 2$ and $M_D = 9.5$ TeV

Figure 8.31: CL_s scans over signal strength of HQM samples ($n = 2$).

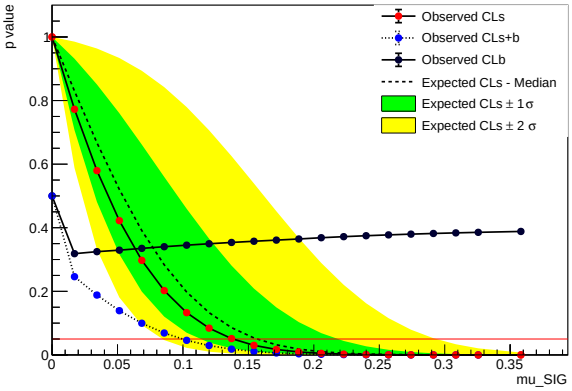

(a) $n = 4$ and $M_D = 6.5$ TeV

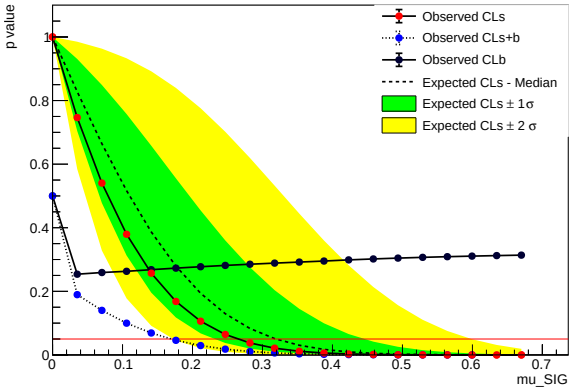

(b) $n = 4$ and $M_D = 7.0$ TeV

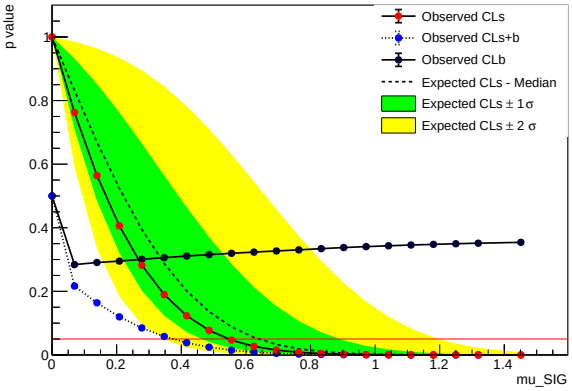

(c) $n = 4$ and $M_D = 7.5$ TeV

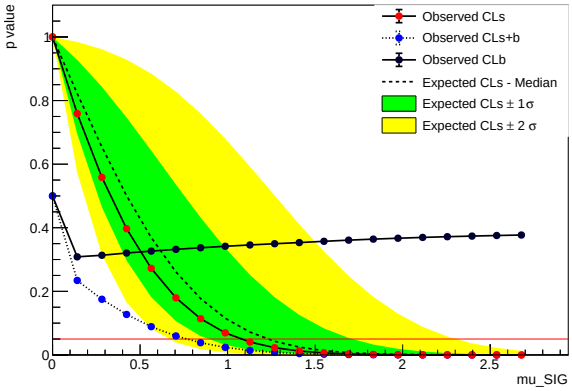

(d) $n = 4$ and $M_D = 8.0$ TeV

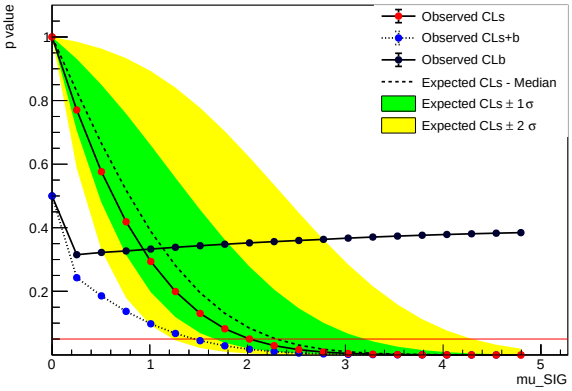

(e) $n = 4$ and $M_D = 8.5$ TeV

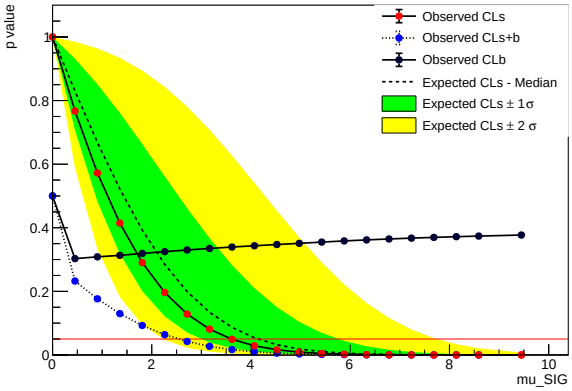

(f) $n = 4$ and $M_D = 9.0$ TeV

Figure 8.32: CL_s scans over signal strength of HQM samples ($n = 4$).

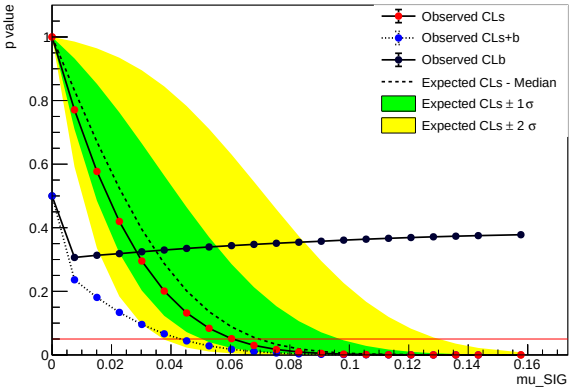

(a) $n = 6$ and $M_D = 5.5$ TeV

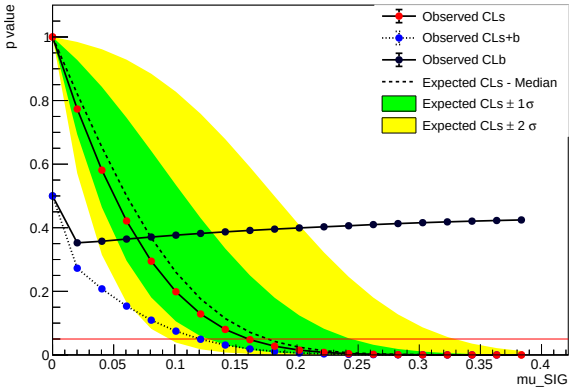

(b) $n = 6$ and $M_D = 6.0$ TeV

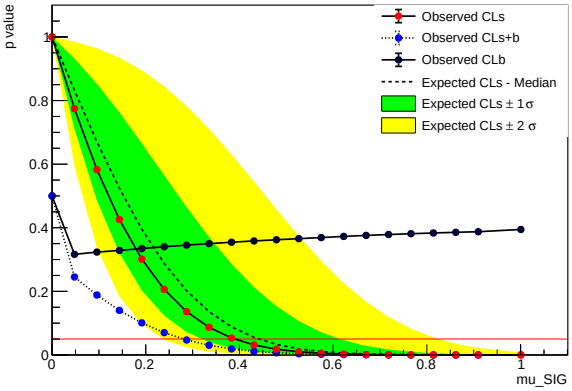

(c) $n = 6$ and $M_D = 6.5$ TeV

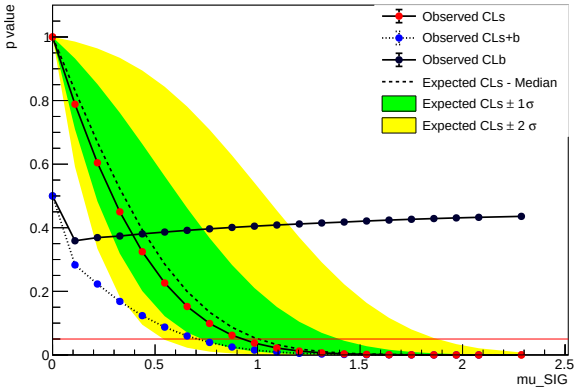

(d) $n = 6$ and $M_D = 7.0$ TeV

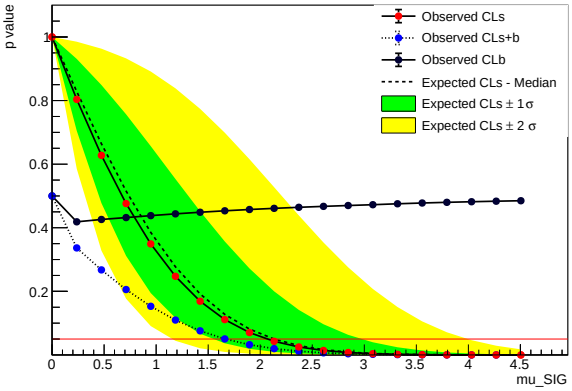

(e) $n = 6$ and $M_D = 7.5$ TeV

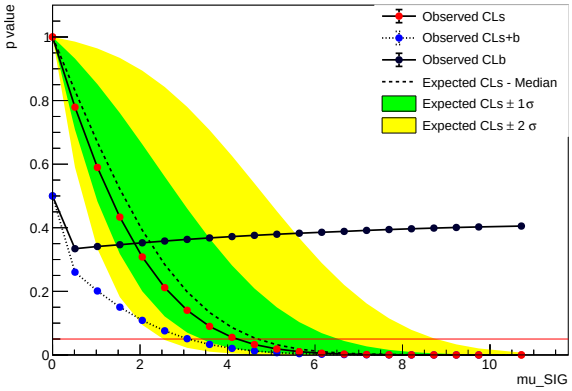

(f) $n = 6$ and $M_D = 8.0$ TeV

Figure 8.33: CL_s scans over signal strength of HQM samples ($n = 6$).

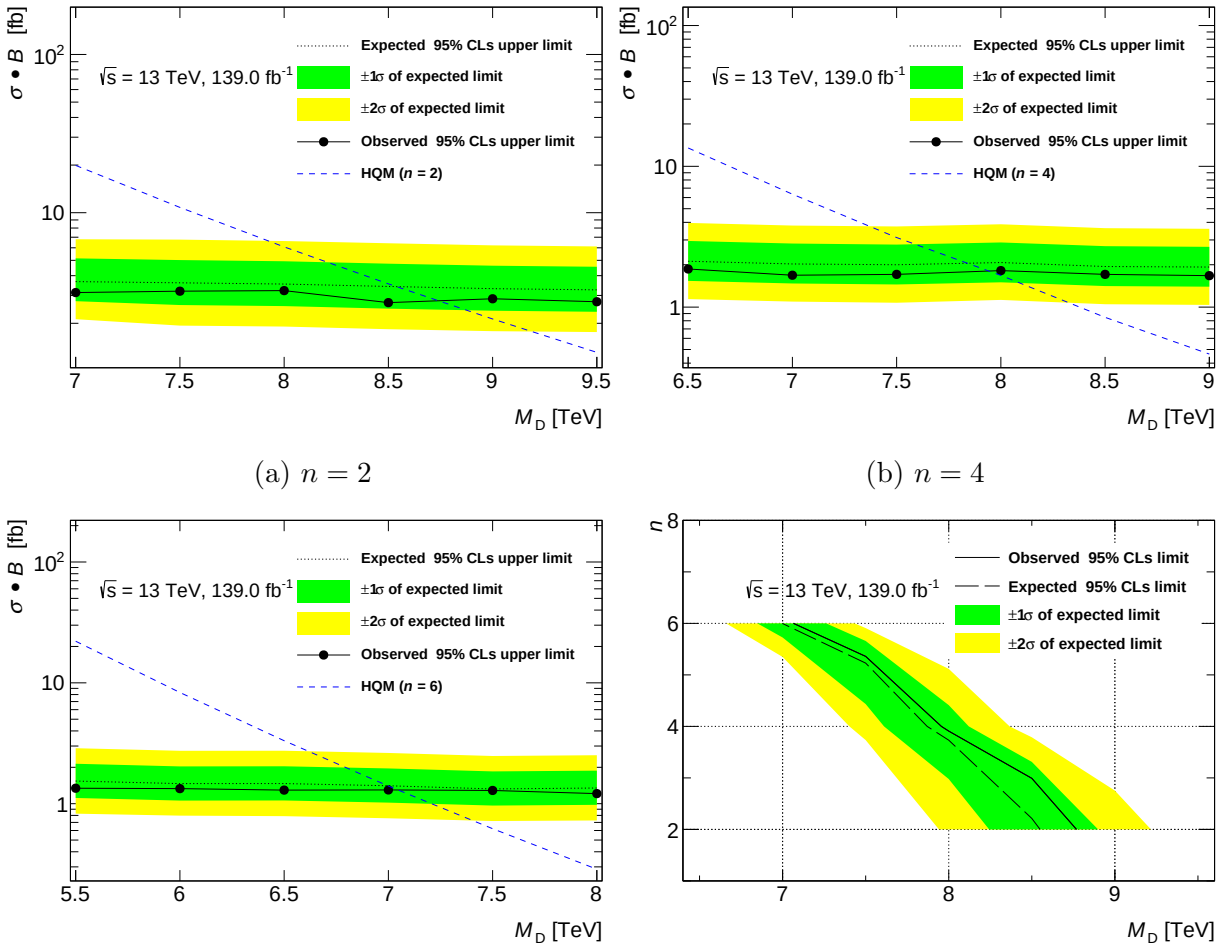

(a) $n = 2$

(b) $n = 4$

(c) $n = 6$

(d) Limit on the 2D plane of M_D and n.

Figure 8.34: Limits on parameters M_D and n, obtained with scaled 2015–16 data.

Table 8.3: Excluion limits on M_D obtained with scaled 2015–16 data.

	M_D (TeV) at 95% CL_s		
dataset of 139 fb^{-1}	$n = 2$	$n = 4$	$n = 6$
Expected (Asimov data)	$8.6^{+0.3}_{-0.3}$	$7.9^{+0.3}_{-0.3}$	$7.0^{+0.2}_{-0.3}$
Observed (pseudo-data)	8.6	7.9	7.1
Observed (scaled 15–16 data)	8.8	8.0	7.1

8.5 Results for 36.2 fb^{-1}

The analysis was targeted to use full Run2 data which could increase the statistical strength for calculating the discovery significance and exclusion limits. As a result, all the procedures described in the thesis proceed with scaled-up datasets/simulations corresponding to 139 fb^{-1}. However, in this scenario, only the expected limits are valid because we are using simulations corresponding to the full Run2 period. The observed limits are not valid because the partial dataset is artificially scaled up. Due to the limited time frame of the program, we are unable to obtain approval from the collaboration to unblind the 2017–18 data. As a compromise, we report the results of using un-scaled 2015–16 data here. The results are valid with an luminosity of 36.2 fb^{-1}. The discovery significance is found to be 0 for all HQM samples. Thus, exclusion limits are calculated. Figure 8.35 shows the exclusion space of the HQM model and Table 8.4 summarize the limits on M_D. The HQM parameter space is excluded where $M_D < 8.0$, 7.4 and 6.7 TeV of $n = 2$, 4 and 6 respectively at 95% confidence level. The corresponding limits on $\sigma \times B$ are 6.5, 3.7 and 2.7 fb. Compared to the results from the scaled-up 2015-16 dataset, we have a better agreement between the expected and observed limits because the statistical fluctuations are not scaled up here.

Table 8.5 summarizes the observed limits on M_D of ADD-model QBH in other analyses. A larger M_D limit is a tighter limit in the parameter space because the cross-section of QBH decreases as M_D increases. We find our limits are not as tight as preceding dijet analyses [14, 36] because of the model difference. HQM events spread more broadly over m_{jj} channels than QBH events, which reduces the signal sensitivity in high m_{jj} channels. However, our limits are still tighter than lepton-involved analyses [38, 41, 42, 46] because of the small branching ratio of QBH to leptons. We suggest future dijet analyses include QBH models and modifications as benchmark models because QBH models are most significant in dijet analyses.

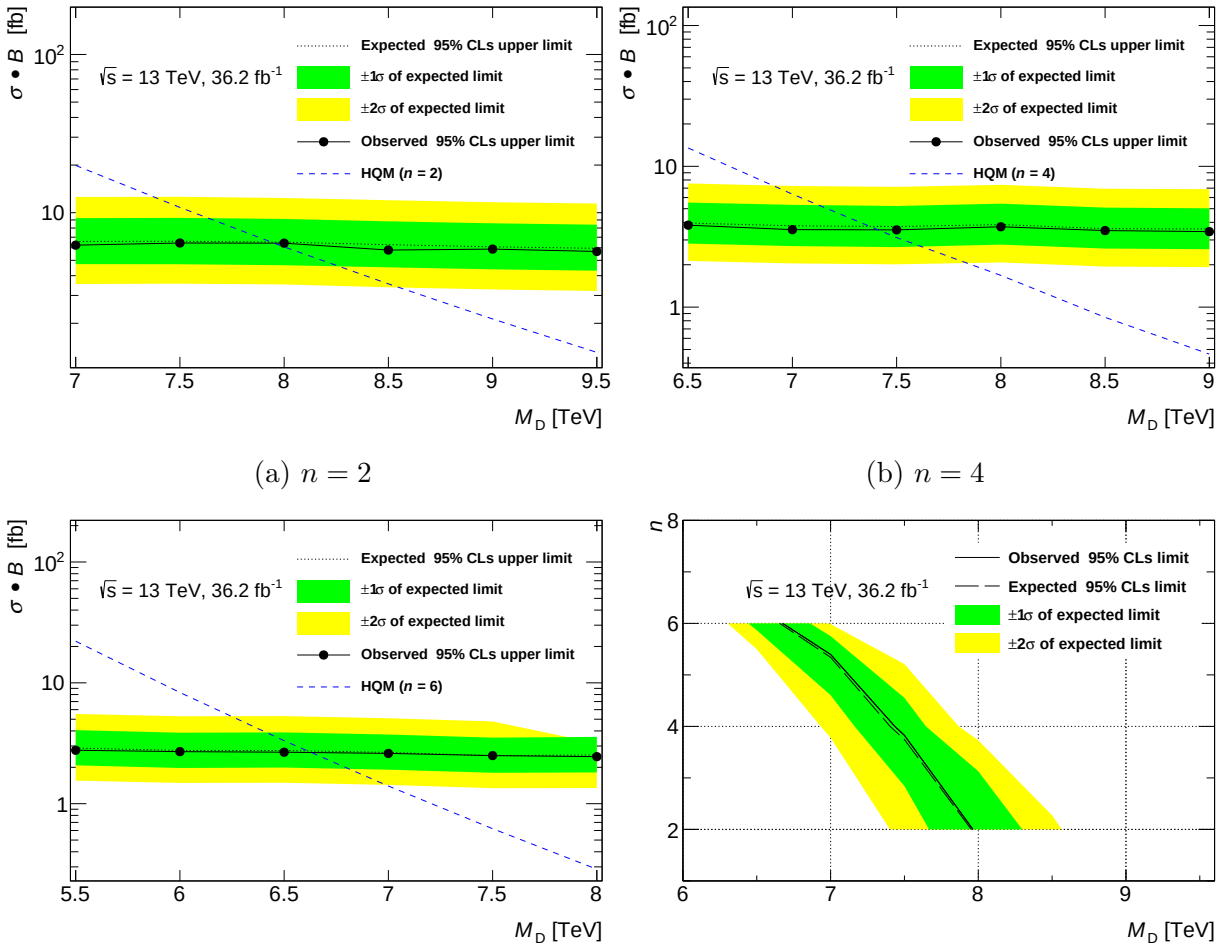

(a) $n = 2$

(b) $n = 4$

(c) $n = 6$

(d) Limit on the 2D plane of M_D and n.

Figure 8.35: Limits on parameters M_D and n, obtained with un-scaled 2015–16 data corresponding to 36.2 fb^{-1}.

Table 8.4: Exclusion limits on M_D obtained with un-scaled 2015–16 data corresponding to 36.2 fb^{-1}.

	M_D (TeV) 95% CL_s limit		
dataset of 36.2 fb^{-1}	$n = 2$	$n = 4$	$n = 6$
Expected	$8.0^{+0.3}_{-0.3}$	$7.4^{+0.2}_{-0.2}$	$6.7^{+0.2}_{-0.2}$
Observed	8.0	7.4	6.7

Table 8.5: Summary of observed limits on M_D of ADD-model quantum black holes.

Analysis	$\sqrt{s}$ (TeV)	Luminosity (fb^{-1})	n	M_D limit (TeV)	Generator
This thesis	13	36.2	2 4 6	8.0 7.4 6.7	QBH with HQM
ATLAS dijet resonance [14]	13	37	6	8.9	BLACKMAX [76]
ATLAS dijet angular [36]	13	3.6	6	8.1 (7.9)	QBH (BLACKMAX)
CMS dijet angular [45]	13	35.9	6	8.2	QBH
ATLAS photon and jet [37]	13	36.7	6	7.1	QBH
ATLAS lepton-flavour violation [38]	13	36.1	6	4.5	QBH
CMS lepton-flavor violation [46]	13	35.9	4 5 6	5.3 5.5 5.6	QBH
ATLAS jet and missing transverse momentum [40]	13	139	2 3 4 5 6	11.2 8.5 7.1 6.4 5.9	Universal extra dimensional model [77]
ATLAS lepton and jet [41]	8	20.3	2	4.7	QBH
ATLAS dilepton resonance [42]	8	20.3	6	3.7	QBH

Chapter 9

Summary

This is the first analysis to search for quantum black holes using the horizon quantum mechanics model in the angular distribution. Compared to the angular analysis performed in 2016 [14], the m_{jj} binning is updated to profit from the increased luminosity of full Run2 data. A new method of constructing PDF uncertainty is studied which provides clearer meanings of the uncertainty than the traditional envelope method. The factors of undermining signal sensitivity are investigated and found to be the background normalization strategy and the uncertainty in the single-particle response measurement.

Data collected in 2015–16 is used and no evidence of HQM signals is found. Therefore, we report the limits on the model parameters n and M_D. We exclude the HQM parameter space where $M_D < 8.0$, 7.4 and 6.7 TeV of $n =$ 2, 4 and 6 respectively at 95% confidence level. Expected limits of using full Run2 data, corresponding to 139 fb^{-1} at $\sqrt{s} = 13$ TeV, are reported. We expect to exclude the parameter space where $M_D < 8.6$, 7.9 and 7.0 TeV of $n = 2$, 4 and 6 respectively at 95% confidence level if no evidence is found after unblinding 2017-18 data.

References

[1] Nima Arkani-Hamed, Savas Dimopoulos, and G. R. Dvali, *The Hierarchy problem and new dimensions at a millimeter*, Phys. Lett. B **429** (1998) 263, arXiv: hep-ph/9803315.

[2] Nima Arkani-Hamed, Savas Dimopoulos, and G. R. Dvali, *Phenomenology, astrophysics and cosmology of theories with submillimeter dimensions and TeV scale quantum gravity*, Phys. Rev. D **59** (1999) 086004, arXiv: hep-ph/9807344.

[3] Lisa Randall and Raman Sundrum, *A Large mass hierarchy from a small extra dimension*, Phys. Rev. Lett. **83** (1999) 3370, arXiv: hep-ph/9905221.

[4] Douglas M. Gingrich, *Quantum black holes with charge, colour, and spin at the LHC*, J. Phys. G **37** (2010) 105008, arXiv: 0912.0826 [hep-ph].

[5] Georges Aad et al., *ATLAS search for new phenomena in dijet mass and angular distributions using pp collisions at* $\sqrt{s} = 7$ *TeV*, JHEP **01** (2013) 029, arXiv: 1210.1718 [hep-ex].

[6] Morad Aaboud et al., *Search for new phenomena in different-flavour high-mass dilepton final states in pp collisions at* $\sqrt{s} = 13$ *Tev with the ATLAS detector*, Eur. Phys. J. C **76** (2016) 541, arXiv: 1607.08079 [hep-ex].

[7] Morad Aaboud et al., *A search for pairs of highly collimated photon-jets in pp collisions at* $\sqrt{s}$ *= 13 TeV with the ATLAS detector*, Phys. Rev. D **99** (2019) 012008, arXiv: 1808.10515 [hep-ex].

[8] Georges Aad et al., *Search for Quantum Black Hole Production in High-Invariant-Mass Lepton+Jet Final States Using pp Collisions at* $\sqrt{s}$ *= 8 TeV and the ATLAS Detector*, Phys. Rev. Lett. **112** (2014) 091804, arXiv: 1311.2006 [hep-ex].

[9] Morad Aaboud et al., *Search for new phenomena in dijet events using 37* fb^{-1} *of pp collision data collected at* $\sqrt{s}$ *=13 TeV with the ATLAS detector*, Phys. Rev. D **96** (2017) 052004, arXiv: 1703.09127 [hep-ex].

[10] Albert M Sirunyan et al., *Search for black holes in high-multiplicity final states in proton-proton collisions at* $\sqrt{s}$ *=13 TeV*, Phys. Lett. B **774** (2017) 279, arXiv: 1705.01403 [hep-ex].

[11] R. Casadio, *Horizons and non-local time evolution of quantum mechanical systems*, Eur. Phys. J. C **75** (2015) 160, arXiv: 1411.5848 [gr-qc].

[12] Roberto Casadio, Rogerio T. Cavalcanti, Andrea Giugno, and Jonas Mureika, *Horizon of quantum black holes in various dimensions*, Phys. Lett. B **760** (2016) 36, arXiv: 1509.09317 [gr-qc].

[13] Douglas M. Gingrich and Brennan Undseth, *Quantum black holes in the horizon quantum mechanics model at the Large Hadron Collider*, Phys. Rev. D **102** (2020) 095020, arXiv: 2005.02548 [hep-ph].

[14] ATLAS Collaboration, *Search for new phenomena in dijet events using* $37\,fb^{-1}$ *of pp collision data collected at* $\sqrt{s} = 13\,TeV$ *with the ATLAS detector*, Phys. Rev. D **96** (2017) 052004, arXiv: 1703.09127 [hep-ex].

[15] S. L. Glashow, *Partial Symmetries of Weak Interactions*, Nucl. Phys. **22** (1961) 579.

[16] Steven Weinberg, *A Model of Leptons*, Phys. Rev. Lett. **19** (1967) 1264.

[17] ATLAS Collaboration, *Observation of a new particle in the search for the Standard Model Higgs boson with the ATLAS detector at the LHC*, Phys. Lett. B **716** (2012) 1, arXiv: 1207.7214 [hep-ex].

[18] F. Englert and R. Brout, *Broken symmetry and the mass of gauge vector mesons*, Phys. Rev. Lett. **13** (1964) 321.

[19] Peter W. Higgs, *Broken symmetries, massless particles and gauge fields*, Phys. Lett. **12** (1964) 132.

[20] Peter W. Higgs, *Broken symmetries and the masses of gauge bosons*, Phys. Rev. Lett. **13** (1964) 508.

[21] G.S. Guralnik, C.R. Hagen, and T.W.B. Kibble, *Global conservation laws and massless particles*, Phys. Rev. Lett. **13** (1964) 585.

[22] Peter W. Higgs, *Spontaneous symmetry breakdown without massless bosons*, Phys. Rev. **145** (1966) 1156.

[23] T.W.B. Kibble, *Symmetry breaking in non-Abelian gauge theories*, Phys. Rev. **155** (1967) 1554.

[24] R. P. Feynman, *The behavior of hadron collisions at extreme energies*, Conf. Proc. C **690905** (1969) 237.

[25] J. Pumplin et al., *New Generation of Parton Distributions with Uncertainties from Global QCD Analysis*, JHEP **07** (2002) 012, arXiv: hep-ph/0201195.

[26] R. Keith Ellis, W. James Stirling, and B. R. Webber, *QCD and collider physics*, vol. 8, Cambridge University Press, 2011.

[27] B. L. Combridge, J. Kripfganz, and J. Ranft, *Hadron Production at Large Transverse Momentum and QCD*, Phys. Lett. B **70** (1977) 234.

[28] Torbjörn Sjöstrand et al., *An introduction to PYTHIA 8.2*, Comput. Phys. Commun. **191** (2015) 159, arXiv: 1410.3012 [hep-ph].

[29] Richard D. Ball et al., *Parton distributions with QED corrections*, Nucl. Phys. B **877** (2013) 290, arXiv: 1308.0598 [hep-ph].

[30] ATLAS Collaboration, *The ATLAS Simulation Infrastructure*, Eur. Phys. J. C **70** (2010) 823, arXiv: 1005.4568 [physics.ins-det].

[31] A. Ribon et al., *Status of Geant4 hadronic physics for the simulation of LHC experiments at the start of the LHC physics program*, (2010), URL: https://lcgapp.cern.ch/project/docs/noteStatusHadronic2010.pdf.

[32] ATLAS Collaboration, *Multijet simulation for* 13 *TeV ATLAS Analyses*, ATL-PHYS-PUB-2019-017, 2019, URL: https://cds.cern.ch/record/2672252.

[33] ATLAS Collaboration, *Luminosity determination in pp collisions at* $\sqrt{s}$ = 13 *TeV using the ATLAS detector at the LHC*, ATLAS-CONF-2019-021, 2019, URL: https://cds.cern.ch/record/2677054.

[34] P. A. Zyla et al., *Review of Particle Physics*, PTEP **2020** (2020) 083C01.

[35] Hirotaka Yoshino and Yasusada Nambu, *Black hole formation in the grazing collision of high-energy particles*, Phys. Rev. D **67** (2003) 024009, arXiv: gr-qc/0209003.

[36] Lene Bryngemark, "Search for new phenomena in dijet angular distributions at $\sqrt{s}$ = 8 and 13 TeV," PhD thesis: Lund U., 2016.

[37] ATLAS Collaboration, *Search for new phenomena in high-mass final states with a photon and a jet from pp collisions at* $\sqrt{s}$ = 13 *TeV with the ATLAS detector*, Eur. Phys. J. C **78** (2018) 102, arXiv: 1709.10440 [hep-ex].

[38] ATLAS Collaboration, *Search for lepton-flavor violation in different-flavor, high-mass final states in pp collisions at* $\sqrt{s}$ = 13 *TeV with the ATLAS detector*, Phys. Rev. D **98** (2018) 092008, arXiv: 1807.06573 [hep-ex].

[39] ATLAS Collaboration, *Search for pairs of highly collimated photon-jets in pp collisions at* $\sqrt{s}$ = 13 *TeV with the ATLAS detector*, Phys. Rev. D **99** (2019) 012008, arXiv: 1808.10515 [hep-ex].

[40] Georges Aad et al., *Search for new phenomena in events with an energetic jet and missing transverse momentum in pp collisions at* $\sqrt{s}$ =13 *TeV with the ATLAS detector*, Phys. Rev. D **103** (2021) 112006, arXiv: 2102.10874 [hep-ex].

[41] ATLAS Collaboration, *Search for Quantum Black Hole Production in High-Invariant-Mass Lepton+Jet Final States Using pp Collisions at* $\sqrt{s}$ = 8 *TeV and the ATLAS Detector*, Phys. Rev. Lett. **112** (2014) 091804, arXiv: 1311.2006 [hep-ex].

[42] ATLAS Collaboration, *Search for high-mass dilepton resonances in pp collisions at $\sqrt{s} = 8$ TeV with the ATLAS detector*, Phys. Rev. D **90** (2014) 052005, arXiv: 1405.4123 [hep-ex].

[43] CMS Collaboration, *Search for lepton flavour violating decays of heavy resonances and quantum black holes to an eμ pair in proton–proton collisions at $\sqrt{s} = 8$ TeV*, Eur. Phys. J. C **76** (2016) 317, arXiv: 1604.05239 [hep-ex].

[44] CMS Collaboration, *Search for black holes and other new phenomena in high-multiplicity final states in proton–proton collisions at $\sqrt{s} = 13$ TeV*, Phys. Lett. B **774** (2017) 279, arXiv: 1705.01403 [hep-ex].

[45] CMS Collaboration, *Search for new physics in dijet angular distributions using proton–proton collisions at $\sqrt{s} = 13$ TeV and constraints on dark matter and other models*, Eur. Phys. J. C **78** (2018) 789, arXiv: 1803.08030 [hep-ex].

[46] CMS Collaboration, *Search for lepton-flavor violating decays of heavy resonances and quantum black holes to eμ final states in proton–proton collisions at $\sqrt{s} = 13$ TeV*, JHEP **04** (2018) 073, arXiv: 1802.01122 [hep-ex].

[47] Savas Dimopoulos and Greg L. Landsberg, *Black holes at the LHC*, Phys. Rev. Lett. **87** (2001) 161602, arXiv: hep-ph/0106295.

[48] Douglas M. Gingrich, *Monte Carlo event generator for black hole production and decay in proton-proton collisions*, Comput. Phys. Commun. **181** (2010) 1917, arXiv: 0911.5370 [hep-ph].

[49] ATLAS Collaboration, *The simulation principle and performance of the ATLAS fast calorimeter simulation FastCaloSim*, ATL-PHYS-PUB-2010-013, 2010, URL: https://cds.cern.ch/record/1300517.

[50] G. Aad et al., *The ATLAS Experiment at the CERN Large Hadron Collider*, JINST **3** (2008) S08003.

[51] Matteo Cacciari, Gavin P. Salam, and Gregory Soyez, *The anti-k_t jet clustering algorithm*, JHEP **04** (2008) 063, arXiv: 0802.1189 [hep-ph].

[52] *CERN Accelerating science*, URL: https://cms.cern/news/jets-cms-and-determination-their-energy-scale.

[53] Georges Aad et al., *Topological cell clustering in the ATLAS calorimeters and its performance in LHC Run 1*, Eur. Phys. J. C **77** (2017) 490, arXiv: 1603.02934 [hep-ex].

[54] Nele Boelaert, "Dijet angular distributions in proton-proton collisions at $\sqrt{s} = 7$ TeV and $\sqrt{s} = 14$ TeV," PhD thesis: Lund U., 2010, URL: http://cds.cern.ch/record/1300762.

[55] Morad Aaboud et al., *Jet reconstruction and performance using particle flow with the ATLAS Detector*, Eur. Phys. J. C **77** (2017) 466, arXiv: 1703.10485 [hep-ex].

[56] ATLAS Collaboration, *Jet energy scale and resolution measured in proton–proton collisions at $\sqrt{s} = 13\,TeV$ with the ATLAS detector*, (2020), arXiv: 2007.02645 [hep-ex].

[57] ATLAS Collaboration, *Jet energy measurement with the ATLAS detector in proton–proton collisions at $\sqrt{s} = 7\,TeV$*, Eur. Phys. J. C **73** (2013) 2304, arXiv: 1112.6426 [hep-ex].

[58] ATLAS Collaboration, *Selection of jets produced in 13 TeV proton–proton collisions with the ATLAS detector*, ATLAS-CONF-2015-029, 2015, URL: https://cds.cern.ch/record/2037702.

[59] Georges Aad et al., *Operation of the ATLAS trigger system in Run 2*, JINST **15** (2020) P10004, arXiv: 2007.12539 [physics.ins-det].

[60] S. Catani and M. H. Seymour, *A General algorithm for calculating jet cross-sections in NLO QCD*, Nucl. Phys. B **485** (1997) 291, [Erratum: Nucl.Phys.B 510, 503–504 (1998)], arXiv: hep-ph/9605323.

[61] Stefan Dittmaier, Alexander Huss, and Christian Speckner, *Weak radiative corrections to dijet production at hadron colliders*, JHEP **11** (2012) 095, arXiv: 1210.0438 [hep-ph].

[62] Georges Aad et al., *Single hadron response measurement and calorimeter jet energy scale uncertainty with the ATLAS detector at the LHC*, Eur. Phys. J. C **73** (2013) 2305, arXiv: 1203.1302 [hep-ex].

[63] ATLAS Collaboration, *ATLAS Pythia 8 tunes to 7 TeV data*, ATL-PHYS-PUB-2014-021, 2014, URL: https://cds.cern.ch/record/1966419.

[64] Marco Guzzi et al., *CT10 parton distributions and other developments in the global QCD analysis*, (2011), arXiv: 1101.0561 [hep-ph].

[65] A. D. Martin, W. J. Stirling, R. S. Thorne, and G. Watt, *Parton distributions for the LHC*, Eur. Phys. J. C **63** (2009) 189, arXiv: 0901.0002 [hep-ph].

[66] Michiel Botje et al., *The PDF4LHC Working Group Interim Recommendations*, (2011), arXiv: 1101.0538 [hep-ph].

[67] Kyle Cranmer, George Lewis, Lorenzo Moneta, Akira Shibata, and Wouter Verkerke, *HistFactory: A tool for creating statistical models for use with RooFit and RooStats*, (2012).

[68] Kyle Cranmer, "Practical Statistics for the LHC," *2011 European School of High-Energy Physics*, 2014, arXiv: 1503.07622 [physics.data-an].

[69] Glen Cowan, Kyle Cranmer, Eilam Gross, and Ofer Vitells, *Asymptotic formulae for likelihood-based tests of new physics*, Eur. Phys. J. C **71** (2011) 1554, arXiv: 1007.1727 [physics.data-an], Erratum: Eur. Phys. J. C **73** (2013) 2501.

[70] Gary J. Feldman and Robert D. Cousins, *A Unified approach to the classical statistical analysis of small signals*, Phys. Rev. D **57** (1998) 3873, arXiv: physics/9711021.

[71] Luca Lista, "Practical Statistics for Particle Physicists," *2016 European School of High-Energy Physics*, 2016, arXiv: 1609.04150 [physics.data-an].

[72] Alexander L. Read, *Presentation of search results: the CL_S technique*, J. Phys. G **28** (2002) 2693.

[73] M. Baak et al., *HistFitter software framework for statistical data analysis*, Eur. Phys. J. C **75** (2015) 153, arXiv: 1410.1280 [hep-ex].

[74] Georges Aad et al., *Combined search for the Standard Model Higgs boson in pp collisions at $\sqrt{s} = 7$ TeV with the ATLAS detector*, Phys. Rev. D **86** (2012) 032003, arXiv: 1207.0319 [hep-ex].

[75] Serguei Chatrchyan et al., *Combined results of searches for the standard model Higgs boson in pp collisions at $\sqrt{s} = 7$ TeV*, Phys. Lett. B **710** (2012) 26, arXiv: 1202.1488 [hep-ex].

[76] De-Chang Dai et al., *BlackMax: A black-hole event generator with rotation, recoil, split branes, and brane tension*, Phys. Rev. D **77** (2008) 076007, arXiv: 0711.3012 [hep-ph].

[77] M. ElKacimi, D. Goujdami, H. Przysiezniak, and Peter Z. Skands, *One Universal Extra Dimension in Pythia*, Comput. Phys. Commun. **181** (2010) 122, arXiv: 0901.4087 [hep-ph].

Appendix A

Simulation and dataset containers

The simulation and dataset containers are listed in this appendix. Table A.1 lists the QCD simulation samples. Table A.2 lists the HQM simulation samples. Tables A.3, A.4, A.5 and A.6 list the datasets taken from 2015 to 2018.

Table A.1: List of QCD simulation containers.

ID	Name of physics abbreviations
364700	Pythia8EvtGen_A14NNPDF23LO_jetjet_JZ0WithSW
364701	Pythia8EvtGen_A14NNPDF23LO_jetjet_JZ1WithSW
364702	Pythia8EvtGen_A14NNPDF23LO_jetjet_JZ2WithSW
364703	Pythia8EvtGen_A14NNPDF23LO_jetjet_JZ3WithSW
364704	Pythia8EvtGen_A14NNPDF23LO_jetjet_JZ4WithSW
364705	Pythia8EvtGen_A14NNPDF23LO_jetjet_JZ5WithSW
364706	Pythia8EvtGen_A14NNPDF23LO_jetjet_JZ6WithSW
364707	Pythia8EvtGen_A14NNPDF23LO_jetjet_JZ7WithSW
364708	Pythia8EvtGen_A14NNPDF23LO_jetjet_JZ8WithSW
364709	Pythia8EvtGen_A14NNPDF23LO_jetjet_JZ9WithSW
364710	Pythia8EvtGen_A14NNPDF23LO_jetjet_JZ10WithSW
364711	Pythia8EvtGen_A14NNPDF23LO_jetjet_JZ11WithSW
364712	Pythia8EvtGen_A14NNPDF23LO_jetjet_JZ12WithSW

Table A.2: List of HQM simulation containers.

ID	Name of physics abbreviations
900002	HQM_n2_MD07000
900003	HQM_n2_MD07500
900004	HQM_n2_MD08000
900005	HQM_n2_MD08500
900006	HQM_n2_MD09000
900007	HQM_n2_MD09500
900008	HQM_n4_MD06500
900009	HQM_n4_MD07000
900010	HQM_n4_MD07500
900011	HQM_n4_MD08000
900012	HQM_n4_MD08500
900013	HQM_n4_MD09000
900014	HQM_n6_MD05500
900015	HQM_n6_MD06000
900016	HQM_n6_MD06500
900017	HQM_n6_MD07000
900018	HQM_n6_MD07500
900019	HQM_n6_MD08000

Table A.3: Data containers of 2015.

Begin of Table
Data container
data15_13TeV.00276181.physics_Main.deriv.DAOD_EXOT2.r9412_p3083_p4016
data15_13TeV.00282992.physics_Main.deriv.DAOD_EXOT2.r9264_p3083_p4016
data15_13TeV.00270806.physics_Main.deriv.DAOD_EXOT2.r9264_p3083_p4016
data15_13TeV.00276954.physics_Main.deriv.DAOD_EXOT2.r9264_p3083_p4016
data15_13TeV.00271048.physics_Main.deriv.DAOD_EXOT2.r9264_p3083_p4016
data15_13TeV.00279685.physics_Main.deriv.DAOD_EXOT2.r9264_p3083_p4016
data15_13TeV.00283608.physics_Main.deriv.DAOD_EXOT2.r9264_p3083_p4016
data15_13TeV.00276952.physics_Main.deriv.DAOD_EXOT2.r9264_p3083_p4016
data15_13TeV.00276731.physics_Main.deriv.DAOD_EXOT2.r9264_p3083_p4016
data15_13TeV.00276212.physics_Main.deriv.DAOD_EXOT2.r9264_p3083_p4016
data15_13TeV.00270588.physics_Main.deriv.DAOD_EXOT2.r9264_p3083_p4016
data15_13TeV.00276689.physics_Main.deriv.DAOD_EXOT2.r9264_p3083_p4016
data15_13TeV.00283155.physics_Main.deriv.DAOD_EXOT2.r9264_p3083_p4016
data15_13TeV.00284484.physics_Main.deriv.DAOD_EXOT2.r9264_p3083_p4016
data15_13TeV.00267167.physics_Main.deriv.DAOD_EXOT2.r9264_p3083_p4016
data15_13TeV.00270448.physics_Main.deriv.DAOD_EXOT2.r9264_p3083_p4016
data15_13TeV.00278968.physics_Main.deriv.DAOD_EXOT2.r9264_p3083_p4016
data15_13TeV.00279169.physics_Main.deriv.DAOD_EXOT2.r9264_p3083_p4016

Continuation of Table A.3

Data container
data15_13TeV.00280862.physics_Main.deriv.DAOD_EXOT2.r9264_p3083_p4016
data15_13TeV.00283780.physics_Main.deriv.DAOD_EXOT2.r9264_p3083_p4016
data15_13TeV.00284473.physics_Main.deriv.DAOD_EXOT2.r9264_p3083_p4016
data15_13TeV.00271595.physics_Main.deriv.DAOD_EXOT2.r9264_p3083_p4016
data15_13TeV.00276245.physics_Main.deriv.DAOD_EXOT2.r9264_p3083_p4016
data15_13TeV.00280977.physics_Main.deriv.DAOD_EXOT2.r9264_p3083_p4016
data15_13TeV.00280464.physics_Main.deriv.DAOD_EXOT2.r9264_p3083_p4016
data15_13TeV.00280853.physics_Main.deriv.DAOD_EXOT2.r9264_p3083_p4016
data15_13TeV.00281381.physics_Main.deriv.DAOD_EXOT2.r9264_p3083_p4016
data15_13TeV.00276073.physics_Main.deriv.DAOD_EXOT2.r9264_p3083_p4016
data15_13TeV.00281075.physics_Main.deriv.DAOD_EXOT2.r9264_p3083_p4016
data15_13TeV.00271388.physics_Main.deriv.DAOD_EXOT2.r9264_p3083_p4016
data15_13TeV.00276778.physics_Main.deriv.DAOD_EXOT2.r9264_p3083_p4016
data15_13TeV.00280368.physics_Main.deriv.DAOD_EXOT2.r9264_p3083_p4016
data15_13TeV.00282712.physics_Main.deriv.DAOD_EXOT2.r9264_p3083_p4016
data15_13TeV.00284154.physics_Main.deriv.DAOD_EXOT2.r9264_p3083_p4016
data15_13TeV.00276176.physics_Main.deriv.DAOD_EXOT2.r9412_p3083_p4016
data15_13TeV.00279813.physics_Main.deriv.DAOD_EXOT2.r9264_p3083_p4016
data15_13TeV.00279984.physics_Main.deriv.DAOD_EXOT2.r9264_p3083_p4016
data15_13TeV.00276336.physics_Main.deriv.DAOD_EXOT2.r9264_p3083_p4016
data15_13TeV.00280500.physics_Main.deriv.DAOD_EXOT2.r9264_p3083_p4016
data15_13TeV.00283429.physics_Main.deriv.DAOD_EXOT2.r9264_p3083_p4016
data15_13TeV.00266904.physics_Main.deriv.DAOD_EXOT2.r9264_p3083_p4016
data15_13TeV.00266919.physics_Main.deriv.DAOD_EXOT2.r9264_p3083_p4016
data15_13TeV.00276183.physics_Main.deriv.DAOD_EXOT2.r9264_p3083_p4016
data15_13TeV.00276790.physics_Main.deriv.DAOD_EXOT2.r9264_p3083_p4016
data15_13TeV.00280273.physics_Main.deriv.DAOD_EXOT2.r9264_p3083_p4016
data15_13TeV.00276329.physics_Main.deriv.DAOD_EXOT2.r9264_p3083_p4016
data15_13TeV.00279284.physics_Main.deriv.DAOD_EXOT2.r9264_p3083_p4016
data15_13TeV.00280520.physics_Main.deriv.DAOD_EXOT2.r9264_p3083_p4016
data15_13TeV.00284006.physics_Main.deriv.DAOD_EXOT2.r9264_p3083_p4016
data15_13TeV.00267162.physics_Main.deriv.DAOD_EXOT2.r9264_p3083_p4016
data15_13TeV.00278727.physics_Main.deriv.DAOD_EXOT2.r9264_p3083_p4016
data15_13TeV.00278970.physics_Main.deriv.DAOD_EXOT2.r9264_p3083_p4016
data15_13TeV.00271298.physics_Main.deriv.DAOD_EXOT2.r9264_p3083_p4016
data15_13TeV.00270949.physics_Main.deriv.DAOD_EXOT2.r9264_p3083_p4016
data15_13TeV.00276416.physics_Main.deriv.DAOD_EXOT2.r9264_p3083_p4016
data15_13TeV.00282631.physics_Main.deriv.DAOD_EXOT2.r9264_p3083_p4016
data15_13TeV.00279598.physics_Main.deriv.DAOD_EXOT2.r9264_p3083_p4016
data15_13TeV.00279932.physics_Main.deriv.DAOD_EXOT2.r9264_p3083_p4016
data15_13TeV.00280950.physics_Main.deriv.DAOD_EXOT2.r9264_p3083_p4016
data15_13TeV.00281070.physics_Main.deriv.DAOD_EXOT2.r9264_p3083_p4016
data15_13TeV.00281411.physics_Main.deriv.DAOD_EXOT2.r9264_p3083_p4016

Continuation of Table A.3
Data container
data15_13TeV.00282784.physics_Main.deriv.DAOD_EXOT2.r9264_p3083_p4016
data15_13TeV.00284285.physics_Main.deriv.DAOD_EXOT2.r9264_p3083_p4016
data15_13TeV.00276511.physics_Main.deriv.DAOD_EXOT2.r9264_p3083_p4016
data15_13TeV.00270816.physics_Main.deriv.DAOD_EXOT2.r9264_p3083_p4016
data15_13TeV.00280231.physics_Main.deriv.DAOD_EXOT2.r9264_p3083_p4016
data15_13TeV.00271421.physics_Main.deriv.DAOD_EXOT2.r9264_p3083_p4016
data15_13TeV.00279259.physics_Main.deriv.DAOD_EXOT2.r9264_p3083_p4016
data15_13TeV.00267639.physics_Main.deriv.DAOD_EXOT2.r9264_p3083_p4016
data15_13TeV.00278880.physics_Main.deriv.DAOD_EXOT2.r9264_p3083_p4016
data15_13TeV.00284213.physics_Main.deriv.DAOD_EXOT2.r9264_p3083_p4016
data15_13TeV.00280614.physics_Main.deriv.DAOD_EXOT2.r9264_p3083_p4016
data15_13TeV.00270441.physics_Main.deriv.DAOD_EXOT2.r9264_p3083_p4016
data15_13TeV.00271516.physics_Main.deriv.DAOD_EXOT2.r9264_p3083_p4016
data15_13TeV.00276189.physics_Main.deriv.DAOD_EXOT2.r9264_p3083_p4016
data15_13TeV.00279515.physics_Main.deriv.DAOD_EXOT2.r9264_p3083_p4016
data15_13TeV.00280753.physics_Main.deriv.DAOD_EXOT2.r9264_p3083_p4016
data15_13TeV.00281317.physics_Main.deriv.DAOD_EXOT2.r9264_p3083_p4016
data15_13TeV.00283074.physics_Main.deriv.DAOD_EXOT2.r9264_p3083_p4016
data15_13TeV.00278748.physics_Main.deriv.DAOD_EXOT2.r9264_p3083_p4016
data15_13TeV.00281385.physics_Main.deriv.DAOD_EXOT2.r9264_p3083_p4016
data15_13TeV.00276262.physics_Main.deriv.DAOD_EXOT2.r9264_p3083_p4016
data15_13TeV.00279345.physics_Main.deriv.DAOD_EXOT2.r9264_p3083_p4016
data15_13TeV.00280319.physics_Main.deriv.DAOD_EXOT2.r9264_p3083_p4016
data15_13TeV.00280673.physics_Main.deriv.DAOD_EXOT2.r11381_p3826_p4016
End of Table A.3

Table A.4: Data containers of 2016.

Begin of Table
Data container
data16_13TeV.00297730.physics_Main.deriv.DAOD_EXOT2.r9264_p3083_p4016
data16_13TeV.00298595.physics_Main.deriv.DAOD_EXOT2.r9264_p3083_p4016
data16_13TeV.00298773.physics_Main.deriv.DAOD_EXOT2.r9264_p3083_p4016
data16_13TeV.00298690.physics_Main.deriv.DAOD_EXOT2.r9264_p3083_p4016
data16_13TeV.00299055.physics_Main.deriv.DAOD_EXOT2.r9264_p3083_p4016
data16_13TeV.00299144.physics_Main.deriv.DAOD_EXOT2.r9264_p3083_p4016
data16_13TeV.00300540.physics_Main.deriv.DAOD_EXOT2.r9264_p3083_p4016
data16_13TeV.00300800.physics_Main.deriv.DAOD_EXOT2.r9264_p3083_p4016
data16_13TeV.00301912.physics_Main.deriv.DAOD_EXOT2.r9264_p3083_p4016
data16_13TeV.00302956.physics_Main.deriv.DAOD_EXOT2.r9264_p3083_p4016
data16_13TeV.00303892.physics_Main.deriv.DAOD_EXOT2.r9264_p3083_p4016
data16_13TeV.00303943.physics_Main.deriv.DAOD_EXOT2.r9264_p3083_p4016

Continuation of Table A.4

Data container
data16_13TeV.00304211.physics_Main.deriv.DAOD_EXOT2.r9264_p3083_p4016
data16_13TeV.00305727.physics_Main.deriv.DAOD_EXOT2.r9264_p3083_p4016
data16_13TeV.00300418.physics_Main.deriv.DAOD_EXOT2.r9264_p3083_p4016
data16_13TeV.00303338.physics_Main.deriv.DAOD_EXOT2.r9264_p3083_p4016
data16_13TeV.00303499.physics_Main.deriv.DAOD_EXOT2.r9264_p3083_p4016
data16_13TeV.00303560.physics_Main.deriv.DAOD_EXOT2.r9264_p3083_p4016
data16_13TeV.00303638.physics_Main.deriv.DAOD_EXOT2.r9264_p3083_p4016
data16_13TeV.00308047.physics_Main.deriv.DAOD_EXOT2.r9264_p3083_p4016
data16_13TeV.00309375.physics_Main.deriv.DAOD_EXOT2.r9264_p3083_p4016
data16_13TeV.00298633.physics_Main.deriv.DAOD_EXOT2.r9264_p3083_p4016
data16_13TeV.00304494.physics_Main.deriv.DAOD_EXOT2.r9264_p3083_p4016
data16_13TeV.00305380.physics_Main.deriv.DAOD_EXOT2.r9264_p3083_p4016
data16_13TeV.00305543.physics_Main.deriv.DAOD_EXOT2.r9264_p3083_p4016
data16_13TeV.00305618.physics_Main.deriv.DAOD_EXOT2.r9264_p3083_p4016
data16_13TeV.00305671.physics_Main.deriv.DAOD_EXOT2.r9264_p3083_p4016
data16_13TeV.00305723.physics_Main.deriv.DAOD_EXOT2.r9264_p3083_p4016
data16_13TeV.00305920.physics_Main.deriv.DAOD_EXOT2.r9264_p3083_p4016
data16_13TeV.00306384.physics_Main.deriv.DAOD_EXOT2.r9264_p3083_p4016
data16_13TeV.00306448.physics_Main.deriv.DAOD_EXOT2.r9264_p3083_p4016
data16_13TeV.00306451.physics_Main.deriv.DAOD_EXOT2.r9264_p3083_p4016
data16_13TeV.00307358.physics_Main.deriv.DAOD_EXOT2.r9264_p3083_p4016
data16_13TeV.00307454.physics_Main.deriv.DAOD_EXOT2.r9264_p3083_p4016
data16_13TeV.00307569.physics_Main.deriv.DAOD_EXOT2.r9264_p3083_p4016
data16_13TeV.00307935.physics_Main.deriv.DAOD_EXOT2.r9264_p3083_p4016
data16_13TeV.00309640.physics_Main.deriv.DAOD_EXOT2.r9264_p3083_p4016
data16_13TeV.00310249.physics_Main.deriv.DAOD_EXOT2.r9264_p3083_p4016
data16_13TeV.00310341.physics_Main.deriv.DAOD_EXOT2.r9264_p3083_p4016
data16_13TeV.00310473.physics_Main.deriv.DAOD_EXOT2.r9264_p3083_p4016
data16_13TeV.00310809.physics_Main.deriv.DAOD_EXOT2.r9264_p3083_p4016
data16_13TeV.00310863.physics_Main.deriv.DAOD_EXOT2.r9264_p3083_p4016
data16_13TeV.00311170.physics_Main.deriv.DAOD_EXOT2.r9264_p3083_p4016
data16_13TeV.00311287.physics_Main.deriv.DAOD_EXOT2.r9264_p3083_p4016
data16_13TeV.00311473.physics_Main.deriv.DAOD_EXOT2.r9264_p3083_p4016
data16_13TeV.00301915.physics_Main.deriv.DAOD_EXOT2.r9264_p3083_p4016
data16_13TeV.00310015.physics_Main.deriv.DAOD_EXOT2.r9264_p3083_p4016
data16_13TeV.00302737.physics_Main.deriv.DAOD_EXOT2.r9264_p3083_p4016
data16_13TeV.00307539.physics_Main.deriv.DAOD_EXOT2.r9264_p3083_p4016
data16_13TeV.00299584.physics_Main.deriv.DAOD_EXOT2.r9264_p3083_p4016
data16_13TeV.00300687.physics_Main.deriv.DAOD_EXOT2.r9264_p3083_p4016
data16_13TeV.00302872.physics_Main.deriv.DAOD_EXOT2.r9264_p3083_p4016
data16_13TeV.00303208.physics_Main.deriv.DAOD_EXOT2.r9264_p3083_p4016
data16_13TeV.00303266.physics_Main.deriv.DAOD_EXOT2.r9264_p3083_p4016
data16_13TeV.00303291.physics_Main.deriv.DAOD_EXOT2.r9264_p3083_p4016

Continuation of Table A.4

Data container
data16_13TeV.00303832.physics_Main.deriv.DAOD_EXOT2.r9264_p3083_p4016
data16_13TeV.00304006.physics_Main.deriv.DAOD_EXOT2.r9264_p3083_p4016
data16_13TeV.00304198.physics_Main.deriv.DAOD_EXOT2.r9264_p3083_p4016
data16_13TeV.00304409.physics_Main.deriv.DAOD_EXOT2.r9264_p3083_p4016
data16_13TeV.00300571.physics_Main.deriv.DAOD_EXOT2.r9264_p3083_p4016
data16_13TeV.00299184.physics_Main.deriv.DAOD_EXOT2.r9264_p3083_p4016
data16_13TeV.00300908.physics_Main.deriv.DAOD_EXOT2.r9264_p3083_p4016
data16_13TeV.00301932.physics_Main.deriv.DAOD_EXOT2.r9264_p3083_p4016
data16_13TeV.00301973.physics_Main.deriv.DAOD_EXOT2.r9264_p3083_p4016
data16_13TeV.00302391.physics_Main.deriv.DAOD_EXOT2.r9264_p3083_p4016
data16_13TeV.00304008.physics_Main.deriv.DAOD_EXOT2.r9264_p3083_p4016
data16_13TeV.00305674.physics_Main.deriv.DAOD_EXOT2.r9264_p3083_p4016
data16_13TeV.00305735.physics_Main.deriv.DAOD_EXOT2.r9264_p3083_p4016
data16_13TeV.00305777.physics_Main.deriv.DAOD_EXOT2.r9264_p3083_p4016
data16_13TeV.00305811.physics_Main.deriv.DAOD_EXOT2.r9264_p3083_p4016
data16_13TeV.00306278.physics_Main.deriv.DAOD_EXOT2.r9264_p3083_p4016
data16_13TeV.00306419.physics_Main.deriv.DAOD_EXOT2.r9264_p3083_p4016
data16_13TeV.00298967.physics_Main.deriv.DAOD_EXOT2.r9264_p3083_p4016
data16_13TeV.00298862.physics_Main.deriv.DAOD_EXOT2.r9264_p3083_p4016
data16_13TeV.00305571.physics_Main.deriv.DAOD_EXOT2.r9264_p3083_p4016
data16_13TeV.00302831.physics_Main.deriv.DAOD_EXOT2.r9264_p3083_p4016
data16_13TeV.00302925.physics_Main.deriv.DAOD_EXOT2.r9264_p3083_p4016
data16_13TeV.00303059.physics_Main.deriv.DAOD_EXOT2.r9264_p3083_p4016
data16_13TeV.00310969.physics_Main.deriv.DAOD_EXOT2.r9264_p3083_p4016
data16_13TeV.00311365.physics_Main.deriv.DAOD_EXOT2.r9264_p3083_p4016
data16_13TeV.00301918.physics_Main.deriv.DAOD_EXOT2.r9264_p3083_p4016
data16_13TeV.00310247.physics_Main.deriv.DAOD_EXOT2.r9264_p3083_p4016
data16_13TeV.00310738.physics_Main.deriv.DAOD_EXOT2.r9264_p3083_p4016
data16_13TeV.00311244.physics_Main.deriv.DAOD_EXOT2.r9264_p3083_p4016
data16_13TeV.00299241.physics_Main.deriv.DAOD_EXOT2.r9264_p3083_p4016
data16_13TeV.00302919.physics_Main.deriv.DAOD_EXOT2.r9264_p3083_p4016
data16_13TeV.00299343.physics_Main.deriv.DAOD_EXOT2.r9264_p3083_p4016
data16_13TeV.00300487.physics_Main.deriv.DAOD_EXOT2.r9264_p3083_p4016
data16_13TeV.00302300.physics_Main.deriv.DAOD_EXOT2.r9264_p3083_p4016
data16_13TeV.00302380.physics_Main.deriv.DAOD_EXOT2.r9264_p3083_p4016
data16_13TeV.00302393.physics_Main.deriv.DAOD_EXOT2.r9264_p3083_p4016
data16_13TeV.00303846.physics_Main.deriv.DAOD_EXOT2.r9264_p3083_p4016
data16_13TeV.00298687.physics_Main.deriv.DAOD_EXOT2.r9264_p3083_p4016
data16_13TeV.00299147.physics_Main.deriv.DAOD_EXOT2.r9264_p3083_p4016
data16_13TeV.00300345.physics_Main.deriv.DAOD_EXOT2.r9264_p3083_p4016
data16_13TeV.00303007.physics_Main.deriv.DAOD_EXOT2.r9264_p3083_p4016
data16_13TeV.00300784.physics_Main.deriv.DAOD_EXOT2.r9264_p3083_p4016
data16_13TeV.00304308.physics_Main.deriv.DAOD_EXOT2.r9264_p3083_p4016

Continuation of Table A.4

Data container
data16_13TeV.00309516.physics_Main.deriv.DAOD_EXOT2.r9264_p3083_p4016
data16_13TeV.00310370.physics_Main.deriv.DAOD_EXOT2.r9264_p3083_p4016
data16_13TeV.00302053.physics_Main.deriv.DAOD_EXOT2.r9264_p3083_p4016
data16_13TeV.00302347.physics_Main.deriv.DAOD_EXOT2.r9264_p3083_p4016
data16_13TeV.00302829.physics_Main.deriv.DAOD_EXOT2.r9264_p3083_p4016
data16_13TeV.00303304.physics_Main.deriv.DAOD_EXOT2.r9264_p3083_p4016
data16_13TeV.00304243.physics_Main.deriv.DAOD_EXOT2.r9264_p3083_p4016
data16_13TeV.00304337.physics_Main.deriv.DAOD_EXOT2.r9264_p3083_p4016
data16_13TeV.00304431.physics_Main.deriv.DAOD_EXOT2.r9264_p3083_p4016
data16_13TeV.00306310.physics_Main.deriv.DAOD_EXOT2.r9264_p3083_p4016
data16_13TeV.00306442.physics_Main.deriv.DAOD_EXOT2.r9264_p3083_p4016
data16_13TeV.00307126.physics_Main.deriv.DAOD_EXOT2.r9264_p3083_p4016
data16_13TeV.00307195.physics_Main.deriv.DAOD_EXOT2.r9264_p3083_p4016
data16_13TeV.00307394.physics_Main.deriv.DAOD_EXOT2.r9264_p3083_p4016
data16_13TeV.00307514.physics_Main.deriv.DAOD_EXOT2.r9264_p3083_p4016
data16_13TeV.00307656.physics_Main.deriv.DAOD_EXOT2.r9264_p3083_p4016
data16_13TeV.00307710.physics_Main.deriv.DAOD_EXOT2.r9264_p3083_p4016
data16_13TeV.00307716.physics_Main.deriv.DAOD_EXOT2.r9264_p3083_p4016
data16_13TeV.00307732.physics_Main.deriv.DAOD_EXOT2.r9264_p3083_p4016
data16_13TeV.00308084.physics_Main.deriv.DAOD_EXOT2.r9264_p3083_p4016
data16_13TeV.00309440.physics_Main.deriv.DAOD_EXOT2.r9264_p3083_p4016
data16_13TeV.00309674.physics_Main.deriv.DAOD_EXOT2.r9264_p3083_p4016
data16_13TeV.00310405.physics_Main.deriv.DAOD_EXOT2.r9264_p3083_p4016
data16_13TeV.00310468.physics_Main.deriv.DAOD_EXOT2.r9264_p3083_p4016
data16_13TeV.00310634.physics_Main.deriv.DAOD_EXOT2.r9264_p3083_p4016
data16_13TeV.00310691.physics_Main.deriv.DAOD_EXOT2.r9264_p3083_p4016
data16_13TeV.00310872.physics_Main.deriv.DAOD_EXOT2.r9264_p3083_p4016
data16_13TeV.00311321.physics_Main.deriv.DAOD_EXOT2.r9264_p3083_p4016
data16_13TeV.00311402.physics_Main.deriv.DAOD_EXOT2.r9264_p3083_p4016
data16_13TeV.00299288.physics_Main.deriv.DAOD_EXOT2.r9264_p3083_p4016
data16_13TeV.00302265.physics_Main.deriv.DAOD_EXOT2.r9264_p3083_p4016
data16_13TeV.00304128.physics_Main.deriv.DAOD_EXOT2.r9264_p3083_p4016
data16_13TeV.00303421.physics_Main.deriv.DAOD_EXOT2.r9264_p3083_p4016
data16_13TeV.00307601.physics_Main.deriv.DAOD_EXOT2.r9264_p3083_p4016
data16_13TeV.00299243.physics_Main.deriv.DAOD_EXOT2.r9264_p3083_p4016
data16_13TeV.00302269.physics_Main.deriv.DAOD_EXOT2.r9264_p3083_p4016
data16_13TeV.00300279.physics_Main.deriv.DAOD_EXOT2.r9264_p3083_p4016
data16_13TeV.00300863.physics_Main.deriv.DAOD_EXOT2.r9264_p3083_p4016
data16_13TeV.00307861.physics_Main.deriv.DAOD_EXOT2.r9264_p3083_p4016
data16_13TeV.00309759.physics_Main.deriv.DAOD_EXOT2.r9264_p3083_p4016
data16_13TeV.00298609.physics_Main.deriv.DAOD_EXOT2.r9264_p3083_p4016
data16_13TeV.00303079.physics_Main.deriv.DAOD_EXOT2.r9264_p3083_p4016
data16_13TeV.00304178.physics_Main.deriv.DAOD_EXOT2.r9264_p3083_p4016

Continuation of Table A.4
Data container
data16_13TeV.00306269.physics_Main.deriv.DAOD_EXOT2.r9264_p3083_p4016
data16_13TeV.00307354.physics_Main.deriv.DAOD_EXOT2.r9264_p3083_p4016
data16_13TeV.00309390.physics_Main.deriv.DAOD_EXOT2.r9264_p3083_p4016
data16_13TeV.00303201.physics_Main.deriv.DAOD_EXOT2.r9264_p3083_p4016
data16_13TeV.00303264.physics_Main.deriv.DAOD_EXOT2.r9264_p3083_p4016
data16_13TeV.00307259.physics_Main.deriv.DAOD_EXOT2.r9264_p3083_p4016
data16_13TeV.00307306.physics_Main.deriv.DAOD_EXOT2.r9264_p3083_p4016
data16_13TeV.00311071.physics_Main.deriv.DAOD_EXOT2.r9264_p3083_p4016
data16_13TeV.00300415.physics_Main.deriv.DAOD_EXOT2.r9264_p3083_p4016
data16_13TeV.00298771.physics_Main.deriv.DAOD_EXOT2.r9264_p3083_p4016
data16_13TeV.00300655.physics_Main.deriv.DAOD_EXOT2.r9264_p3083_p4016
data16_13TeV.00311481.physics_Main.deriv.DAOD_EXOT2.r9264_p3083_p4016
data16_13TeV.00307619.physics_Main.deriv.DAOD_EXOT2.r9264_p3083_p4016
data16_13TeV.00302137.physics_Main.deriv.DAOD_EXOT2.r9264_p3083_p4016
data16_13TeV.00300600.physics_Main.deriv.DAOD_EXOT2.r9264_p3083_p4016
End of Table A.4

Table A.5: Data containers of 2017.

Begin of Table
Data container
data17_13TeV.00326695.physics_Main.deriv.DAOD_EXOT2.r10250_p3399_p4016
data17_13TeV.00326657.physics_Main.deriv.DAOD_EXOT2.r10250_p3399_p4016
data17_13TeV.00326439.physics_Main.deriv.DAOD_EXOT2.r10250_p3399_p4016
data17_13TeV.00326923.physics_Main.deriv.DAOD_EXOT2.r10250_p3399_p4016
data17_13TeV.00327057.physics_Main.deriv.DAOD_EXOT2.r11380_p3825_p4016
data17_13TeV.00326834.physics_Main.deriv.DAOD_EXOT2.r10250_p3399_p4016
data17_13TeV.00325790.physics_Main.deriv.DAOD_EXOT2.r10250_p3399_p4016
data17_13TeV.00326446.physics_Main.deriv.DAOD_EXOT2.r10250_p3399_p4016
data17_13TeV.00326870.physics_Main.deriv.DAOD_EXOT2.r10250_p3399_p4016
data17_13TeV.00326551.physics_Main.deriv.DAOD_EXOT2.r10250_p3399_p4016
data17_13TeV.00325789.physics_Main.deriv.DAOD_EXOT2.r10250_p3399_p4016
data17_13TeV.00331020.physics_Main.deriv.DAOD_EXOT2.r10203_p3399_p4016
data17_13TeV.00333367.physics_Main.deriv.DAOD_EXOT2.r10203_p3399_p4016
data17_13TeV.00338897.physics_Main.deriv.DAOD_EXOT2.r10258_p3399_p4016
data17_13TeV.00328221.physics_Main.deriv.DAOD_EXOT2.r10203_p3399_p4016
data17_13TeV.00334317.physics_Main.deriv.DAOD_EXOT2.r10203_p3399_p4016
data17_13TeV.00334413.physics_Main.deriv.DAOD_EXOT2.r11379_p3825_p4016
data17_13TeV.00328042.physics_Main.deriv.DAOD_EXOT2.r10203_p3399_p4016
data17_13TeV.00330328.physics_Main.deriv.DAOD_EXOT2.r10203_p3399_p4016
data17_13TeV.00329484.physics_Main.deriv.DAOD_EXOT2.r10203_p3399_p4016
data17_13TeV.00341294.physics_Main.deriv.DAOD_EXOT2.r10803_p3630_p4016

Continuation of Table A.5

Data container
data17_13TeV.00330166.physics_Main.deriv.DAOD_EXOT2.r10203_p3399_p4016
data17_13TeV.00335131.physics_Main.deriv.DAOD_EXOT2.r10258_p3399_p4016
data17_13TeV.00338377.physics_Main.deriv.DAOD_EXOT2.r10258_p3399_p4016
data17_13TeV.00331466.physics_Main.deriv.DAOD_EXOT2.r10203_p3399_p4016
data17_13TeV.00333487.physics_Main.deriv.DAOD_EXOT2.r10203_p3399_p4016
data17_13TeV.00337833.physics_Main.deriv.DAOD_EXOT2.r10258_p3399_p4016
data17_13TeV.00339070.physics_Main.deriv.DAOD_EXOT2.r10258_p3399_p4016
data17_13TeV.00339562.physics_Main.deriv.DAOD_EXOT2.r10258_p3399_p4016
data17_13TeV.00339758.physics_Main.deriv.DAOD_EXOT2.r10258_p3399_p4016
data17_13TeV.00340368.physics_Main.deriv.DAOD_EXOT2.r10426_p3399_p4016
data17_13TeV.00330470.physics_Main.deriv.DAOD_EXOT2.r10203_p3399_p4016
data17_13TeV.00337491.physics_Main.deriv.DAOD_EXOT2.r10259_p3399_p4016
data17_13TeV.00327745.physics_Main.deriv.DAOD_EXOT2.r10203_p3399_p4016
data17_13TeV.00331697.physics_Main.deriv.DAOD_EXOT2.r10203_p3399_p4016
data17_13TeV.00333192.physics_Main.deriv.DAOD_EXOT2.r10203_p3399_p4016
data17_13TeV.00330160.physics_Main.deriv.DAOD_EXOT2.r10203_p3399_p4016
data17_13TeV.00341419.physics_Main.deriv.DAOD_EXOT2.r10803_p3630_p4016
data17_13TeV.00336548.physics_Main.deriv.DAOD_EXOT2.r10259_p3399_p4016
data17_13TeV.00326468.physics_Main.deriv.DAOD_EXOT2.r10250_p3399_p4016
data17_13TeV.00332915.physics_Main.deriv.DAOD_EXOT2.r10203_p3399_p4016
data17_13TeV.00336630.physics_Main.deriv.DAOD_EXOT2.r10259_p3399_p4016
data17_13TeV.00336782.physics_Main.deriv.DAOD_EXOT2.r10258_p3399_p4016
data17_13TeV.00336852.physics_Main.deriv.DAOD_EXOT2.r10258_p3399_p4016
data17_13TeV.00337107.physics_Main.deriv.DAOD_EXOT2.r10258_p3399_p4016
data17_13TeV.00337542.physics_Main.deriv.DAOD_EXOT2.r10258_p3399_p4016
data17_13TeV.00338498.physics_Main.deriv.DAOD_EXOT2.r10258_p3399_p4016
data17_13TeV.00334890.physics_Main.deriv.DAOD_EXOT2.r10258_p3399_p4016
data17_13TeV.00329385.physics_Main.deriv.DAOD_EXOT2.r10202_p3399_p4016
data17_13TeV.00338675.physics_Main.deriv.DAOD_EXOT2.r10258_p3399_p4016
data17_13TeV.00340030.physics_Main.deriv.DAOD_EXOT2.r10426_p3399_p4016
data17_13TeV.00334384.physics_Main.deriv.DAOD_EXOT2.r10203_p3399_p4016
data17_13TeV.00332720.physics_Main.deriv.DAOD_EXOT2.r10202_p3399_p4016
data17_13TeV.00334710.physics_Main.deriv.DAOD_EXOT2.r10203_p3399_p4016
data17_13TeV.00335022.physics_Main.deriv.DAOD_EXOT2.r10258_p3399_p4016
data17_13TeV.00338608.physics_Main.deriv.DAOD_EXOT2.r10258_p3399_p4016
data17_13TeV.00328374.physics_Main.deriv.DAOD_EXOT2.r10203_p3399_p4016
data17_13TeV.00333469.physics_Main.deriv.DAOD_EXOT2.r10203_p3399_p4016
data17_13TeV.00339346.physics_Main.deriv.DAOD_EXOT2.r10258_p3399_p4016
data17_13TeV.00338220.physics_Main.deriv.DAOD_EXOT2.r10259_p3399_p4016
data17_13TeV.00339205.physics_Main.deriv.DAOD_EXOT2.r10258_p3399_p4016
data17_13TeV.00339849.physics_Main.deriv.DAOD_EXOT2.r10258_p3399_p4016
data17_13TeV.00340072.physics_Main.deriv.DAOD_EXOT2.r10426_p3399_p4016
data17_13TeV.00331129.physics_Main.deriv.DAOD_EXOT2.r10203_p3399_p4016

Continuation of Table A.5

Data container
data17_13TeV.00333828.physics_Main.deriv.DAOD_EXOT2.r10203_p3399_p4016
data17_13TeV.00334487.physics_Main.deriv.DAOD_EXOT2.r10203_p3399_p4016
data17_13TeV.00336719.physics_Main.deriv.DAOD_EXOT2.r10258_p3399_p4016
data17_13TeV.00339435.physics_Main.deriv.DAOD_EXOT2.r10258_p3399_p4016
data17_13TeV.00330294.physics_Main.deriv.DAOD_EXOT2.r10203_p3399_p4016
data17_13TeV.00338349.physics_Main.deriv.DAOD_EXOT2.r10258_p3399_p4016
data17_13TeV.00337176.physics_Main.deriv.DAOD_EXOT2.r10258_p3399_p4016
data17_13TeV.00337005.physics_Main.deriv.DAOD_EXOT2.r10258_p3399_p4016
data17_13TeV.00329780.physics_Main.deriv.DAOD_EXOT2.r10203_p3399_p4016
data17_13TeV.00334564.physics_Main.deriv.DAOD_EXOT2.r10203_p3399_p4016
data17_13TeV.00331019.physics_Main.deriv.DAOD_EXOT2.r10203_p3399_p4016
data17_13TeV.00335056.physics_Main.deriv.DAOD_EXOT2.r10258_p3399_p4016
data17_13TeV.00329716.physics_Main.deriv.DAOD_EXOT2.r10203_p3399_p4016
data17_13TeV.00331772.physics_Main.deriv.DAOD_EXOT2.r10203_p3399_p4016
data17_13TeV.00338834.physics_Main.deriv.DAOD_EXOT2.r10258_p3399_p4016
data17_13TeV.00328017.physics_Main.deriv.DAOD_EXOT2.r10203_p3399_p4016
data17_13TeV.00329835.physics_Main.deriv.DAOD_EXOT2.r10203_p3399_p4016
data17_13TeV.00331239.physics_Main.deriv.DAOD_EXOT2.r10203_p3399_p4016
data17_13TeV.00333994.physics_Main.deriv.DAOD_EXOT2.r10203_p3399_p4016
data17_13TeV.00335083.physics_Main.deriv.DAOD_EXOT2.r10258_p3399_p4016
data17_13TeV.00339957.physics_Main.deriv.DAOD_EXOT2.r10258_p3399_p4016
data17_13TeV.00339037.physics_Main.deriv.DAOD_EXOT2.r10258_p3399_p4016
data17_13TeV.00330074.physics_Main.deriv.DAOD_EXOT2.r10203_p3399_p4016
data17_13TeV.00333979.physics_Main.deriv.DAOD_EXOT2.r10203_p3399_p4016
data17_13TeV.00334350.physics_Main.deriv.DAOD_EXOT2.r10203_p3399_p4016
data17_13TeV.00334960.physics_Main.deriv.DAOD_EXOT2.r10258_p3399_p4016
data17_13TeV.00335170.physics_Main.deriv.DAOD_EXOT2.r10258_p3399_p4016
data17_13TeV.00335177.physics_Main.deriv.DAOD_EXOT2.r10258_p3399_p4016
data17_13TeV.00338712.physics_Main.deriv.DAOD_EXOT2.r10258_p3399_p4016
data17_13TeV.00339500.physics_Main.deriv.DAOD_EXOT2.r10258_p3399_p4016
data17_13TeV.00341615.physics_Main.deriv.DAOD_EXOT2.r10803_p3630_p4016
data17_13TeV.00329964.physics_Main.deriv.DAOD_EXOT2.r10203_p3399_p4016
data17_13TeV.00331975.physics_Main.deriv.DAOD_EXOT2.r10203_p3399_p4016
data17_13TeV.00334878.physics_Main.deriv.DAOD_EXOT2.r10259_p3399_p4016
data17_13TeV.00327636.physics_Main.deriv.DAOD_EXOT2.r10203_p3399_p4016
data17_13TeV.00327582.physics_Main.deriv.DAOD_EXOT2.r10203_p3399_p4016
data17_13TeV.00336497.physics_Main.deriv.DAOD_EXOT2.r10258_p3399_p4016
data17_13TeV.00336505.physics_Main.deriv.DAOD_EXOT2.r10258_p3399_p4016
data17_13TeV.00333519.physics_Main.deriv.DAOD_EXOT2.r10203_p3399_p4016
data17_13TeV.00336678.physics_Main.deriv.DAOD_EXOT2.r10258_p3399_p4016
data17_13TeV.00338259.physics_Main.deriv.DAOD_EXOT2.r10258_p3399_p4016
data17_13TeV.00338846.physics_Main.deriv.DAOD_EXOT2.r10250_p3399_p4016
data17_13TeV.00328263.physics_Main.deriv.DAOD_EXOT2.r10203_p3399_p4016

Continuation of Table A.5

Data container
data17_13TeV.00332896.physics_Main.deriv.DAOD_EXOT2.r10203_p3399_p4016
data17_13TeV.00334443.physics_Main.deriv.DAOD_EXOT2.r10203_p3399_p4016
data17_13TeV.00337662.physics_Main.deriv.DAOD_EXOT2.r10258_p3399_p4016
data17_13TeV.00339590.physics_Main.deriv.DAOD_EXOT2.r10258_p3399_p4016
data17_13TeV.00330025.physics_Main.deriv.DAOD_EXOT2.r10203_p3399_p4016
data17_13TeV.00331710.physics_Main.deriv.DAOD_EXOT2.r10203_p3399_p4016
data17_13TeV.00334993.physics_Main.deriv.DAOD_EXOT2.r10259_p3399_p4016
data17_13TeV.00338767.physics_Main.deriv.DAOD_EXOT2.r10258_p3399_p4016
data17_13TeV.00337215.physics_Main.deriv.DAOD_EXOT2.r10258_p3399_p4016
data17_13TeV.00334588.physics_Main.deriv.DAOD_EXOT2.r10203_p3399_p4016
data17_13TeV.00334637.physics_Main.deriv.DAOD_EXOT2.r10203_p3399_p4016
data17_13TeV.00337263.physics_Main.deriv.DAOD_EXOT2.r10258_p3399_p4016
data17_13TeV.00338263.physics_Main.deriv.DAOD_EXOT2.r10258_p3399_p4016
data17_13TeV.00326945.physics_Main.deriv.DAOD_EXOT2.r10250_p3399_p4016
data17_13TeV.00331033.physics_Main.deriv.DAOD_EXOT2.r10203_p3399_p4016
data17_13TeV.00338933.physics_Main.deriv.DAOD_EXOT2.r10258_p3399_p4016
data17_13TeV.00339387.physics_Main.deriv.DAOD_EXOT2.r10259_p3399_p4016
data17_13TeV.00327490.physics_Main.deriv.DAOD_EXOT2.r10203_p3399_p4016
data17_13TeV.00329542.physics_Main.deriv.DAOD_EXOT2.r10203_p3399_p4016
data17_13TeV.00329869.physics_Main.deriv.DAOD_EXOT2.r10203_p3399_p4016
data17_13TeV.00331085.physics_Main.deriv.DAOD_EXOT2.r10203_p3399_p4016
data17_13TeV.00331951.physics_Main.deriv.DAOD_EXOT2.r10203_p3399_p4016
data17_13TeV.00332303.physics_Main.deriv.DAOD_EXOT2.r11379_p3825_p4016
data17_13TeV.00335290.physics_Main.deriv.DAOD_EXOT2.r10258_p3399_p4016
data17_13TeV.00337335.physics_Main.deriv.DAOD_EXOT2.r10258_p3399_p4016
data17_13TeV.00331479.physics_Main.deriv.DAOD_EXOT2.r10203_p3399_p4016
data17_13TeV.00337705.physics_Main.deriv.DAOD_EXOT2.r10258_p3399_p4016
data17_13TeV.00327764.physics_Main.deriv.DAOD_EXOT2.r10203_p3399_p4016
data17_13TeV.00337404.physics_Main.deriv.DAOD_EXOT2.r10258_p3399_p4016
data17_13TeV.00330203.physics_Main.deriv.DAOD_EXOT2.r10203_p3399_p4016
data17_13TeV.00327103.physics_Main.deriv.DAOD_EXOT2.r10250_p3399_p4016
data17_13TeV.00331905.physics_Main.deriv.DAOD_EXOT2.r10203_p3399_p4016
data17_13TeV.00333426.physics_Main.deriv.DAOD_EXOT2.r10203_p3399_p4016
data17_13TeV.00331082.physics_Main.deriv.DAOD_EXOT2.r10203_p3399_p4016
data17_13TeV.00334264.physics_Main.deriv.DAOD_EXOT2.r10203_p3399_p4016
data17_13TeV.00331875.physics_Main.deriv.DAOD_EXOT2.r10203_p3399_p4016
data17_13TeV.00330101.physics_Main.deriv.DAOD_EXOT2.r10203_p3399_p4016
data17_13TeV.00325713.physics_Main.deriv.DAOD_EXOT2.r10260_p3399_p4016
data17_13TeV.00334907.physics_Main.deriv.DAOD_EXOT2.r10258_p3399_p4016
data17_13TeV.00341312.physics_Main.deriv.DAOD_EXOT2.r10803_p3630_p4016
data17_13TeV.00335082.physics_Main.deriv.DAOD_EXOT2.r10258_p3399_p4016
data17_13TeV.00330874.physics_Main.deriv.DAOD_EXOT2.r10203_p3399_p4016
data17_13TeV.00327265.physics_Main.deriv.DAOD_EXOT2.r10250_p3399_p4016

Continuation of Table A.5

Data container
data17_13TeV.00328393.physics_Main.deriv.DAOD_EXOT2.r10203_p3399_p4016
data17_13TeV.00332953.physics_Main.deriv.DAOD_EXOT2.r10203_p3399_p4016
data17_13TeV.00333650.physics_Main.deriv.DAOD_EXOT2.r10203_p3399_p4016
data17_13TeV.00333853.physics_Main.deriv.DAOD_EXOT2.r10203_p3399_p4016
data17_13TeV.00334580.physics_Main.deriv.DAOD_EXOT2.r10203_p3399_p4016
data17_13TeV.00334849.physics_Main.deriv.DAOD_EXOT2.r10258_p3399_p4016
data17_13TeV.00336567.physics_Main.deriv.DAOD_EXOT2.r10258_p3399_p4016
data17_13TeV.00336915.physics_Main.deriv.DAOD_EXOT2.r10258_p3399_p4016
data17_13TeV.00338183.physics_Main.deriv.DAOD_EXOT2.r10258_p3399_p4016
data17_13TeV.00333181.physics_Main.deriv.DAOD_EXOT2.r10203_p3399_p4016
data17_13TeV.00330875.physics_Main.deriv.DAOD_EXOT2.r10203_p3399_p4016
data17_13TeV.00333380.physics_Main.deriv.DAOD_EXOT2.r11379_p3825_p4016
data17_13TeV.00333904.physics_Main.deriv.DAOD_EXOT2.r10203_p3399_p4016
data17_13TeV.00334779.physics_Main.deriv.DAOD_EXOT2.r10203_p3399_p4016
data17_13TeV.00333778.physics_Main.deriv.DAOD_EXOT2.r10203_p3399_p4016
data17_13TeV.00336832.physics_Main.deriv.DAOD_EXOT2.r10259_p3399_p4016
data17_13TeV.00336944.physics_Main.deriv.DAOD_EXOT2.r10258_p3399_p4016
data17_13TeV.00337052.physics_Main.deriv.DAOD_EXOT2.r10258_p3399_p4016
data17_13TeV.00337451.physics_Main.deriv.DAOD_EXOT2.r10258_p3399_p4016
data17_13TeV.00338480.physics_Main.deriv.DAOD_EXOT2.r10258_p3399_p4016
data17_13TeV.00341649.physics_Main.deriv.DAOD_EXOT2.r10803_p3630_p4016
data17_13TeV.00329778.physics_Main.deriv.DAOD_EXOT2.r10203_p3399_p4016
data17_13TeV.00330079.physics_Main.deriv.DAOD_EXOT2.r10203_p3399_p4016
data17_13TeV.00332955.physics_Main.deriv.DAOD_EXOT2.r10203_p3399_p4016
data17_13TeV.00334455.physics_Main.deriv.DAOD_EXOT2.r10203_p3399_p4016
data17_13TeV.00334678.physics_Main.deriv.DAOD_EXOT2.r10203_p3399_p4016
data17_13TeV.00336927.physics_Main.deriv.DAOD_EXOT2.r10258_p3399_p4016
data17_13TeV.00338987.physics_Main.deriv.DAOD_EXOT2.r10258_p3399_p4016
data17_13TeV.00339396.physics_Main.deriv.DAOD_EXOT2.r10258_p3399_p4016
data17_13TeV.00341534.physics_Main.deriv.DAOD_EXOT2.r10803_p3630_p4016
data17_13TeV.00327860.physics_Main.deriv.DAOD_EXOT2.r10203_p3399_p4016
data17_13TeV.00329829.physics_Main.deriv.DAOD_EXOT2.r10203_p3399_p4016
data17_13TeV.00330857.physics_Main.deriv.DAOD_EXOT2.r10202_p3399_p4016
data17_13TeV.00335282.physics_Main.deriv.DAOD_EXOT2.r10258_p3399_p4016
data17_13TeV.00337371.physics_Main.deriv.DAOD_EXOT2.r10258_p3399_p4016
data17_13TeV.00327342.physics_Main.deriv.DAOD_EXOT2.r10203_p3399_p4016
data17_13TeV.00327662.physics_Main.deriv.DAOD_EXOT2.r10203_p3399_p4016
data17_13TeV.00331462.physics_Main.deriv.DAOD_EXOT2.r10203_p3399_p4016
data17_13TeV.00333707.physics_Main.deriv.DAOD_EXOT2.r10203_p3399_p4016
data17_13TeV.00327761.physics_Main.deriv.DAOD_EXOT2.r10203_p3399_p4016
data17_13TeV.00327862.physics_Main.deriv.DAOD_EXOT2.r10203_p3399_p4016
data17_13TeV.00328099.physics_Main.deriv.DAOD_EXOT2.r10203_p3399_p4016
data17_13TeV.00328333.physics_Main.deriv.DAOD_EXOT2.r10203_p3399_p4016

Continuation of Table A.5
Data container
data17_13TeV.00331742.physics_Main.deriv.DAOD_EXOT2.r10203_p3399_p4016
data17_13TeV.00331804.physics_Main.deriv.DAOD_EXOT2.r10203_p3399_p4016
data17_13TeV.00331825.physics_Main.deriv.DAOD_EXOT2.r10203_p3399_p4016
data17_13TeV.00332304.physics_Main.deriv.DAOD_EXOT2.r10203_p3399_p4016
data17_13TeV.00334737.physics_Main.deriv.DAOD_EXOT2.r10203_p3399_p4016
data17_13TeV.00334842.physics_Main.deriv.DAOD_EXOT2.r10258_p3399_p4016
data17_13TeV.00335016.physics_Main.deriv.DAOD_EXOT2.r10258_p3399_p4016
data17_13TeV.00335222.physics_Main.deriv.DAOD_EXOT2.r10258_p3399_p4016
data17_13TeV.00336998.physics_Main.deriv.DAOD_EXOT2.r10258_p3399_p4016
data17_13TeV.00337156.physics_Main.deriv.DAOD_EXOT2.r10258_p3399_p4016
data17_13TeV.00340453.physics_Main.deriv.DAOD_EXOT2.r10426_p3399_p4016
data17_13TeV.00331215.physics_Main.deriv.DAOD_EXOT2.r10203_p3399_p4016
data17_13TeV.00331860.physics_Main.deriv.DAOD_EXOT2.r10203_p3399_p4016
data17_13TeV.00336506.physics_Main.deriv.DAOD_EXOT2.r10258_p3399_p4016
data17_13TeV.00338967.physics_Main.deriv.DAOD_EXOT2.r10258_p3399_p4016
data17_13TeV.00339535.physics_Main.deriv.DAOD_EXOT2.r10258_p3399_p4016
End of Table A.5

Table A.6: Data containers of 2018.

Begin of Table
Data container
data18_13TeV.00356250.physics_Main.deriv.DAOD_EXOT2.f956_m2004_p4016
data18_13TeV.00359678.physics_Main.deriv.DAOD_EXOT2.f964_m2020_p4016
data18_13TeV.00349534.physics_Main.deriv.DAOD_EXOT2.f937_m1972_p4016
data18_13TeV.00354893.physics_Main.deriv.DAOD_EXOT2.f947_m1993_p4016
data18_13TeV.00351160.physics_Main.deriv.DAOD_EXOT2.f937_m1972_p4016
data18_13TeV.00354476.physics_Main.deriv.DAOD_EXOT2.f947_m1993_p4016
data18_13TeV.00354359.physics_Main.deriv.DAOD_EXOT2.f947_m1993_p4016
data18_13TeV.00357500.physics_Main.deriv.DAOD_EXOT2.f958_m2010_p4016
data18_13TeV.00358325.physics_Main.deriv.DAOD_EXOT2.f961_m2015_p4016
data18_13TeV.00355848.physics_Main.deriv.DAOD_EXOT2.f950_m1999_p4016
data18_13TeV.00355995.physics_Main.deriv.DAOD_EXOT2.f950_m2004_p4016
data18_13TeV.00357821.physics_Main.deriv.DAOD_EXOT2.f961_m2015_p4016
data18_13TeV.00357887.physics_Main.deriv.DAOD_EXOT2.f961_m2015_p4016
data18_13TeV.00348894.physics_Main.deriv.DAOD_EXOT2.f937_m1972_p4016
data18_13TeV.00360244.physics_Main.deriv.DAOD_EXOT2.f969_m2020_p4016
data18_13TeV.00351832.physics_Main.deriv.DAOD_EXOT2.f938_m1979_p4016
data18_13TeV.00355008.physics_Main.deriv.DAOD_EXOT2.f943_m1993_p4016
data18_13TeV.00350431.physics_Main.deriv.DAOD_EXOT2.f934_m1960_p4016
data18_13TeV.00351062.physics_Main.deriv.DAOD_EXOT2.f937_m1972_p4016
data18_13TeV.00356205.physics_Main.deriv.DAOD_EXOT2.f956_m2004_p4016

Continuation of Table A.6

Data container
data18_13TeV.00358333.physics_Main.deriv.DAOD_EXOT2.f961_m2015_p4016
data18_13TeV.00359766.physics_Main.deriv.DAOD_EXOT2.f964_m2020_p4016
data18_13TeV.00355563.physics_Main.deriv.DAOD_EXOT2.f950_m1999_p4016
data18_13TeV.00356177.physics_Main.deriv.DAOD_EXOT2.f956_m2004_p4016
data18_13TeV.00357077.physics_Main.deriv.DAOD_EXOT2.f956_m2004_p4016
data18_13TeV.00358215.physics_Main.deriv.DAOD_EXOT2.f966_m2020_p4016
data18_13TeV.00350803.physics_Main.deriv.DAOD_EXOT2.f936_m1972_p4016
data18_13TeV.00355599.physics_Main.deriv.DAOD_EXOT2.f950_m1999_p4016
data18_13TeV.00355651.physics_Main.deriv.DAOD_EXOT2.f950_m1999_p4016
data18_13TeV.00357772.physics_Main.deriv.DAOD_EXOT2.f958_m2015_p4016
data18_13TeV.00359124.physics_Main.deriv.DAOD_EXOT2.f964_m2020_p4016
data18_13TeV.00359286.physics_Main.deriv.DAOD_EXOT2.f964_m2020_p4016
data18_13TeV.00355861.physics_Main.deriv.DAOD_EXOT2.f950_m2004_p4016
data18_13TeV.00359677.physics_Main.deriv.DAOD_EXOT2.f964_m2020_p4016
data18_13TeV.00360373.physics_Main.deriv.DAOD_EXOT2.f969_m2020_p4016
data18_13TeV.00352137.physics_Main.deriv.DAOD_EXOT2.f938_m1979_p4016
data18_13TeV.00358175.physics_Main.deriv.DAOD_EXOT2.f966_m2020_p4016
data18_13TeV.00360414.physics_Main.deriv.DAOD_EXOT2.f971_m2020_p4016
data18_13TeV.00359593.physics_Main.deriv.DAOD_EXOT2.f964_m2020_p4016
data18_13TeV.00359472.physics_Main.deriv.DAOD_EXOT2.f964_m2020_p4016
data18_13TeV.00362354.physics_Main.deriv.DAOD_EXOT2.f993_m2032_p4016
data18_13TeV.00355529.physics_Main.deriv.DAOD_EXOT2.f948_m1999_p4016
data18_13TeV.00358096.physics_Main.deriv.DAOD_EXOT2.f966_m2020_p4016
data18_13TeV.00359171.physics_Main.deriv.DAOD_EXOT2.f964_m2020_p4016
data18_13TeV.00359872.physics_Main.deriv.DAOD_EXOT2.f969_m2020_p4016
data18_13TeV.00361689.physics_Main.deriv.DAOD_EXOT2.f979_m2025_p4016
data18_13TeV.00354311.physics_Main.deriv.DAOD_EXOT2.f947_m1993_p4016
data18_13TeV.00357750.physics_Main.deriv.DAOD_EXOT2.f958_m2015_p4016
data18_13TeV.00359735.physics_Main.deriv.DAOD_EXOT2.f964_m2020_p4016
data18_13TeV.00360348.physics_Main.deriv.DAOD_EXOT2.f969_m2020_p4016
data18_13TeV.00361795.physics_Main.deriv.DAOD_EXOT2.f988_m2025_p4016
data18_13TeV.00359191.physics_Main.deriv.DAOD_EXOT2.f964_m2020_p4016
data18_13TeV.00352340.physics_Main.deriv.DAOD_EXOT2.f938_m1979_p4016
data18_13TeV.00357539.physics_Main.deriv.DAOD_EXOT2.f958_m2010_p4016
data18_13TeV.00357679.physics_Main.deriv.DAOD_EXOT2.f958_m2015_p4016
data18_13TeV.00358395.physics_Main.deriv.DAOD_EXOT2.f961_m2015_p4016
data18_13TeV.00358577.physics_Main.deriv.DAOD_EXOT2.f961_m2015_p4016
data18_13TeV.00359058.physics_Main.deriv.DAOD_EXOT2.f964_m2020_p4016
data18_13TeV.00360293.physics_Main.deriv.DAOD_EXOT2.f969_m2020_p4016
data18_13TeV.00361635.physics_Main.deriv.DAOD_EXOT2.f979_m2025_p4016
data18_13TeV.00354176.physics_Main.deriv.DAOD_EXOT2.f947_m1993_p4016
data18_13TeV.00356259.physics_Main.deriv.DAOD_EXOT2.f956_m2004_p4016
data18_13TeV.00359623.physics_Main.deriv.DAOD_EXOT2.f964_m2020_p4016

Continuation of Table A.6

Data container
data18_13TeV.00359717.physics_Main.deriv.DAOD_EXOT2.f964_m2020_p4016
data18_13TeV.00354826.physics_Main.deriv.DAOD_EXOT2.f947_m1993_p4016
data18_13TeV.00364292.physics_Main.deriv.DAOD_EXOT2.f1002_m2037_p4016
data18_13TeV.00352107.physics_Main.deriv.DAOD_EXOT2.f938_m1979_p4016
data18_13TeV.00355109.physics_Main.deriv.DAOD_EXOT2.f943_m1993_p4016
data18_13TeV.00355273.physics_Main.deriv.DAOD_EXOT2.f943_m1993_p4016
data18_13TeV.00363910.physics_Main.deriv.DAOD_EXOT2.f1002_m2037_p4016
data18_13TeV.00349582.physics_Main.deriv.DAOD_EXOT2.f937_m1972_p4016
data18_13TeV.00349841.physics_Main.deriv.DAOD_EXOT2.f937_m1979_p4016
data18_13TeV.00354494.physics_Main.deriv.DAOD_EXOT2.f947_m1993_p4016
data18_13TeV.00355181.physics_Main.deriv.DAOD_EXOT2.f943_m1993_p4016
data18_13TeV.00364098.physics_Main.deriv.DAOD_EXOT2.f1002_m2037_p4016
data18_13TeV.00360063.physics_Main.deriv.DAOD_EXOT2.f969_m2020_p4016
data18_13TeV.00352123.physics_Main.deriv.DAOD_EXOT2.f938_m1979_p4016
data18_13TeV.00352274.physics_Main.deriv.DAOD_EXOT2.f938_m1979_p4016
data18_13TeV.00359586.physics_Main.deriv.DAOD_EXOT2.f964_m2020_p4016
data18_13TeV.00349944.physics_Main.deriv.DAOD_EXOT2.f933_m1960_p4016
data18_13TeV.00350144.physics_Main.deriv.DAOD_EXOT2.f933_m1960_p4016
data18_13TeV.00351550.physics_Main.deriv.DAOD_EXOT2.f937_m1972_p4016
data18_13TeV.00354309.physics_Main.deriv.DAOD_EXOT2.f947_m1993_p4016
data18_13TeV.00354315.physics_Main.deriv.DAOD_EXOT2.f947_m1993_p4016
data18_13TeV.00354396.physics_Main.deriv.DAOD_EXOT2.f947_m1993_p4016
data18_13TeV.00359541.physics_Main.deriv.DAOD_EXOT2.f964_m2020_p4016
data18_13TeV.00360309.physics_Main.deriv.DAOD_EXOT2.f969_m2020_p4016
data18_13TeV.00358233.physics_Main.deriv.DAOD_EXOT2.f961_m2015_p4016
data18_13TeV.00362345.physics_Main.deriv.DAOD_EXOT2.f988_m2032_p4016
data18_13TeV.00358300.physics_Main.deriv.DAOD_EXOT2.f966_m2020_p4016
data18_13TeV.00360209.physics_Main.deriv.DAOD_EXOT2.f969_m2020_p4016
data18_13TeV.00355650.physics_Main.deriv.DAOD_EXOT2.f950_m1999_p4016
data18_13TeV.00358516.physics_Main.deriv.DAOD_EXOT2.f961_m2015_p4016
data18_13TeV.00359310.physics_Main.deriv.DAOD_EXOT2.f964_m2020_p4016
data18_13TeV.00359398.physics_Main.deriv.DAOD_EXOT2.f964_m2020_p4016
data18_13TeV.00360161.physics_Main.deriv.DAOD_EXOT2.f969_m2020_p4016
data18_13TeV.00361696.physics_Main.deriv.DAOD_EXOT2.f979_m2025_p4016
data18_13TeV.00359823.physics_Main.deriv.DAOD_EXOT2.f964_m2020_p4016
data18_13TeV.00349842.physics_Main.deriv.DAOD_EXOT2.f937_m1979_p4016
data18_13TeV.00355053.physics_Main.deriv.DAOD_EXOT2.f943_m1993_p4016
data18_13TeV.00361690.physics_Main.deriv.DAOD_EXOT2.f979_m2025_p4016
data18_13TeV.00357355.physics_Main.deriv.DAOD_EXOT2.f960_m2015_p4016
data18_13TeV.00358615.physics_Main.deriv.DAOD_EXOT2.f961_m2020_p4016
data18_13TeV.00355544.physics_Main.deriv.DAOD_EXOT2.f950_m1999_p4016
data18_13TeV.00356124.physics_Main.deriv.DAOD_EXOT2.f950_m2004_p4016
data18_13TeV.00357451.physics_Main.deriv.DAOD_EXOT2.f958_m2010_p4016

Continuation of Table A.6

Data container
data18_13TeV.00359010.physics_Main.deriv.DAOD_EXOT2.f964_m2020_p4016
data18_13TeV.00359918.physics_Main.deriv.DAOD_EXOT2.f969_m2020_p4016
data18_13TeV.00357620.physics_Main.deriv.DAOD_EXOT2.f958_m2010_p4016
data18_13TeV.00358656.physics_Main.deriv.DAOD_EXOT2.f961_m2020_p4016
data18_13TeV.00358985.physics_Main.deriv.DAOD_EXOT2.f964_m2020_p4016
data18_13TeV.00358115.physics_Main.deriv.DAOD_EXOT2.f966_m2020_p4016
data18_13TeV.00359279.physics_Main.deriv.DAOD_EXOT2.f964_m2020_p4016
data18_13TeV.00359441.physics_Main.deriv.DAOD_EXOT2.f964_m2020_p4016
data18_13TeV.00360129.physics_Main.deriv.DAOD_EXOT2.f969_m2020_p4016
data18_13TeV.00357409.physics_Main.deriv.DAOD_EXOT2.f958_m2010_p4016
data18_13TeV.00357713.physics_Main.deriv.DAOD_EXOT2.f958_m2015_p4016
data18_13TeV.00357962.physics_Main.deriv.DAOD_EXOT2.f961_m2015_p4016
data18_13TeV.00351364.physics_Main.deriv.DAOD_EXOT2.f937_m1972_p4016
data18_13TeV.00351455.physics_Main.deriv.DAOD_EXOT2.f937_m1972_p4016
data18_13TeV.00351636.physics_Main.deriv.DAOD_EXOT2.f938_m1979_p4016
data18_13TeV.00351671.physics_Main.deriv.DAOD_EXOT2.f938_m1979_p4016
data18_13TeV.00351698.physics_Main.deriv.DAOD_EXOT2.f938_m1979_p4016
data18_13TeV.00351969.physics_Main.deriv.DAOD_EXOT2.f938_m1979_p4016
data18_13TeV.00354174.physics_Main.deriv.DAOD_EXOT2.f947_m1993_p4016
data18_13TeV.00354863.physics_Main.deriv.DAOD_EXOT2.f947_m1993_p4016
data18_13TeV.00354944.physics_Main.deriv.DAOD_EXOT2.f947_m1993_p4016
data18_13TeV.00355261.physics_Main.deriv.DAOD_EXOT2.f943_m1993_p4016
data18_13TeV.00355331.physics_Main.deriv.DAOD_EXOT2.f948_m1993_p4016
data18_13TeV.00355389.physics_Main.deriv.DAOD_EXOT2.f948_m1993_p4016
data18_13TeV.00355416.physics_Main.deriv.DAOD_EXOT2.f948_m1993_p4016
data18_13TeV.00355468.physics_Main.deriv.DAOD_EXOT2.f948_m1993_p4016
data18_13TeV.00363710.physics_Main.deriv.DAOD_EXOT2.f1001_m2037_p4016
data18_13TeV.00363738.physics_Main.deriv.DAOD_EXOT2.f1006_m2037_p4016
data18_13TeV.00363830.physics_Main.deriv.DAOD_EXOT2.f1002_m2037_p4016
data18_13TeV.00363979.physics_Main.deriv.DAOD_EXOT2.f1002_m2037_p4016
data18_13TeV.00364030.physics_Main.deriv.DAOD_EXOT2.f1002_m2037_p4016
data18_13TeV.00364160.physics_Main.deriv.DAOD_EXOT2.f1002_m2037_p4016
data18_13TeV.00364214.physics_Main.deriv.DAOD_EXOT2.f1002_m2037_p4016
data18_13TeV.00351223.physics_Main.deriv.DAOD_EXOT2.f937_m1972_p4016
data18_13TeV.00348895.physics_Main.deriv.DAOD_EXOT2.f937_m1972_p4016
data18_13TeV.00349011.physics_Main.deriv.DAOD_EXOT2.f937_m1972_p4016
data18_13TeV.00349014.physics_Main.deriv.DAOD_EXOT2.f937_m1972_p4016
data18_13TeV.00349033.physics_Main.deriv.DAOD_EXOT2.f937_m1972_p4016
data18_13TeV.00349051.physics_Main.deriv.DAOD_EXOT2.f937_m1972_p4016
data18_13TeV.00349111.physics_Main.deriv.DAOD_EXOT2.f937_m1972_p4016
data18_13TeV.00349263.physics_Main.deriv.DAOD_EXOT2.f937_m1972_p4016
data18_13TeV.00349268.physics_Main.deriv.DAOD_EXOT2.f937_m1972_p4016
data18_13TeV.00349309.physics_Main.deriv.DAOD_EXOT2.f937_m1972_p4016

Continuation of Table A.6

Data container
data18_13TeV.00349637.physics_Main.deriv.DAOD_EXOT2.f937_m1979_p4016
data18_13TeV.00350184.physics_Main.deriv.DAOD_EXOT2.f934_m1960_p4016
data18_13TeV.00351628.physics_Main.deriv.DAOD_EXOT2.f937_m1972_p4016
data18_13TeV.00351894.physics_Main.deriv.DAOD_EXOT2.f938_m1979_p4016
data18_13TeV.00352394.physics_Main.deriv.DAOD_EXOT2.f938_m1979_p4016
data18_13TeV.00362204.physics_Main.deriv.DAOD_EXOT2.f988_m2032_p4016
data18_13TeV.00363664.physics_Main.deriv.DAOD_EXOT2.f1001_m2037_p4016
data18_13TeV.00349327.physics_Main.deriv.DAOD_EXOT2.f937_m1972_p4016
data18_13TeV.00362661.physics_Main.deriv.DAOD_EXOT2.f993_m2032_p4016
data18_13TeV.00363198.physics_Main.deriv.DAOD_EXOT2.f997_m2032_p4016
data18_13TeV.00350440.physics_Main.deriv.DAOD_EXOT2.f934_m1960_p4016
data18_13TeV.00349335.physics_Main.deriv.DAOD_EXOT2.f937_m1972_p4016
data18_13TeV.00349498.physics_Main.deriv.DAOD_EXOT2.f937_m1972_p4016
data18_13TeV.00349526.physics_Main.deriv.DAOD_EXOT2.f937_m1972_p4016
data18_13TeV.00352514.physics_Main.deriv.DAOD_EXOT2.f938_m1979_p4016
data18_13TeV.00362445.physics_Main.deriv.DAOD_EXOT2.f993_m2032_p4016
data18_13TeV.00362619.physics_Main.deriv.DAOD_EXOT2.f993_m2032_p4016
data18_13TeV.00362776.physics_Main.deriv.DAOD_EXOT2.f993_m2032_p4016
data18_13TeV.00363400.physics_Main.deriv.DAOD_EXOT2.f997_m2032_p4016
data18_13TeV.00361862.physics_Main.deriv.DAOD_EXOT2.f988_m2025_p4016
data18_13TeV.00362297.physics_Main.deriv.DAOD_EXOT2.f988_m2032_p4016
data18_13TeV.00349169.physics_Main.deriv.DAOD_EXOT2.f937_m1972_p4016
data18_13TeV.00363262.physics_Main.deriv.DAOD_EXOT2.f997_m2032_p4016
data18_13TeV.00355754.physics_Main.deriv.DAOD_EXOT2.f950_m1999_p4016
data18_13TeV.00354124.physics_Main.deriv.DAOD_EXOT2.f947_m1993_p4016
data18_13TeV.00362388.physics_Main.deriv.DAOD_EXOT2.f993_m2032_p4016
data18_13TeV.00362552.physics_Main.deriv.DAOD_EXOT2.f993_m2032_p4016
data18_13TeV.00352436.physics_Main.deriv.DAOD_EXOT2.f938_m1979_p4016
data18_13TeV.00349533.physics_Main.deriv.DAOD_EXOT2.f937_m1972_p4016
data18_13TeV.00352494.physics_Main.deriv.DAOD_EXOT2.f938_m1979_p4016
data18_13TeV.00363033.physics_Main.deriv.DAOD_EXOT2.f993_m2032_p4016
data18_13TeV.00363129.physics_Main.deriv.DAOD_EXOT2.f993_m2032_p4016
data18_13TeV.00358541.physics_Main.deriv.DAOD_EXOT2.f961_m2015_p4016
data18_13TeV.00352056.physics_Main.deriv.DAOD_EXOT2.f938_m1979_p4016
data18_13TeV.00349451.physics_Main.deriv.DAOD_EXOT2.f937_m1972_p4016
data18_13TeV.00349481.physics_Main.deriv.DAOD_EXOT2.f937_m1972_p4016
data18_13TeV.00363096.physics_Main.deriv.DAOD_EXOT2.f1005_m2037_p4016
data18_13TeV.00349646.physics_Main.deriv.DAOD_EXOT2.f937_m1979_p4016
data18_13TeV.00349693.physics_Main.deriv.DAOD_EXOT2.f937_m1979_p4016
data18_13TeV.00349114.physics_Main.deriv.DAOD_EXOT2.f937_m1972_p4016
data18_13TeV.00352448.physics_Main.deriv.DAOD_EXOT2.f938_m1979_p4016
data18_13TeV.00349977.physics_Main.deriv.DAOD_EXOT2.f933_m1960_p4016
data18_13TeV.00350013.physics_Main.deriv.DAOD_EXOT2.f933_m1960_p4016

Continuation of Table A.6

Data container
data18_13TeV.00350067.physics_Main.deriv.DAOD_EXOT2.f933_m1960_p4016
data18_13TeV.00350121.physics_Main.deriv.DAOD_EXOT2.f933_m1960_p4016
data18_13TeV.00350160.physics_Main.deriv.DAOD_EXOT2.f934_m1960_p4016
data18_13TeV.00350220.physics_Main.deriv.DAOD_EXOT2.f934_m1960_p4016
data18_13TeV.00350310.physics_Main.deriv.DAOD_EXOT2.f934_m1960_p4016
data18_13TeV.00350361.physics_Main.deriv.DAOD_EXOT2.f934_m1960_p4016
data18_13TeV.00350479.physics_Main.deriv.DAOD_EXOT2.f934_m1960_p4016
data18_13TeV.00350531.physics_Main.deriv.DAOD_EXOT2.f934_m1960_p4016
data18_13TeV.00350682.physics_Main.deriv.DAOD_EXOT2.f936_m1972_p4016
data18_13TeV.00350749.physics_Main.deriv.DAOD_EXOT2.f936_m1972_p4016
data18_13TeV.00350751.physics_Main.deriv.DAOD_EXOT2.f936_m1972_p4016
data18_13TeV.00350842.physics_Main.deriv.DAOD_EXOT2.f936_m1972_p4016
data18_13TeV.00350848.physics_Main.deriv.DAOD_EXOT2.f936_m1972_p4016
data18_13TeV.00350880.physics_Main.deriv.DAOD_EXOT2.f937_m1972_p4016
data18_13TeV.00350923.physics_Main.deriv.DAOD_EXOT2.f937_m1972_p4016
data18_13TeV.00351296.physics_Main.deriv.DAOD_EXOT2.f937_m1972_p4016
data18_13TeV.00351325.physics_Main.deriv.DAOD_EXOT2.f937_m1972_p4016
data18_13TeV.00351359.physics_Main.deriv.DAOD_EXOT2.f937_m1972_p4016
data18_13TeV.00361738.physics_Main.deriv.DAOD_EXOT2.f988_m2025_p4016
data18_13TeV.00356095.physics_Main.deriv.DAOD_EXOT2.f950_m2004_p4016
data18_13TeV.00359170.physics_Main.deriv.DAOD_EXOT2.f964_m2020_p4016
data18_13TeV.00360402.physics_Main.deriv.DAOD_EXOT2.f969_m2020_p4016
data18_13TeV.00349592.physics_Main.deriv.DAOD_EXOT2.f937_m1972_p4016
data18_13TeV.00355224.physics_Main.deriv.DAOD_EXOT2.f943_m1993_p4016
data18_13TeV.00363947.physics_Main.deriv.DAOD_EXOT2.f1002_m2037_p4016
data18_13TeV.00364076.physics_Main.deriv.DAOD_EXOT2.f1002_m2037_p4016
data18_13TeV.00348885.physics_Main.deriv.DAOD_EXOT2.f937_m1972_p4016
data18_13TeV.00357193.physics_Main.deriv.DAOD_EXOT2.f958_m2010_p4016
data18_13TeV.00357293.physics_Main.deriv.DAOD_EXOT2.f958_m2010_p4016
data18_13TeV.00358031.physics_Main.deriv.DAOD_EXOT2.f961_m2015_p4016
data18_13TeV.00352131.physics_Main.deriv.DAOD_EXOT2.f938_m1979_p4016
data18_13TeV.00355877.physics_Main.deriv.DAOD_EXOT2.f950_m2004_p4016
data18_13TeV.00359355.physics_Main.deriv.DAOD_EXOT2.f964_m2020_p4016
data18_13TeV.00361695.physics_Main.deriv.DAOD_EXOT2.f979_m2025_p4016
data18_13TeV.00356077.physics_Main.deriv.DAOD_EXOT2.f950_m2004_p4016
data18_13TeV.00360026.physics_Main.deriv.DAOD_EXOT2.f969_m2020_p4016
data18_13TeV.00357283.physics_Main.deriv.DAOD_EXOT2.f958_m2010_p4016

End of Table A.6

Appendix B

Selections of simulated HQM samples

This appendix shows the selections of simulated HQM samples. They are obtained using the MC16a campaign. For quick access, the table indexes are listed in Table B.1.

Table B.1: Table indexes of HQM selections.

n	M_D [TeV]	Table index
2	7.0	4.4
	7.5	B.2
	8.0	B.3
	8.5	B.4
	9.0	B.5
	9.5	B.6
4	6.5	B.7
	7.0	B.8
	7.5	B.9
	8.0	B.10
	8.5	B.11
	9.0	B.12
6	5.5	B.13
	6.0	B.14
	6.5	B.15
	7.0	B.16
	7.5	B.17
	8.0	B.18

Table B.2: Selections of the HQM sample ($n = 2$, $M_D = 7.5$ TeV).

	Selection	Num. of Events	Rela. Decrease [%]	Cumulative Eff. [%]
Pre-selections	Init	20000.00	0.00	100.00
	Jet cleaning	19833.00	0.83	99.17
	NPV	19833.00	0.00	99.17
	Trigger (`HLT_j420 or HLT_j380`)	19297.00	2.70	96.48
	Jet select	17584.00	8.88	87.92
	Skimming	17584.00	0.00	87.92
Post-selections	`HLT_j420`	17503.00	0.46	87.52
	abs(y^*)< 1.7	16800.00	4.02	84.00
	abs(y_b)< 1.1	16315.00	2.89	81.58

Table B.3: Selections of the HQM sample ($n = 2$, $M_D = 8.0$ TeV).

	Selection	Num. of Events	Rela. Decrease [%]	Cumulative Eff. [%]
Pre-selections	Init	20000.00	0.00	100.00
	Jet cleaning	19836.00	0.82	99.18
	NPV	19836.00	0.00	99.18
	Trigger (`HLT_j420 or HLT_j380`)	19276.00	2.82	96.38
	Jet select	17483.00	9.30	87.41
	Skimming	17483.00	0.00	87.41
Post-selections	`HLT_j420`	17383.00	0.57	86.91
	abs(y^*)< 1.7	16723.00	3.80	83.61
	abs(y_b)< 1.1	16256.00	2.79	81.28

Table B.4: Selections of the HQM sample ($n = 2$, $M_D = 8.5$ TeV).

	Selection	Num. of Events	Rela. Decrease [%]	Cumulative Eff. [%]
Pre-selections	Init	20000.00	0.00	100.00
	Jet cleaning	19834.00	0.83	99.17
	NPV	19834.00	0.00	99.17
	Trigger (`HLT_j420 or HLT_j380`)	19293.00	2.73	96.47
	Jet select	17544.00	9.07	87.72
	Skimming	17544.00	0.00	87.72
Post-selections	`HLT_j420`	17453.00	0.52	87.27
	abs(y^*)< 1.7	16815.00	3.66	84.08
	abs(y_b)< 1.1	16353.00	2.75	81.77

Table B.5: Selections of the HQM sample ($n = 2$, $M_D = 9.0$ TeV).

	Selection	Num. of Events	Rela. Decrease [%]	Cumulative Eff. [%]
Pre-selections	Init	20000.00	0.00	100.00
	Jet cleaning	19832.00	0.84	99.16
	NPV	19832.00	0.00	99.16
	Trigger (`HLT_j420 or HLT_j380`)	19317.00	2.60	96.58
	Jet select	17516.00	9.32	87.58
	Skimming	17516.00	0.00	87.58
Post-selections	`HLT_j420`	17418.00	0.56	87.09
	abs(y^*)< 1.7	16722.00	4.00	83.61
	abs(y_b)< 1.1	16255.00	2.79	81.27

Table B.6: Selections of the HQM sample ($n = 2$, $M_D = 9.5$ TeV).

	Selection	Num. of Events	Rela. Decrease [%]	Cumulative Eff. [%]
Pre-selections	Init	20000.00	0.00	100.00
	Jet cleaning	19827.00	0.87	99.13
	NPV	19827.00	0.00	99.13
	Trigger (`HLT_j420 or HLT_j380`)	19349.00	2.41	96.75
	Jet select	17555.00	9.27	87.78
	Skimming	17555.00	0.00	87.78
Post-selections	`HLT_j420`	17468.00	0.50	87.34
	abs(y^*)< 1.7	16781.00	3.93	83.91
	abs(y_b)< 1.1	16311.00	2.80	81.56

Table B.7: Selections of the HQM sample ($n = 4$, $M_D = 6.5$ TeV).

	Selection	Num. of Events	Rela. Decrease [%]	Cumulative Eff. [%]
Pre-selections	Init	20000.00	0.00	100.00
	Jet cleaning	19813.00	0.93	99.06
	NPV	19813.00	0.00	99.06
	Trigger (`HLT_j420 or HLT_j380`)	19441.00	1.88	97.20
	Jet select	17556.00	9.70	87.78
	Skimming	17556.00	0.00	87.78
Post-selections	`HLT_j420`	17493.00	0.36	87.47
	abs(y^*)< 1.7	16757.00	4.21	83.78
	abs(y_b)< 1.1	16312.00	2.66	81.56

Table B.8: Selections of the HQM sample ($n = 4$, $M_D = 7.0$ TeV).

	Selection	Num. of Events	Rela. Decrease [%]	Cumulative Eff. [%]
Pre-selections	Init	20000.00	0.00	100.00
	Jet cleaning	19820.00	0.90	99.10
	NPV	19820.00	0.00	99.10
	Trigger (`HLT_j420 or HLT_j380`)	19457.00	1.83	97.28
	Jet select	17609.00	9.50	88.05
	Skimming	17609.00	0.00	88.05
Post-selections	`HLT_j420`	17551.00	0.33	87.76
	abs(y^*)< 1.7	16787.00	4.35	83.94
	abs(y_b)< 1.1	16338.00	2.67	81.69

Table B.9: Selections of the HQM sample ($n = 4$, $M_D = 7.5$ TeV).

	Selection	Num. of Events	Rela. Decrease [%]	Cumulative Eff. [%]
Pre-selections	Init	20000.00	0.00	100.00
	Jet cleaning	19799.00	1.01	99.00
	NPV	19799.00	0.00	99.00
	Trigger (`HLT_j420 or HLT_j380`)	19417.00	1.93	97.08
	Jet select	17685.00	8.92	88.42
	Skimming	17685.00	0.00	88.42
Post-selections	`HLT_j420`	17616.00	0.39	88.08
	abs(y^*)< 1.7	16890.00	4.12	84.45
	abs(y_b)< 1.1	16461.00	2.54	82.30

Table B.10: Selections of the HQM sample ($n = 4$, $M_D = 8.0$ TeV).

	Selection	Num. of Events	Rela. Decrease [%]	Cumulative Eff. [%]
Pre-selections	Init	20000.00	0.00	100.00
	Jet cleaning	19818.00	0.91	99.09
	NPV	19818.00	0.00	99.09
	Trigger (`HLT_j420 or HLT_j380`)	19440.00	1.91	97.20
	Jet select	17638.00	9.27	88.19
	Skimming	17638.00	0.00	88.19
Post-selections	`HLT_j420`	17593.00	0.26	87.97
	abs(y^*)< 1.7	16872.00	4.10	84.36
	abs(y_b)< 1.1	16441.00	2.55	82.20

Table B.11: Selections of the HQM sample ($n = 4$, $M_D = 8.5$ TeV).

	Selection	Num. of Events	Rela. Decrease [%]	Cumulative Eff. [%]
Pre-selections	Init	20000.00	0.00	100.00
	Jet cleaning	19795.00	1.02	98.98
	NPV	19795.00	0.00	98.98
	Trigger (`HLT_j420 or HLT_j380`)	19420.00	1.89	97.10
	Jet select	17591.00	9.42	87.96
	Skimming	17591.00	0.00	87.96
Post-selections	`HLT_j420`	17536.00	0.31	87.68
	abs(y^*)< 1.7	16720.00	4.65	83.60
	abs(y_b)< 1.1	16264.00	2.73	81.32

Table B.12: Selections of the HQM sample ($n = 4$, $M_D = 9.0$ TeV).

	Selection	Num. of Events	Rela. Decrease [%]	Cumulative Eff. [%]
Pre-selections	Init	20000.00	0.00	100.00
	Jet cleaning	19798.00	1.01	98.99
	NPV	19798.00	0.00	98.99
	Trigger (`HLT_j420 or HLT_j380`)	19432.00	1.85	97.16
	Jet select	17651.00	9.17	88.25
	Skimming	17651.00	0.00	88.25
Post-selections	`HLT_j420`	17585.00	0.37	87.92
	abs(y^*)< 1.7	16727.00	4.88	83.64
	abs(y_b)< 1.1	16331.00	2.37	81.66

Table B.13: Selections of the HQM sample ($n = 6$, $M_D = 5.5$ TeV).

	Selection	Num. of Events	Rela. Decrease [%]	Cumulative Eff. [%]
Pre-selections	Init	20000.00	0.00	100.00
	Jet cleaning	19794.00	1.03	98.97
	NPV	19794.00	0.00	98.97
	Trigger (`HLT_j420 or HLT_j380`)	19508.00	1.44	97.54
	Jet select	17713.00	9.20	88.56
	Skimming	17713.00	0.00	88.56
Post-selections	`HLT_j420`	17669.00	0.25	88.34
	abs(y^*)< 1.7	16851.00	4.63	84.25
	abs(y_b)< 1.1	16417.00	2.58	82.08

Table B.14: Selections of the HQM sample ($n = 6$, $M_D = 6.0$ TeV).

	Selection	Num. of Events	Rela. Decrease [%]	Cumulative Eff. [%]
Pre-selections	Init	20000.00	0.00	100.00
	Jet cleaning	19784.00	1.08	98.92
	NPV	19784.00	0.00	98.92
	Trigger (`HLT_j420 or HLT_j380`)	19490.00	1.49	97.45
	Jet select	17665.00	9.36	88.33
	Skimming	17665.00	0.00	88.33
Post-selections	`HLT_j420`	17619.00	0.26	88.09
	abs(y^*)< 1.7	16837.00	4.44	84.19
	abs(y_b)< 1.1	16487.00	2.08	82.44

Table B.15: Selections of the HQM sample ($n = 6$, $M_D = 6.5$ TeV).

	Selection	Num. of Events	Rela. Decrease [%]	Cumulative Eff. [%]
Pre-selections	Init	20000.00	0.00	100.00
	Jet cleaning	19797.00	1.01	98.98
	NPV	19797.00	0.00	98.98
	Trigger (`HLT_j420 or HLT_j380`)	19505.00	1.47	97.52
	Jet select	17769.00	8.90	88.84
	Skimming	17769.00	0.00	88.84
Post-selections	`HLT_j420`	17721.00	0.27	88.61
	abs(y^*)< 1.7	16910.00	4.58	84.55
	abs(y_b)< 1.1	16516.00	2.33	82.58

Table B.16: Selections of the HQM sample ($n = 6$, $M_D = 7.0$ TeV).

	Selection	Num. of Events	Rela. Decrease [%]	Cumulative Eff. [%]
Pre-selections	Init	20000.00	0.00	100.00
	Jet cleaning	19795.00	1.02	98.98
	NPV	19795.00	0.00	98.98
	Trigger (`HLT_j420 or HLT_j380`)	19524.00	1.37	97.62
	Jet select	17666.00	9.52	88.33
	Skimming	17666.00	0.00	88.33
Post-selections	`HLT_j420`	17620.00	0.26	88.10
	abs(y^*)< 1.7	16809.00	4.60	84.05
	abs(y_b)< 1.1	16411.00	2.37	82.06

Table B.17: Selections of the HQM sample ($n = 6$, $M_D = 7.5$ TeV).

	Selection	Num. of Events	Rela. Decrease [%]	Cumulative Eff. [%]
Pre-selections	Init	20000.00	0.00	100.00
	Jet cleaning	19805.00	0.98	99.02
	NPV	19805.00	0.00	99.02
	Trigger (`HLT_j420 or HLT_j380`)	19543.00	1.32	97.72
	Jet select	17793.00	8.95	88.97
	Skimming	17792.00	0.01	88.96
Post-selections	`HLT_j420`	17740.00	0.29	88.70
	abs(y^*)< 1.7	16945.00	4.48	84.72
	abs(y_b)< 1.1	16546.00	2.35	82.73

Table B.18: Selections of the HQM sample ($n = 6$, $M_D = 8.0$ TeV).

	Selection	Num. of Events	Rela. Decrease [%]	Cumulative Eff. [%]
Pre-selections	Init	20000.00	0.00	100.00
	Jet cleaning	19777.00	1.11	98.89
	NPV	19777.00	0.00	98.89
	Trigger (`HLT_j420 or HLT_j380`)	19492.00	1.44	97.46
	Jet select	17720.00	9.09	88.60
	Skimming	17720.00	0.00	88.60
Post-selections	`HLT_j420`	17689.00	0.17	88.44
	abs(y^*)$<$ 1.7	16856.00	4.71	84.28
	abs(y_b)$<$ 1.1	16446.00	2.43	82.23

Appendix C

Kinematic distributions of HQM samples

Figure C.1, Figure C.2 and Figure C.3 shows the kinematic distributions of HQM samples of $n = 2$, 4, 6 respectively. Selections described in Section 4.4 are applied.

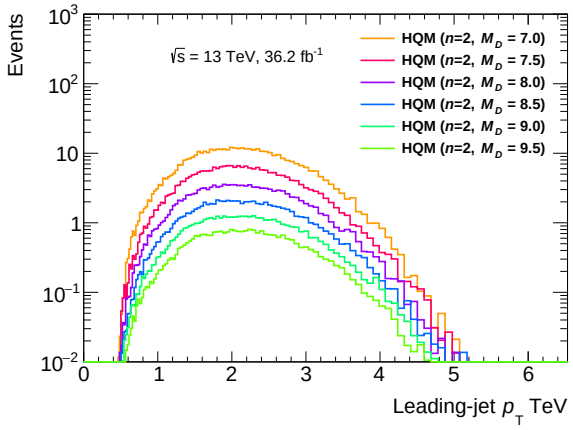

(a) Leading-jet p_{T}

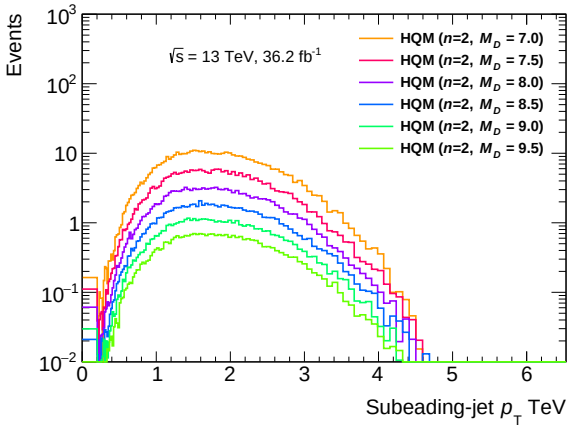

(b) Subleading-jet p_{T}

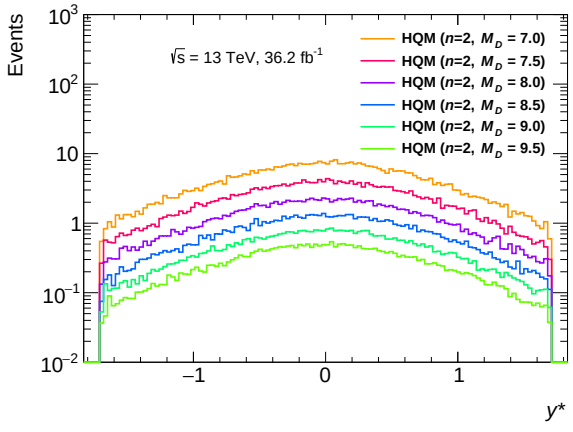

(c) y^*

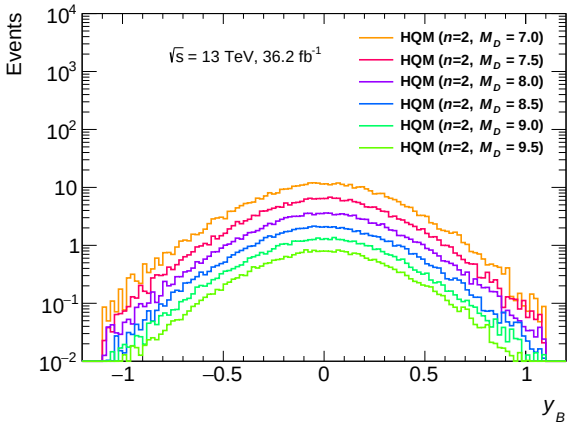

(d) y_b

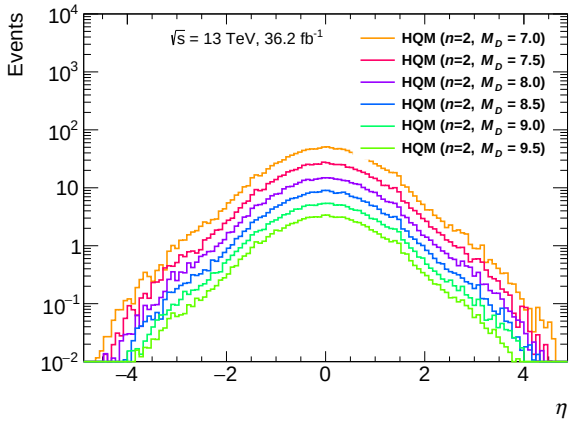

(e) η

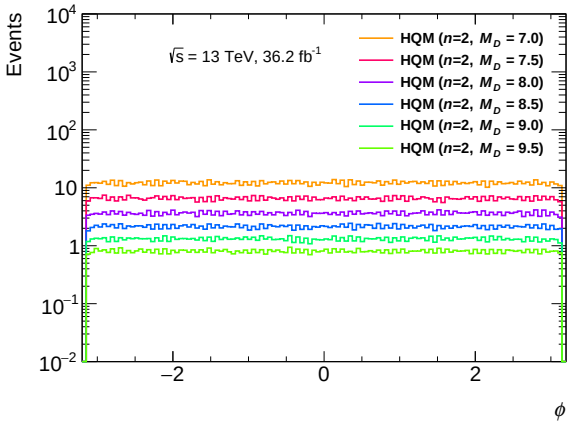

(f) ϕ

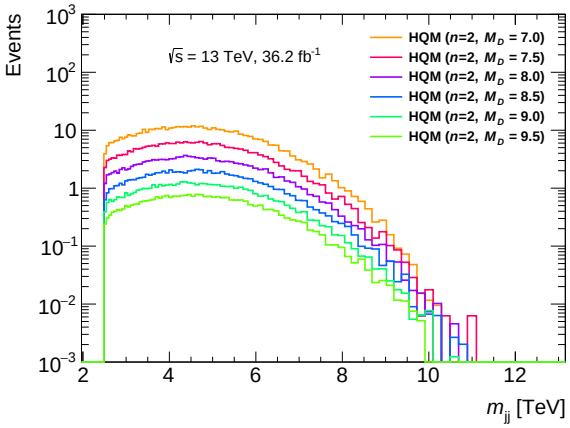

(g) m_{jj}

Figure C.1: Kinematic distributions of HQM samples $n = 2$.

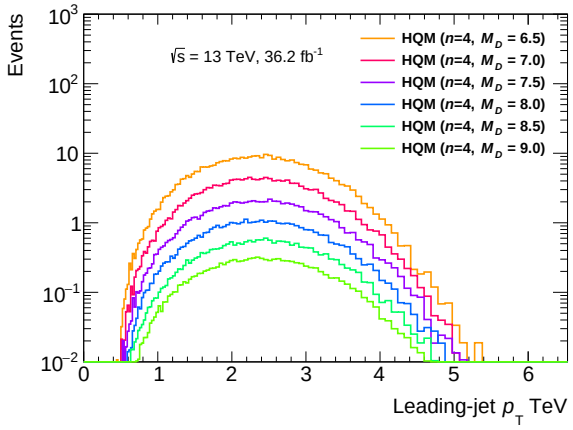

(a) Leading-jet p_{T}

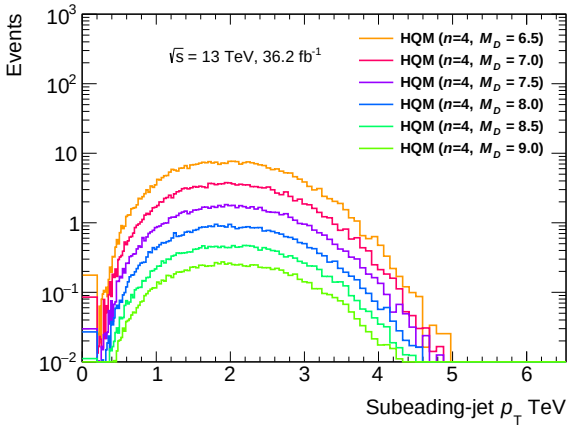

(b) Subleading-jet p_{T}

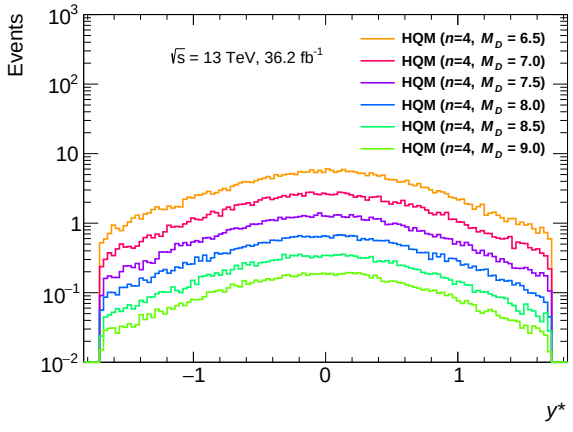

(c) y^*

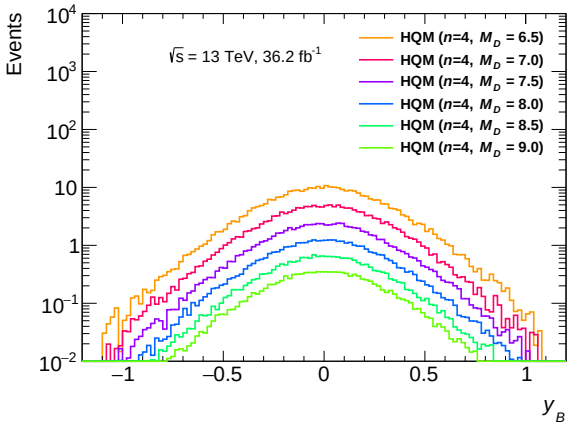

(d) y_b

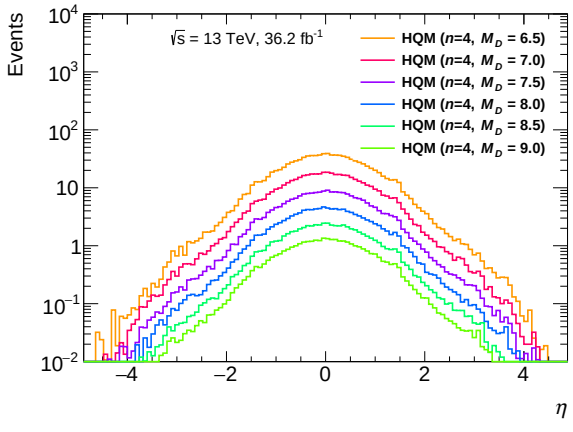

(e) η

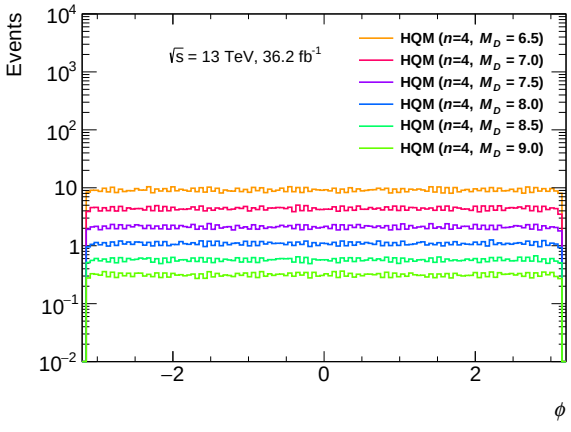

(f) ϕ

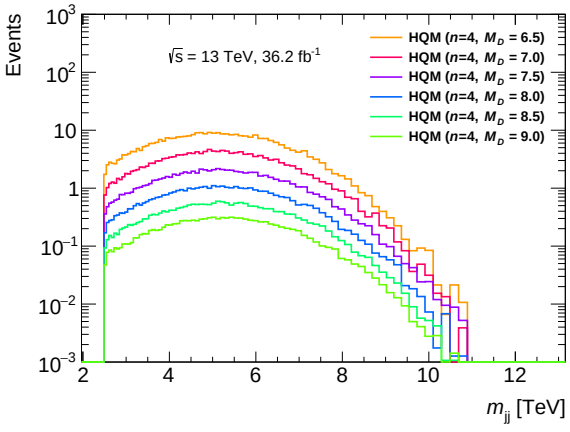

(g) m_{jj}

Figure C.2: Kinematic distributions of HQM samples $n = 4$.

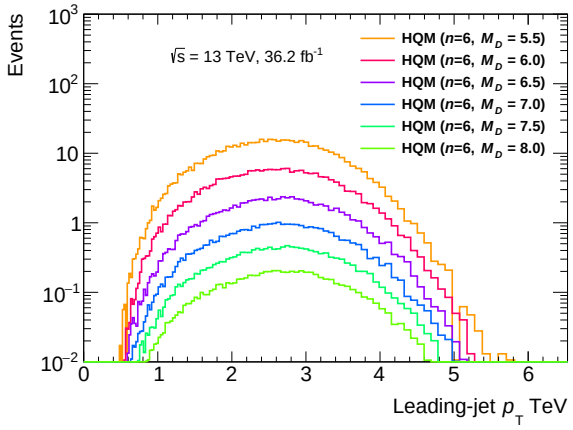

(a) Leading-jet p_{T}

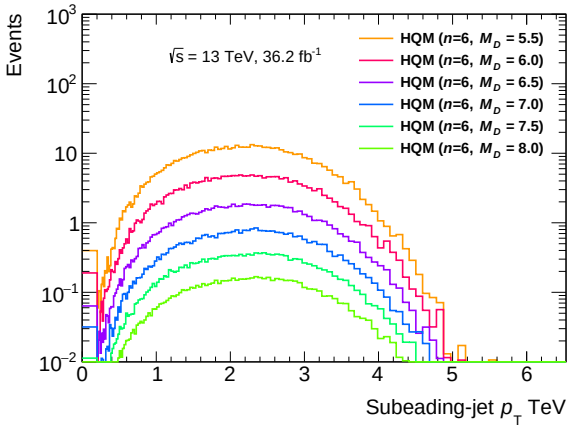

(b) Subleading-jet p_{T}

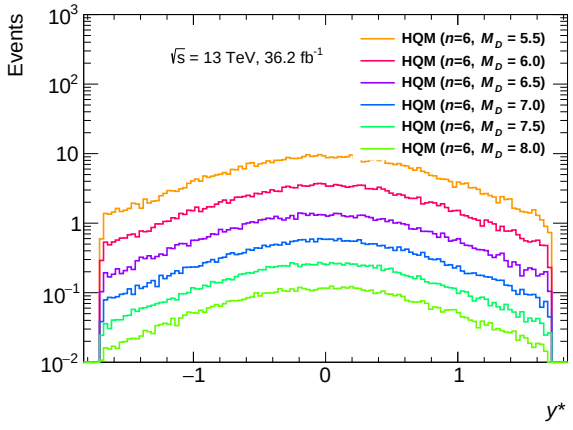

(c) y^*

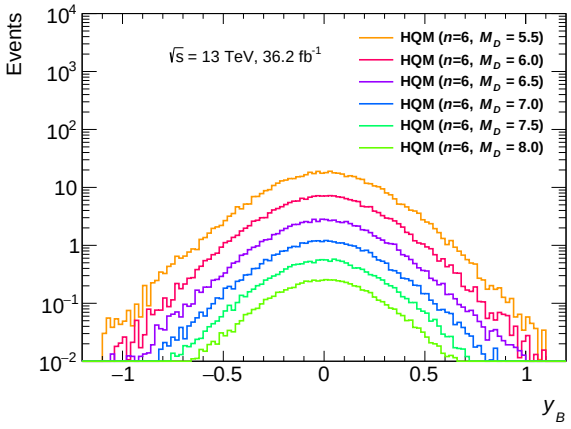

(d) y_b

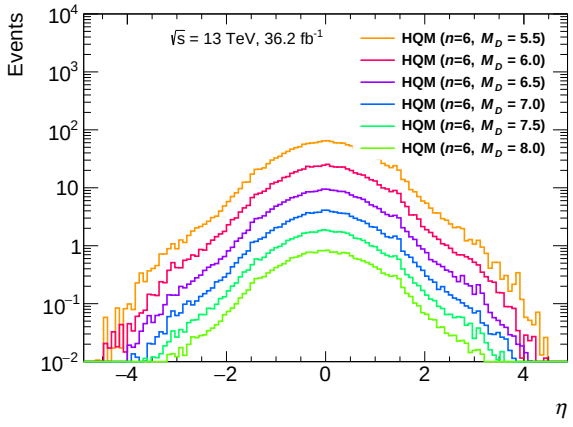

(e) η

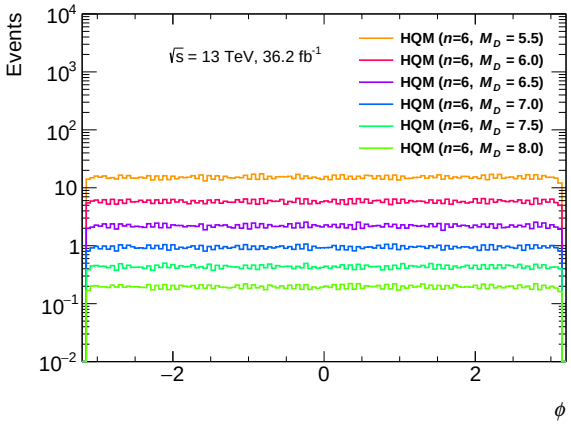

(f) ϕ

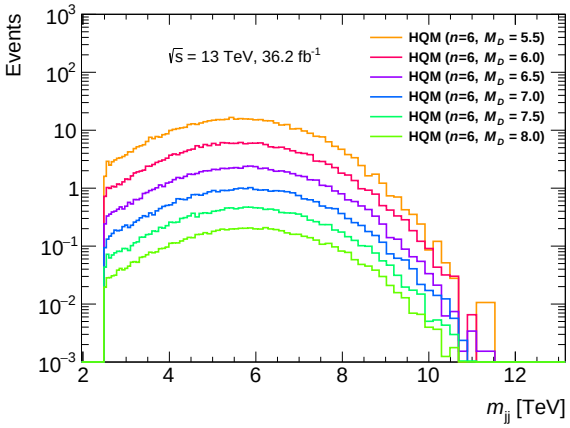

(g) m_{jj}

Figure C.3: Kinematic distributions of HQM samples $n = 6$.

Appendix D

Background uncertainties

This section shows the experimental and theoretical uncertainties of the first seven m_{jj} slices. For quick access, the contents of the figures are summarized in Table D.1, including the ones of the highest m_{jj} slice shown in Chapter 6

Table D.1: Figure indexes of the background systematic uncertainties.

	m_{jj} slices [TeV]							
	3.4–3.7	3.7–4.0	4.0–4.3	4.3–4.6	4.6–4.9	4.9–5.4	5.4–5.7	5.7 –13.0
Figure of JES uncertainties	D.1	D.3	D.5	D.7	D.9	D.11	D.13	6.1
Figure of reduced JES/JER uncertainties	D.2	D.4	D.6	D.8	D.10	D.12	D.14	6.2
Figure of theorectial uncertainties	D.15	D.16	D.17	D.18	D.19	D.20	D.21	6.3

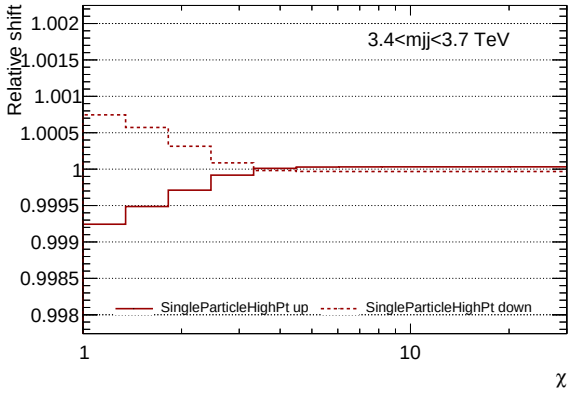

(a) Uncertainty in the single particle response measurement.

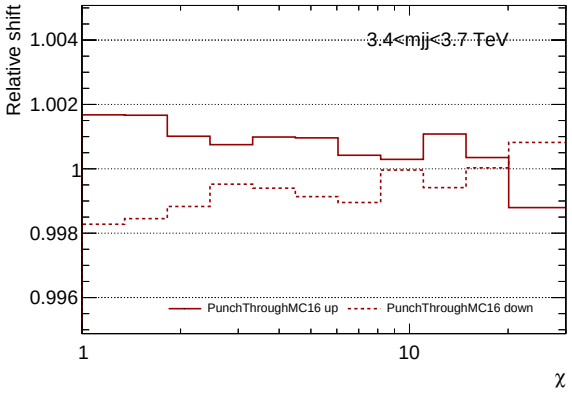

(b) Uncertainty in the remaining difference between data and MC simulation.

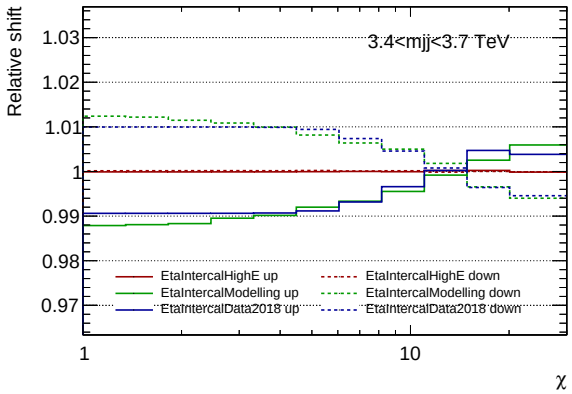

(c) Uncertainties on modelling and describing non-closure in high energy, and tile calibration.

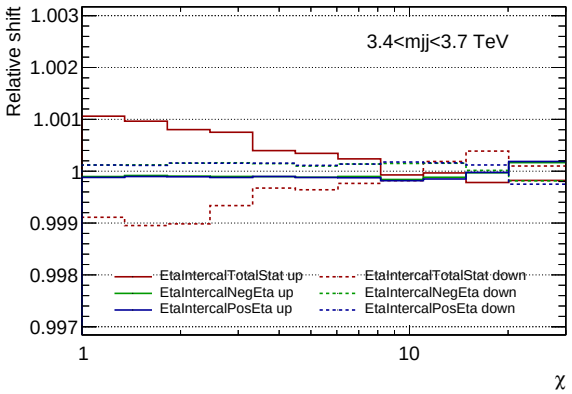

(d) Statistical uncertainty in η intercalibration and systematic uncertainty on describing non-closure at $\eta \approx \pm 2.4$.

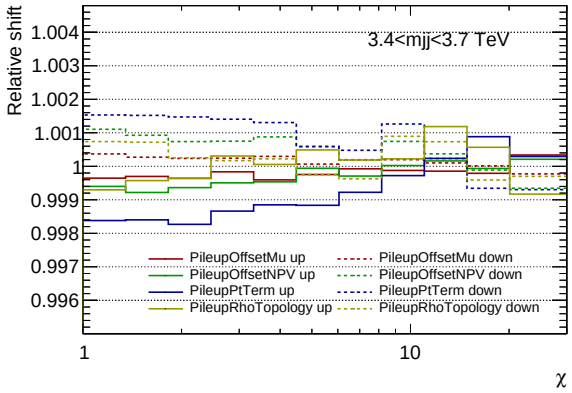

(e) Uncertainties on modelling the pile-up offset term and residual correction.

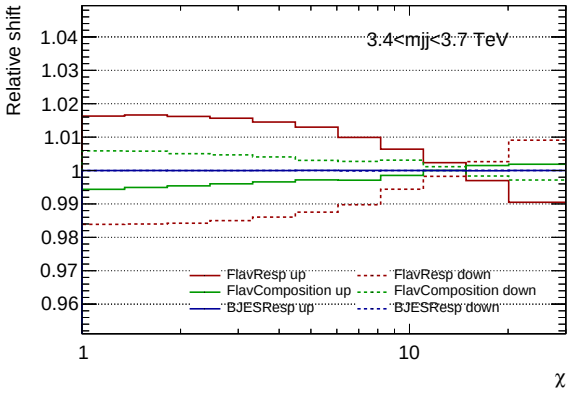

(f) Uncertainty in the response of gluon-initiated and b-quark initiated jets and the composition of quarks and gluons.

Figure D.1: Experimental uncertainties of the background prediction in $3.4 < m_{jj} < 3.7$ TeV.

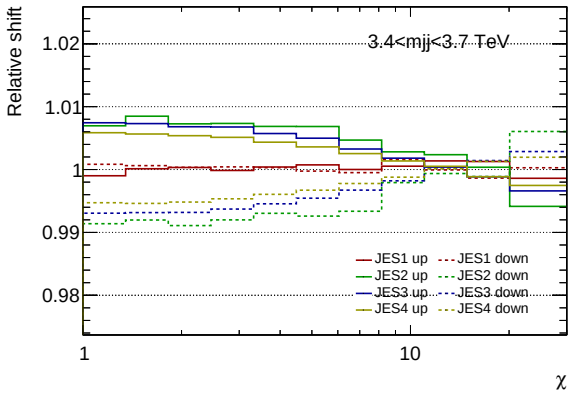

(a) Reduced *in situ* JES uncertainties 1–4.

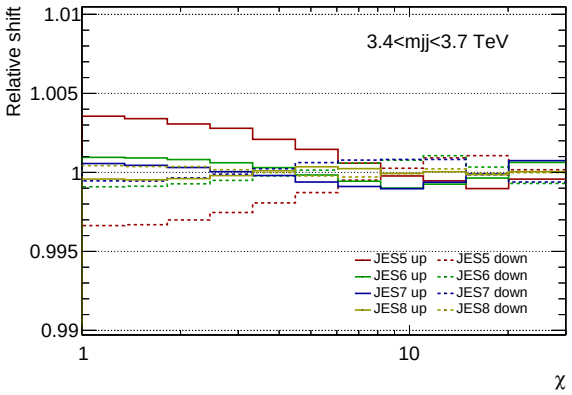

(b) Reduced *in situ* JES uncertainties 5–8.

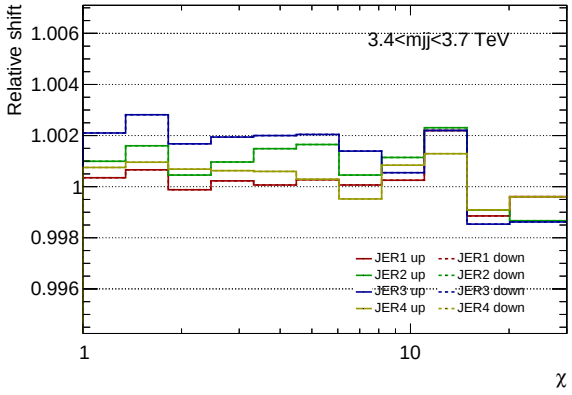

(c) Reduced JER uncertainties 1–4.

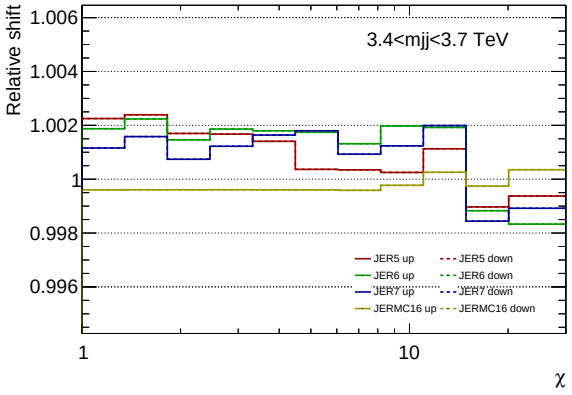

(d) Reduced JER uncertainties 5–7 and uncertainty in difference between simulation and data.

Figure D.2: Reduced experimental uncertainties of the background prediction in $3.4 < m_{jj} < 3.7$ TeV.

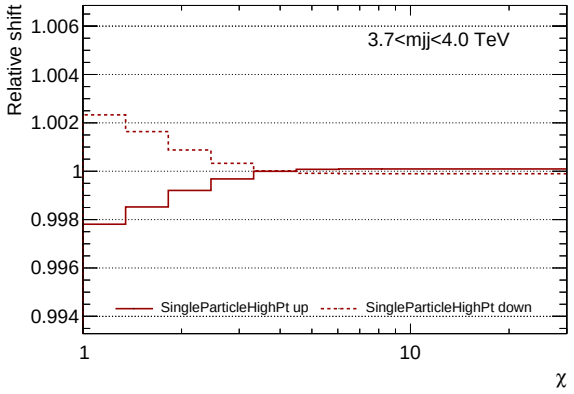

(a) Uncertainty in the single particle response measurement.

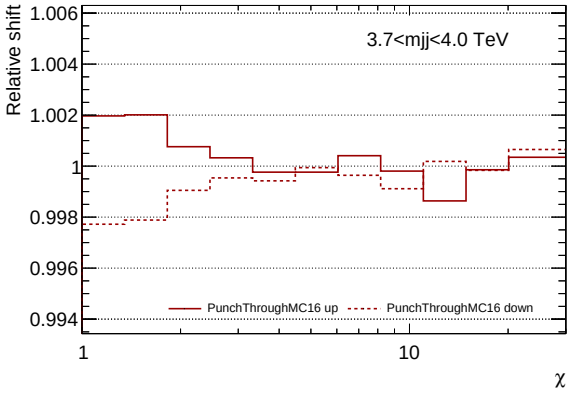

(b) Uncertainty in the remaining difference between data and MC simulation.

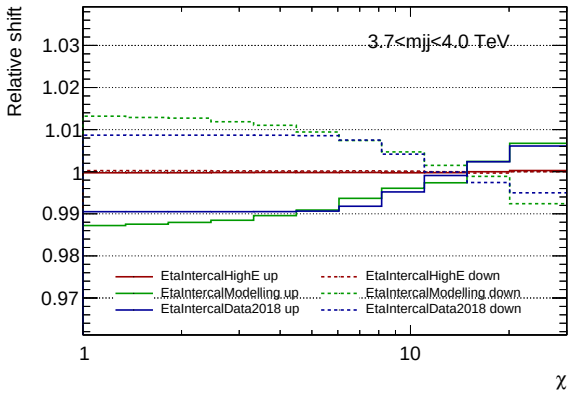

(c) Uncertainties on modelling and describing non-closure in high energy, and tile calibration, and tile calibration.

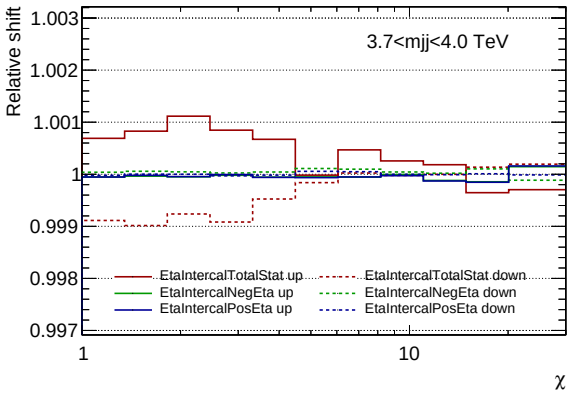

(d) Statistical uncertainty in η intercalibration and systematic uncertainty on describing non-closure at $\eta \approx \pm 2.4$.

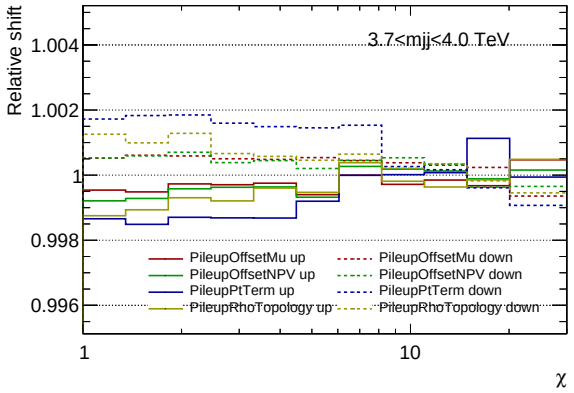

(e) Uncertainties on modelling the pile-up offset term and residual correction.

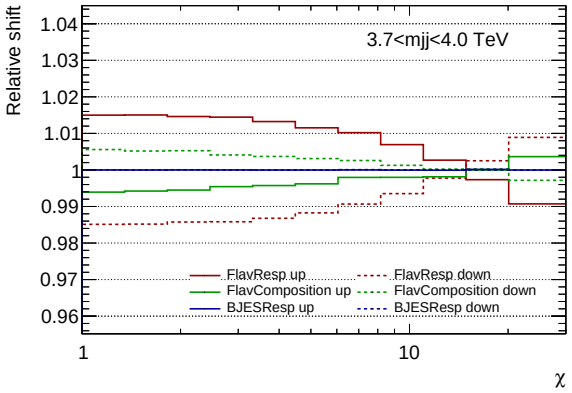

(f) Uncertainty in the response of gluon-initiated and b-quark initiated jets and the composition of quarks and gluons.

Figure D.3: Experimental uncertainties of the background prediction in $3.7 < m_{jj} < 4.0$ TeV.

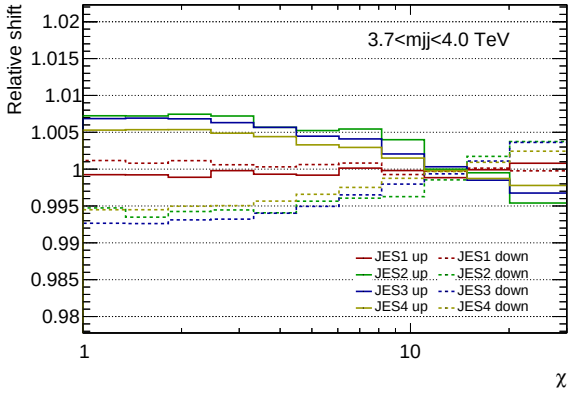

(a) Reduced *in situ* JES uncertainties 1–4.

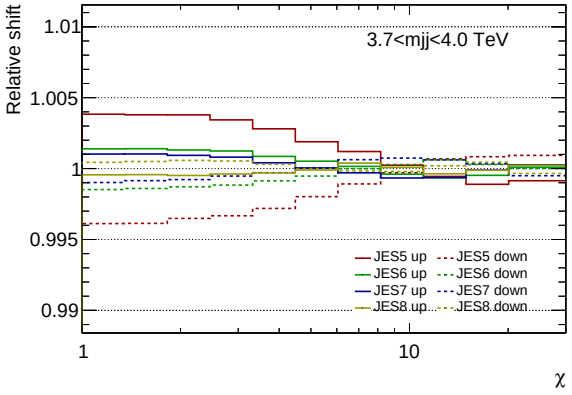

(b) Reduced *in situ* JES uncertainties 5–8.

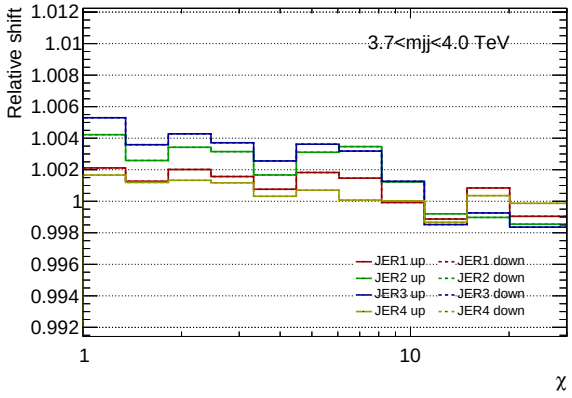

(c) Reduced JER uncertainties 1–4.

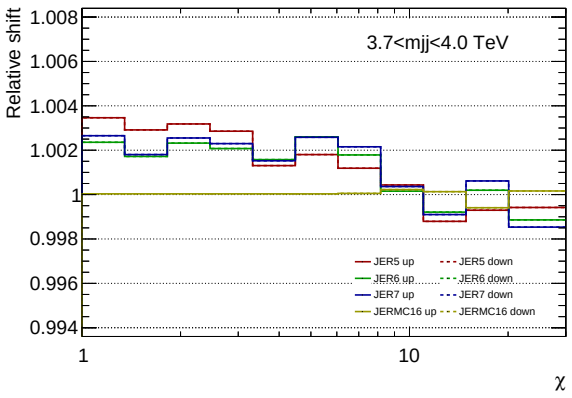

(d) Reduced JER uncertainties 5–7 and uncertainty in difference between simulation and data.

Figure D.4: Reduced experimental uncertainties of the background prediction in $3.7 < m_{jj} < 4.0$ TeV.

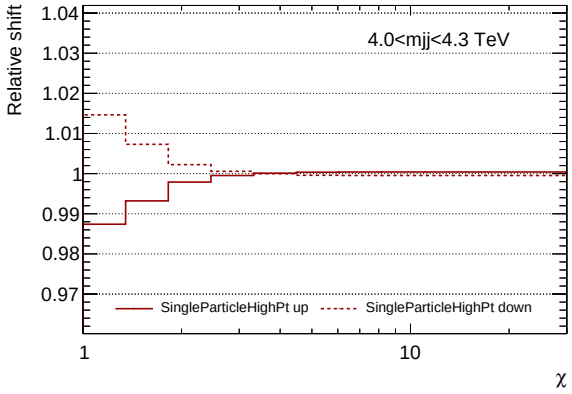

(a) Uncertainty in the single particle response measurement.

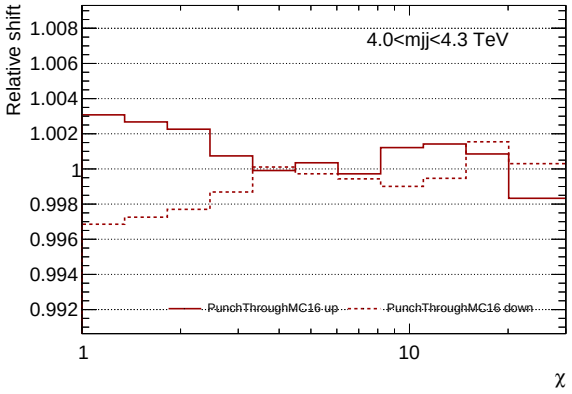

(b) Uncertainty in the remaining difference between data and MC simulation.

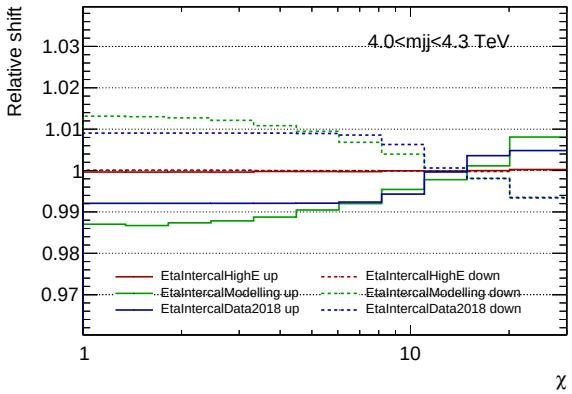

(c) Uncertainties on modelling and describing non-closure in high energy, and tile calibration.

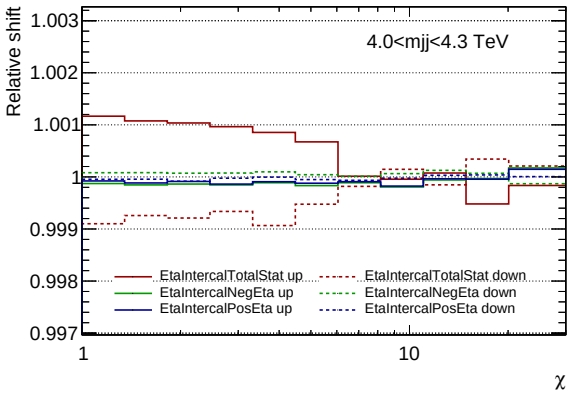

(d) Statistical uncertainty in η intercalibration and systematic uncertainty on describing non-closure at $\eta \approx \pm 2.4$.

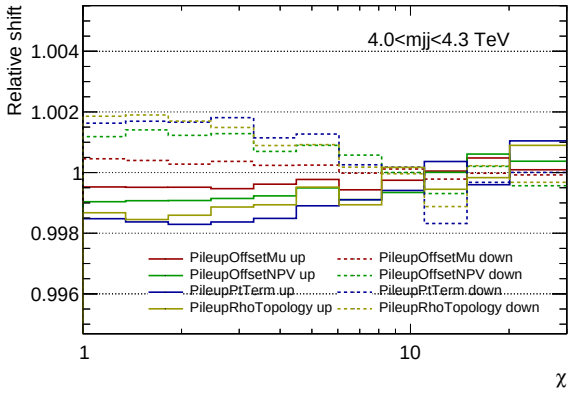

(e) Uncertainties on modelling the pile-up offset term and residual correction.

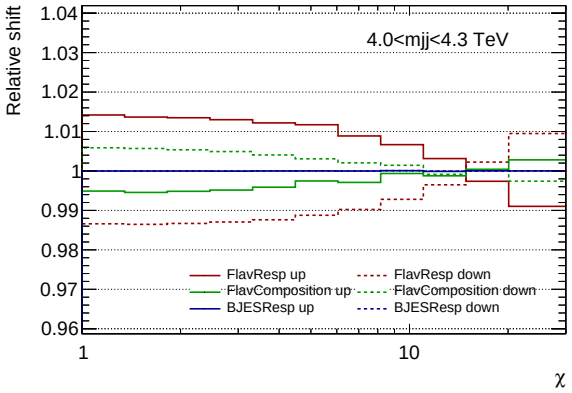

(f) Uncertainty in the response of gluon-initiated and b-quark initiated jets and the composition of quarks and gluons.

Figure D.5: Experimental uncertainties of the background prediction in $4.0 < m_{jj} < 4.3$ TeV.

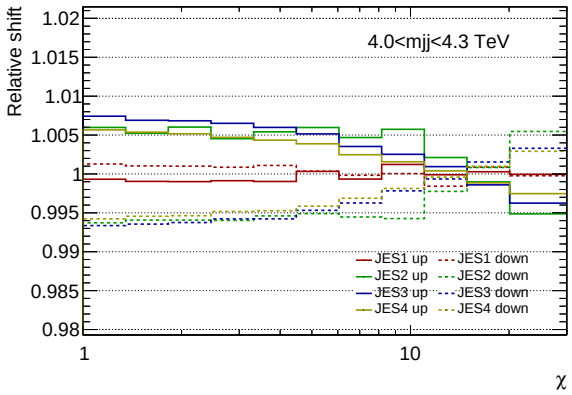

(a) Reduced *in situ* JES uncertainties 1–4.

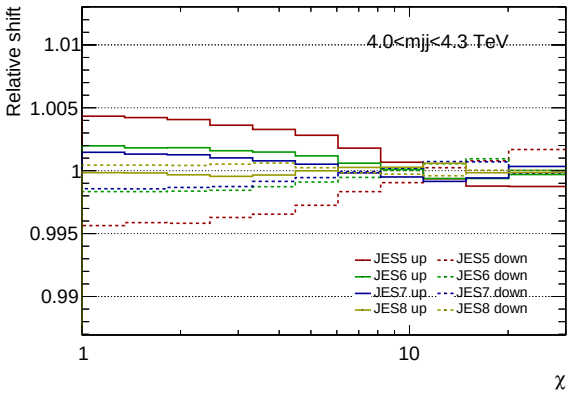

(b) Reduced *in situ* JES uncertainties 5–8.

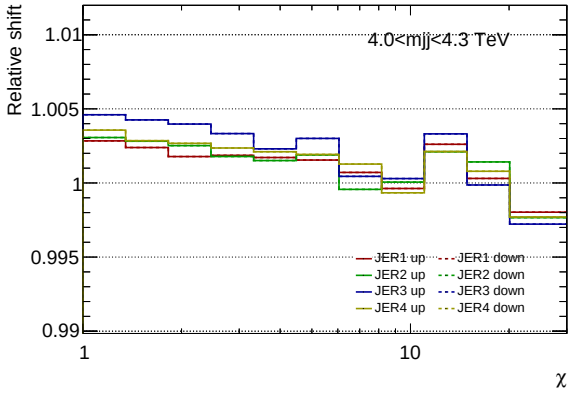

(c) Reduced JER uncertainties 1–4.

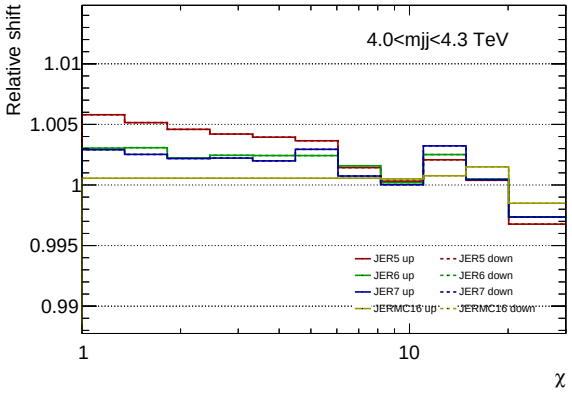

(d) Reduced JER uncertainties 5–7 and uncertainty in difference between simulation and data.

Figure D.6: Reduced experimental uncertainties of the background prediction in $4.0 < m_{jj} < 4.3$ TeV.

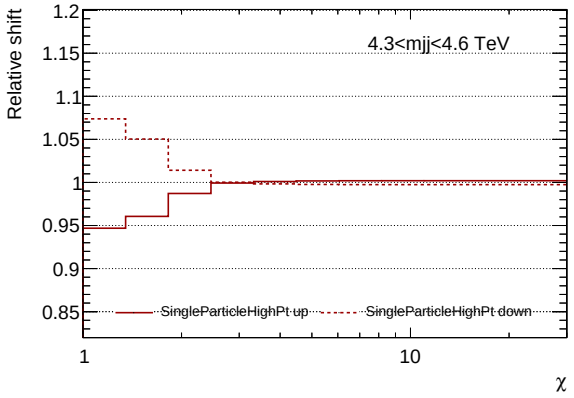

(a) Uncertainty in the single particle response measurement.

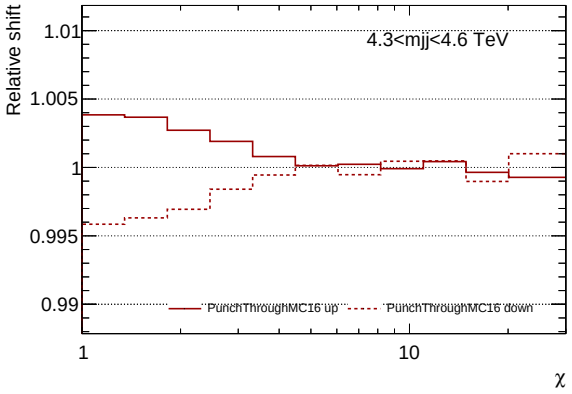

(b) Uncertainty in the remaining difference between data and MC simulation.

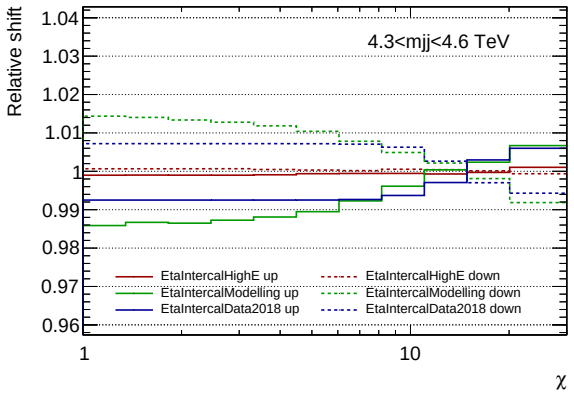

(c) Uncertainties on modelling and describing non-closure in high energy, and tile calibration.

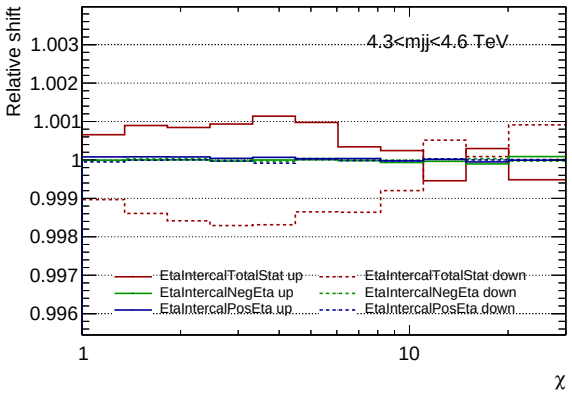

(d) Statistical uncertainty in η intercalibration and systematic uncertainty on describing non-closure at $\eta \approx \pm 2.4$.

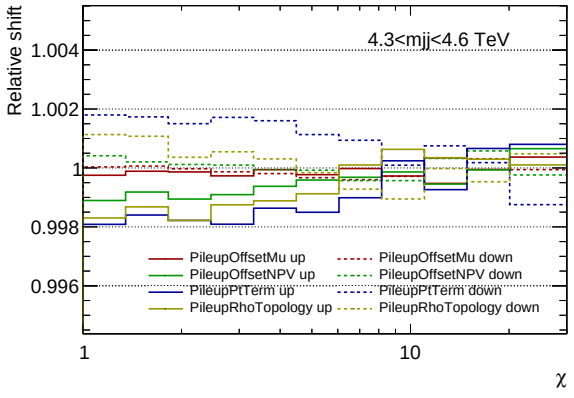

(e) Uncertainties on modelling the pile-up offset term and residual correction.

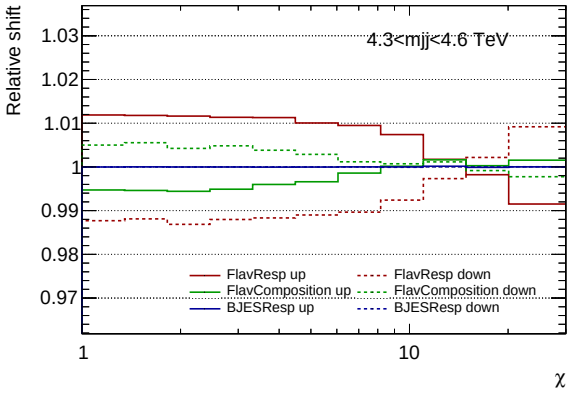

(f) Uncertainty in the response of gluon-initiated and b-quark initiated jets and the composition of quarks and gluons.

Figure D.7: Experimental uncertainties of the background prediction in $4.3 < m_{jj} < 4.6$ TeV.

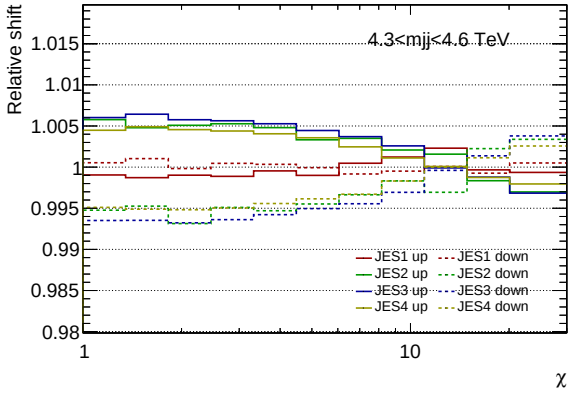

(a) Reduced *in situ* JES uncertainties 1–4.

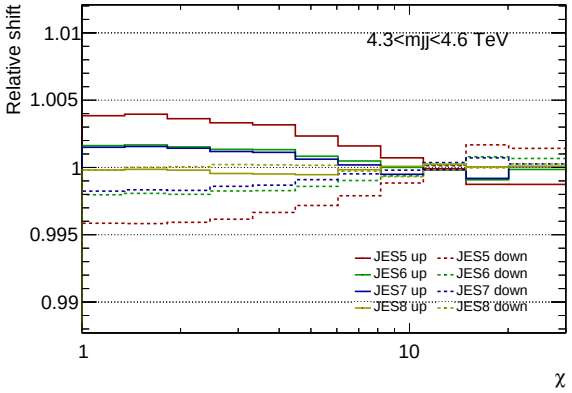

(b) Reduced *in situ* JES uncertainties 5–8.

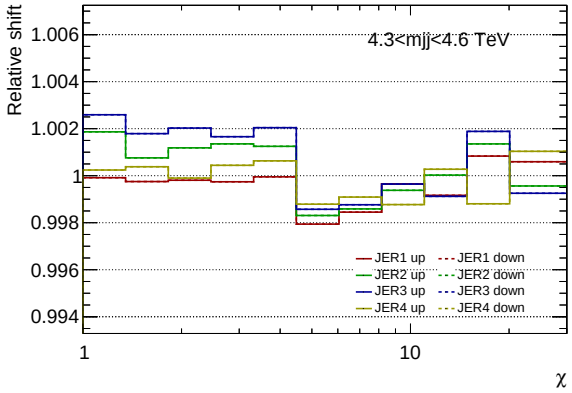

(c) Reduced JER uncertainties 1–4.

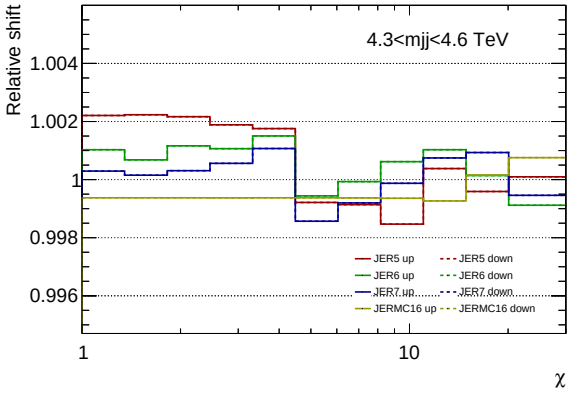

(d) Reduced JER uncertainties 5–7 and uncertainty in difference between simulation and data.

Figure D.8: Reduced experimental uncertainties of the background prediction in $4.3 < m_{jj} < 4.6$ TeV.

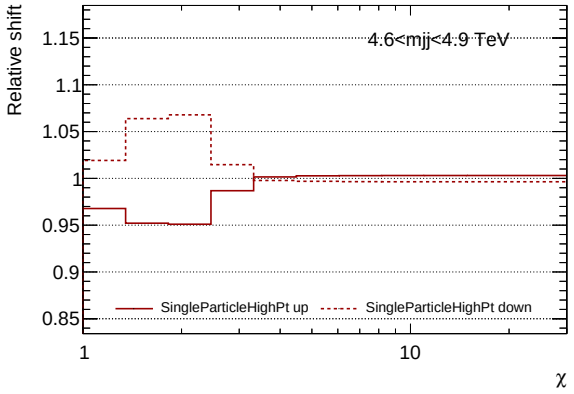

(a) Uncertainty in the single particle response measurement.

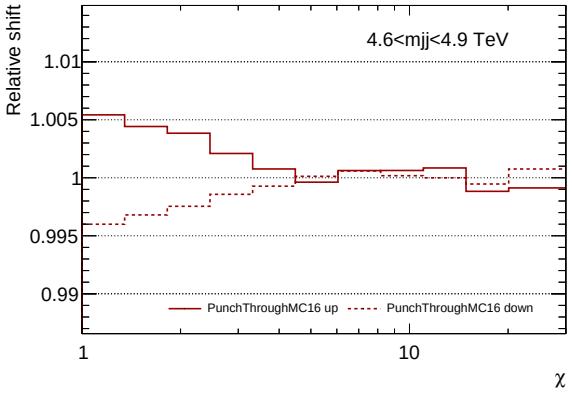

(b) Uncertainty in the remaining difference between data and MC simulation.

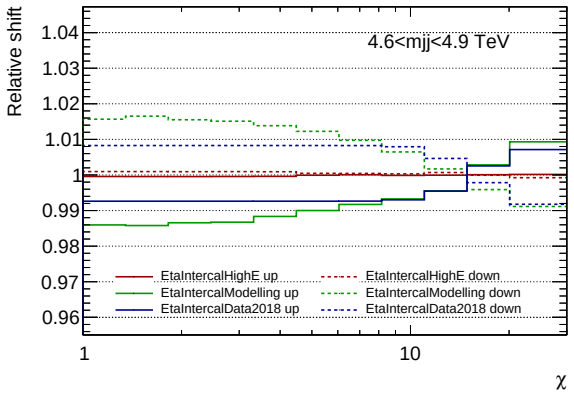

(c) Uncertainties on modelling and describing non-closure in high energy, and tile calibration.

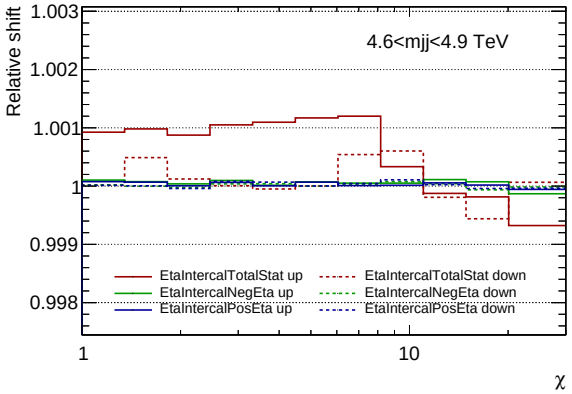

(d) Statistical uncertainty in η intercalibration and systematic uncertainty on describing non-closure at $\eta \approx \pm 2.4$.

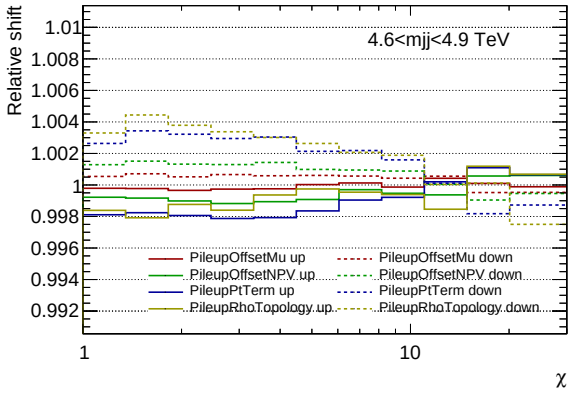

(e) Uncertainties on modelling the pile-up offset term and residual correction.

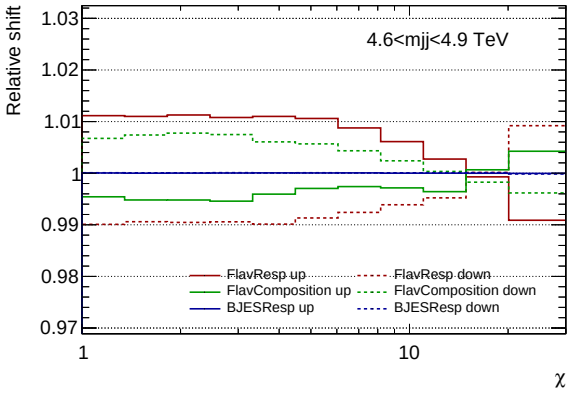

(f) Uncertainty in the response of gluon-initiated and b-quark initiated jets and the composition of quarks and gluons.

Figure D.9: Experimental uncertainties of the background prediction in $4.6 < m_{jj} < 4.9$ TeV.

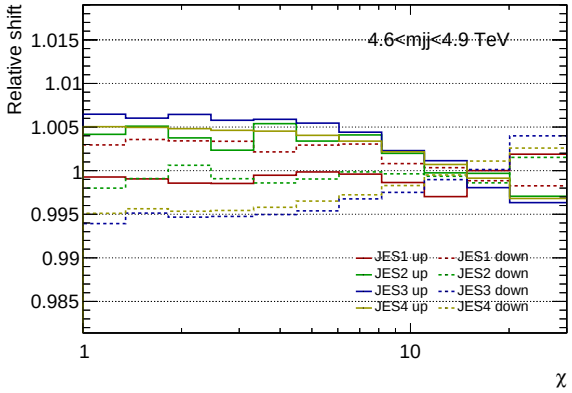

(a) Reduced *in situ* JES uncertainties 1–4.

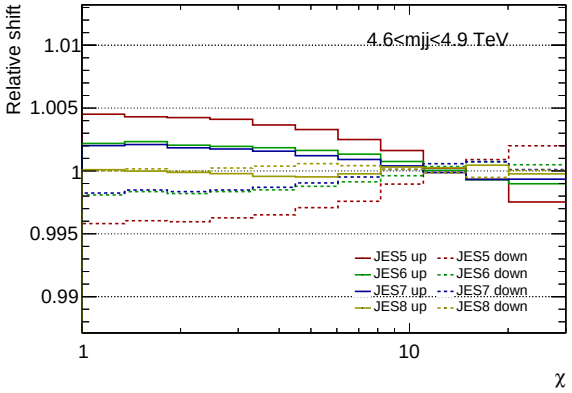

(b) Reduced *in situ* JES uncertainties 5–8.

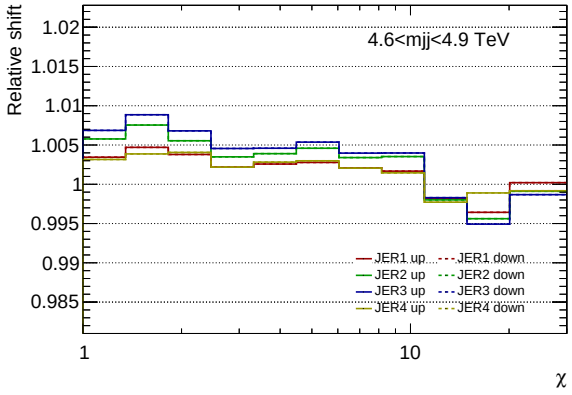

(c) Reduced JER uncertainties 1–4.

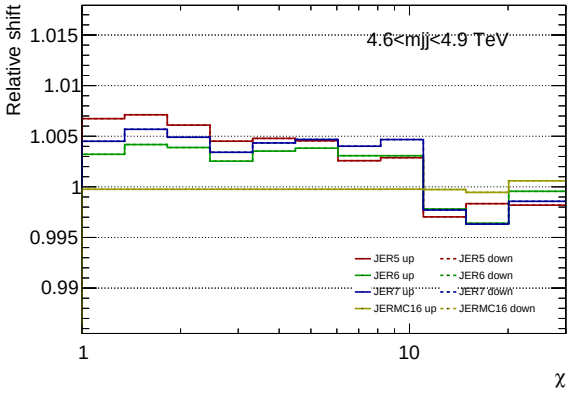

(d) Reduced JER uncertainties 5–7 and uncertainty in difference between simulation and data.

Figure D.10: Reduced experimental uncertainties of the background prediction in $4.6 < m_{jj} < 4.9$ TeV.

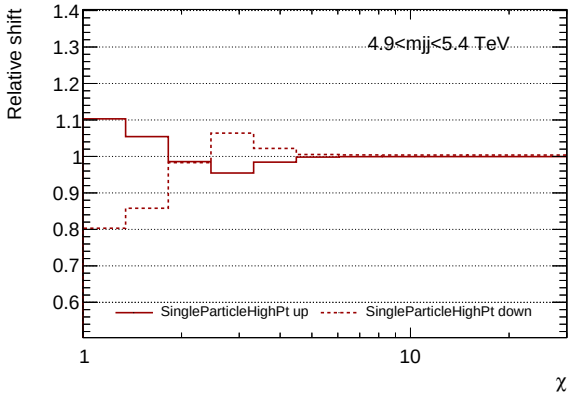

(a) Uncertainty in the single particle response measurement.

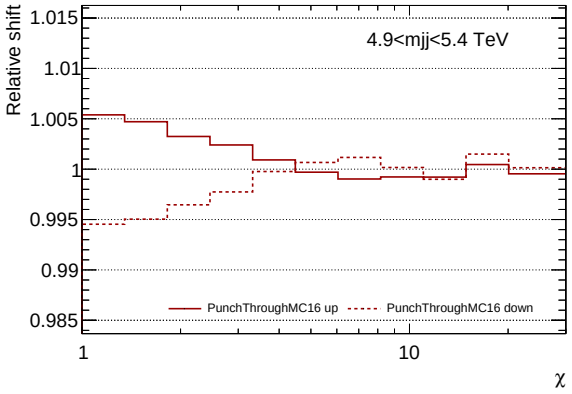

(b) Uncertainty in the remaining difference between data and MC simulation.

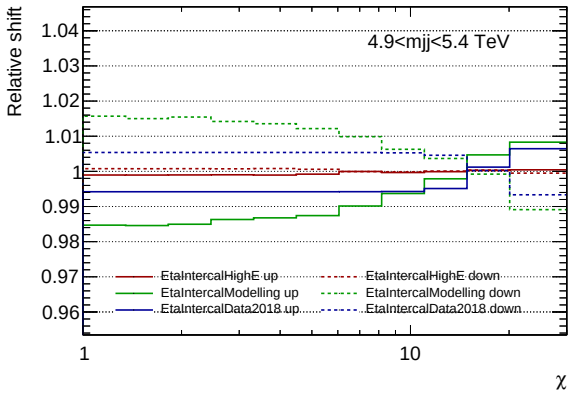

(c) Uncertainties on modelling and describing non-closure in high energy, and tile calibration.

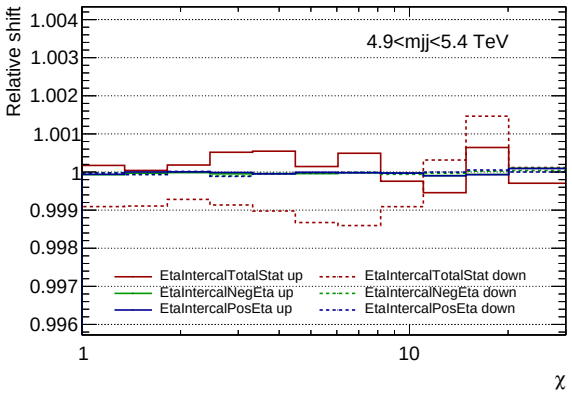

(d) Statistical uncertainty in η intercalibration and systematic uncertainty on describing non-closure at $\eta \approx \pm 2.4$.

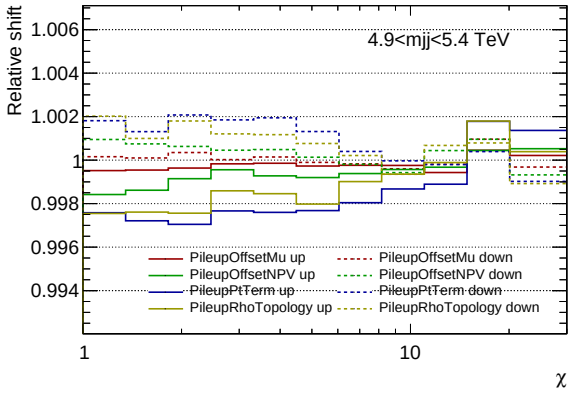

(e) Uncertainties on modelling the pile-up offset term and residual correction.

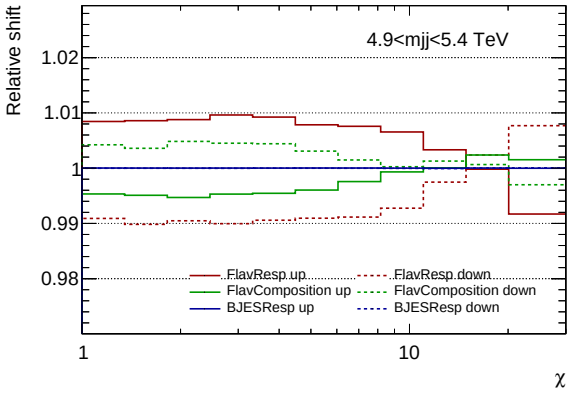

(f) Uncertainty in the response of gluon-initiated and b-quark initiated jets and the composition of quarks and gluons.

Figure D.11: Experimental uncertainties of the background prediction in $4.9 < m_{jj} < 5.4$ TeV.

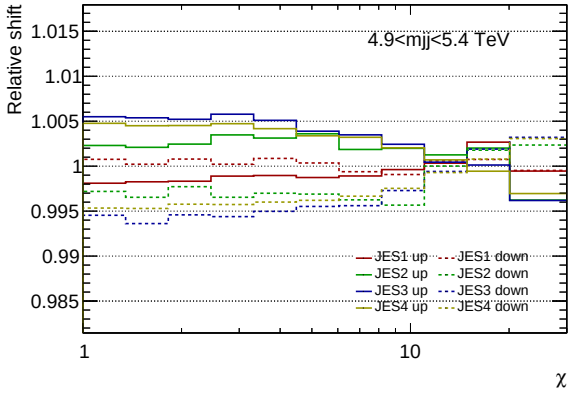

(a) Reduced *in situ* JES uncertainties 1–4.

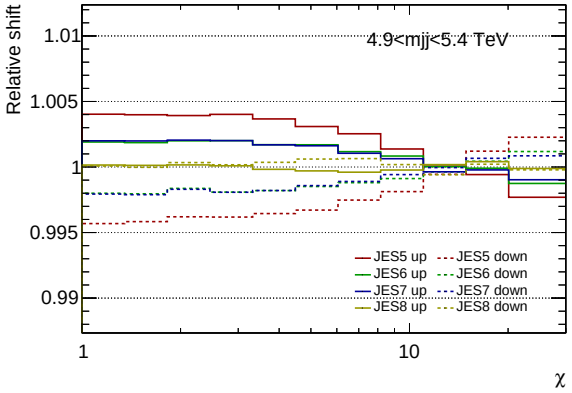

(b) Reduced *in situ* JES uncertainties 5–8.

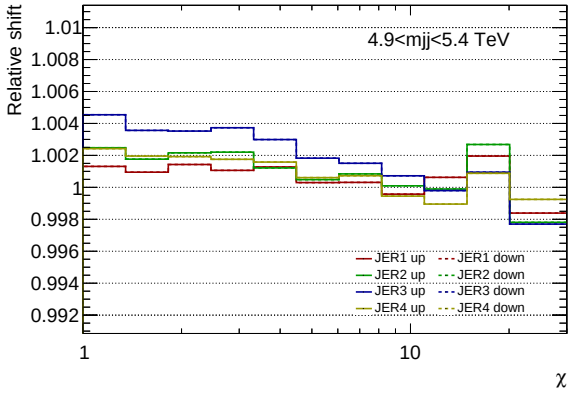

(c) Reduced JER uncertainties 1–4.

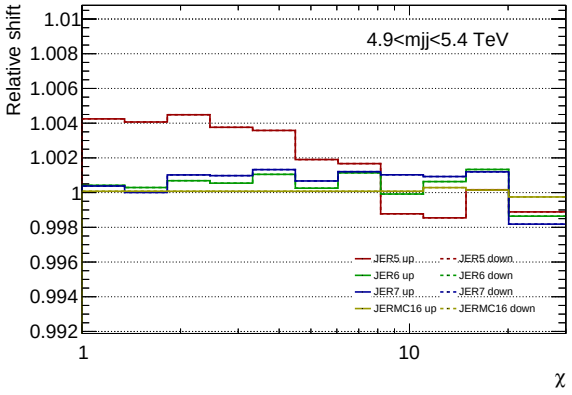

(d) Reduced JER uncertainties 5–7 and uncertainty in difference between simulation and data.

Figure D.12: Reduced experimental uncertainties of the background prediction in $4.9 < m_{jj} < 5.4$ TeV.

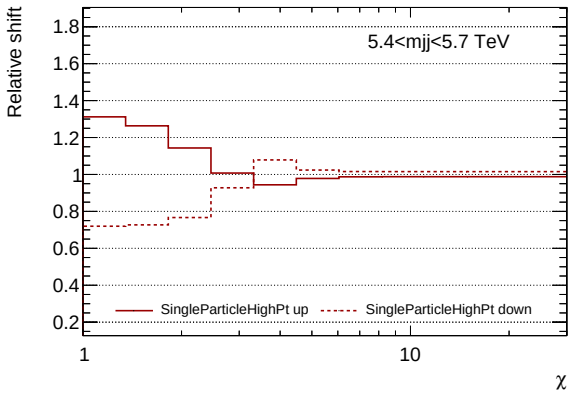

(a) Uncertainty in the single particle response measurement.

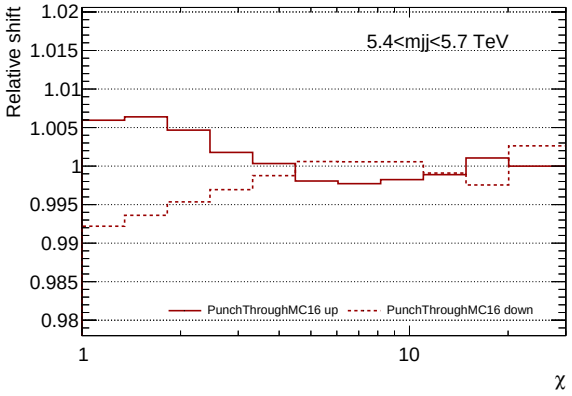

(b) Uncertainty in the remaining difference between data and MC simulation.

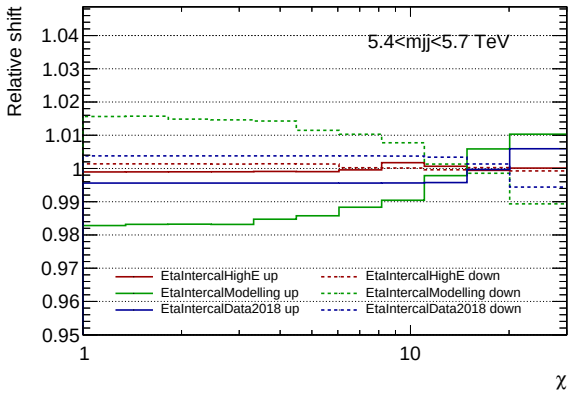

(c) Uncertainties on modelling and describing non-closure in high energy, and tile calibration.

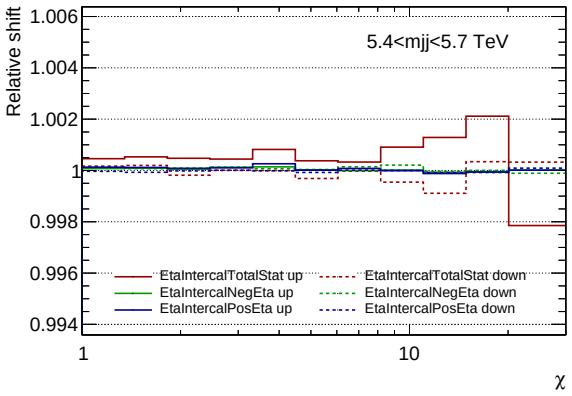

(d) Statistical uncertainty in η intercalibration and systematic uncertainty on describing non-closure at $\eta \approx \pm 2.4$.

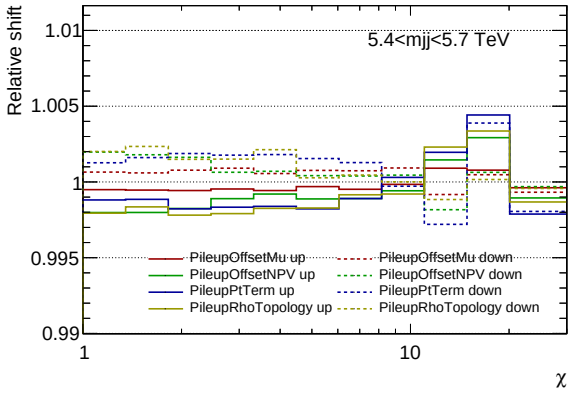

(e) Uncertainties on modelling the pile-up offset term and residual correction.

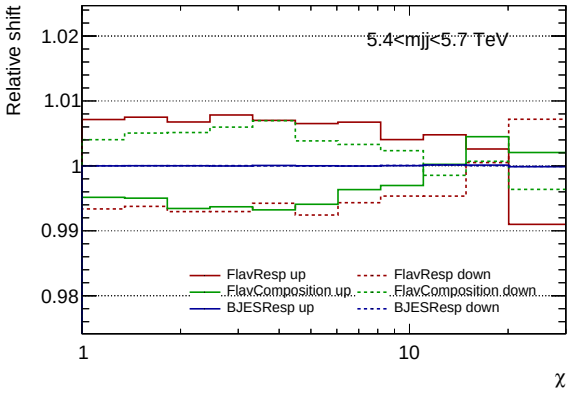

(f) Uncertainty in the response of gluon-initiated and b-quark initiated jets and the composition of quarks and gluons.

Figure D.13: Experimental uncertainties of the background prediction in $5.4 < m_{jj} < 5.7$ TeV.

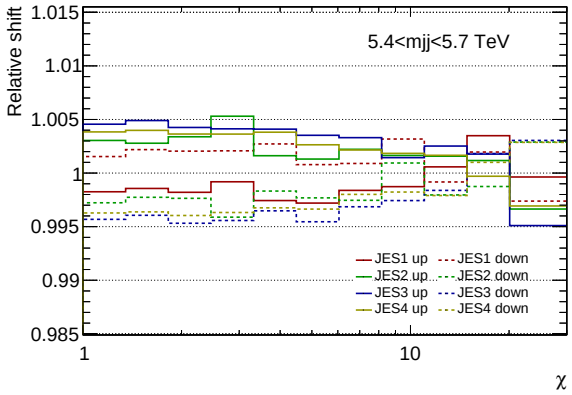

(a) Reduced *in situ* JES uncertainties 1–4.

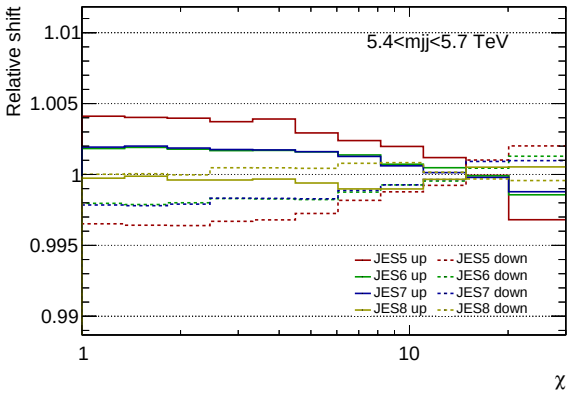

(b) Reduced *in situ* JES uncertainties 5–8.

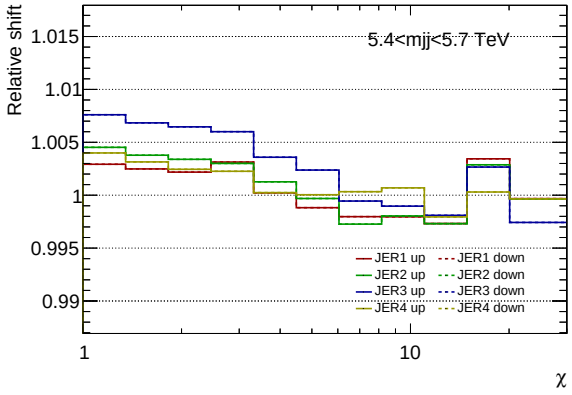

(c) Reduced JER uncertainties 1–4.

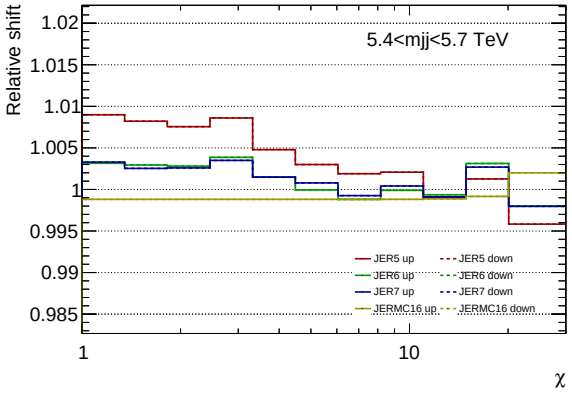

(d) Reduced JER uncertainties 5–7 and uncertainty in difference between simulation and data.

Figure D.14: Reduced experimental uncertainties of the background prediction in $5.4 < m_{jj} < 5.7$ TeV.

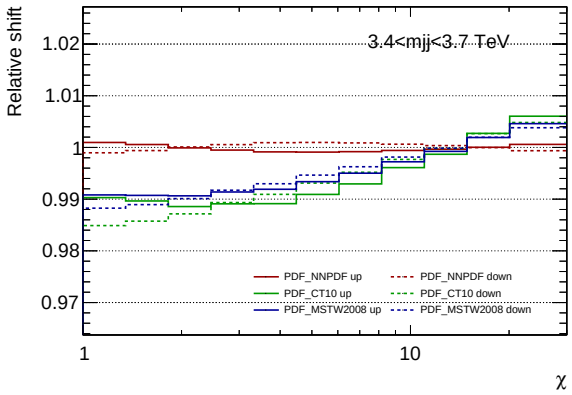

(a) PDF uncertainties in NNPDF2.3, CT10 and MSTW2008.

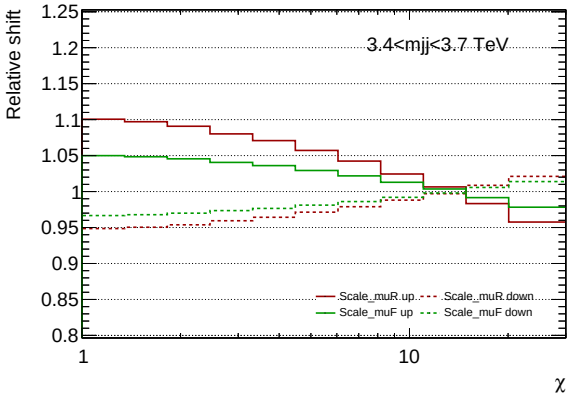

(b) Scale uncertainties in μ_R and μ_F.

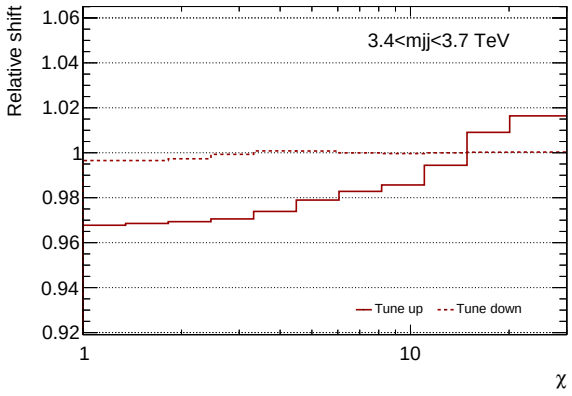

(c) Tune uncertainty.

Figure D.15: Theoretical uncertainties of the background χ distribution in $3.4 < m_{jj} < 3.7$ TeV.

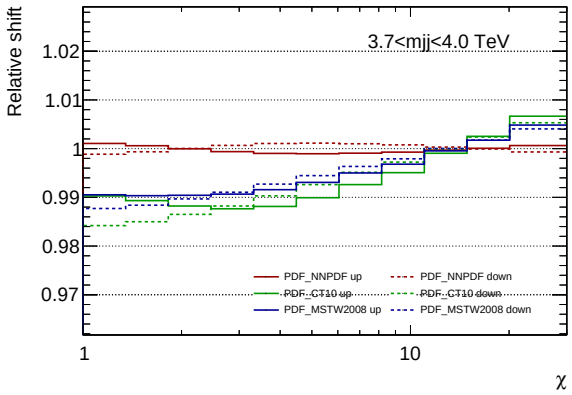

(a) PDF uncertainties in NNPDF2.3, CT10 and MSTW2008.

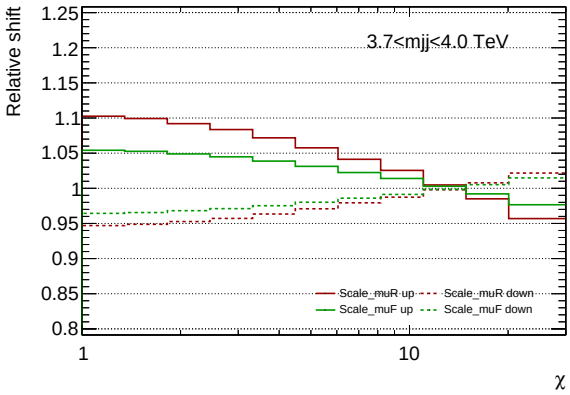

(b) Scale uncertainties in μ_R and μ_F.

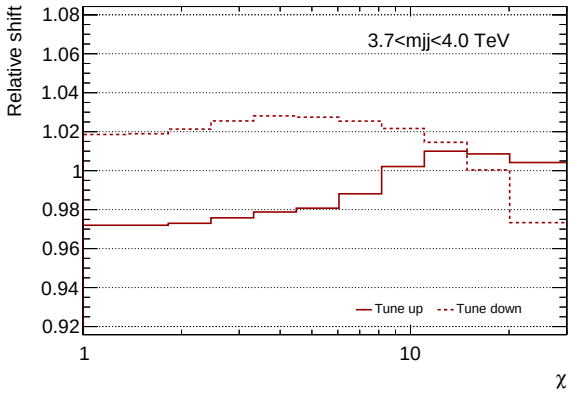

(c) Tune uncertainty.

Figure D.16: Theoretical uncertainties of the background χ distribution in $3.7 < m_{jj} < 4.0$ TeV.

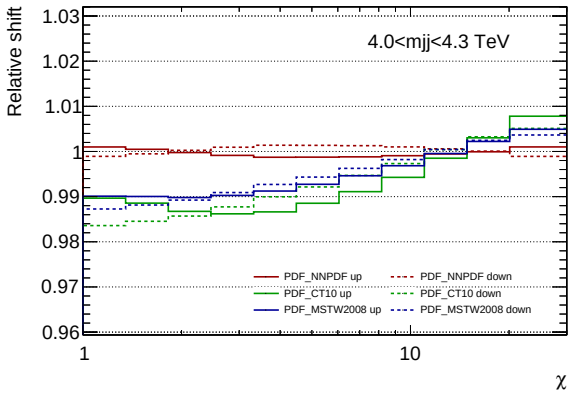

(a) PDF uncertainties in NNPDF2.3, CT10 and MSTW2008.

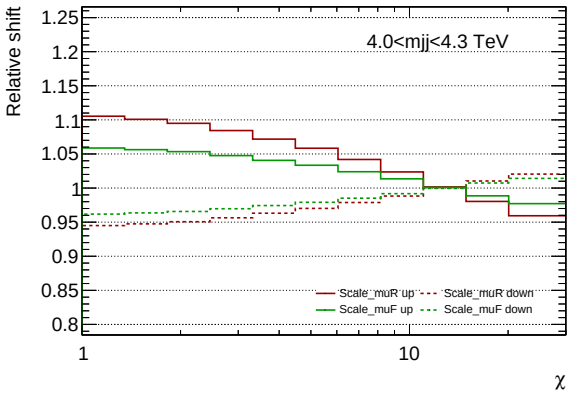

(b) Scale uncertainties in μ_R and μ_F.

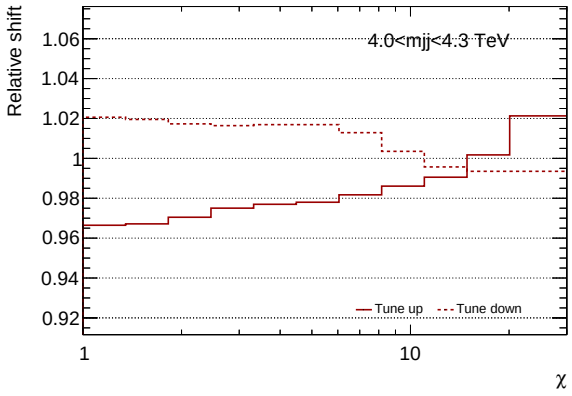

(c) Tune uncertainty.

Figure D.17: Theoretical uncertainties of the background χ distribution in $4.0 < m_{jj} < 4.3$ TeV.

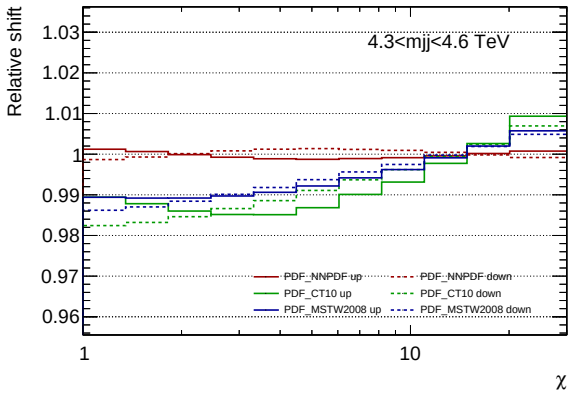

(a) PDF uncertainties in NNPDF2.3, CT10 and MSTW2008.

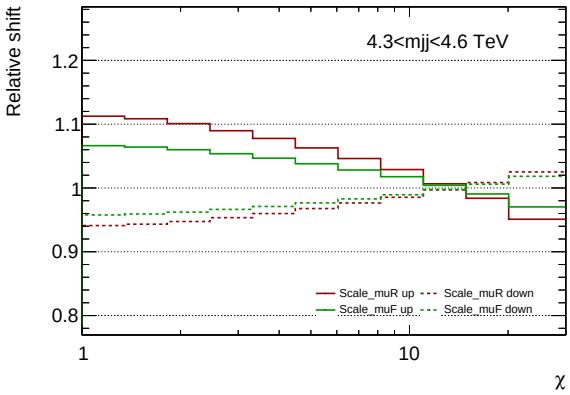

(b) Scale uncertainties in μ_R and μ_F.

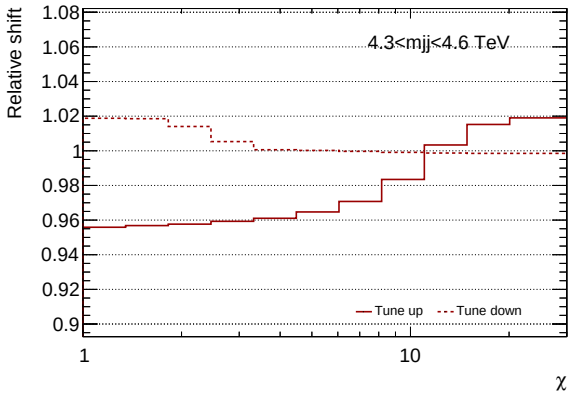

(c) Tune uncertainty.

Figure D.18: Theoretical uncertainties of the background χ distribution in $4.3 < m_{jj} < 4.6$ TeV.

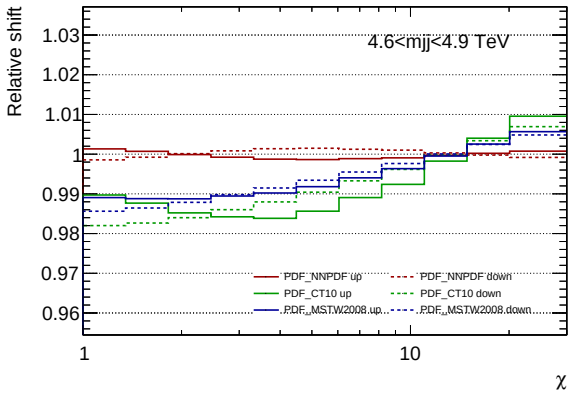

(a) PDF uncertainties in NNPDF2.3, CT10 and MSTW2008.

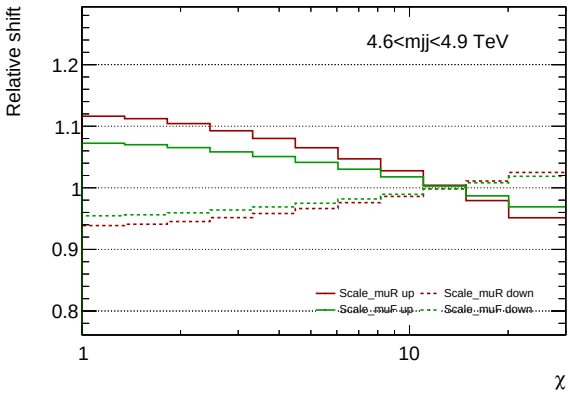

(b) Scale uncertainties in μ_R and μ_F.

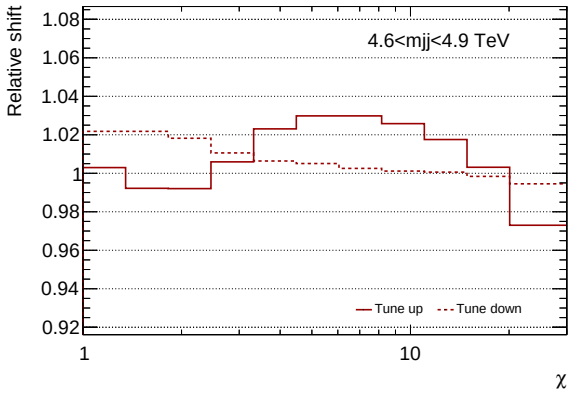

(c) Tune uncertainty.

Figure D.19: Theoretical uncertainties of the background χ distribution in $4.6 < m_{jj} < 4.9$ TeV.

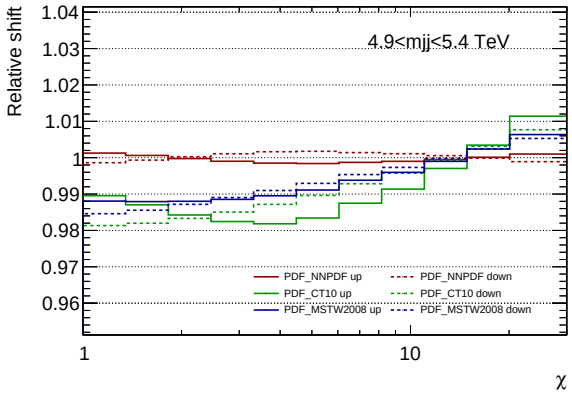

(a) PDF uncertainties in NNPDF2.3, CT10 and MSTW2008.

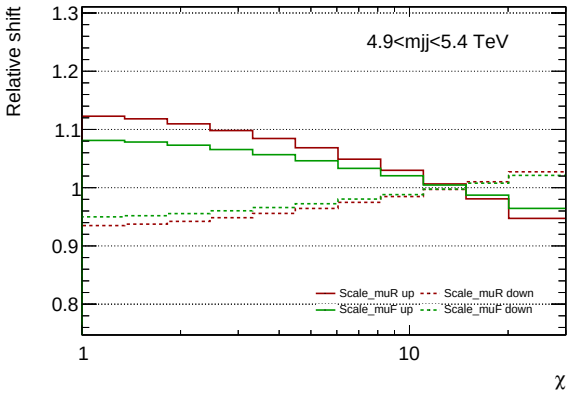

(b) Scale uncertainties in μ_R and μ_F.

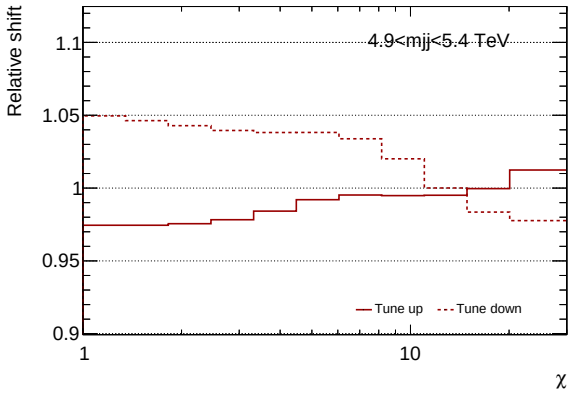

(c) Tune uncertainty.

Figure D.20: Theoretical uncertainties of the background χ distribution in $4.9 < m_{jj} < 5.4$ TeV.

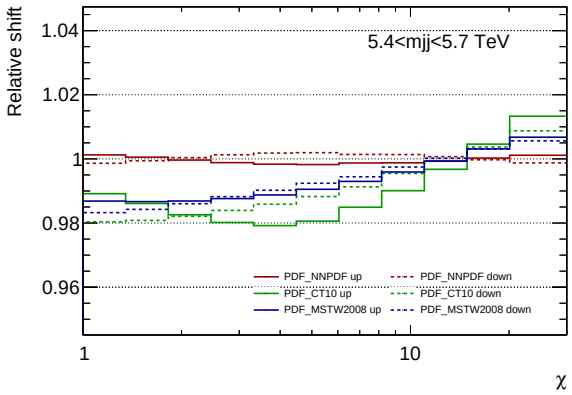

(a) PDF uncertainties in NNPDF2.3, CT10 and MSTW2008.

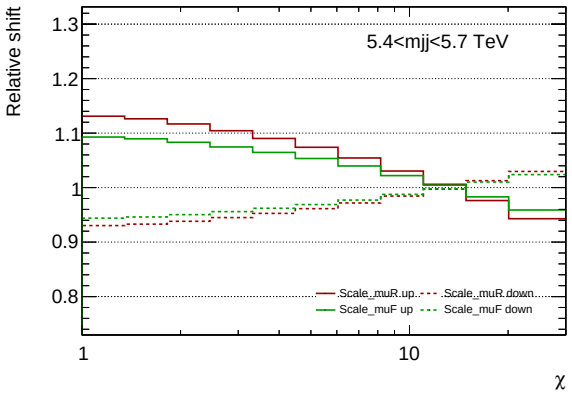

(b) Scale uncertainties in μ_R and μ_F.

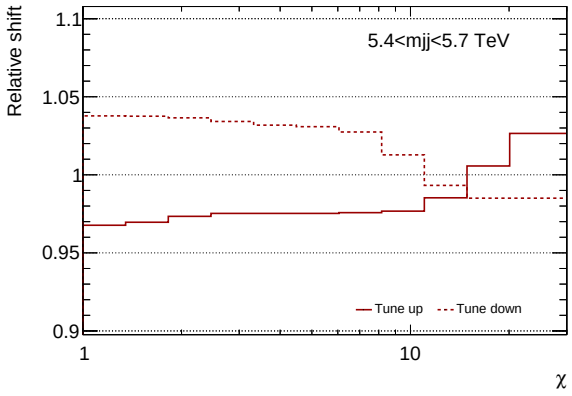

(c) Tune uncertainty.

Figure D.21: Theoretical uncertainties of the background χ distribution in $5.4 < m_{jj} < 5.7$ TeV.

Appendix E

Uncertainty on parton density functions

The angular distributions calculated with three PDF sets: NNPDF2.3, MSTW2008 and CT10 are available for constructing the PDF uncertainty of background. These sets have 100, 41 and 53 PDF subsets respectively. The angular distributions constructed with the nominal PDFs are shown in Figure E.1. The figure indicates that the difference caused by using different PDFs is less than 2% which is very small when compared with JES/JER uncertainties. The angular distributions of the varied PDFs relative to the nominal one within each PDF set are shown in Figure. E.2. All the relative distributions are approximately flat in all PDF sets, which suggests that the shapes of the varied PDFs are close to the nominal one. Thus, their impact on the analysis is expected to be small.

Ref. [66] suggests building envelopes covering the 68% CL errors of each PDF set at first, and then combine the envelopes. Due to the different natures of the PDF sets, the implementations of building $\pm 1\sigma$ variations differ from set to set. As for NNPDF2.3, they are built as

$$\sigma_+ = \sigma_- = \sqrt{\frac{1}{99}\sum_{i=1}^{i=99}(N_i - N_0)^2} \tag{E.1}$$

where the N_i is the expected yield from varied PDF and N_0 is the one from the nominal PDF. The variations of NNPDF2.3 is built symmetrically. As for

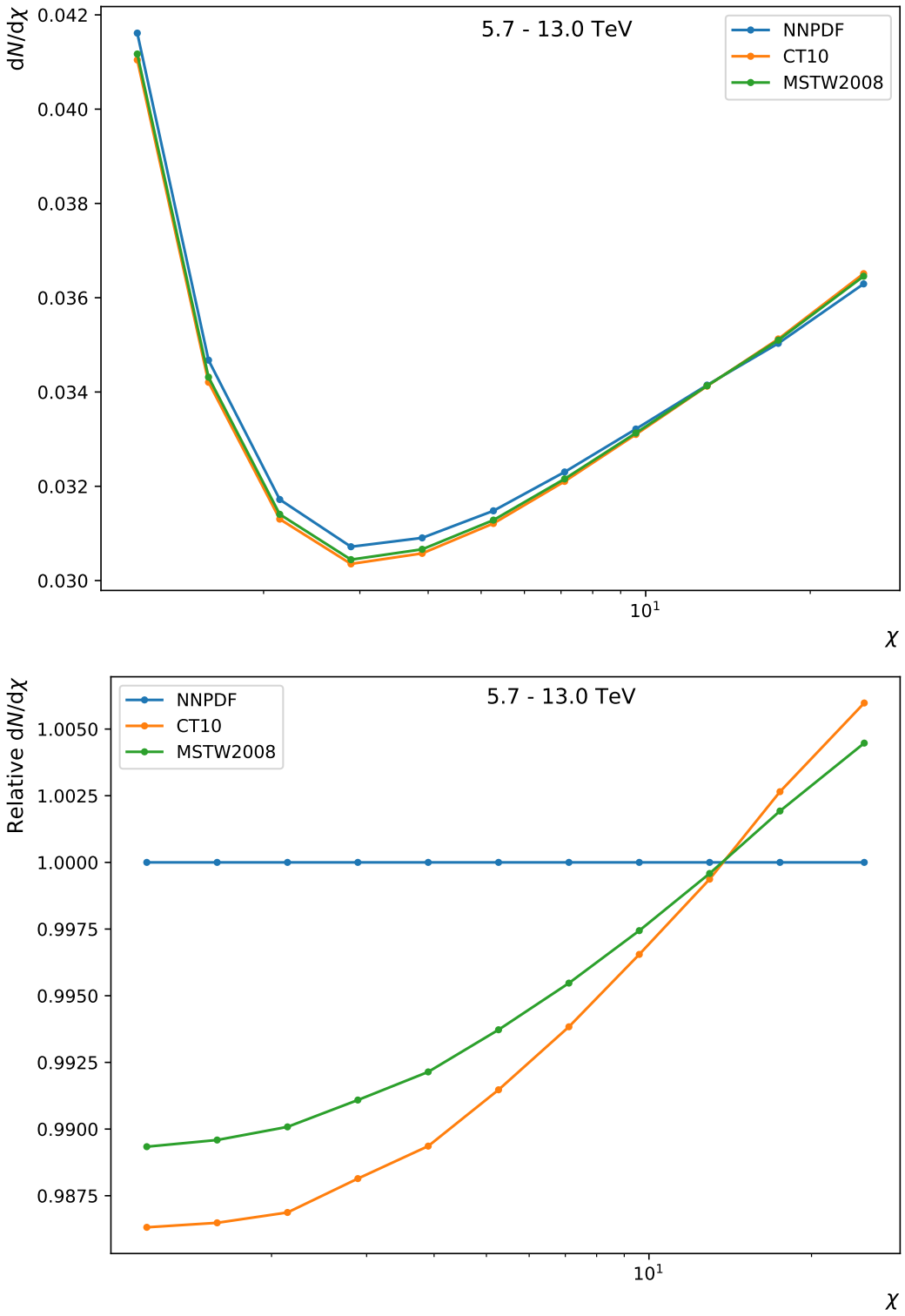

Figure E.1: The top plot shows the normalized angular distributions of the nominal PDFs. The bottom plot shows the angular distributions relative to the one of NNPDF2.3.

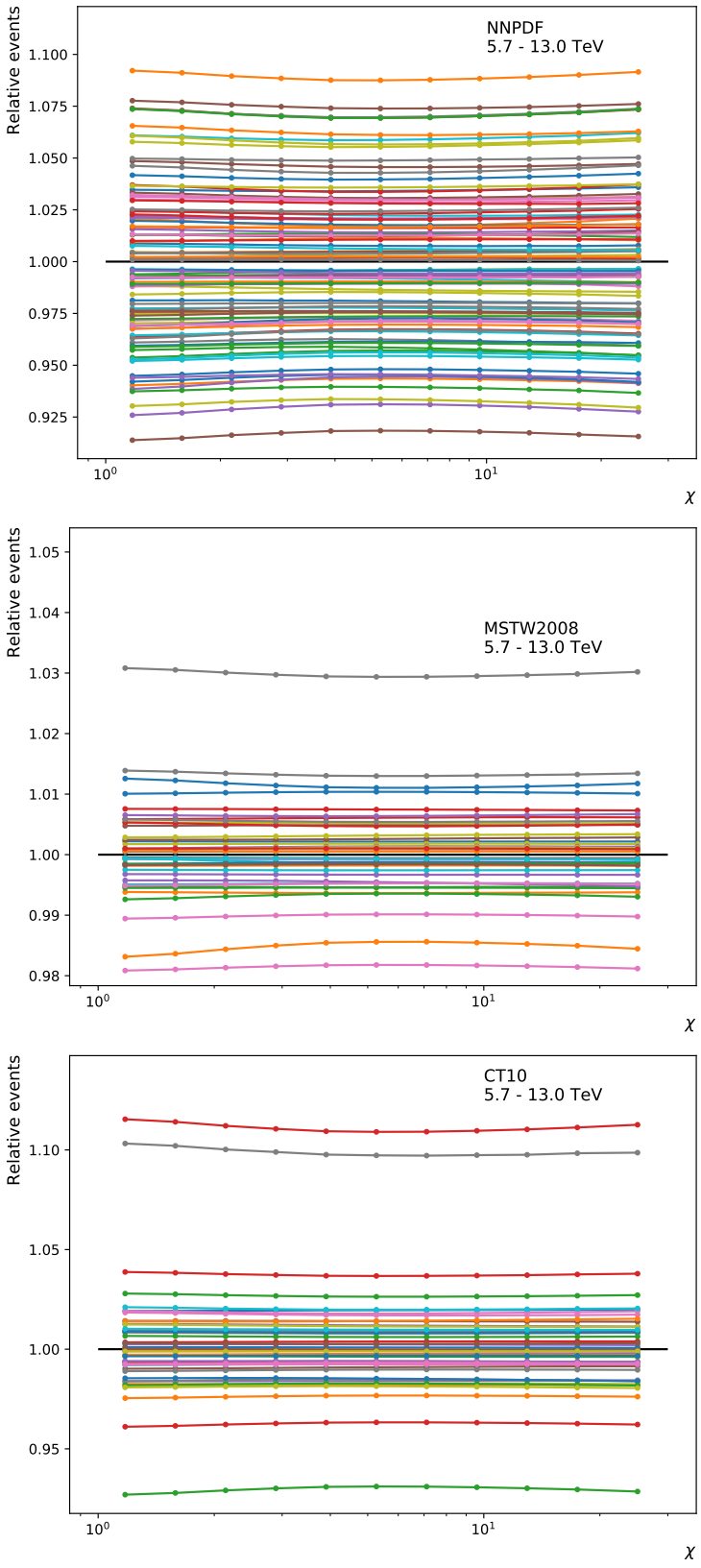

Figure E.2: The relative angular distributions of varied PDFs in (top) NNPDF2.3, (middle) MSTW2008 and (bottom) CT10. Each coloured line represents a varied PDF subset and the black flat line is the base line at 1.

MSTW2008 and CT10, the $\pm 1\sigma$ variations are built as

$$\begin{aligned} \sigma_+ &= w \cdot \sqrt{\sum_i (N_i - N_0)^2} \\ \sigma_- &= w \cdot \sqrt{\sum_j (N_j - N_0)^2} \end{aligned} \tag{E.2}$$

where N_i (N_j) is the expected yield from positively (negatively) varied PDFs. The factor w scales the envelope to 68% CL coverage which is 1 for MSTW2008 and 1/1.64485 for CT10. With the constructed $\pm 1\sigma$ variations, the up-bound and down-bound of the combined envelope are built as

$$\begin{aligned} B_+ &= \max(N_0^{NNPDF} + \sigma_+^{NNPDF}, N_0^{MSTW} + \sigma_+^{MSTW}, N_0^{CT10} + \sigma_+^{CT10}), \\ B_- &= \max(N_0^{NNPDF} - \sigma_-^{NNPDF}, N_0^{MSTW} - \sigma_-^{MSTW}, N_0^{CT10} - \sigma_-^{CT10}), \\ Mid &= (B_{up} + B_{down})/2. \end{aligned} \tag{E.3}$$

Finally, the combined PDF uncertainty is built as

$$\begin{aligned} S_+ &= B_{up}/Mid - 1, \\ S_- &= 1 - B_{down}/Mid, \end{aligned} \tag{E.4}$$

which is considered as the relative uncertainty to the nominal angular distribution. However, this prescription is built for typical analyses but not for shape analyses. Equations E.3 and E.4 bring problems to this analysis. On the one hand, a systematic uncertainty is expected to have a clear physics meaning of its source. Equations E.3 mixes up the variations of the PDF sets when building the up and down bounds. It leads to a mixed shape difference among the PDF sets which makes physics meaning obscure. On the other hand, taking the middle point as the reference centre in Equation E.4 further destroys the shape information of the PDF sets. The built uncertainty is symmetric, which is also not physically motivated. To address these problems, a modified method is developed. The modifications treat the three PDF sets as independent uncertainty sources. The bounds are simplify built as

$$\begin{aligned} B_+^{pdf} &= N_0^{pdf} + \sigma_+^{pdf}, \\ B_-^{pdf} &= N_0^{pdf} - \sigma_-^{pdf}. \end{aligned} \tag{E.5}$$

The up and down uncertainties are built relative to the nominal PDF of the NNPDF2.3 set instead of the median value:

$$\begin{aligned} S_{+}^{pdf} &= B_{+}^{pdf}/N_{0}^{NNPDF} - 1. \\ S_{-}^{pdf} &= 1 - B_{-}^{pdf}/N_{0}^{NNPDF}. \end{aligned} \tag{E.6}$$

These modifications give the uncertainties more physics meaning in terms of shape analysis. The uncertainty from NNPDF2.3 can be translated as the shape variance sourced from its varied PDF subsets. The uncertainties from MSTW2008 and CT10 can be translated as the shape difference between them and NNPDF2.3.

Appendix F

Signal uncertainties

This appendix shows both the raw and smoothed experimental uncertainties of the first seven m_{jj} slices on the HQM sample of $n = 2$ and $M_D = 7$ TeV. For quick access, the contents of the figures are summarized in Table F.1, including the ones of the highest m_{jj} slice shown in Chapter 6.

Table F.1: Figure indexes of experimental systematic uncertainties of the HQM sample ($n = 2$ and $M_D = 7$ TeV) in all m_{jj} slices.

	m_{jj} slices [TeV]							
	3.4–3.7	3.7–4.0	4.0–4.3	4.3–4.6	4.6–4.9	4.9–5.4	5.4–5.7	5.7 –13.0
JES uncertainties	F.1	F.3	F.5	F.7	F.9	F.11	F.13	6.4
Reduced JES/JER uncertainties	F.2	F.4	F.6	F.8	F.10	F.12	F.14	6.5
Smoothed JES uncertainties	F.15	F.17	F.19	F.21	F.23	F.25	F.27	6.6
Smoothed and reduced JES/JER uncertainties	F.16	F.18	F.20	F.22	F.24	F.26	F.28	6.7

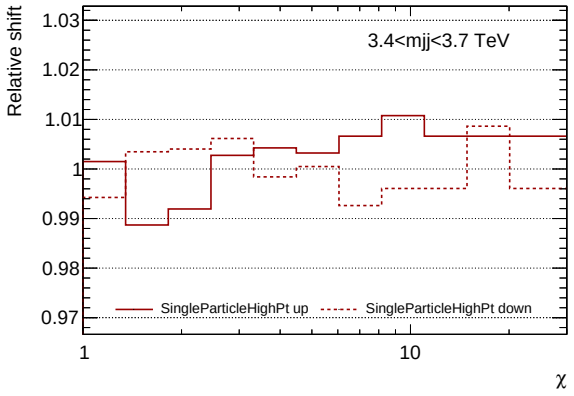

(a) Uncertainty in the single particle response measurement.

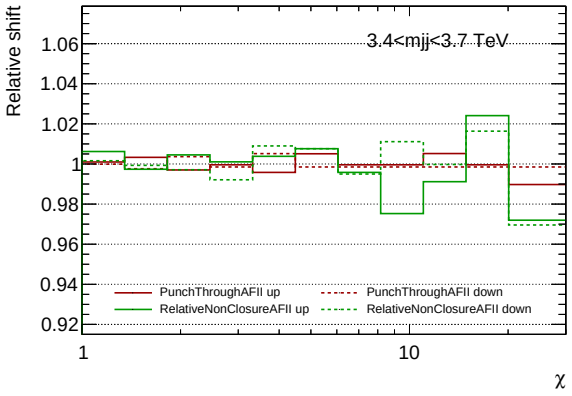

(b) Uncertainties in the correction of partially contained jets and remaining difference between data and MC simulation.

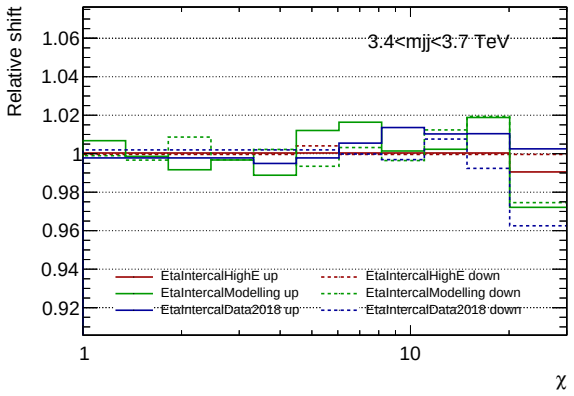

(c) Uncertainties on modelling and describing non-closure in high energy, and tile calibration.

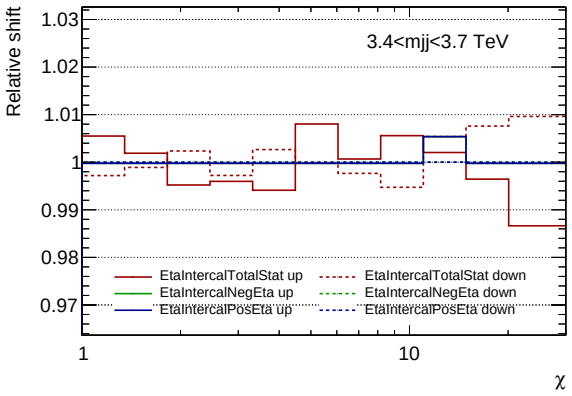

(d) Statistical uncertainty in η intercalibration and systematic uncertainty on describing non-closure at $\eta \approx \pm 2.4$.

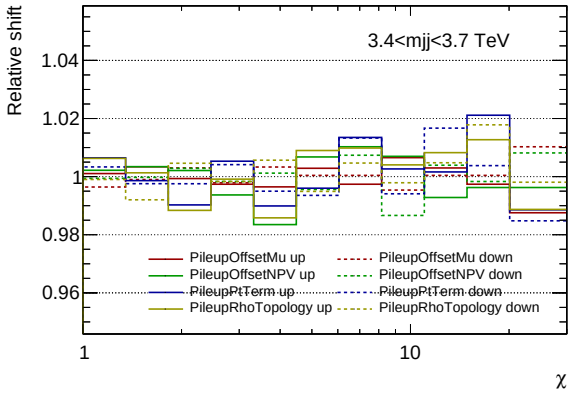

(e) Uncertainties on modelling the pile-up offset term and residual correction.

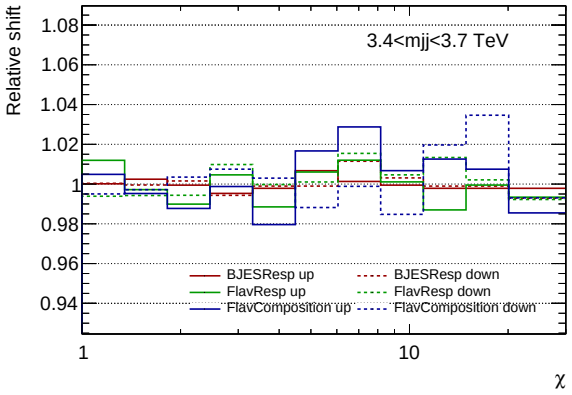

(f) Uncertainty in the response of gluon-initiated and b-quark initiated jets and the composition of quarks and gluons.

Figure F.1: Non-smoothed experimental uncertainties on the HQM sample ($n = 2$ and $M_D = 7$) TeV in $3.4 < m_{jj} < 3.7$ TeV.

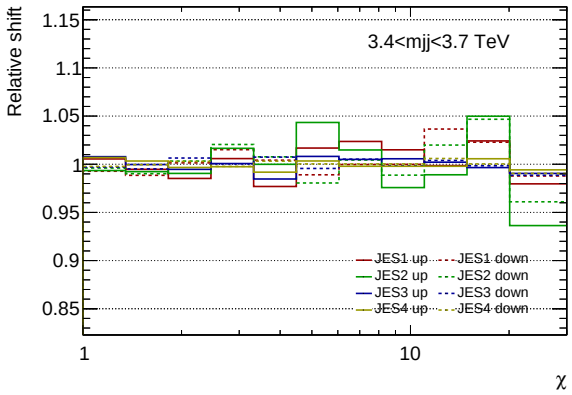

(a) Reduced *in situ* JES uncertainties 1–4.

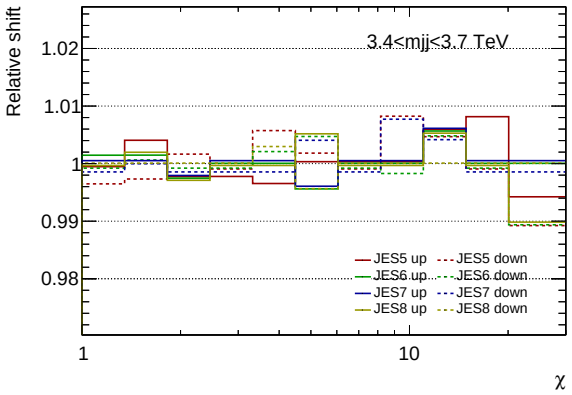

(b) Reduced *in situ* JES uncertainties 5–8.

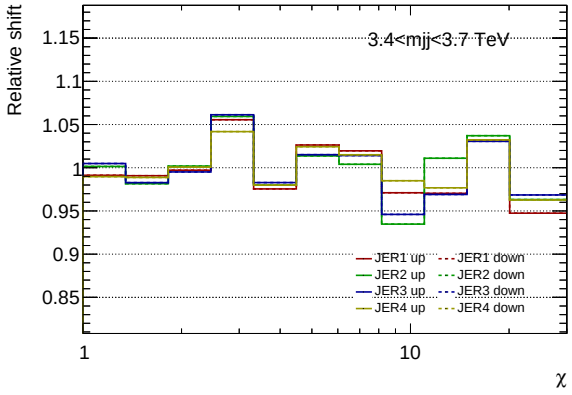

(c) Reduced JER uncertainties 1–4.

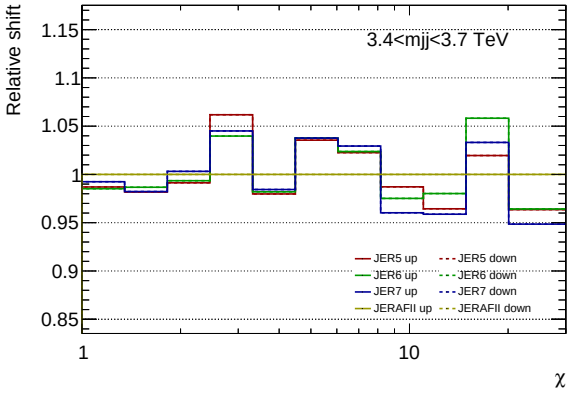

(d) Reduced JER uncertainties 5–7 and uncertainty in difference between simulation and data.

Figure F.2: Non-smoothed reduced experimental uncertainties on the HQM sample ($n = 2$ and $M_D = 7$) TeV in $3.4 < m_{jj} < 3.7$ TeV.

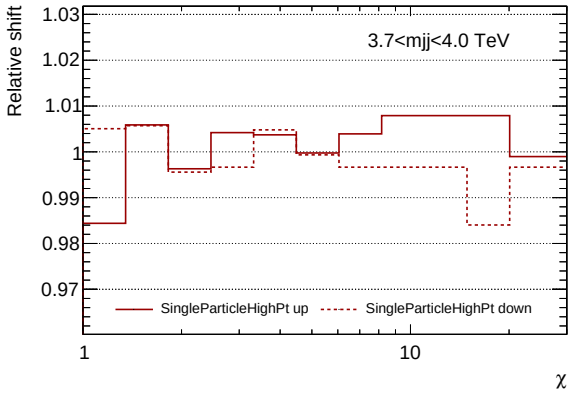

(a) Uncertainty in the single particle response measurement.

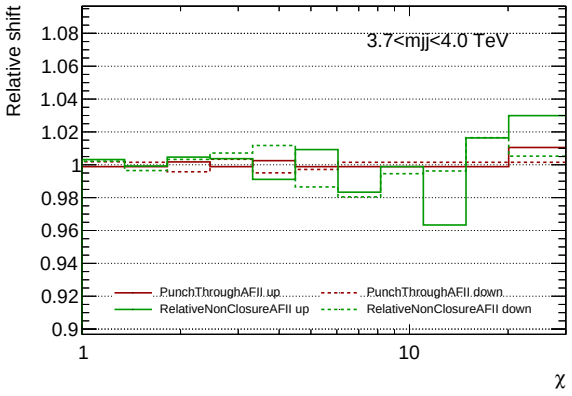

(b) Uncertainties in the correction of partially contained jets and remaining difference between data and MC simulation.

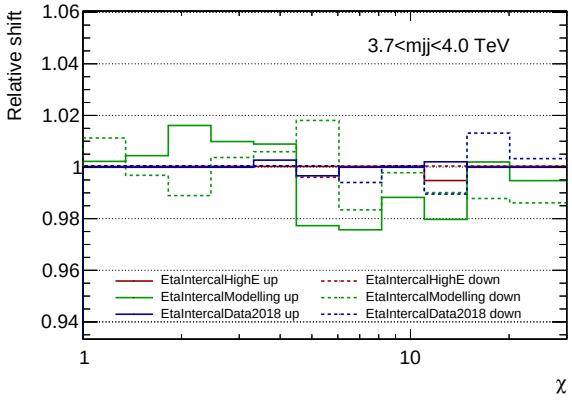

(c) Uncertainties on modelling and describing non-closure in high energy, and tile calibration.

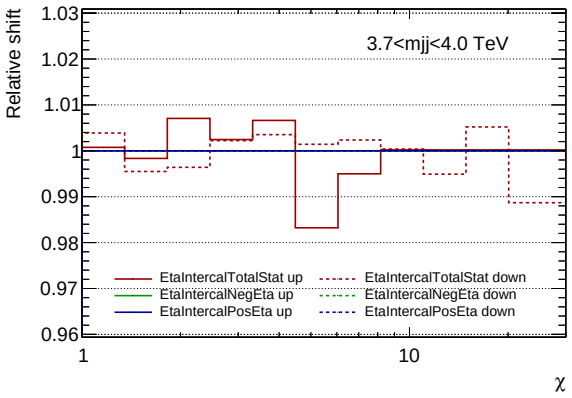

(d) Statistical uncertainty in η intercalibration and systematic uncertainty on describing non-closure at $\eta \approx \pm 2.4$.

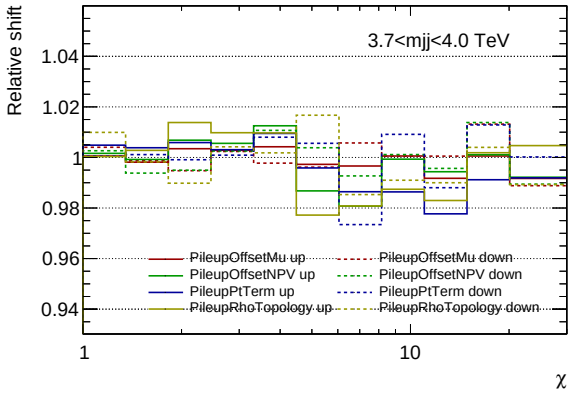

(e) Uncertainties on modelling the pile-up offset term and residual correction.

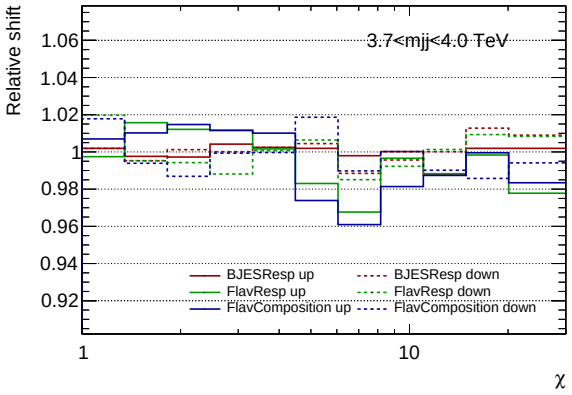

(f) Uncertainty in the response of gluon-initiated and b-quark initiated jets and the composition of quarks and gluons.

Figure F.3: Non-smoothed experimental uncertainties on the HQM sample ($n = 2$ and $M_D = 7$) TeV in $3.7 < m_{jj} < 4.0$ TeV.

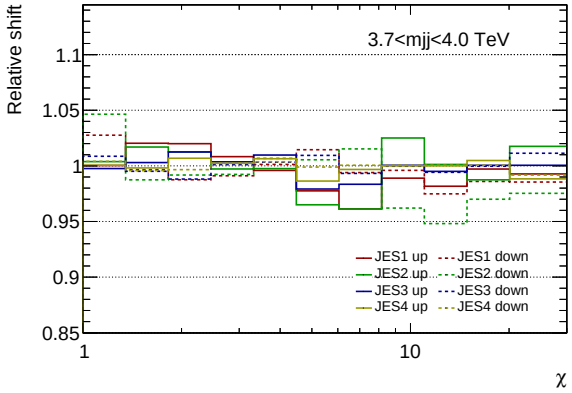

(a) Reduced *in situ* JES uncertainties 1–4.

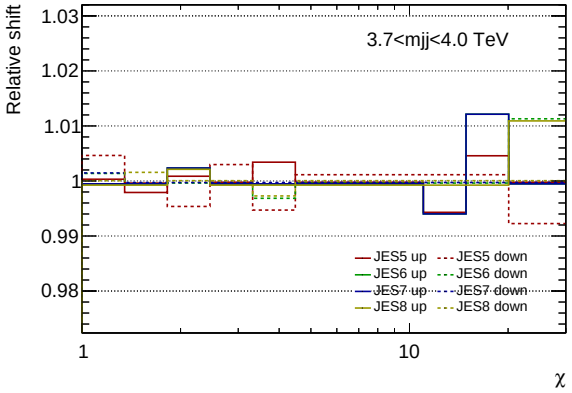

(b) Reduced *in situ* JES uncertainties 5–8.

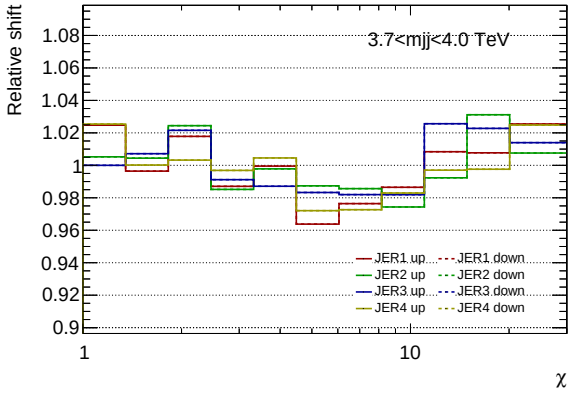

(c) Reduced JER uncertainties 1–4.

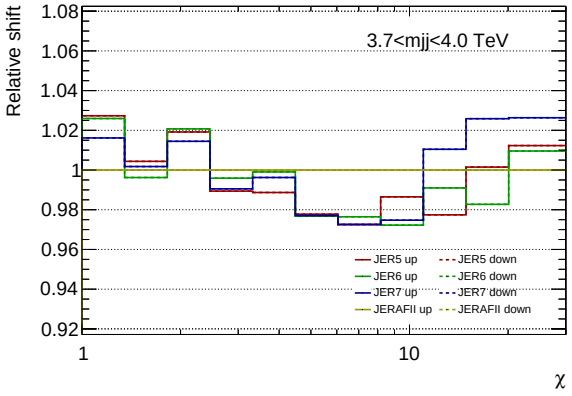

(d) Reduced JER uncertainties 5–7 and uncertainty in difference between simulation and data.

Figure F.4: Non-smoothed reduced experimental uncertainties on the HQM sample ($n = 2$ and $M_D = 7$) TeV in $3.7 < m_{jj} < 4.0$ TeV.

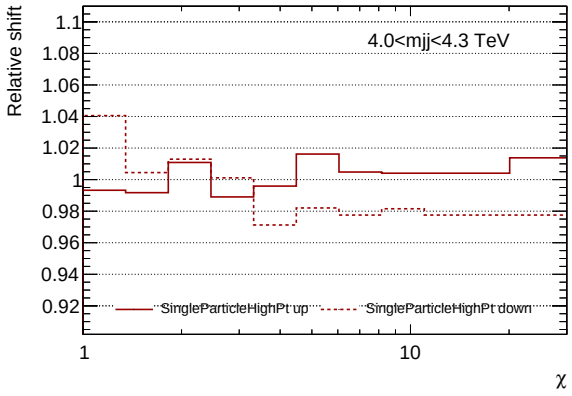

(a) Uncertainty in the single particle response measurement.

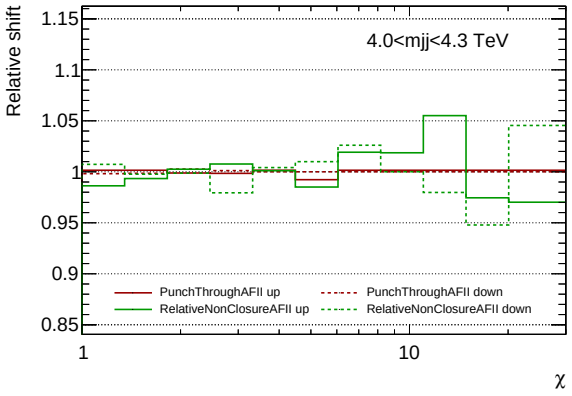

(b) Uncertainties in the correction of partially contained jets and remaining difference between data and MC simulation.

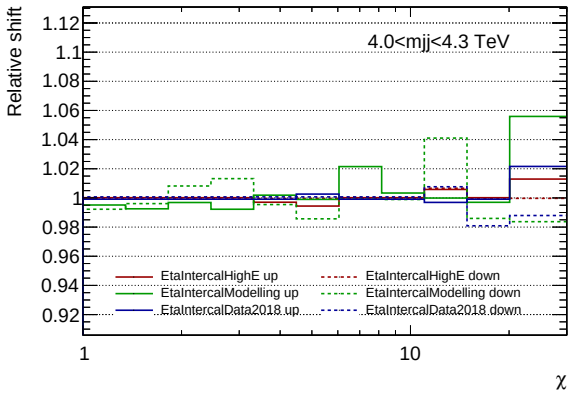

(c) Uncertainties on modelling and describing non-closure in high energy, and tile calibration.

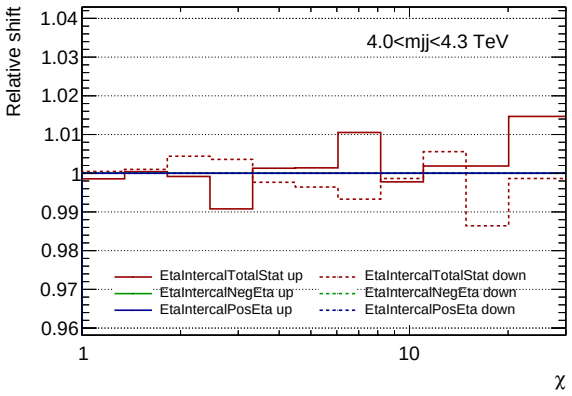

(d) Statistical uncertainty in η intercalibration and systematic uncertainty on describing non-closure at $\eta \approx \pm 2.4$.

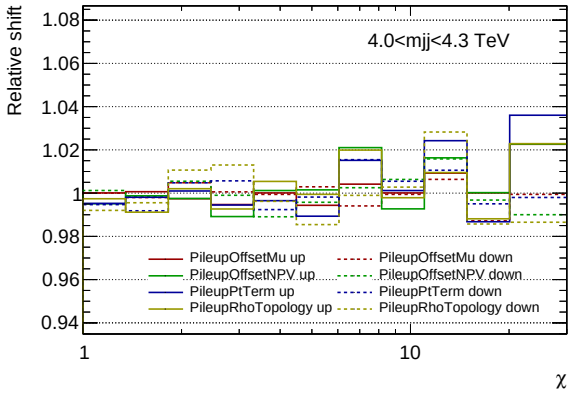

(e) Uncertainties on modelling the pile-up offset term and residual correction.

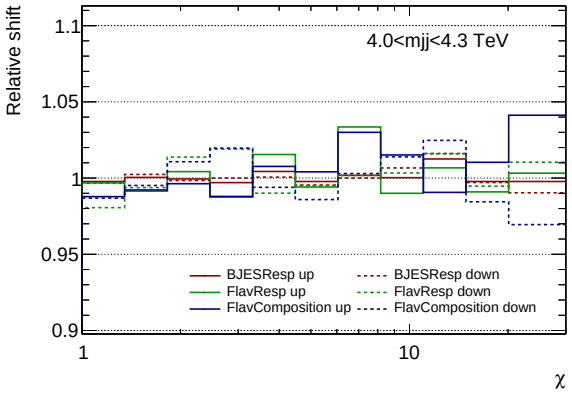

(f) Uncertainty in the response of gluon-initiated and b-quark initiated jets and the composition of quarks and gluons.

Figure F.5: Non-smoothed experimental uncertainties on the HQM sample ($n = 2$ and $M_D = 7$) TeV in $4.0 < m_{jj} < 4.3$ TeV.

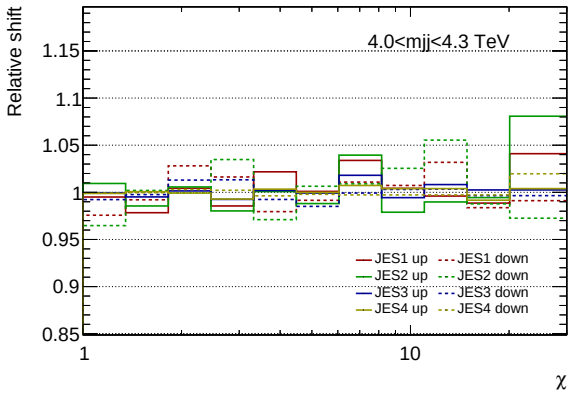

(a) Reduced *in situ* JES uncertainties 1–4.

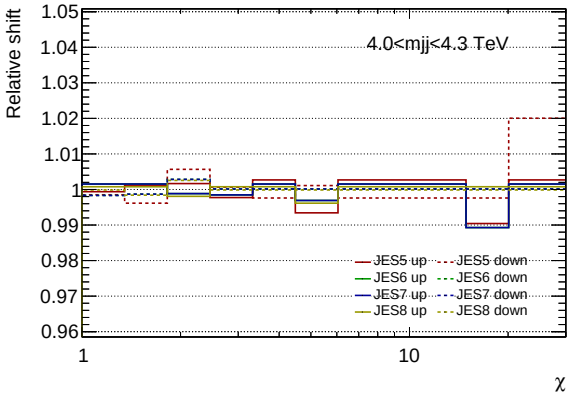

(b) Reduced *in situ* JES uncertainties 5–8.

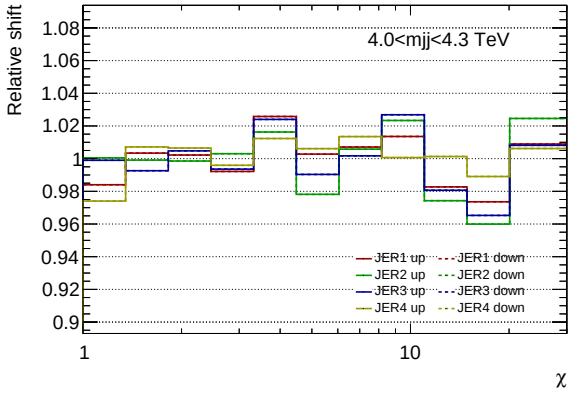

(c) Reduced JER uncertainties 1–4.

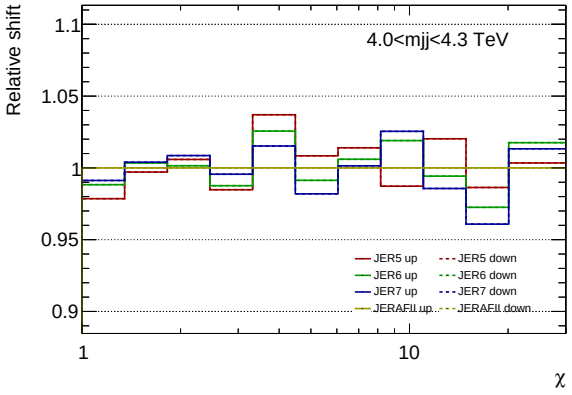

(d) Reduced JER uncertainties 5–7 and uncertainty in difference between simulation and data.

Figure F.6: Non-smoothed reduced experimental uncertainties on the HQM sample ($n = 2$ and $M_D = 7$) TeV in $4.0 < m_{jj} < 4.3$ TeV.

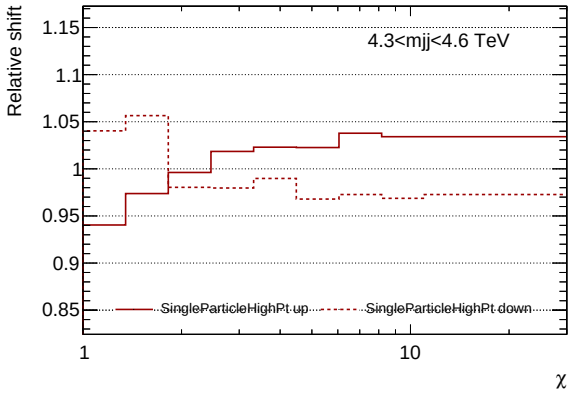

(a) Uncertainty in the single particle response measurement.

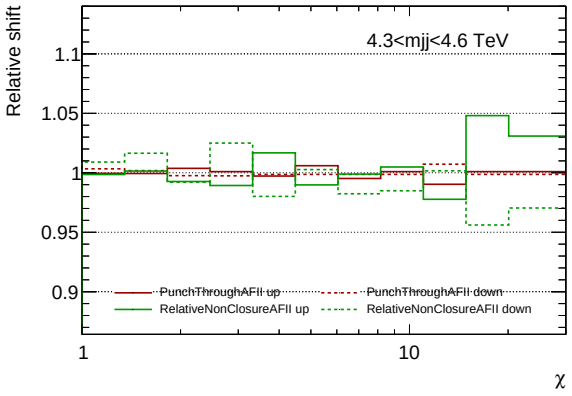

(b) Uncertainties in the correction of partially contained jets and remaining difference between data and MC simulation.

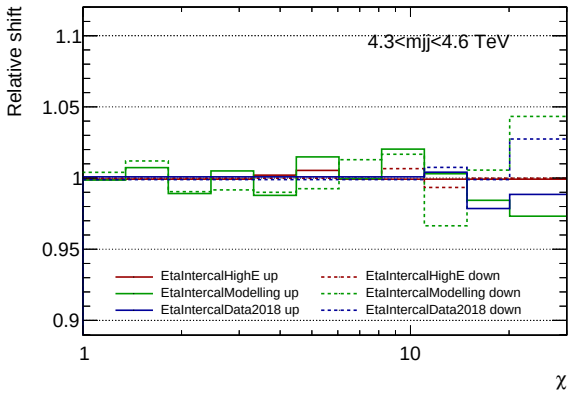

(c) Uncertainties on modelling and describing non-closure in high energy, and tile calibration.

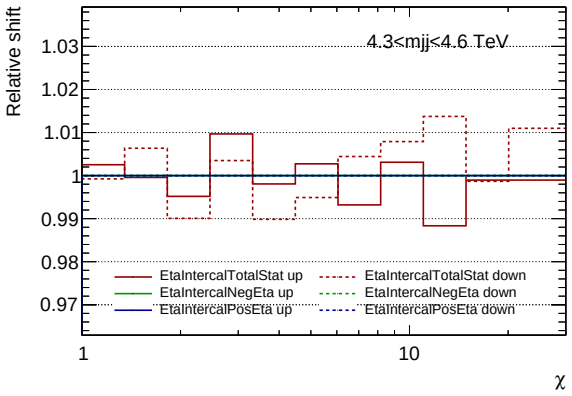

(d) Statistical uncertainty in η intercalibration and systematic uncertainty on describing non-closure at $\eta \approx \pm 2.4$.

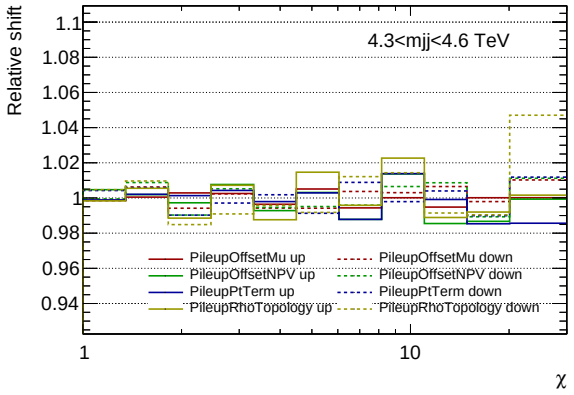

(e) Uncertainties on modelling the pile-up offset term and residual correction.

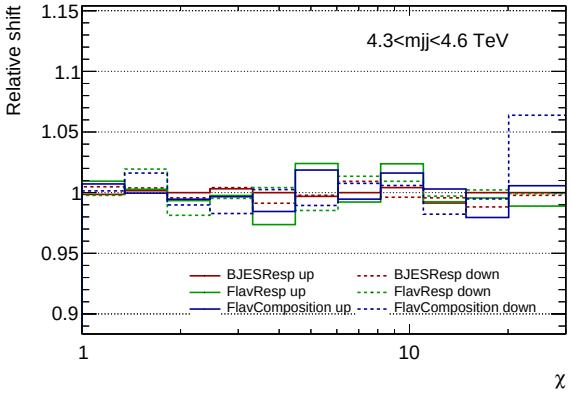

(f) Uncertainty in the response of gluon-initiated and b-quark initiated jets and the composition of quarks and gluons.

Figure F.7: Non-smoothed experimental uncertainties on the HQM sample ($n = 2$ and $M_D = 7$) TeV in $4.3 < m_{jj} < 4.6$ TeV.

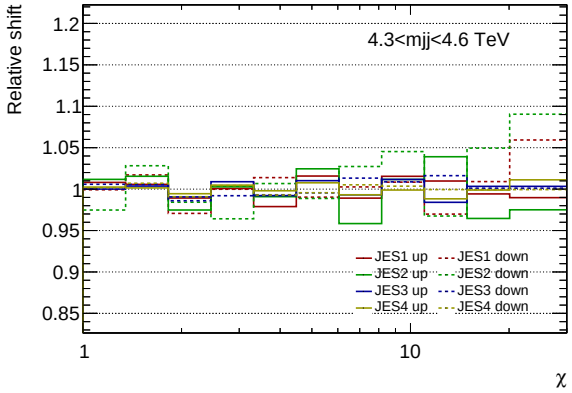

(a) Reduced *in situ* JES uncertainties 1–4.

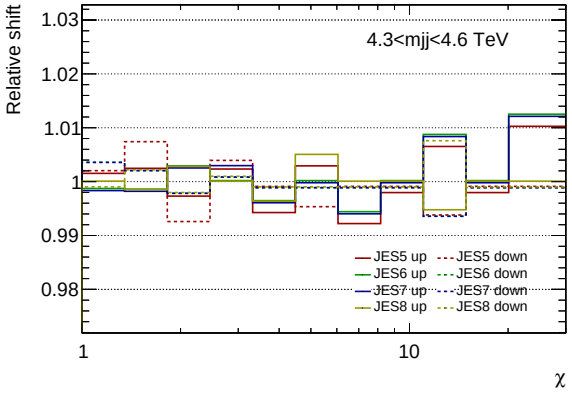

(b) Reduced *in situ* JES uncertainties 5–8.

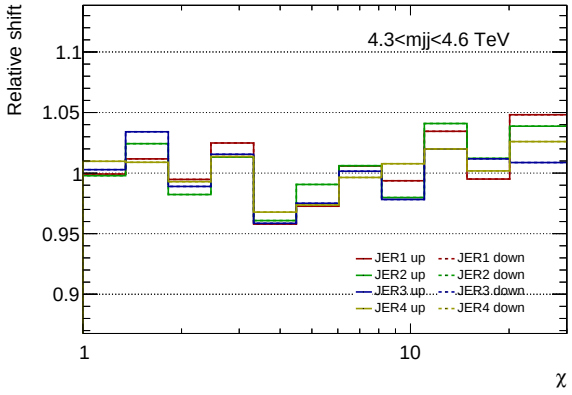

(c) Reduced JER uncertainties 1–4.

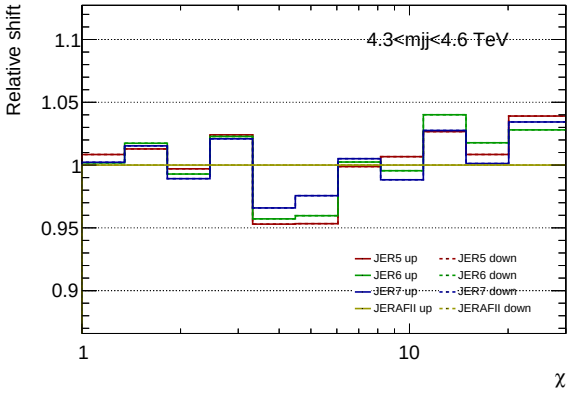

(d) Reduced JER uncertainties 5–7 and uncertainty in difference between simulation and data.

Figure F.8: Non-smoothed reduced experimental uncertainties on the HQM sample ($n = 2$ and $M_D = 7$) TeV in $4.3 < m_{jj} < 4.6$ TeV.

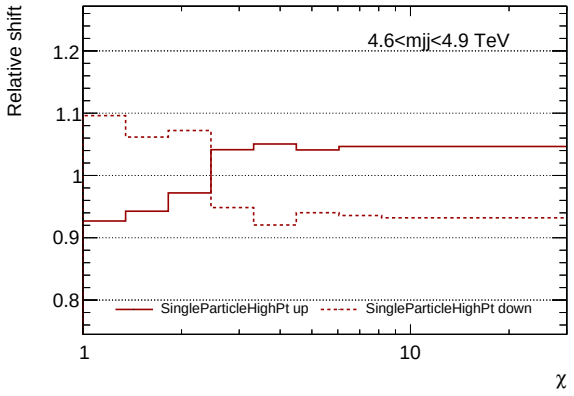

(a) Uncertainty in the single particle response measurement.

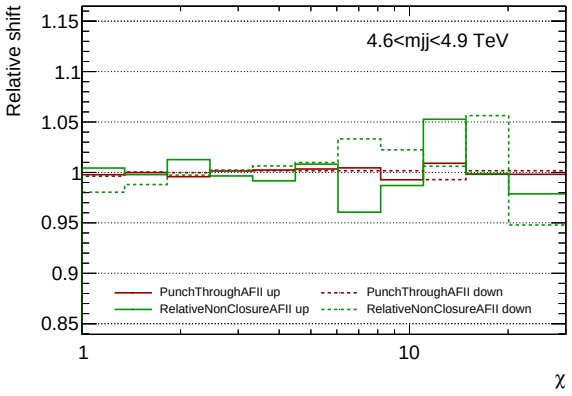

(b) Uncertainties in the correction of partially contained jets and remaining difference between data and MC simulation.

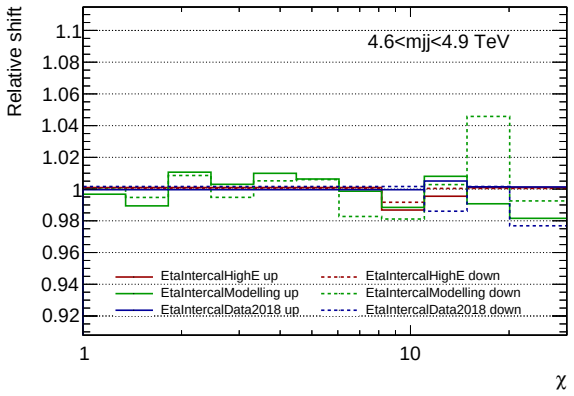

(c) Uncertainties on modelling and describing non-closure in high energy, and tile calibration.

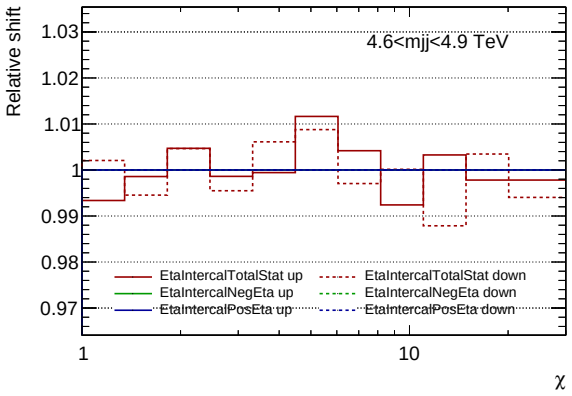

(d) Statistical uncertainty in η intercalibration and systematic uncertainty on describing non-closure at $\eta \approx \pm 2.4$.

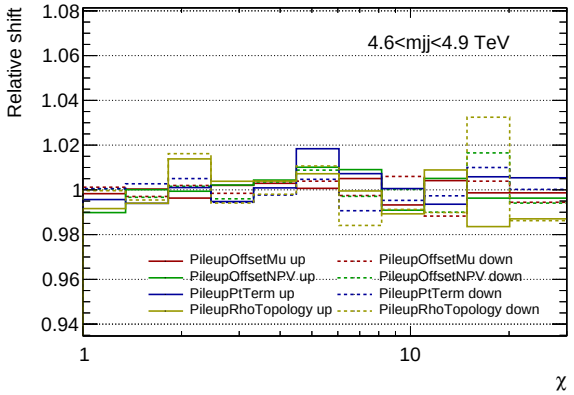

(e) Uncertainties on modelling the pile-up offset term and residual correction.

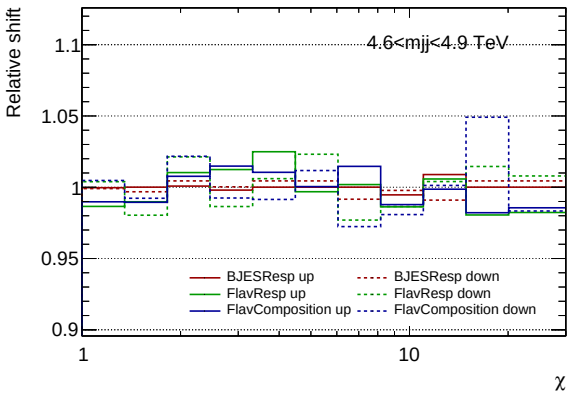

(f) Uncertainty in the response of gluon-initiated and b-quark initiated jets and the composition of quarks and gluons.

Figure F.9: Non-smoothed experimental uncertainties on the HQM sample ($n = 2$ and $M_D = 7$) TeV in $4.6 < m_{jj} < 4.9$ TeV.

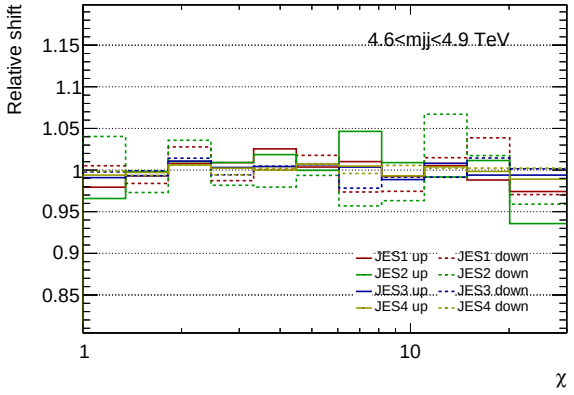

(a) Reduced *in situ* JES uncertainties 1–4.

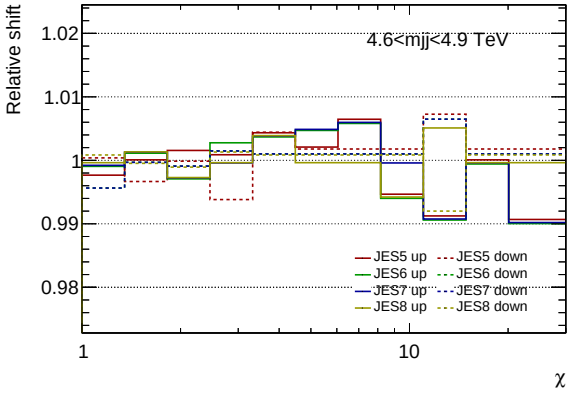

(b) Reduced *in situ* JES uncertainties 5–8.

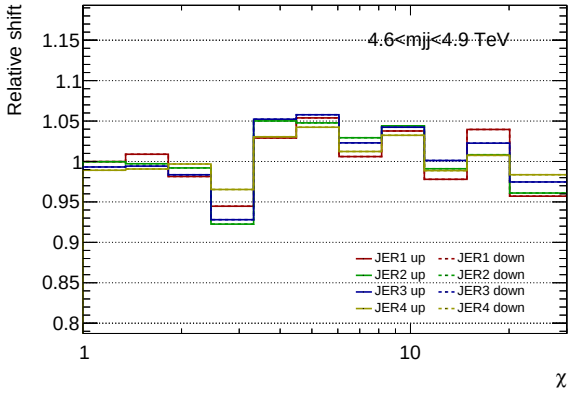

(c) Reduced JER uncertainties 1–4.

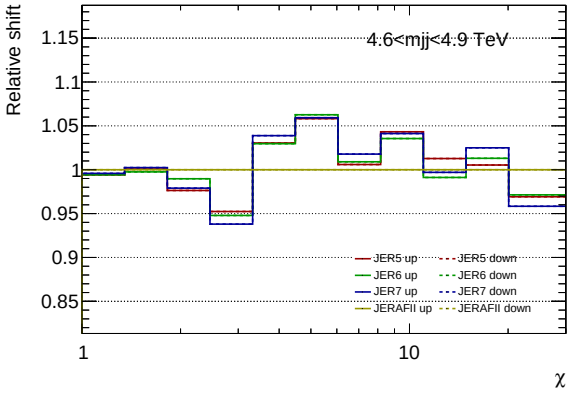

(d) Reduced JER uncertainties 5–7 and uncertainty in difference between simulation and data.

Figure F.10: Non-moothed reduced experimental uncertainties on the HQM sample ($n = 2$ and $M_D = 7$) TeV in $4.6 < m_{jj} < 4.9$ TeV.

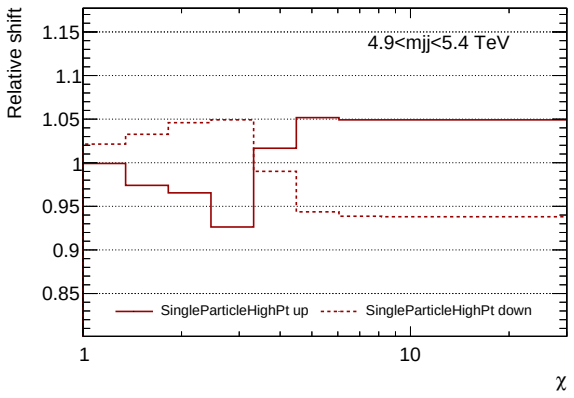

(a) Uncertainty in the single particle response measurement.

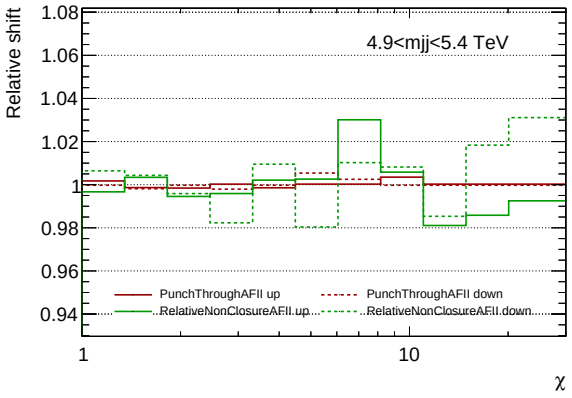

(b) Uncertainties in the correction of partially contained jets and remaining difference between data and MC simulation.

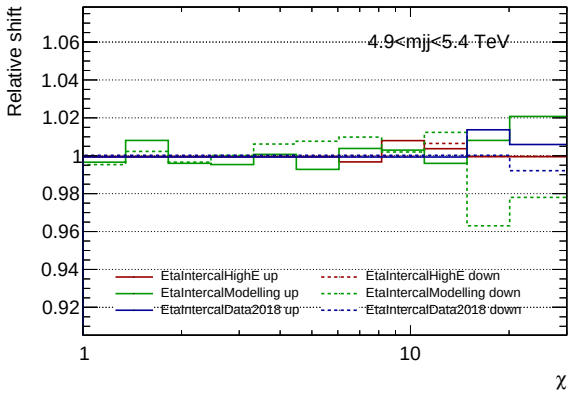

(c) Uncertainties on modelling and describing non-closure in high energy, and tile calibration.

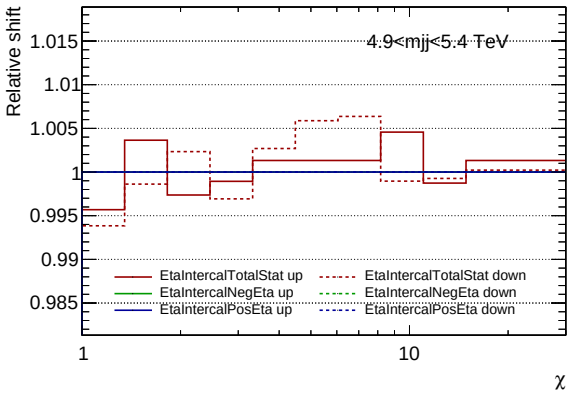

(d) Statistical uncertainty in η intercalibration and systematic uncertainty on describing non-closure at $\eta \approx \pm 2.4$.

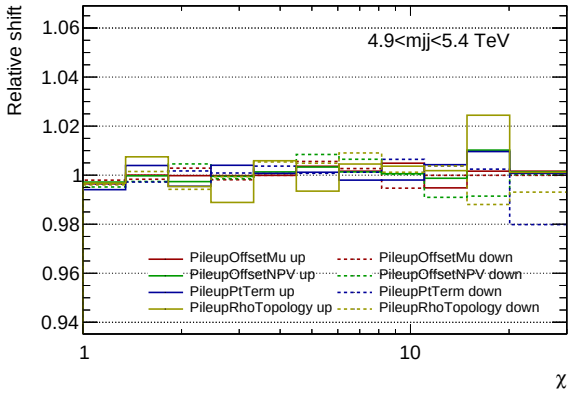

(e) Uncertainties on modelling the pile-up offset term and residual correction.

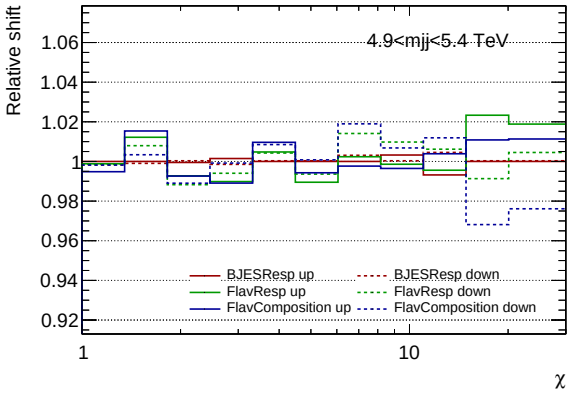

(f) Uncertainty in the response of gluon-initiated and b-quark initiated jets and the composition of quarks and gluons.

Figure F.11: Non-smoothed experimental uncertainties on the HQM sample ($n = 2$ and $M_D = 7$) TeV in $4.9 < m_{jj} < 5.4$ TeV.

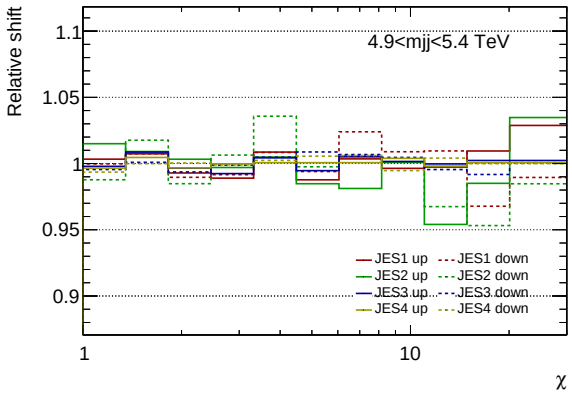

(a) Reduced *in situ* JES uncertainties 1–4.

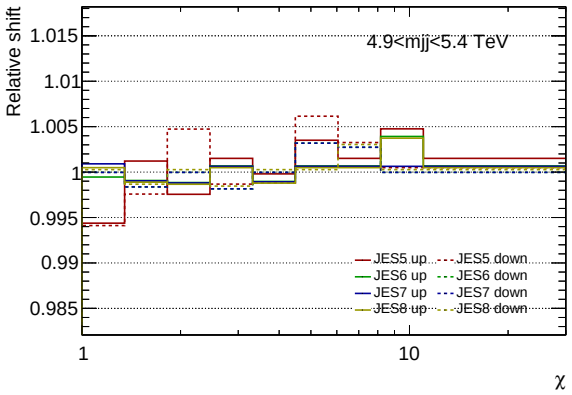

(b) Reduced *in situ* JES uncertainties 5–8.

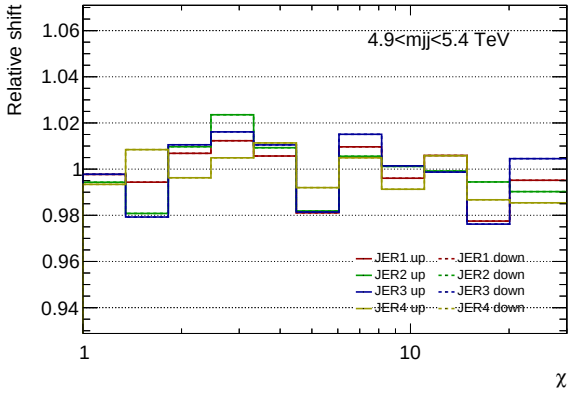

(c) Reduced JER uncertainties 1–4.

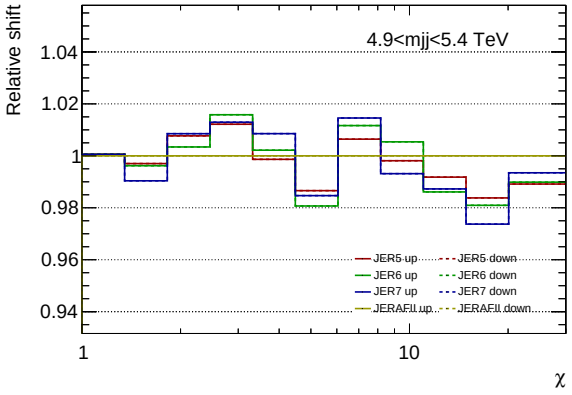

(d) Reduced JER uncertainties 5–7 and uncertainty in difference between simulation and data.

Figure F.12: Non-moothed reduced experimental uncertainties on the HQM sample ($n = 2$ and $M_D = 7$) TeV in $4.9 < m_{jj} < 5.4$ TeV.

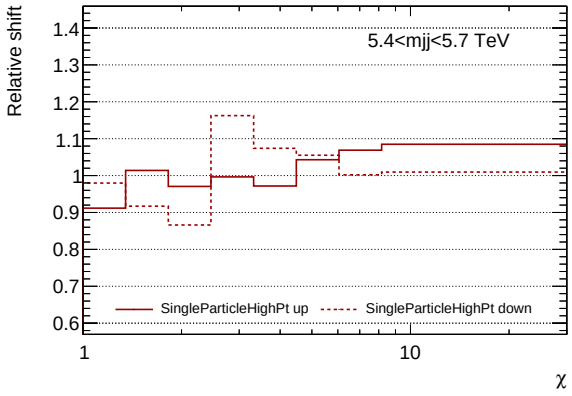

(a) Uncertainty in the single particle response measurement.

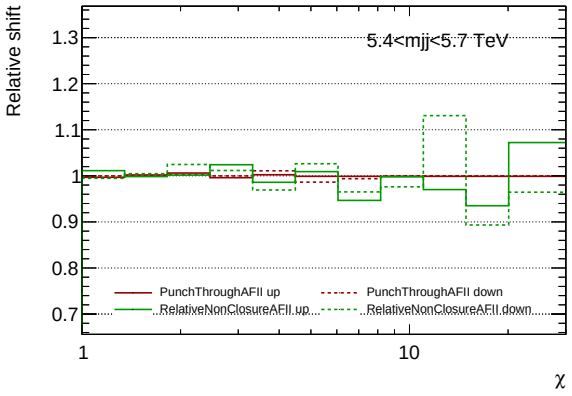

(b) Uncertainties in the correction of partially contained jets and remaining difference between data and MC simulation.

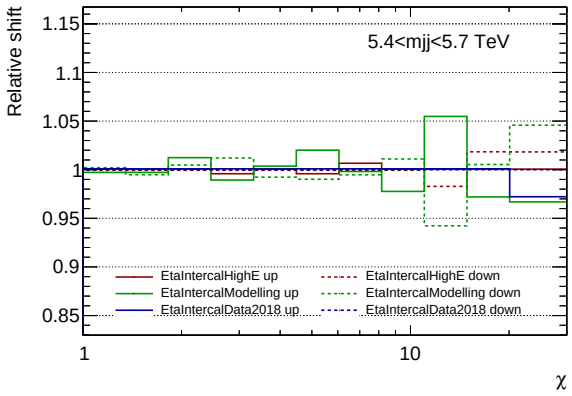

(c) Uncertainties on modelling and describing non-closure in high energy, and tile calibration.

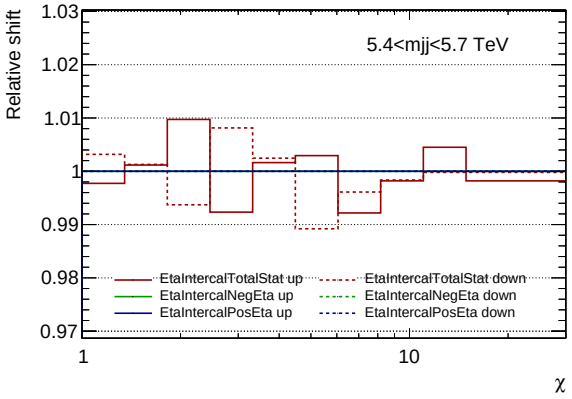

(d) Statistical uncertainty in η intercalibration and systematic uncertainty on describing non-closure at $\eta \approx \pm 2.4$.

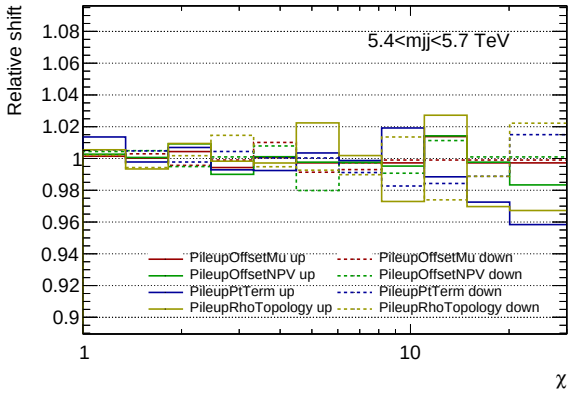

(e) Uncertainties on modelling the pile-up offset term and residual correction.

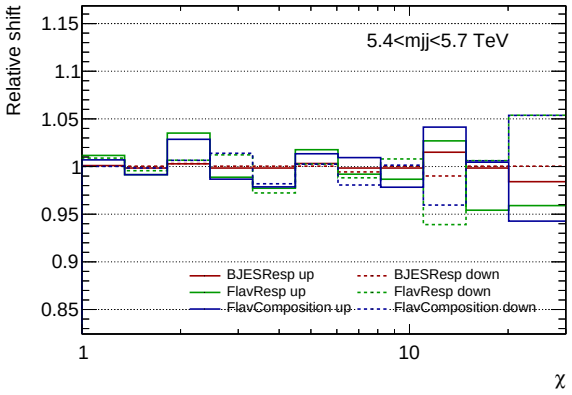

(f) Uncertainty in the response of gluon-initiated and b-quark initiated jets and the composition of quarks and gluons.

Figure F.13: Non-smoothed experimental uncertainties on the HQM sample ($n = 2$ and $M_D = 7$) TeV in $5.4 < m_{jj} < 5.7$ TeV.

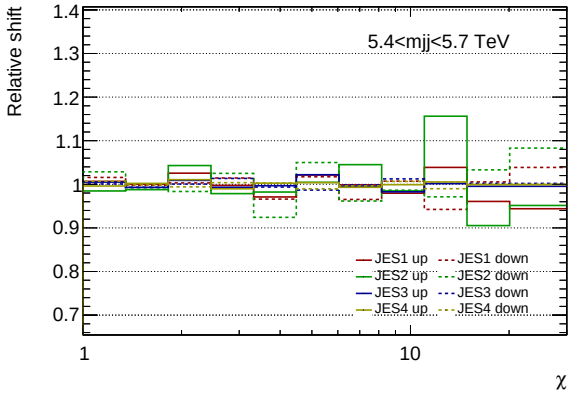

(a) Reduced *in situ* JES uncertainties 1–4.

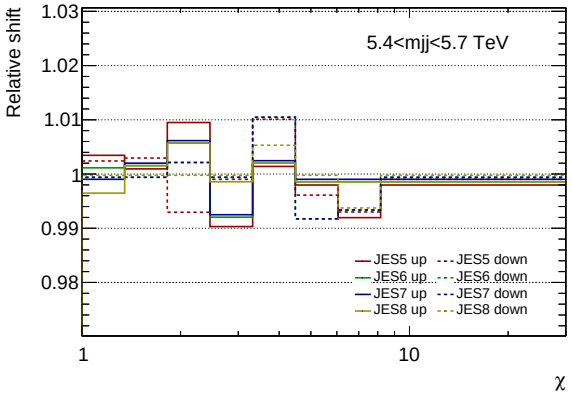

(b) Reduced *in situ* JES uncertainties 5–8.

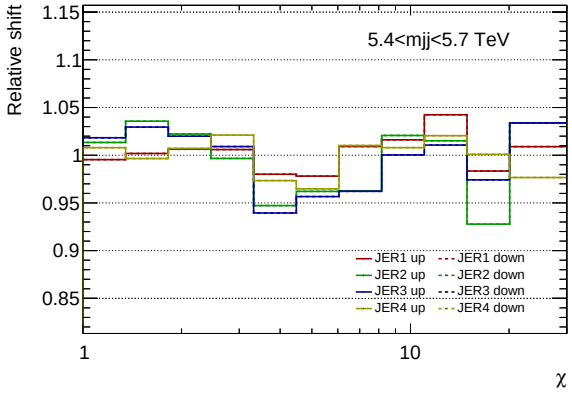

(c) Reduced JER uncertainties 1–4.

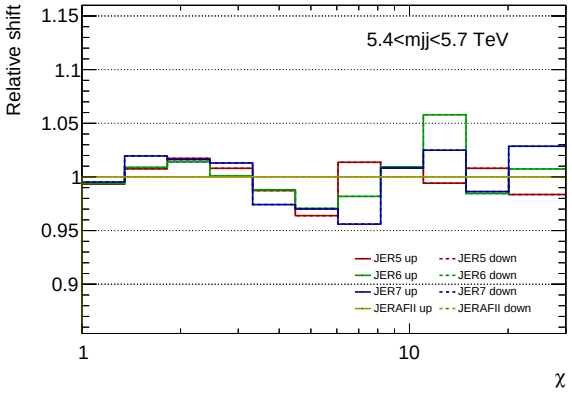

(d) Reduced JER uncertainties 5–7 and uncertainty in difference between simulation and data.

Figure F.14: Non-smoothed reduced experimental uncertainties on the HQM sample ($n = 2$ and $M_D = 7$) TeV in $5.4 < m_{jj} < 5.7$ TeV.

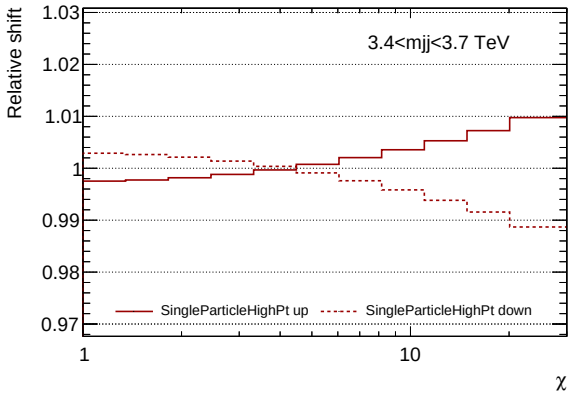

(a) Uncertainty in the single particle response measurement.

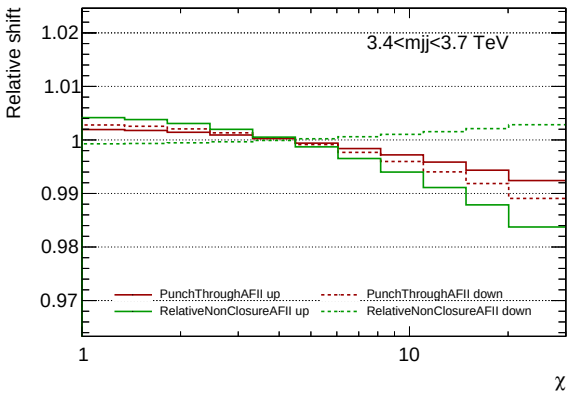

(b) Uncertainties in the correction of partially contained jets and remaining difference between data and MC simulation.

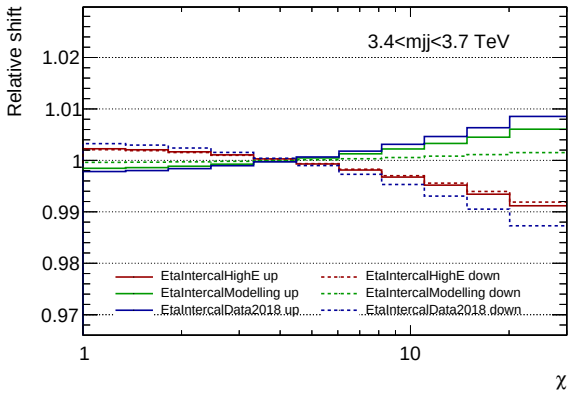

(c) Uncertainties on modelling and describing non-closure in high energy, and tile calibration.

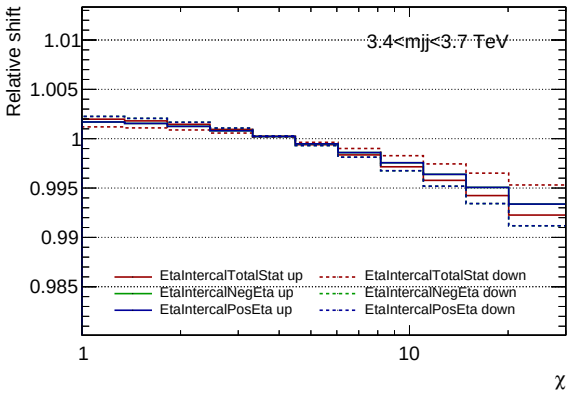

(d) Statistical uncertainty in η intercalibration and systematic uncertainty on describing non-closure at $\eta \approx \pm 2.4$.

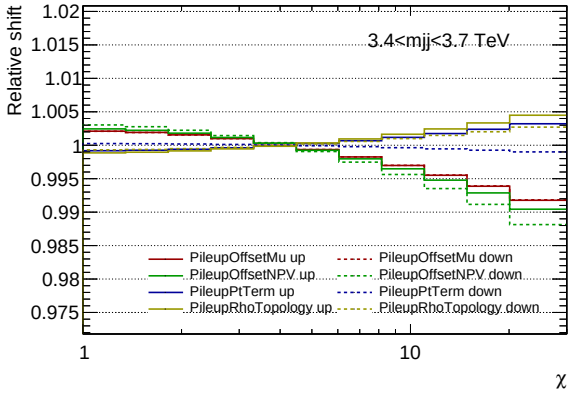

(e) Uncertainties on modelling the pile-up offset term and residual correction.

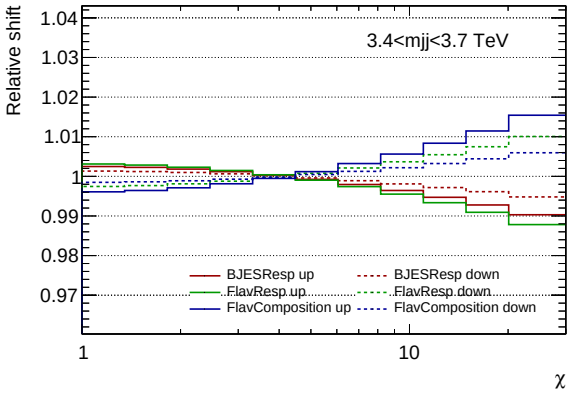

(f) Uncertainty in the response of gluon-initiated and b-quark initiated jets and the composition of quarks and gluons.

Figure F.15: Smoothed experimental uncertainties on the HQM sample ($n = 2$ and $M_D = 7$) TeV in $3.4 < m_{jj} < 3.7$ TeV.

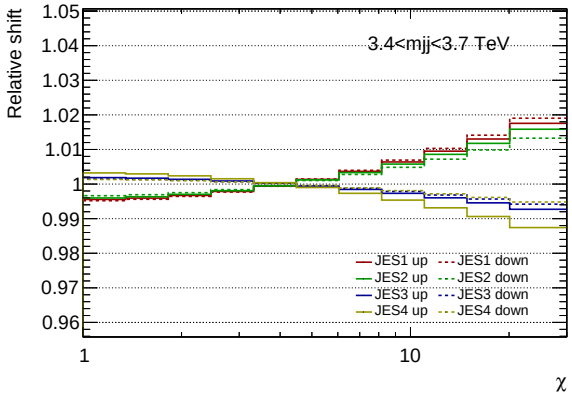

(a) Reduced *in situ* JES uncertainties 1–4.

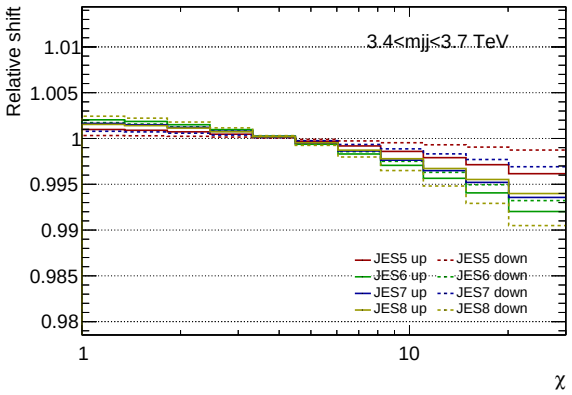

(b) Reduced *in situ* JES uncertainties 5–8.

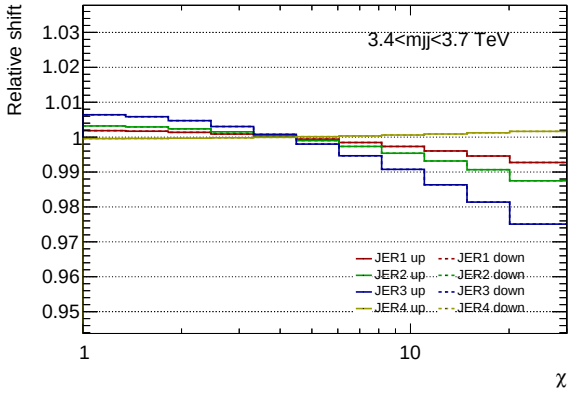

(c) Reduced JER uncertainties 1–4.

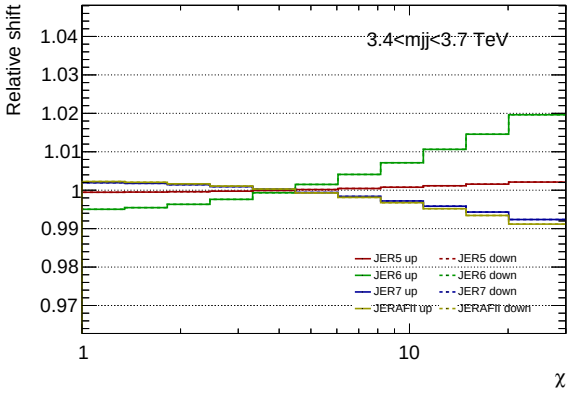

(d) Reduced JER uncertainties 5–7 and uncertainty in difference between simulation and data.

Figure F.16: Smoothed reduced experimental uncertainties on the HQM sample ($n = 2$ and $M_D = 7$) TeV in $3.4 < m_{jj} < 3.7$ TeV.

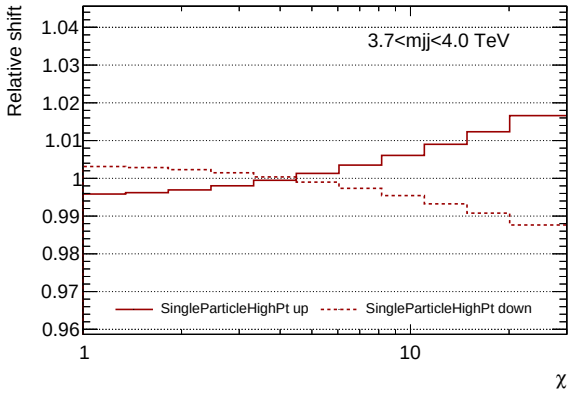

(a) Uncertainty in the single particle response measurement.

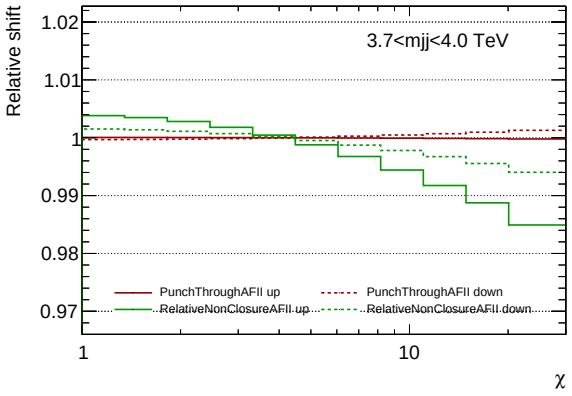

(b) Uncertainties in the correction of partially contained jets and remaining difference between data and MC simulation.

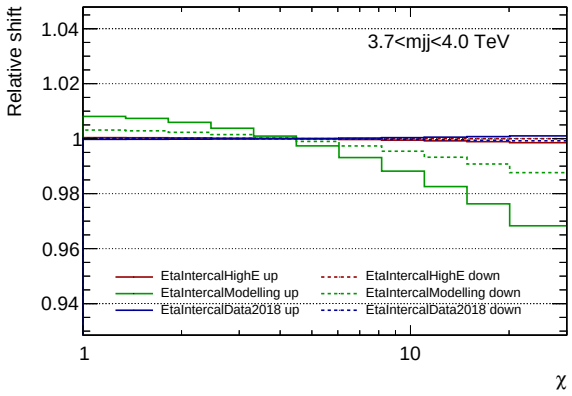

(c) Uncertainties on modelling and describing non-closure in high energy, and tile calibration.

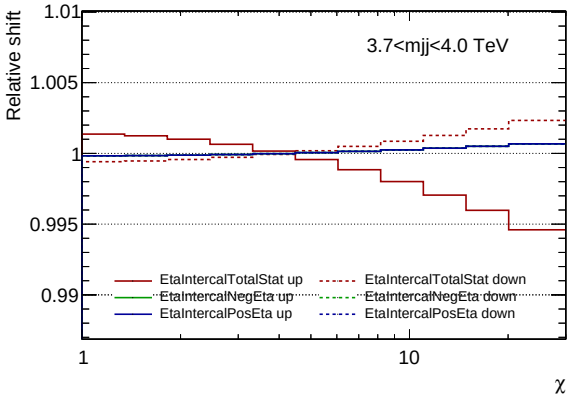

(d) Statistical uncertainty in η intercalibration and systematic uncertainty on describing non-closure at $\eta \approx \pm 2.4$.

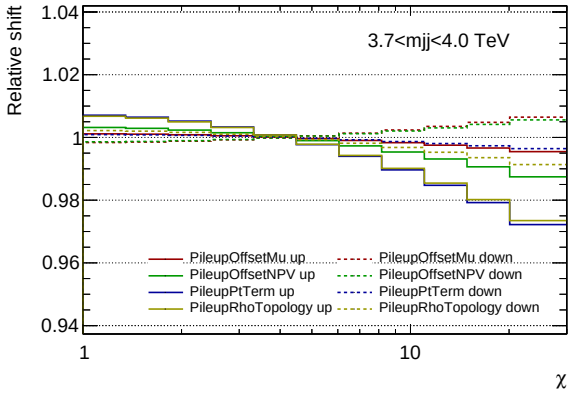

(e) Uncertainties on modelling the pile-up offset term and residual correction.

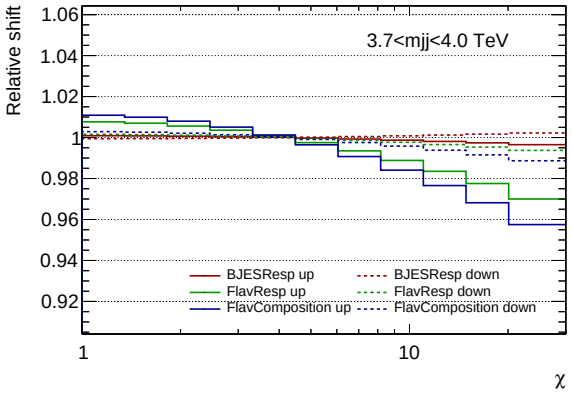

(f) Uncertainty in the response of gluon-initiated and b-quark initiated jets and the composition of quarks and gluons.

Figure F.17: Smoothed experimental uncertainties on the HQM sample ($n = 2$ and $M_D = 7$) TeV in $3.7 < m_{jj} < 4.0$ TeV.

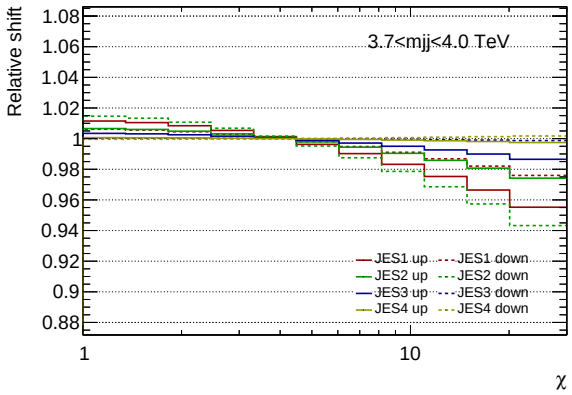

(a) Reduced *in situ* JES uncertainties 1–4.

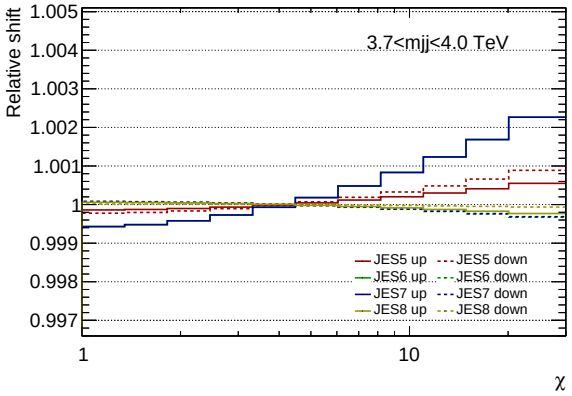

(b) Reduced *in situ* JES uncertainties 5–8.

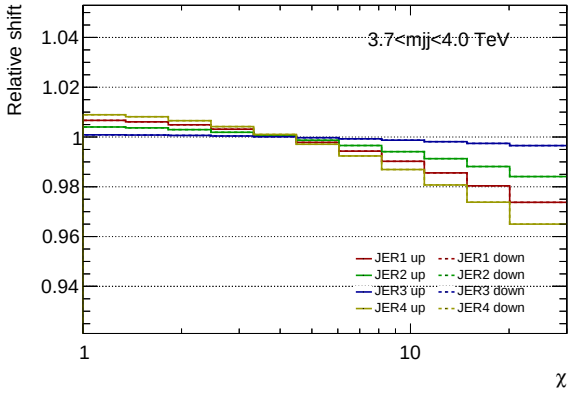

(c) Reduced JER uncertainties 1–4.

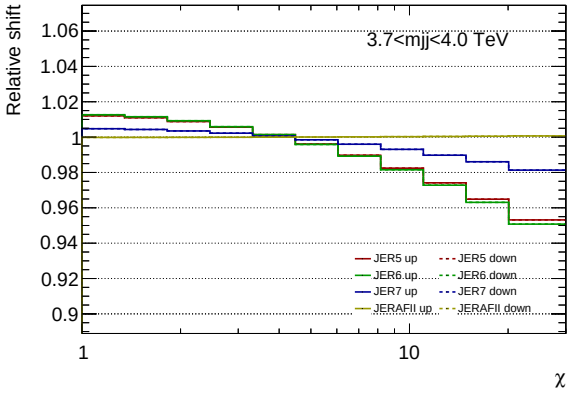

(d) Reduced JER uncertainties 5–7 and uncertainty in difference between simulation and data.

Figure F.18: Smoothed reduced experimental uncertainties on the HQM sample ($n = 2$ and $M_D = 7$) TeV in $3.7 < m_{jj} < 4.0$ TeV.

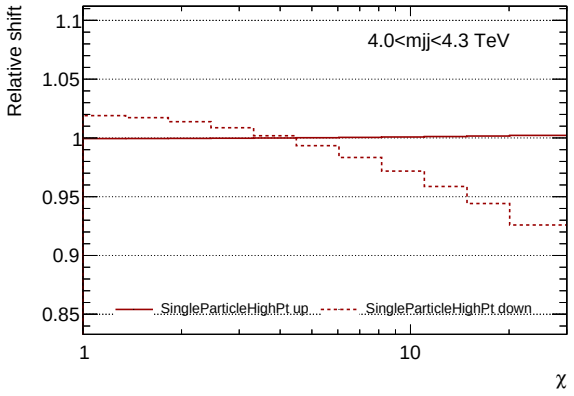

(a) Uncertainty in the single particle response measurement.

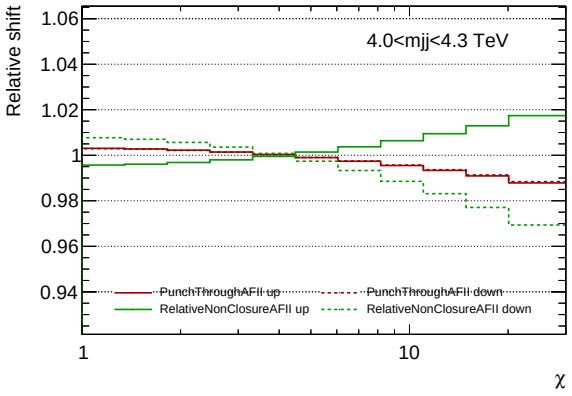

(b) Uncertainties in the correction of partially contained jets and remaining difference between data and MC simulation.

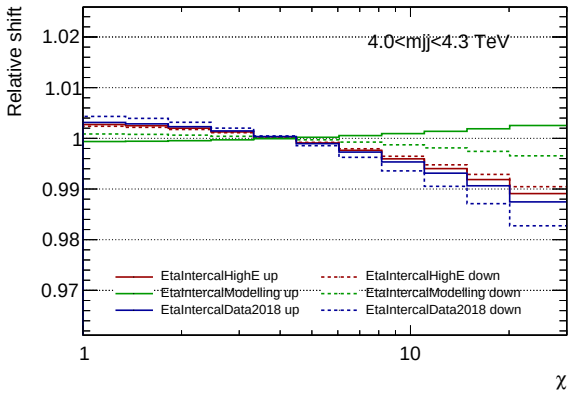

(c) Uncertainties on modelling and describing non-closure in high energy, and tile calibration.

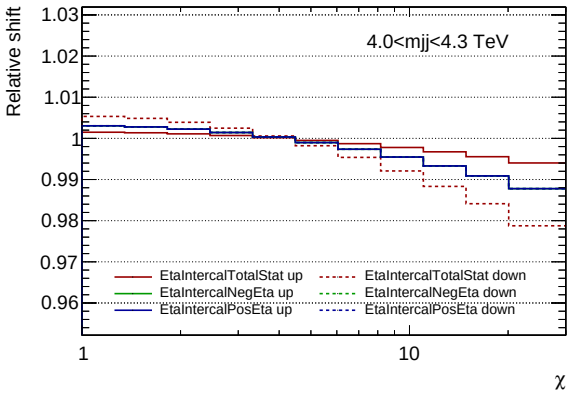

(d) Statistical uncertainty in η intercalibration and systematic uncertainty on describing non-closure at $\eta \approx \pm 2.4$.

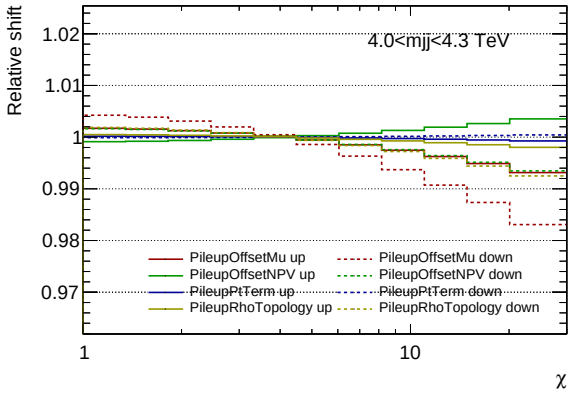

(e) Uncertainties on modelling the pile-up offset term and residual correction.

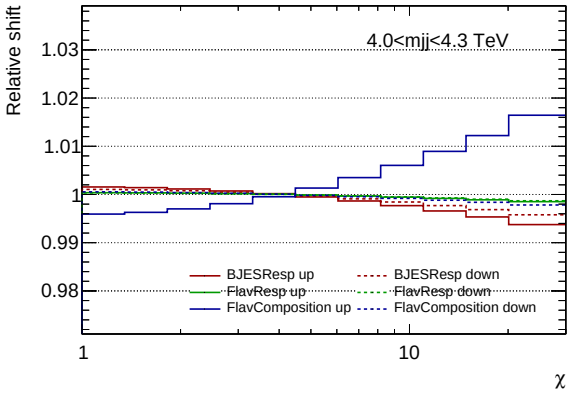

(f) Uncertainty in the response of gluon-initiated and b-quark initiated jets and the composition of quarks and gluons.

Figure F.19: Smoothed experimental uncertainties on the HQM sample ($n = 2$ and $M_D = 7$) TeV in $4.0 < m_{jj} < 4.3$ TeV.

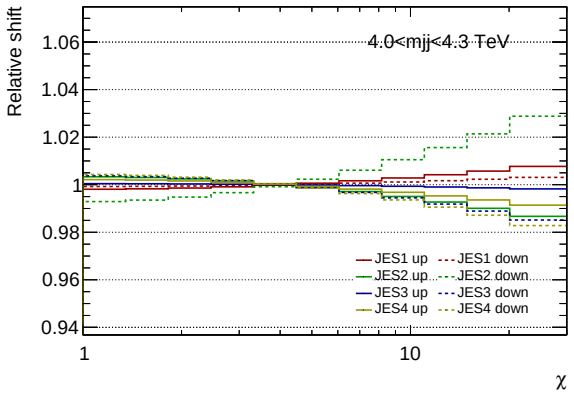

(a) Reduced *in situ* JES uncertainties 1–4.

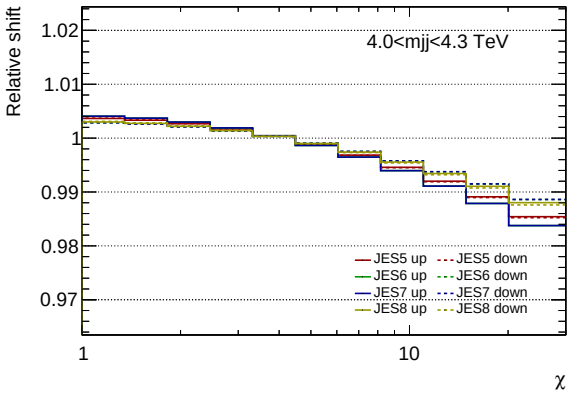

(b) Reduced *in situ* JES uncertainties 5–8.

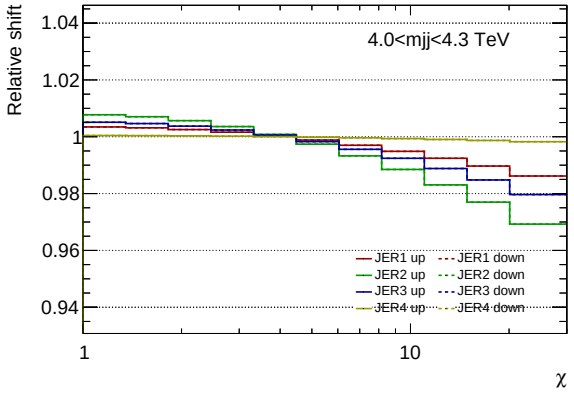

(c) Reduced JER uncertainties 1–4.

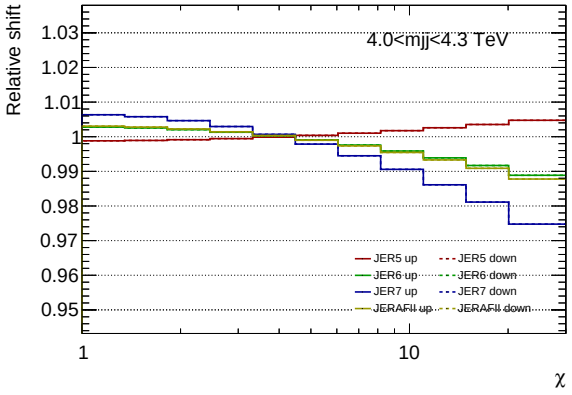

(d) Reduced JER uncertainties 5–7 and uncertainty in difference between simulation and data.

Figure F.20: Smoothed reduced experimental uncertainties on the HQM sample ($n = 2$ and $M_D = 7$) TeV in $4.0 < m_{jj} < 4.3$ TeV.

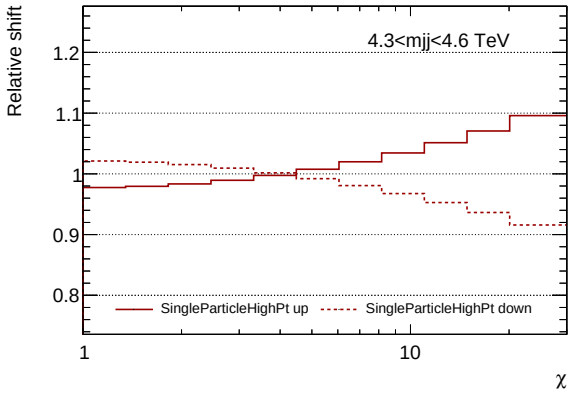

(a) Uncertainty in the single particle response measurement.

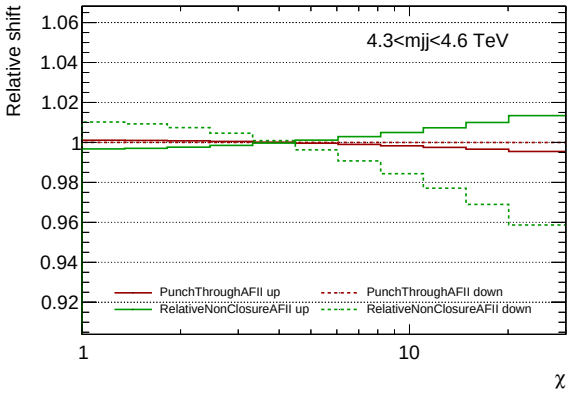

(b) Uncertainties in the correction of partially contained jets and remaining difference between data and MC simulation.

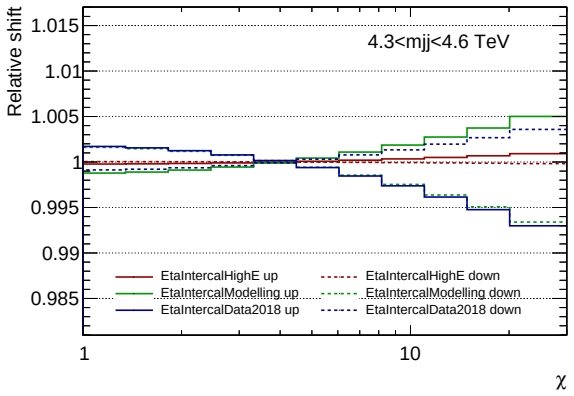

(c) Uncertainties on modelling and describing non-closure in high energy, and tile calibration.

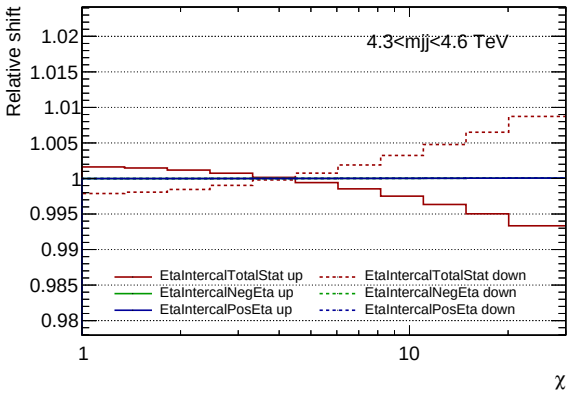

(d) Statistical uncertainty in η intercalibration and systematic uncertainty on describing non-closure at $\eta \approx \pm 2.4$.

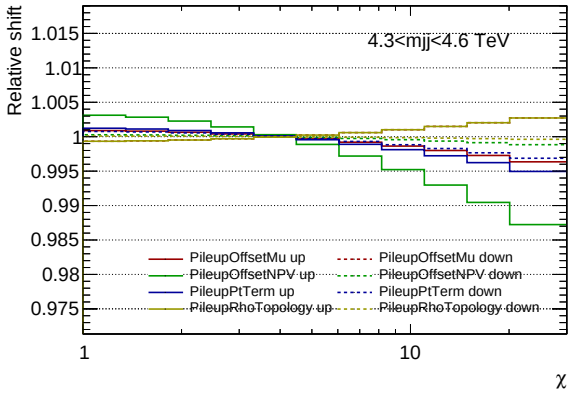

(e) Uncertainties on modelling the pile-up offset term and residual correction.

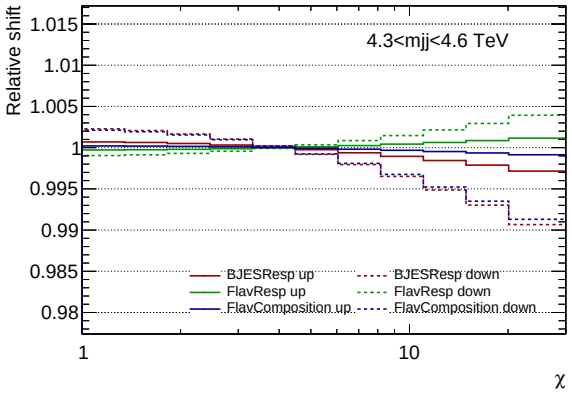

(f) Uncertainty in the response of gluon-initiated and b-quark initiated jets and the composition of quarks and gluons.

Figure F.21: Smoothed experimental uncertainties on the HQM sample ($n = 2$ and $M_D = 7$) TeV in $4.3 < m_{jj} < 4.6$ TeV.

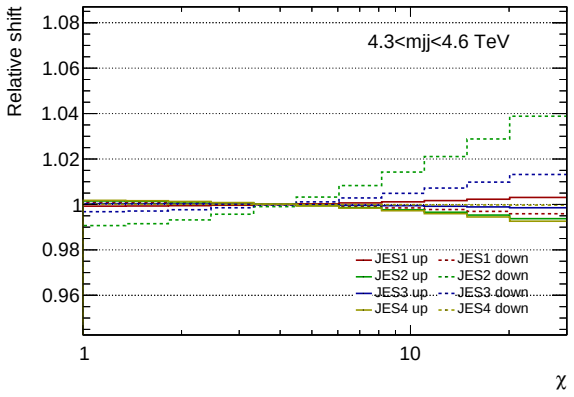

(a) Reduced *in situ* JES uncertainties 1–4.

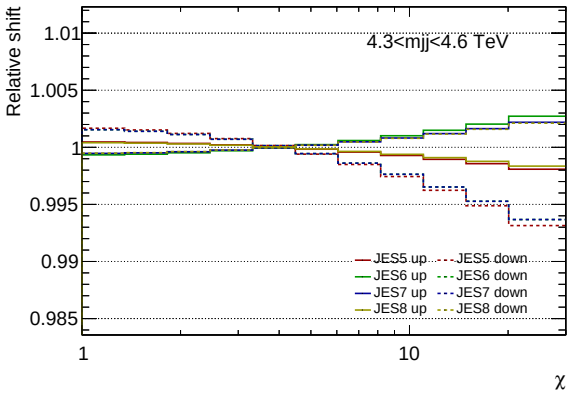

(b) Reduced *in situ* JES uncertainties 5–8.

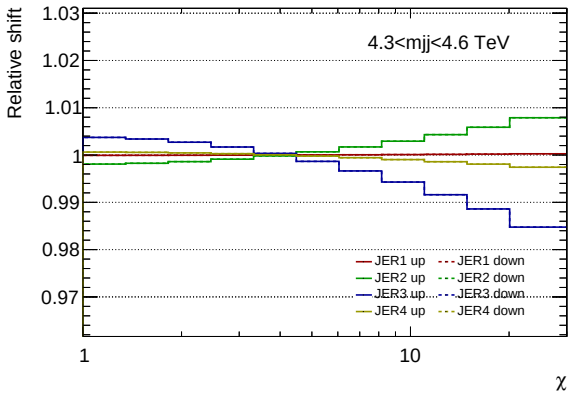

(c) Reduced JER uncertainties 1–4.

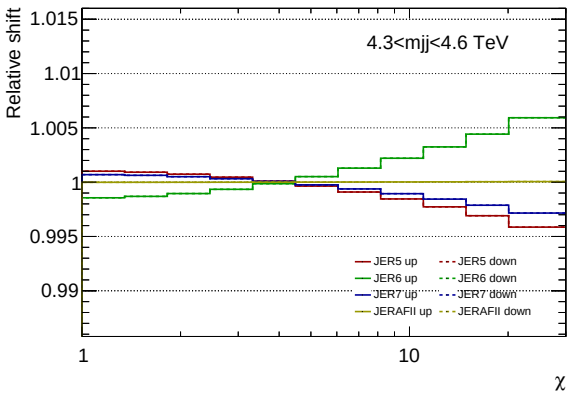

(d) Reduced JER uncertainties 5–7 and uncertainty in difference between simulation and data.

Figure F.22: Smoothed reduced experimental uncertainties on the HQM sample ($n = 2$ and $M_D = 7$) TeV in $4.3 < m_{jj} < 4.6$ TeV.

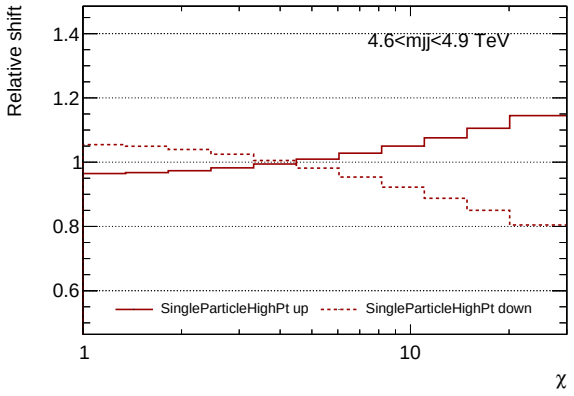

(a) Uncertainty in the single particle response measurement.

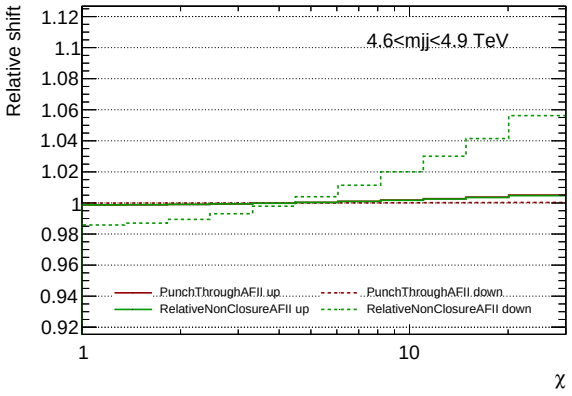

(b) Uncertainties in the correction of partially contained jets and remaining difference between data and MC simulation.

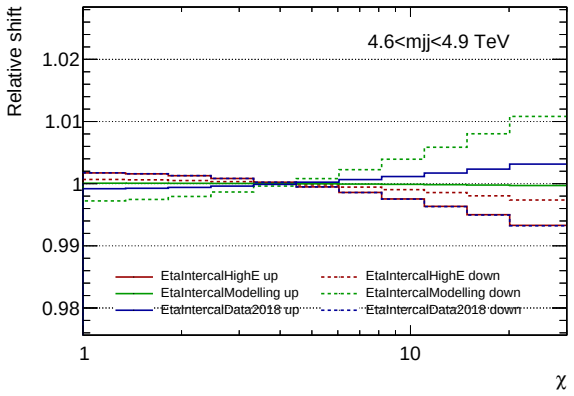

(c) Uncertainties on modelling and describing non-closure in high energy, and tile calibration.

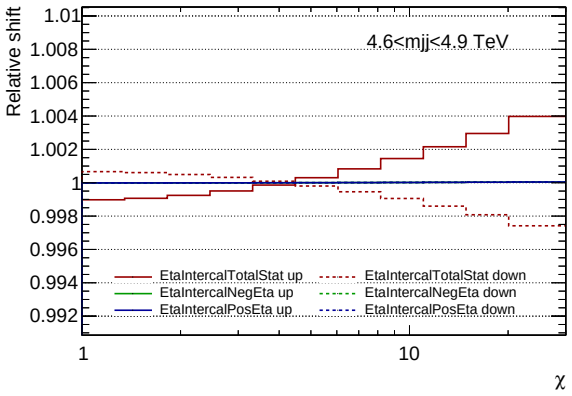

(d) Statistical uncertainty in η intercalibration and systematic uncertainty on describing non-closure at $\eta \approx \pm 2.4$.

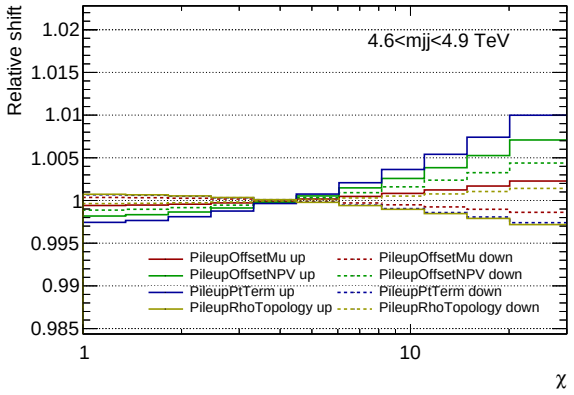

(e) Uncertainties on modelling the pile-up offset term and residual correction.

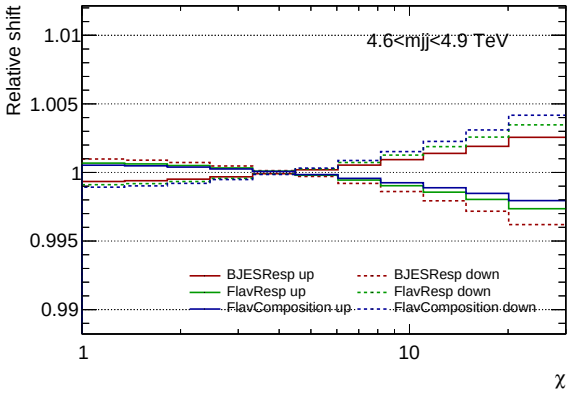

(f) Uncertainty in the response of gluon-initiated and b-quark initiated jets and the composition of quarks and gluons.

Figure F.23: Smoothed experimental uncertainties on the HQM sample ($n = 2$ and $M_D = 7$) TeV in $4.6 < m_{jj} < 4.9$ TeV.

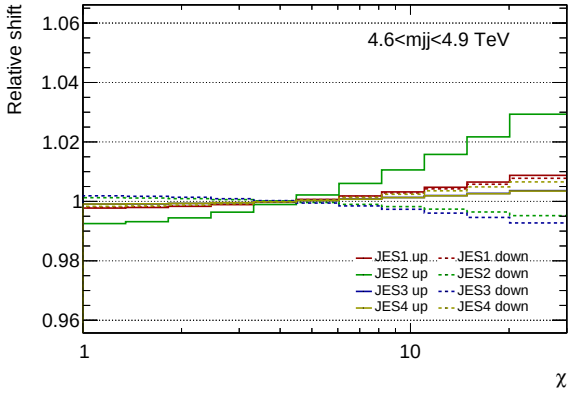

(a) Reduced *in situ* JES uncertainties 1–4.

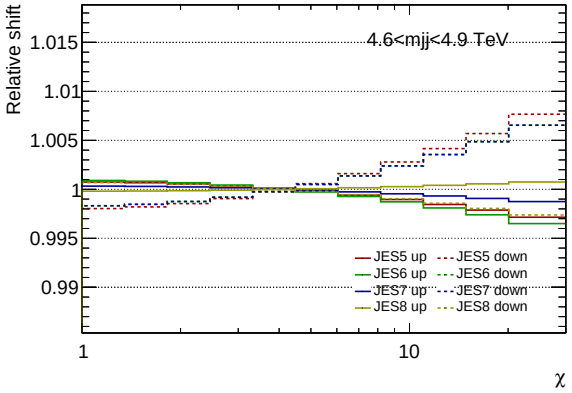

(b) Reduced *in situ* JES uncertainties 5–8.

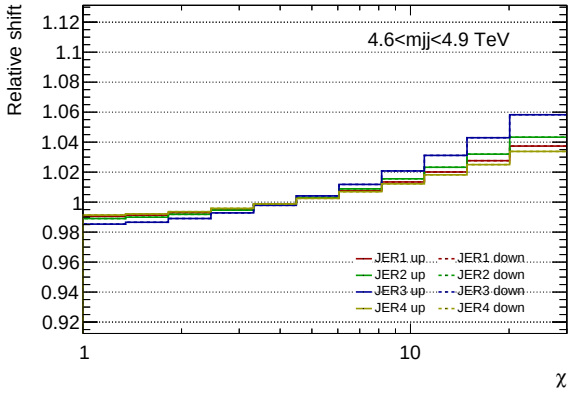

(c) Reduced JER uncertainties 1–4.

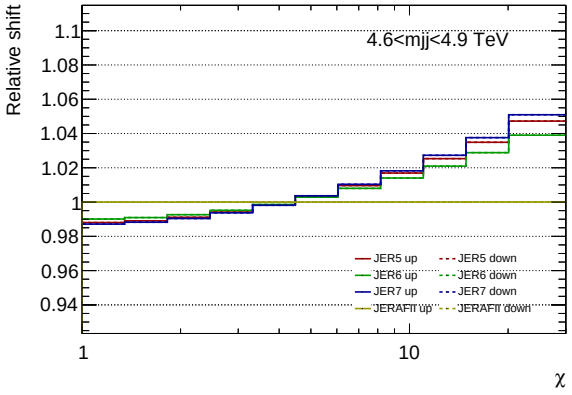

(d) Reduced JER uncertainties 5–7 and uncertainty in difference between simulation and data.

Figure F.24: Smoothed reduced experimental uncertainties on the HQM sample ($n = 2$ and $M_D = 7$) TeV in $4.6 < m_{jj} < 4.9$ TeV.

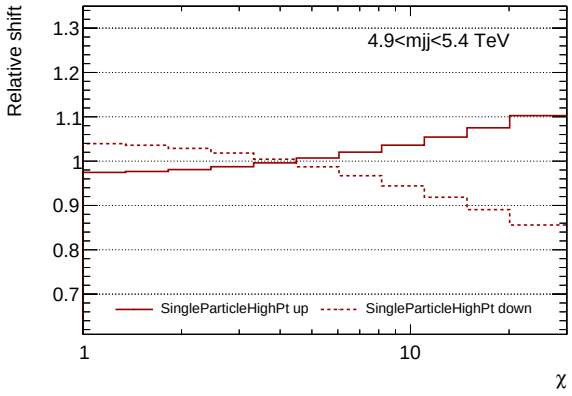

(a) Uncertainty in the single particle response measurement.

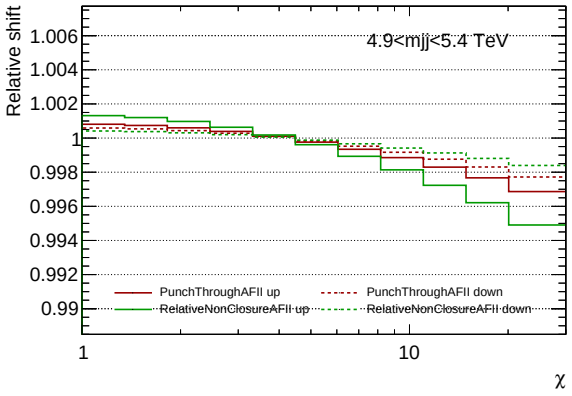

(b) Uncertainties in the correction of partially contained jets and remaining difference between data and MC simulation.

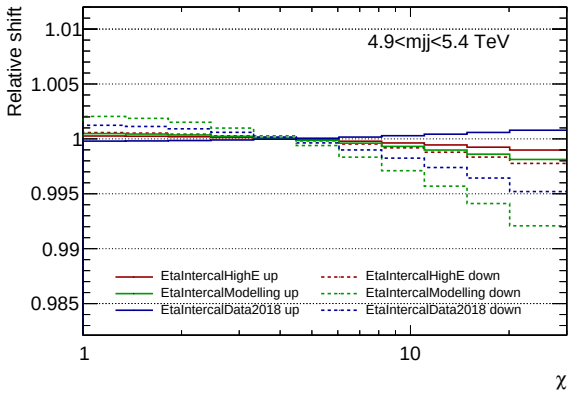

(c) Uncertainties on modelling and describing non-closure in high energy, and tile calibration.

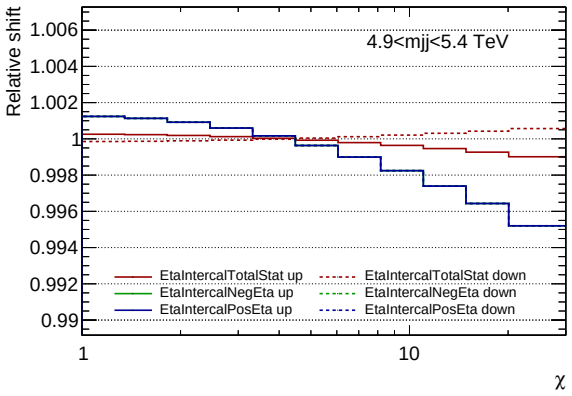

(d) Statistical uncertainty in η intercalibration and systematic uncertainty on describing non-closure at $\eta \approx \pm 2.4$.

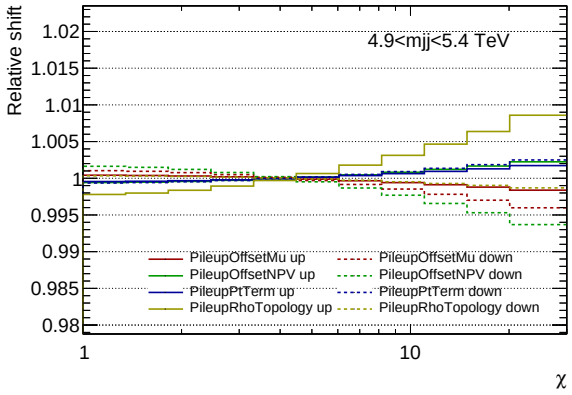

(e) Uncertainties on modelling the pile-up offset term and residual correction.

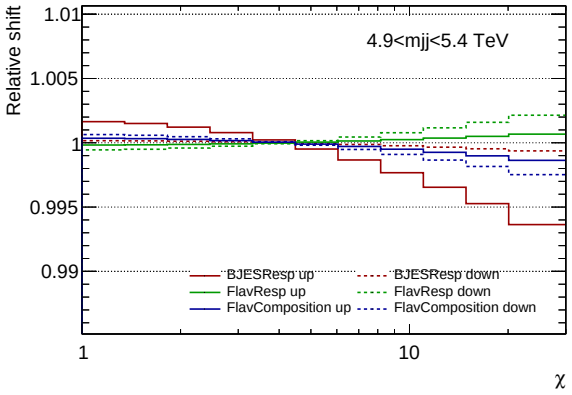

(f) Uncertainty in the response of gluon-initiated and b-quark initiated jets and the composition of quarks and gluons.

Figure F.25: Smoothed experimental uncertainties on the HQM sample ($n = 2$ and $M_D = 7$) TeV in $4.9 < m_{jj} < 5.4$ TeV.

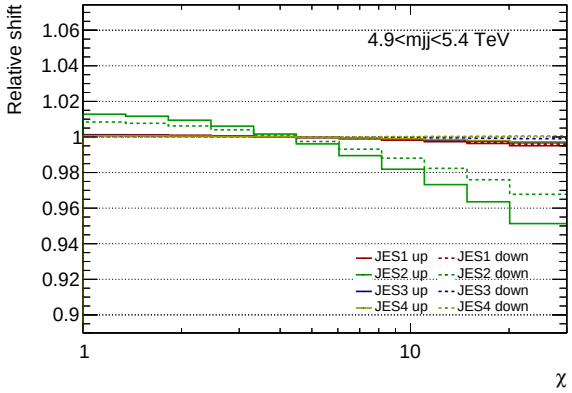

(a) Reduced *in situ* JES uncertainties 1–4.

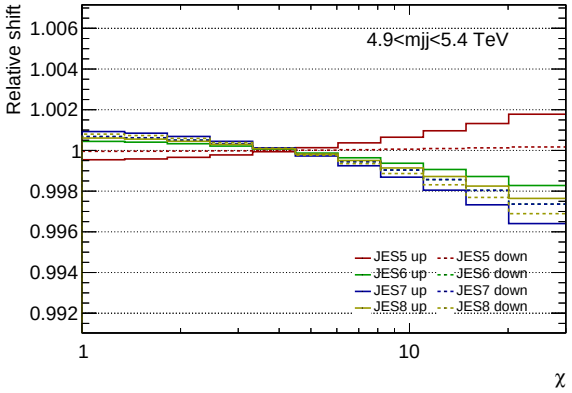

(b) Reduced *in situ* JES uncertainties 5–8.

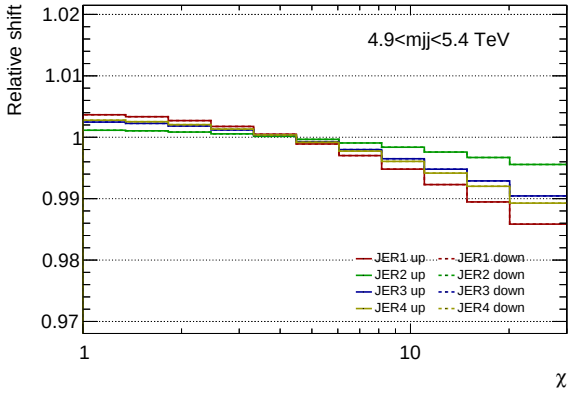

(c) Reduced JER uncertainties 1–4.

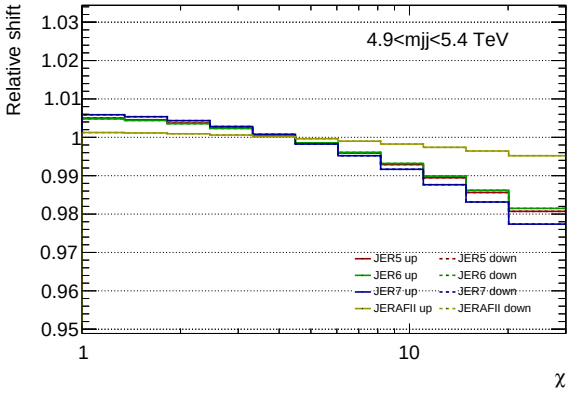

(d) Reduced JER uncertainties 5–7 and uncertainty in difference between simulation and data.

Figure F.26: Smoothed reduced experimental uncertainties on the HQM sample ($n = 2$ and $M_D = 7$) TeV in $4.9 < m_{jj} < 5.4$ TeV.

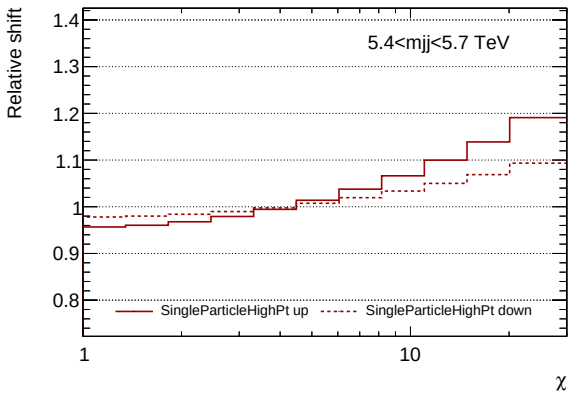

(a) Uncertainty in the single particle response measurement.

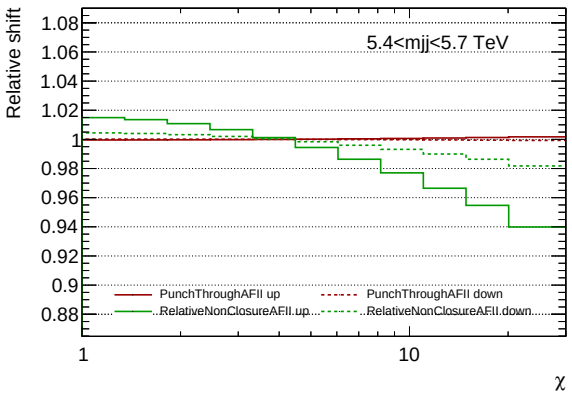

(b) Uncertainties in the correction of partially contained jets and remaining difference between data and MC simulation.

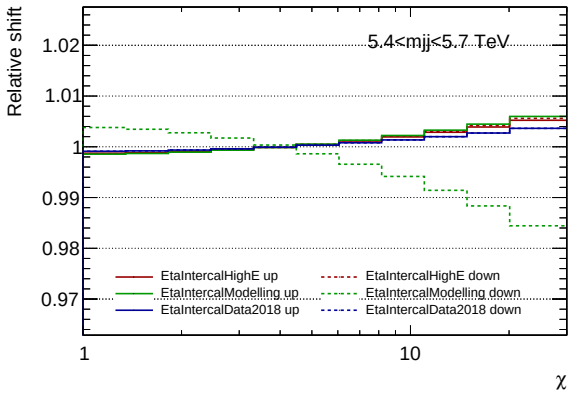

(c) Uncertainties on modelling and describing non-closure in high energy, and tile calibration.

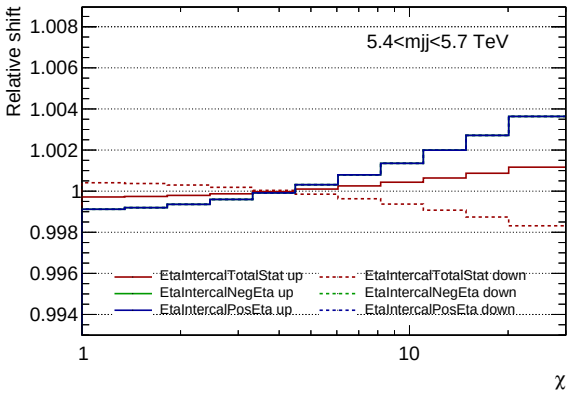

(d) Statistical uncertainty in η intercalibration and systematic uncertainty on describing non-closure at $\eta \approx \pm 2.4$.

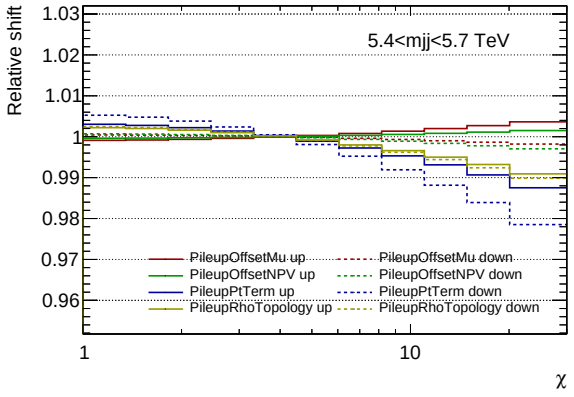

(e) Uncertainties on modelling the pile-up offset term and residual correction.

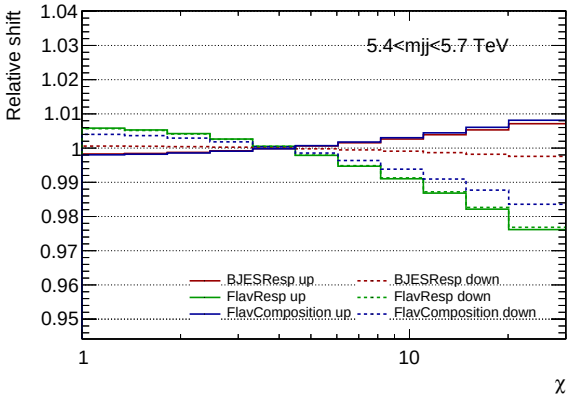

(f) Uncertainty in the response of gluon-initiated and b-quark initiated jets and the composition of quarks and gluons.

Figure F.27: Smoothed experimental uncertainties on the HQM sample ($n = 2$ and $M_D = 7$) TeV in $5.4 < m_{jj} < 5.7$ TeV.

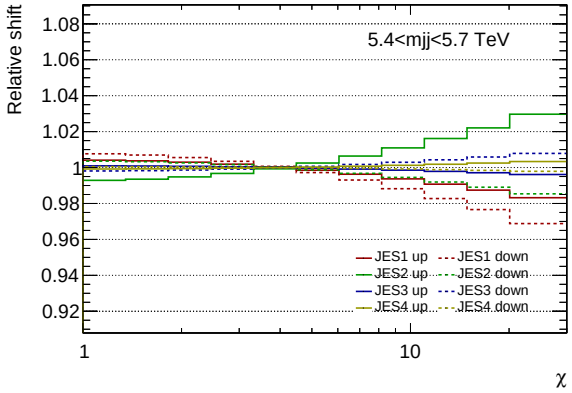

(a) Reduced *in situ* JES uncertainties 1–4.

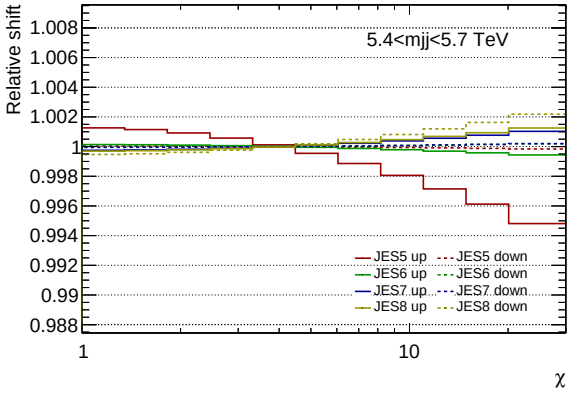

(b) Reduced *in situ* JES uncertainties 5–8.

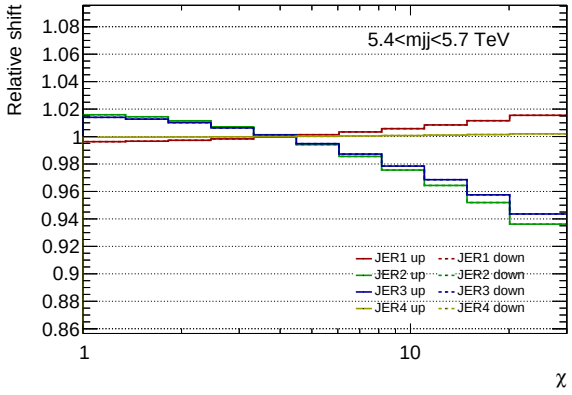

(c) Reduced JER uncertainties 1–4.

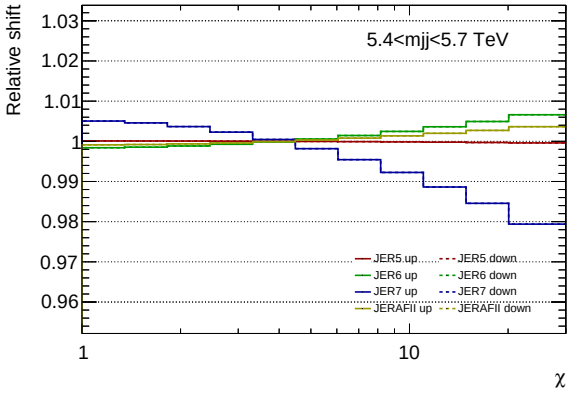

(d) Reduced JER uncertainties 5–7 and uncertainty in difference between simulation and data.

Figure F.28: Smoothed reduced experimental uncertainties on the HQM sample ($n = 2$ and $M_D = 7$) TeV in $5.4 < m_{jj} < 5.7$ TeV.